TECHNISCHE UNIVERSITÄT MÜNCHEN

TUM School of Medicine and Health

Quantitative Susceptibility Mapping Outside the Brain

Christof Andreas Böhm

Abstract

Quantitative susceptibility mapping (QSM) estimates the magnetic susceptibility of tissue and constitutes an unique contrast in magnetic resonance imaging (MRI). The field of QSM has seen a surge of research attention and focus since the early 2010s, with an ever-growing number of studies being conducted. QSM has been applied mainly in the brain to investigate physiology, pathology, and function. Specifically, QSM has been used to measure blood oxygen saturation, to quantify iron deposition in multiple sclerosis, to detect cerebral microbleeds, to measure iron accumulation in demyelinating disease, to distinguish intracranial calcifications from hemorrhages and many more. However, QSM is also of high interest for applications outside the brain, which has traditionally been an under-explored area of research. Nevertheless, a few studies have been performed proposing QSM for the quantification of hepatic iron overload, the visualization of prostatic calcifications, the assessment of bone mineral density (BMD), the measurement of heart chamber oxygenation, the detection of hemosiderin deposition in hemophilic arthropathy, the measurement of placental oxygenation, the characterization liver fibrosis, the assessment of renal tissue microstructure, the assessment of cartilage degeneration and calcium changes in the fetal spine.

The majority of existing applications for QSM in the body have been explored using methodologies originally developed for brain studies. Directly adopting these approaches for body regions may result in inaccurate susceptibility estimations, as some methods, such as the widely used Laplacian Boundary Value (LBV) technique for background field removal, contravene inherent assumptions when applied outside the brain. Moreover, an accurate field map is sometimes simply not available. As a result, the primary objective of this thesis is to devise and implement technical methodologies explicitly designed for QSM applications within the body, while validating these proposed techniques through in silico and in vivo assessments.

The present cumulative thesis bundles five journal publications in the field of body QSM aiming i) to show that accurate field-mapping is an essential prerequisite to estimate accurate local susceptibility, ii) to use advanced QSM reconstruction algorithm to reliably remove susceptibility induced phase changes, iii) to develop advanced body

QSM reconstruction algorithms to allow robust QSM in the presence of multiple chemical species (water, fat, and silicone) for the first time, and iv) to develop a new acquisition methodology that allows for substantially faster acquisitions of QSM images in the body.

In the first journal publication, a graph-cut based optimization algorithm was developed for the estimation of high-resolution field maps. Traditionally, the field map has often been regarded as a secondary parameter, and the performance of the algorithms has largely been assessed with respect to the accuracy of the water- and fat-separated images or the estimation of a proton density fat fraction (PDFF). Since the field map parameter was of limited interest, extensive smoothing was frequently applied to achieve more robust water/fat separation results. However, this smoothing of the field map significantly constrained the estimation of susceptibility, as values at interfaces of different tissue types largely determine the bulk susceptibility of the tissue. The proposed methodology was examined through simulations and in vivo scans and was found to produce non-wrapped, non-smoothed high-resolution field maps in a reduced processing time. Susceptibility maps based on the field maps obtained using the proposed method demonstrated a significant increase in both accuracy and precision.

The second journal publication proposes the use of an specifically tailored QSM algorithm to estimate and remove susceptibility-induced phase changes in double-echo gradient-echo magnetic resonance (MR) thermometry measurements. The proton resonance frequency shift (PRFS) of water with temperature allows for the volumetric estimation of temperature changes. This can be of high value in mild hyperthermia assisted chemotherapy or high intensity focused ultrasound (HIFU) ablation treatments. However, the phase is often dominated by susceptibility artifacts from the movement of air between shots and can be a few orders of magnitude larger than the temperature-induced phase shift. The proposed method showed significantly improved accuracy and precision over conventional B_0-drift corrected temperature maps or temperature maps corrected by previously proposed methods for susceptibility-induced phase removal.

In the third journal publication, a novel dipole inversion algorithm was proposed, designed to estimate susceptibility directly from complex multi-echo gradient-echo data in regions where both water and fat coexist. As the multi-echo data contain Gaussian noise, the negative log-likelihood of the probability density function takes the well-known form $||y - Ax||_2^2$, where y represents the measurements, A denotes the forward model, and x signifies the parameter of interest. Due to the accurate noise modeling, the proposed method exhibited reduced noise amplification in silico and in vivo compared to previously proposed methods. Moreover, this approach inherently

eliminates the need for heuristic modeling of input data accuracy, which is commonly performed in most dipole inversion methods. In a small patient study, QSM maps based on the proposed method successfully differentiated between osteolytic and osteoblastic bone metastases, corroborating the findings of reference computed tomography (CT) images.

In the fourth journal publication, *effective* multipeak in-phase echo times were devised for the simplified acquisition of QSM maps in water/fat regions. This novel methodology suggested utilizing meticulously chosen echo times to eliminate the phase contributions of fat. The derived echo times allow for the reduction of acquired echoes and enabled a more streamlined and accelerated field map estimation. Through a simulation, a phantom study, and in vivo examinations across various anatomies, the proposed methodology demonstrated quantitative performance equivalent to water/fat separation-based techniques, while offering a considerably faster approach.

In the fifth journal publication, a preconditioned total field dipole inversion algorithm was proposed for the direct estimation of susceptibility from complex multi-echo gradient-echo data in the breast, accounting for the presence of water, fat, and silicone. This method expands upon the approach presented in the second journal publication to accommodate three chemical species. However, addressing the chemical shift of silicone is not the sole challenge; the substantial susceptibility difference compared to breast tissue must also be considered. Firstly, silicone implants are utilized to enhance the problem's conditioning when present. Secondly, the spatial homogeneity of the silicone implant is exploited by incorporating a regularization term that enforces uniform susceptibility within the silicone. The proposed method results in significantly reduced quantitative and qualitative errors in both in silico and in vivo evaluations.

List of Included Journal Publications

The present dissertation is based on the following five journal publications:

JP-I **C. Boehm**, M. N. Diefenbach, M. R. Makowski, and D. C. Karampinos, "Improved body quantitative susceptibility mapping by using a variable-layer single-min-cut graph-cut for field-mapping," *Magnetic Resonance in Medicine*, vol. 85, no. 3, pp. 1697–1712, 2020.

JP-II **C. Boehm**, M. Goeger-Neff, H. T. Mulder, B. Zilles, L. H. Lindner, G. C. van Rhoon, D. C. Karampinos, and M. Wu, "Susceptibility artifact correction in mr thermometry for monitoring of mild radiofrequency hyperthermia using total field inversion," *Magnetic Resonance in Medicine*, vol. 88, no. 1, pp. 120–132, 2022.

JP-III **C. Boehm**, N. Sollmann, J. Meineke, S. Ruschke, M. Dieckmeyer, K. Weiss, C. Zimmer, M. R. Makowski, T. Baum, and D. C. Karampinos, "Preconditioned water-fat total field inversion: Application to spine quantitative susceptibility mapping," *Magnetic Resonance in Medicine*, vol. 87, no. 1, pp. 417–430, 2021.

JP-IV **C. Boehm**, S. Schlaeger, J. Meineke, K. Weiss, M. R. Makowski, and D. C. Karampinos, "On the water-fat in-phase assumption for quantitative susceptibility mapping," *Magnetic Resonance in Medicine*, vol. 89, no. 3, pp. 1068–1082, 2022.

JP-V **C. Boehm**, J. K. Stelter, J. Meineke, K. Weiss, T. Borde M. R. Makowski, E. M. Fallenberg and D. C. Karampinos, "Robust quantitative susceptibility mapping in the breast using a preconditioned water–fat–silicone total field inversion algorithm," *Magnetic Resonance in Medicine*, vol. n/a, no. n/a.

Please refer to Chapter 3 for the publications.

List of Related Publications

The author contributed also to the following subject-related journal publications (ordered by year of appearance):

J1 N. Sollmann, M. T. Löffler, S. Kronthaler, **C. Böhm**, M. Dieckmeyer, S. Ruschke, J. S. Kirschke, J. Carballido-Gamio, D. C. Karampinos, R. Krug, and T. Baum, "MRI-based quantitative osteoporosis imaging at the spine and femur," *Journal of Magnetic Resonance Imaging*, vol. 54, no. 1, pp. 12–35, 2021.

J2 B. J. Schwaiger, C. Schneider, S. Kronthaler, F. T. Gassert, **C. Boehm**, D. Pfeiffer, T. Baum, J. S. Kirschke, D. C. Karampinos, M. R. Makowski, K. Woertler, M. Wurm, and A. S. Gersing, "CT-like images based on T1 spoiled gradient-echo and ultra-short echo time MRI sequences for the assessment of vertebral fractures and degenerative bone changes of the spine," *European radiology*, vol. 31, pp. 4680–4689, 7 2021.

J3 D. Weidlich, J. Honecker, **C. Boehm**, S. Ruschke, D. Junker, A. T. Van, M. R. Makowski, C. Holzapfel, M. Claussnitzer, H. Hauner, and D. C. Karampinos, "Lipid droplet–size mapping in human adipose tissue using a clinical 3T system," *Magnetic Resonance in Medicine*, vol. 86, no. 3, pp. 1256–1270, 2021.

J4 Y. Leonhardt, F. T. Gassert, G. Feuerriegel, F. G. Gassert, S. Kronthaler, **C. Boehm**, A. Kufner, S. Ruschke, T. Baum, B. J. Schwaiger, M. R. Makowski, D. C. Karampinos, and A. S. Gersing, "Vertebral bone marrow T2* mapping using chemical shift encoding-based water-fat separation in the quantitative analysis of lumbar osteoporosis and osteoporotic fractures," *Quantitative imaging in medicine and surgery*, vol. 11, pp. 3715–3725, 8 2021.

J5 G. C. Feuerriegel, F. K. Kopp, D. Pfeiffer, J. Pogorzelski, M. Wurm, Y. Leonhardt, **C. Boehm**, S. Kronthaler, D. C. Karampinos, J. Neumann, B. J. Schwaiger, M. R. Makowski, K. Woertler, and A. S. Gersing, "Evaluation of MR-derived simulated CT-like images and simulated radiographs compared to conventional

radiography in patients with shoulder pain: a proof-of-concept study," *BMC Musculoskeletal Disorders*, vol. 23, p. 122, 2 2022.

J6　S. Kronthaler, **C. Boehm**, G. Feuerriegel, P. Börnert, U. Katscher, K. Weiss, M. R. Makowski, B. J. Schwaiger, A. S. Gersing, and D. C. Karampinos, "Assessment of vertebral fractures and edema of the thoracolumbar spine based on water-fat and susceptibility-weighted images derived from a single ultra-short echo time scan," *Magnetic Resonance in Medicine*, vol. 87, no. 4, pp. 1771–1783, 2022.

J7　N. Sollmann, E. A. Becherucci, **C. Boehm**, M. E. Husseini, S. Ruschke, E. Burian, J. S. Kirschke, T. M. Link, K. Subburaj, D. C. Karampinos, R. Krug, T. Baum, and M. Dieckmeyer, "Texture analysis using CT and chemical shift encoding-based water-fat MRI can improve differentiation between patients with and without osteoporotic vertebral fractures," *Frontiers in Endocrinology*, vol. 12, 2022.

J8　F. T. Gassert, A. Kufner, F. G. Gassert, Y. Leonhardt, S. Kronthaler, B. J. Schwaiger, **C. Boehm**, M. R. Makowski, J. S. Kirschke, T. Baum, D. C. Karampinos, and A. S. Gersing, "MR-based proton density fat fraction (PDFF) of the vertebral bone marrow differentiates between patients with and without osteoporotic vertebral fractures," *Osteoporosis international : a journal established as result of cooperation between the European Foundation for Osteoporosis and the National Osteoporosis Foundation of the USA*, vol. 33, pp. 487–496, 2 2022.

J9　S. Kronthaler, M. N. Diefenbach, **C. Boehm**, M. Zamskiy, M. R. Makowski, T. Baum, N. Sollmann, and D. C. Karampinos, "On quantification errors of R_2^* and proton density fat fraction mapping in trabecularized bone marrow in the static dephasing regime," *Magnetic Resonance in Medicine*, vol. 88, no. 3, pp. 1126–1139, 2022.

J10　N. Sollmann, J. S. Kirschke, S. Kronthaler, **C. Boehm**, M. Dieckmeyer, D. Vogele, C. Kloth, C. G. Lisson, J. Carballido-Gamio, T. M. Link, D. C. Karampinos, S. Karuppasamy, M. Beer, R. Krug, and T. Baum, "Imaging of the osteoporotic spine - quantitative approaches in diagnostics and for the prediction of the individual fracture risk," *RöFo - Fortschritte auf dem Gebiet der Röntgenstrahlen und der bildgebenden Verfahren*, vol. 194, no. 10, pp. 1088–1099, 2022.

J11　J. K. Stelter, **C. Boehm**, S. Ruschke, K. Weiss, M. N. Diefenbach, M. Wu, T. Borde, G. P. Schmidt, M. R. Makowski, E. M. Fallenberg, and D. C. Karampinos, "Hierarchical multi-resolution graph-cuts for water-fat-silicone separation in breast

MRI" *IEEE Transactions on Medical Imaging*, vol. 41, no. 11, pp. 3253–3265, 2022.

J12 T. Greve, N. M. Rayudu, M. Dieckmeyer, **C. Boehm**, S. Ruschke, E. Burian, C. Kloth, J. S. Kirschke, D. C. Karampinos, T. Baum, K. Subburaj, and N. Sollmann, "Finite element analysis of osteoporotic and osteoblastic vertebrae and its association with the proton density fat fraction from chemical shift encoding-based water-fat MRI - a preliminary study," *Frontiers in Endocrinology*, vol. 13, 2022.

J13 G. C. Feuerriegel, S. Kronthaler, **C. Boehm**, M. Renz, Y. Leonhardt, F. Gassert, S. C. Foreman, K. Weiss, M. Wurm, T. Liebig, M. R. Makowski, B. J. Schwaiger, D. C. Karampinos, and A. S. Gersing, "Diagnostic value of water-fat-separated images and CT-like susceptibility-weighted images extracted from a single ultrashort echo time sequence for the evaluation of vertebral fractures and degenerative changes of the spine," *European Radiology*, vol. 33, no. 2, pp. 1445-1455, 2022.

J14 F. T. Gassert, L. Glanz, **C. Boehm**, J. Stelter, F. G. Gassert, Y. Leonhardt, G. C. Feuerriegel, M. Graf, M. Wurm, T. Baum, R. F. Braren, B. J. Schwaiger, M. R. Makowski, D. Karampinos, and A. S. Gersing, "Associations between bone mineral density and longitudinal changes of vertebral bone marrow and paraspinal muscle composition assessed using mr-based proton density fat fraction and T2* maps in patients with and without osteoporosis," *Diagnostics*, vol. 12, no. 10, p. 2467, 2022.

J15 T. Borde, M. Wu, S. Ruschke, **C. Boehm**, J. Stelter, K. Weiss, S. Metz, M. R. Makowski, D. C. Karampinos, and E. M. Fallenberg, "Assessing breast density using the chemical-shift encoding-based proton density fat fraction in 3-T MRI," *European Radiology*, online ahead of print, 2022.

The author contributed also to the following book chapter:

B1 S. Ruschke, C. Zoellner, **C. Boehm**, M. N. Diefenbach, and D. C. Karampinos, "Chapter 14 - chemical shift encoding-based water-fat separation," in *Magnetic Resonance Image Reconstruction* (M. Akçakaya, M. Doneva, and C. Prieto, eds.), vol. 7 of *Advances in Magnetic Resonance Technology and Applications*, pp. 391–418, Academic Press, 2022.

The author contributed also to the following conference abstracts (ordered by year of appearance):

C1 **C. Böhm**, M. N. Diefenbach, A. Haase, and D. C. Karampinos, "Accelerated Single-Min-Cut Graph-Cut Algorithm Using a Variable-Layer Graph Construction Improves Field-Mapping in Water–Fat Regions," in *Proceedings 27. Annual Meeting International Society for Magnetic Resonance in Medicine*, vol. 27, (Montreal, Canada), p. 4007, `https://index.mirasmart.com/ISMRM2019/PDFfiles/4007.html`, 2019. Digital Poster.

C2 **C. Böhm**, M. N. Diefenbach, J. Meineke, A. Haase, and D. C. Karampinos, "Improved Body Quantitative Susceptibility Mapping by Using a Variable-Layer Single-Min-Cut Graph-Cut Algorithm for Field-Mapping," in *Proceedings 27. Annual Meeting International Society for Magnetic Resonance in Medicine*, vol. 27, (Montreal, Canada), p. 0693, `https://index.mirasmart.com/ISMRM2019/PDFfiles/0693.html`, 2019. Oral presentation, **Magna cum laude merit award**.

C3 M. N. Diefenbach, **C. Böhm**, J. Meineke, C. Liu, and D. C. Karampinos, "One-Dimensional k-Space Metrics on Cone Surfaces for Quantitative Susceptibility Mapping," in *Proceedings 27. Annual Meeting International Society for Magnetic Resonance in Medicine*, vol. 27, (Montreal, Canada), p. 0322, `https://cds.ismrm.org/protected/19MPresentations/abstracts/0322.html`, 2019. Oral presentation, Magna cum laude merit award.

C4 C. Zoellner, S. Kronthaler, **C. Böhm**, S. Ruschke, M. Diefenbach, D. Franz, and D. C. Karampinos, "Fat deblurring in golden angle radial stack-of-stars multi-echo gradient echo for navigator-gated high-resolution water-fat imaging," in *ISMRM Workshop on MRI of Obesity & Metabolic Disorders*, (Singapore, Singapore), 2019.

C5 **C. Böhm**, M. N. Diefenbach, J. Meineke, A. Haase, and D. C. Karampinos, "Improved Body Quantitative Susceptibility Mapping by Using a Variable-Layer Single-Min-Cut Graph-Cut Algorithm for Field-Mapping," in *5th International Workshop on MRI Phase Contrast & QSM*, vol. 5, (Seoul, Korea), p. 81, 2019.

C6 **C. Böhm**, M. N. Diefenbach, J. Meineke, and D. C. Karampinos, "Fusion of Susceptibility Maps in k-Space based on One-Dimensional Error Metrics on Field-Map Data improves QSM," in *5th International Workshop on MRI Phase Contrast & QSM*, vol. 5, (Seoul, Korea), p. 25, 2019.

C7 **C. Böhm**, M. N. Diefenbach, J. Meineke, and D. C. Karampinos, "Estimating Magnetic Susceptibility Within a Hollow Cylinder and its Implications in Body

QSM," in *5th International Workshop on MRI Phase Contrast & QSM*, vol. 5, (Seoul, Korea), p. 26, 2019.

C8 **C. Böhm**, S. Kronthaler, M. N. Diefenbach, J. Meineke, and D. C. Karampinos, "Sampling and Modeling UTE Signals is Important to Estimate Bone Marrow Susceptibility," in *Proceedings 28. Annual Meeting International Society for Magnetic Resonance in Medicine*, vol. 28, (online), p. 3212, `http://archive.ismrm.org/2020/3212.html`, 2020.

C9 S. Kronthaler, **C. Böhm**, D. Weidlich, M. N. Diefenbach, and D. C. Karampinos, "Simultaneous imaging of trabecular and cortical bone by analyzing the multi-echo signal decay at UTEs and conventional TEs," in *Proceedings 28. Annual Meeting International Society for Magnetic Resonance in Medicine*, vol. 28, (Paris, France), p. 2767, `http://archive.ismrm.org/2020/2767.html`, 2020.

C10 **C. Böhm**, J. Oscanoa, S. Kronthaler, M. N. Diefenbach, A. Gersing, J. Meineke, and D. C. Karampinos, "Highly Accelerated Compressed-Sensing-Based Field-mapping is Possible for Body QSM Applications," in *Proceedings 28. Annual Meeting International Society for Magnetic Resonance in Medicine*, vol. 28, (online), p. 3209, `http://archive.ismrm.org/2020/3209.html`, 2020.

C11 **C. Böhm**, D. Weidlich, S. Kronthaler, and D. C. Karampinos, "On the Carbon Footprint of ISMRM's Annual Meeting: Analysis and Implications," in *Proceedings 28. Annual Meeting International Society for Magnetic Resonance in Medicine*, vol. 28, (online), p. 4156, `http://archive.ismrm.org/2020/4156.html`, 2020.

C12 B. Schwaiger, C. Schneider, S. Kronthaler, **C. Böhm**, C. Zöllner, S. Ruschke, J. Zapf, T. Baum, J. Kirschke, E. Rummeny, K. Wörtler, D. Karampinos, M. Wurm, and A. Gersing, "MR-derived CT-like images in comparison to conventional CT for the assessment of vertebral fractures and osseous degenerative changes in the thoracolumbar spine," in *54. Jahrestagung der deutschen Gesellschaft für Neuroradiologie e.V.*, vol. 54, (Frankfurt am Main, Germany), 2019.

C13 B. Schwaiger, C. Schneider, S. Kronthaler, **C. Böhm**, C. Zöllner, S. Ruschke, J. Zapf, T. Baum, J. Kirschke, E. Rummeny, K. Wörtler, D. Karampinos, M. Wurm, and A. Gersing, "MR-derived CT-like images in comparison to conventional CT for the assessment of vertebral fractures and osseous degenerative changes in the thoracolumbar spine," in *54. Jahrestagung der deutschen*

Gesellschaft für Neuroradiologie e.V., vol. 54, (Paris, France), `http://archive.ismrm.org/2020/4156.html`, 2019.

C14 **C. Boehm**, N. Sollmann, J. Meineke, S. Kronthaler, S. Ruschke, M. Dieckmeyer, K. Weiss, C. Zimmer, M. R. Makowski, T. Baum, and D. C. Karampinos, "Preconditioned water-fat total field inversion: application to spine quantitative susceptibility mapping (QSM)," in *Proceedings 29. Annual Meeting International Society for Magnetic Resonance in Medicine*, vol. 29, (online), p. 0792, 2021. **Summa Cum Laude Merit Award**.

C15 **C. Boehm**, M. Goeger-Neff, H. T. Mulder, B. Zilles, L. H. Lindner, G. C. van Rhoon, D. C. Karampinos, and M. Wu, "Susceptibility artifact correction in MR thermometry for monitoring of mild RF hyperthermia using total field inversion," in *Proceedings 29. Annual Meeting International Society for Magnetic Resonance in Medicine*, vol. 29, (online), p. 0247, 2021. **Magna cum laude merit award**.

C16 **C. Boehm**, M. N. Diefenbach, S. Kronthaler, J. Meineke, K. Weiss, M. R. Makowski, and D. C. Karampinos, "Quantitative susceptibility mapping in water–fat regions using in-phase echoes introduces significant quantification bias," in *Proceedings 29. Annual Meeting International Society for Magnetic Resonance in Medicine*, vol. 29, (online), p. 3972, `http://archive.ismrm.org/2021/3972.html`, 2021.

C17 D. Weidlich, J. Honecker, **C. Boehm**, S. Ruschke, D. Junker, A. Van, M. Makowski, C. Holzapfel, M. Claussnitzer, H. Hauner, and D. C. Karampinos, "Lipid droplet size mapping in human adipose tissue using a clinical 3 T system," in *Proceedings 29. Annual Meeting International Society for Magnetic Resonance in Medicine*, vol. 29, (online), p. 0752, 2021. **Magna cum laude merit award**.

C18 T. Borde, M. Wu, S. Ruschke, **C. Boehm**, K. Weiss, S. Metz, M. R. Makowski, and D. Karampinos, "Assessing breast density using the standardized proton density fat fraction based on chemical shift encoding-based water-fat separation," in *Proceedings 29. Annual Meeting International Society for Magnetic Resonance in Medicine*, vol. 29, (online), p. 0743, 2021.

C19 S. Kronthaler, **C. Boehm**, P. Börnert, U. Katscher, K. Weiss, M. R. Makowski, B. J. Schwaiger, A. S. Gersing, and D. C. Karampinos, "Simultaneous assessment of vertebral fractures and edema of the thoracolumbar spine on water-fat and SW

images derived from a single-TE UTE scan," in *Proceedings 29. Annual Meeting International Society for Magnetic Resonance in Medicine*, vol. 29, (Virtual Conference), p. 0527, 2021.

C20 S. Kronthaler, **C. Boehm**, K. Weiss, M. R. Makowski, and D. C. Karampinos, "On quantification errors of R2* and PDFF mapping in trabecularized bone marrow induced by the static dephasing regime," in *Proceedings 29. Annual Meeting International Society for Magnetic Resonance in Medicine*, vol. 29, (Virtual Conference), p. 0443, 2021. **Summa cum laude merit award**.

C21 J. K. Stelter, **C. Boehm**, S. Ruschke, M. N. Diefenbach, M. Wu, K. Weiss, T. Borde, S. Metz, M. R. Makowski, and D. C. Karampinos, "Optimal experimental design for quantitative water, fat and silicone separation using a variable projection method with 4 or 6 echoes at 3T," in *Proceedings 29. Annual Meeting International Society for Magnetic Resonance in Medicine*, vol. 29, (Virtual Conference), p. 3848, 2021.

C22 J. K. Stelter, **C. Boehm**, K. Weiss, M. N. Diefenbach, and D. C. Karampinos, "Layered graph-cuts for water–fat–silicone separation in chemical shift encoding-based breast MRI," in *23. Jahrestagung der Deutschen Sektion der ISMRM e.V.*, vol. 23, (Zurich, Switzerland), p. 13, 2021.

C23 F. Gassert, A. Kufner, F. Gassert, Y. Leonhardt, S. Kronthaler, B. Schwaiger, **C. Böhm**, M. Makowski, J. Kirschke, T. Baum, D. Karampinos, and A. Gersing, "MR-basierte proton-density fat fraction (PDFF) der lendenwirbelsäule zur differenzierung von osteoporotischen patienten mit und ohne wirbelkörperfrakturen," in *102. Deutscher Röntgenkongress der Deutschen Röntgengesellschaft e. V.*, 2021.

C24 C. Zoellner, S. Kronthaler, **C. Boehm**, S. Ruschke, M. Diefenbach, D. Franz, A. Hock, G. M. Beck, J. M. Peeters, and D. C. Karampinos, "Fat deblurring in golden angle radial stack-of-stars multi-echo gradient echo for navigator-gated high-resolution water-fat imaging," (Rotterdam, Netherlands), 2019.

C25 **C. Boehm**, J. K. Stelter, J. Meineke, S. Ruschke, K. Weiss, M. Wu, T. Borde, M. R. Makowski, E. M. Fallenberg, and D. C. Karampinos, "Mammography-like MR images using a preconditioned water-fat-silicone total field inversion QSM algorithm," in *Proceedings 30. Annual Meeting International Society for*

Magnetic Resonance in Medicine, vol. 30, (London, England), p. 1588, `http://archive.ismrm.org/2022/1588.html`, 2022.

C26 **C. Boehm**, J. Meineke, K. Weiss, M. R. Makowski, and D. C. Karampinos, "On the water–fat in-phase assumption for quantitative susceptibility mapping (QSM)," in *Proceedings 30. Annual Meeting International Society for Magnetic Resonance in Medicine*, vol. 30, (London, England), p. 2466, `http://archive.ismrm.org/2022/2466.html`, 2022.

C27 J. K. Stelter, **C. Boehm**, S. Ruschke, K. Weiss, M. N. Diefenbach, M. Wu, T. Borde, M. R. Makowski, E. M. Fallenberg, and D. C. Karampinos, "Hierarchical multi-resolution graph-cuts for water–fat–silicone separation in breast MRI," in *Proceedings 30. Annual Meeting International Society for Magnetic Resonance in Medicine*, vol. 30, (London, England), p. 0184, `http://archive.ismrm.org/2022/0184.html`, 2022.

C28 T. Borde, A. Wiedemann, J. Stelter, **C. Boehm**, S. Ruschke, K. Weiss, M. Wu, M. R. Makowski, D. C. Karampinos, and E. M. Fallenberg, "Silicone implant and fibrous capsule assessment based on water- fat-silicone images from a chemical shift encoding-based species separation," in *Proceedings 30. Annual Meeting International Society for Magnetic Resonance in Medicine*, vol. 30, (London, England), p. 7535, `http://archive.ismrm.org/2022/7535.html`, 2022.

C29 **C. Boehm**, J. K. Stelter, J. Meineke, S. Ruschke, K. Weiss, M. Wu, T. Borde, M. R. Makowski, E. M. Fallenberg, , and D. C. Karampinos, "Robust QSM in the breast using silicone-regularized water—fat—silicone total inversion," in *Joint Workshop on MR phase, magnetic susceptibility and electrical properties mapping*, vol. 5, (Lucca, Italy), 2022.

C30 **C. Boehm**, N. Sollmann, J. Meineke, S. Kronthaler, S. Ruschke, M. Dieckmeyer, K. Weiss, C. Zimmer, M. R. Makowski, T. Baum, and D. C. Karampinos, "Preconditioned water-fat total field inversion: application to spine quantitative susceptibility mapping (QSM)," in *24. Jahrestagung der Deutschen Sektion der ISMRM*, vol. 24, (Aachen, Germany), p. 162, 2022. **1. Place Gorter-Preis**.

Honors & Awards

2019 ISMRM Magna Cum Laude Merit Award (see C2)

2021 ISMRM Summa Cum Laude Merit Award (see C14)

2021 Best trainee abstract 2021 on susceptibility: technology - 3rd place, by Electro-Magnetic Tissue Properties Study Group (ISMRM) (see C14)

2021 ISMRM Magna Cum Laude Merit Award (see C15)

2021 Editor's pick in Magnetic Resonance in Medicine Journal in March (see JP-I)

2022 Cover image of the Magnetic Resonance in Medicine Journal in January (see JP-III)

2022 Gorter-Preis of the German Chapter of ISMRM (see C30)

Contents

Contents

1 Introduction

Tomographic imaging is an integral part of modern medicine as it allows for the non-invasive assessment of pathologies that don't have manifestations that are readily apparent on a clinical exam. Among others, magnetic resonance imaging (MRI) is one of these techniques. MRI is especially known for its high soft tissue contrast in comparison to X-ray based methodolgies such as computed tomography (CT). Conventionally, MRI has been used as qualitative imaging modality, where pixel values have no intrinsic value but are assessed visually by relative differences between different tissue types. MRI not only features an outstanding soft tissue contrast, but furthermore allows to yield an abundance of different tissue contrasts. MRI is the only imaging methodology, where the measured signal is emitted by the tissue itself. This allows to design a plethora of different imaging experiments that yield the different contrasts, including but not limited to T1- and T2-weighted imaging, diffusion-weighted imaging (DWI) [1], perfusion-weighted imaging (PWI) [2], susceptibility-weighted imaging (SWI) [3–5], functional MRI (fMRI) [6], magnetic resonance spectroscopy (MRS) [7], magnetic resonance elastography (MRE) [8, 9], chemical exchange saturation transfer (CEST) [10, 11] or magnetization transfer imaging (MT) [12].

In recent years there have been significant efforts to develop so-called quantitative magnetic resonance imaging (qMRI) techniques. Rather than obtaining qualitative contrast, qMRI techniques aim for the measurement of quantitative parameters that are independent of hardware, software, pulse sequences or other experimental factors. The pixel value of a quantitative parameter itself is aimed to be conclusive whether or not the imaged tissue is healthy or if there are any pathological changes.

The magnetic susceptibility is such a quantitative parameter and represents a fundamental physical tissue property. Quantitative susceptibility mapping (QSM) techniques aim to estimate the magnetic susceptibility [13, 14]. This can be achieved by performing multi-echo gradient-echo experiments where the phase contains two main components. Firstly, the chemical shift induced phase changes of hydrogen containing bonds other then water, for example fat or silicone in silicone breast implants. Secondly, the susceptibility-induced phase changes. While the first effect is a local effect due to the

polarization of electron clouds in different components, the susceptibility-induced phase is a non-local distortion of the main magnetic field. Most QSM methods estimate the mean bulk susceptibility of a voxel. However, there have also been efforts to estimate paramagnetic and diamagnetic sources independently [15–18]. QSM has one intrinsic characteristic that sets it apart from most other MR contrasts. Due to the non-local nature of susceptibility-induced phase changes in the imaging experiment, QSM can even approximate susceptibility values of MR invisible structures such as air, or materials with a very short relaxation time such as calcified structures. Calcified structures are of particular interest for medical MR applications as they constitute the main component of bony structures. The skeletal system can hardly be imaged with conventional relaxation-based MR techniques due to the short relaxation time. Therefore, the skeletal system is mainly imaged using X-ray based techniques. In contrast to MR, X-ray is an ionizing radiation delivering immediate damage to the tissue it passes through. For repeated examinations such as screening for breast cancer or for young patients, which are more susceptible to ionizing radiation, an X-ray free methodology would be desirable. QSM constitutes such a MR-based contrast that might allow the assessment of calcified structures.

Early works have indicated the value of QSM for body applications [14]. However, body QSM is challenging due to various reasons, including i) the presence of different materials such as fat and silicone and their corresponding chemical shift, ii) the strong susceptibility difference between different tissue types such as muscle, adipose tissue and bone, iii) frequently the very short relaxation time of tissue of interest such as of bone or other calcifications or iv) low SNR due to the large distance of the tissue from the imaging coils. Furthermore, QSM methods were predominantly developed for brain applications, where the challenges are different, and have been applied directly to body regions meanwhile sometimes violating their intrinsic assumptions. Therefore, there is a need for general purpose body QSM methodologies to alleviate artifacts that can be introduced by the challenging conditions introduced above.

1.1 Thesis Purpose

To obtain susceptibility maps from multi-echo data-echo data four major steps have to be performed including i) the estimation of the susceptibility induced B_0 field inhomogeneities, ii) unwrapping of the obtained inhomogeneity map, iii) the background field removal, and iv) the field-to-susceptibility inversion. Only a few studies have attempted to develop tailored methods for body applications ([19], steps 1 and 2)

and primarily for the dipole inversion step in liver applications [20–22]. Nevertheless, considering the broad spectrum of potential applications—including visualizing calcified structures like breast, aortic, or prostatic calcifications; measuring liver iron overload; assessing blood oxygenation levels in the heart or placenta; and ultimately estimating bone mineral density as a biomarker for fracture risk—it is desirable to develop methods tailored to the QSM technology stack. Previous results indicate that accuracy and precision must be substantially improved, particularly for the quantitative evaluation of bone health [23–25]. A comprehensive visual representation of the (body) QSM pipeline can be found in Figure 1.1, which also highlights the specific stages where each publication within this cumulative thesis makes its contributions.

Consequently, the objective of this work is to develop advanced algorithms to enhance the accuracy and precision of body QSM to foster clinical applicability of the susceptibility contrast. Furthermore, the work aims to develop optimized acquisition methodologies that allow for faster acquisition of data for body QSM.
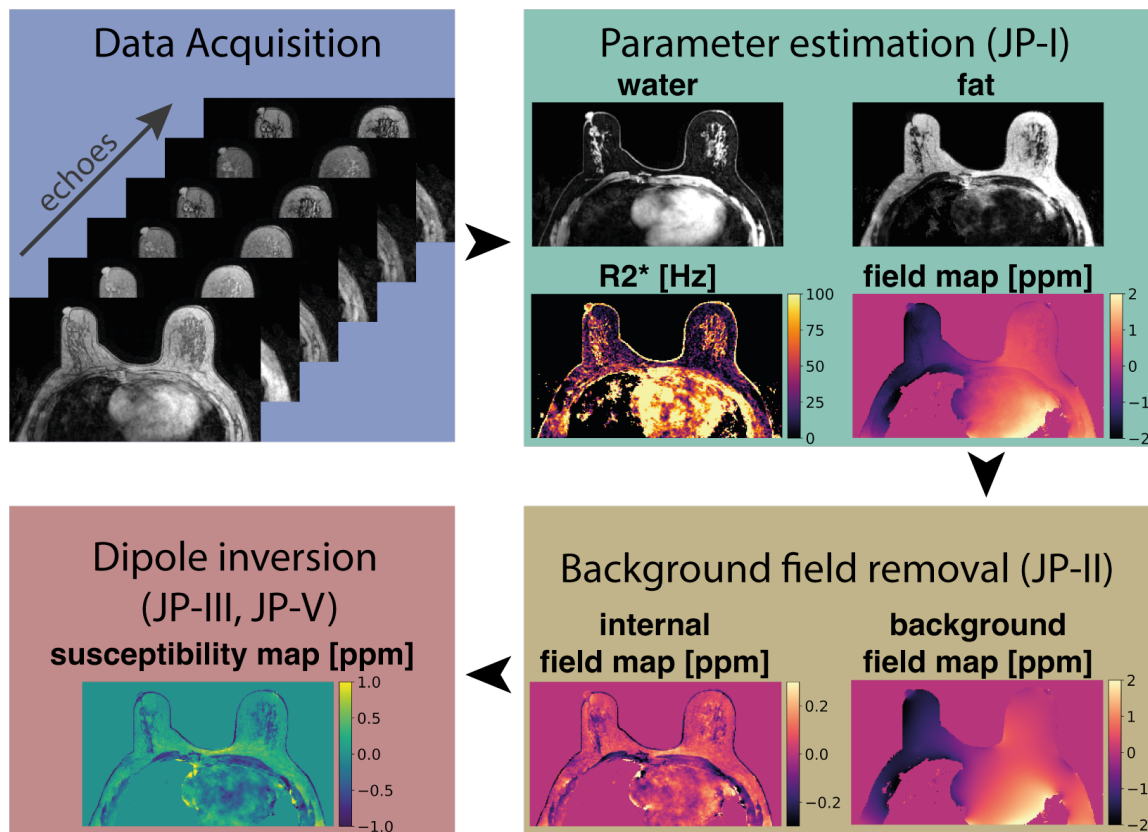
Figure 1.1: An illustrative depiction of the (body) QSM technology stack is presented. Initially, a multi-echo gradient-echo sequence is executed to acquire complex images at various echo times. Subsequently, the B_0 field inhomogeneities must be assessed by estimating all pertinent model parameters, such as water, fat, R_2^*, and the field map. Following this step, the background field is removed from the total field map. Ultimately, the internal field map is inverted to generate a susceptibility map. In the accompanying figure, the individual journal publications of this cumulative thesis are denoted as JP-I through JP-V, indicating the corresponding processing steps. JP-IV is omitted, as it pertains to optimizing the data acquisition step for accelerated acquisition. However, this method precludes the estimation of water, fat, and allows to estimate R_2^* only under specific circumstances, and thus represents an alternative pipeline.

1.2 Thesis Structure

The present cumulative thesis is structured in the three following parts. In chapter 2, a brief introduction into the theoretical background for body QSM is given. In chapter 3 the comprised journal publications are presented. Chapter 4 of the work provides a context of the cumulative thesis with respect to the literature, analyzing the results, and suggesting potential avenues for future research.

2 Quantitative Susceptibility Mapping in the Body

In order to extract susceptibility information, multi-echo gradient echo (mGRE) images must be acquired. The mGRE protocol is a versatile MR experiment that has been employed to obtain various quantitative MR contrasts, such as chemical shift encoding-based water-fat separation and corresponding parameters like proton density fat fraction (PDFF) [26] or proton density silicone fraction (PDSF) [27]. Additionally, it has been utilized for myelin water imaging [28], metabolite imaging [29], and fatty acid composition imaging [30].

The complex voxel signal evolution in an mGRE experiment at echo time t_n can be described as [31]

$$s_n = \sum_{m=1}^{P} \rho_m e^{i\phi_m} e^{(i\omega_m - r_m)t_n}, \tag{2.1}$$

where P represents the number of chemical species in the voxel, each with a corresponding magnitude ρ_m, phase at $t = 0$ given by ϕ_m, resonance frequency ω_m, and transverse relaxation rate r_m.

To derive susceptibility maps from mGRE data, four key steps must be performed, comprising i) estimation of the B_0 field inhomogeneities induced by susceptibility (field-mapping), ii) unwrapping of the resulting inhomogeneity map, iii) removal of the background field, and iv) inversion of the field-to-susceptibility relationship, as described in detail below.

2.1 Field-mapping

2.1.1 The water–fat signal model

In body regions, fat is the most prevalent chemical species and is composed of various types, each exhibiting a distinctive chemical shift and an anatomic specific composition [32–34]. Most body tissue types contain water and fat, where fat itself exhibits 9

individual resonance frequencies. Based on Equation 2.1, the total number of free parameters per chemical species is four, resulting in 40 parameters when 10 spectral peaks (9 fat and water) are present. That would require a minimum of 20 complex echo images acquired at different time points to estimate the 40 free parameters. However, MRI acquisitions are notoursely slow, especially when compared to X-ray based techniques. For example a scan of the breast with an FOV of $220 \times 382 \times 192.4 \text{mm}^3$, an isotropic voxel size of 1.3mm and 6 echo times results in a scan time of over 25 min when no acceleration is used. 25 min are already a clinically infeasible long scan time, especially considering the limited spatial resolution. For a 20 echo acquisition the same scan would take well above 1hr. However, assuming the resonance frequency of water to be $f_B = \omega_1$, a priori known fat spectrum obtained from MR spectroscopy such that $\rho_m e^{\phi_p} = \rho_F a_{p=m-1}$, $\omega_m = f_B - \Delta\omega_{p=m-1}$, and a shared transverse relaxation rate $R_2^* = r_m$ and assign $\rho_W = \rho_1 e^{i\phi_1}$ and $\rho_F a_p = \rho_2 e^{i\phi_2}$, the signal evolution simplifies to the well-established single-R_2^* water–fat signal model [35]:

$$s(t_n) = (\rho_W + c_n \rho_F) e^{\gamma t_n}, \quad \gamma = i2\pi f_B - R_2^* \tag{2.2}$$

$$c_n = \sum_{p=1}^{P} a_p e^{i2\pi \Delta f_p t_n}, \quad \text{with} \quad \sum_{p=1}^{P} a_p = 1,$$

where the parameters are better known as, ρ_W and ρ_F as the complex signal of the water and fat components and f_B as the field map. The fat spectrum with P spectral peaks with corresponding relative amplitudes a_p and chemical shift Δf_p. In this formulation, the amount of free parameters is reduced to 6 and is independent of the fat model. As a result, the number of required echo times is reduced to 3 and the field map parameter f_B predominantly exhibits the susceptibility-induced phase contributions. In Figure 2.1 the individual recorded echo time magnitude images and parameters of Equation 2.2 are illustrated for the above 6 echo breast scan.

To obtain the parameters, Equation 2.2 can be rewritten into its matrix representation

$$\mathbf{s} = \underbrace{\begin{bmatrix} e^{\gamma t_1} & e^{\gamma t_1} \sum_{p=1}^{P} a_p e^{i2\pi(\Delta f_p)t_1} \\ \vdots & \vdots \\ e^{\gamma t_n} & e^{\gamma t_n} \sum_{p=1}^{P} a_p e^{i2\pi(\Delta f_p)t_n} \end{bmatrix}}_{\boldsymbol{A}(\gamma)} \underbrace{\begin{bmatrix} \rho_W \\ \rho_F \end{bmatrix}}_{\rho}, \tag{2.3}$$

and the least-squares parameter estimation can hence be formulated as

$$\{\rho_{\mathrm{W}}, \rho_{\mathrm{F}}, f_B, R_2^*\} = \arg\min_{\rho', \gamma'} ||\boldsymbol{A}(\gamma')\boldsymbol{\rho}' - \hat{\mathbf{s}}||_2^2, \tag{2.4}$$

where $\hat{\mathbf{s}}$ are the acquired complex echo data.

2.1.2 Field map estimation

The above cost function can be solved using gradient descent methods [31, 36]. However, this only yields accurate results in the case of reasonably small field map variations. When field inhomogeneities are large, the estimated parameters are susceptible to artifacts, particularly water-fat swaps. These swaps lead to errors in the field map parameter and incorrectly assign energy between ρ_W and ρ_F. Therefore, the accurate estimation of field maps is crucial for obtaining reliable parameter estimates.

To reformulate the problem as a field map estimation problem and to reveal the whole residual space in dependence on the field map parameter, Variable Projection (VARPRO) can be used to substitute the linear parameters by [37]

$$\boldsymbol{\rho} = \mathbf{A}^+(\gamma_{f_B} = i2\pi f_B)\mathbf{s}, \tag{2.5}$$

where $\mathbf{A}^+(\gamma_{f_B})$ is the Moore-Penrose pseudo-inverse of $\mathbf{A}(\gamma_{f_B})$ and R_2^* was neglected for the field map estimation as both parameters are sufficiently uncorrelated [38]. This results in the following field map only dependent least-squares VARPRO formulation of Equation 2.4

$$f_B = \arg\min_{\gamma_{f_B}} \left|\left|\left(\mathbf{I} - \mathbf{A}(\gamma_{f_B})\mathbf{A}^+(\gamma_{f_B})\right)\hat{\mathbf{s}}\right|\right|_2^2. \tag{2.6}$$

This minimization problem can efficiently be solved by rewriting $\mathbf{A}^+(\gamma_{f_B}) = \boldsymbol{\Lambda}(\gamma_{f_B})\boldsymbol{\Phi}$, where

$$\boldsymbol{\Lambda}(\gamma_{f_B}) = \mathrm{diag}\left[e^{\gamma t_1}, \cdots, e^{\gamma t_n}\right], \quad \boldsymbol{\Phi}(\gamma_{f_B}) = \begin{bmatrix} 1 & \sum_{p=1}^{P} a_p e^{i2\pi(\Delta f_p)t_1} \\ \vdots & \vdots \\ 1 & \sum_{p=1}^{P} a_p e^{i2\pi(\Delta f_p)t_n} \end{bmatrix}. \tag{2.7}$$

The pseudo-inverse can subsequently be rewritten to $\mathbf{A}^+(\gamma_{f_B}) = \boldsymbol{\Phi}^+\boldsymbol{\Lambda}(-\gamma_{f_B})$, considering that $\boldsymbol{\Lambda}^{-1}(\gamma_{f_B}) = \boldsymbol{\Lambda}(-\gamma_{f_B})$. In this formulation, only one pseudo-inverse has to be calculated for the whole field map range as it is not dependent on it. Hence, equation 2.6 can efficiently be solved using search methods and parallel programming techniques

[27, 37].

Although the VARPRO formulation allows for the estimation of the global voxel-wise minimum, this method shows problems in voxels which are predominantly water or fat or voxels with low SNR. Both cases exhibit two dominant minima with similar values, and determining the absolute minimum strongly depends on the noise. To overcome the problems of voxel wise parameter estimation, different approaches such as region-growing and global problem formulations have been proposed. Methods that incorporate a neighborhood regularization term, which enforces spatial smoothness on the field map, have been particularly successful [38–40]

$$
f_B = \arg\min_{\gamma_{f_B}} \sum_{\mathbf{r}} \left[\left\| \left(\mathbf{I} - \mathbf{A}(\gamma_{f_B})\mathbf{A}^+(\gamma_{f_B}) \right) \hat{\mathbf{s}} \right\|_2^2 + \lambda \sum_{\mathbf{r}' \in \mathcal{N}(\mathbf{r})} \frac{w(\mathbf{r})}{i2\pi} |\gamma_{f_B}(\mathbf{r}) - \gamma_{f_B}(\mathbf{r}')|^2 \right],
$$
(2.8)

where $\mathcal{N}(\mathbf{r})$ contains the neighbouring voxels at position $\mathbf{r}$, λ is the regularization parameter balancing data consistency and regularization term, and $w(\mathbf{r}) \in [0,1]$ is a voxel-wise weighting term that can be used to incorporate the reliability of the individual voxel in the minimization problem, for instance, by setting it as the signal magnitude. The above minimization problem in Equation 2.8 can be solved using graph cut methods. Despite being successful for water-fat separation tasks, the proposed methods suffer from field map smoothing, long computation times, or limitations in the problem formulation or graph construction.

2.1.3 The water–fat–silicone signal model

When the FOV contains multiple chemical species, such as silicone in breast implants, the conventional water-fat signal model presented in Equation 2.2 can be extended to a water-fat-silicone signal model.

$$
s(t_n) = \left(\rho_W + c_n \rho_F + \rho_s e^{i2\pi \Delta f_S t_n} \right) e^{\gamma t_n},
$$
(2.9)

where ρ_S is the complex signal of silicone and Δf_S is the chemical shift of silicone. For field-mapping, the above VARPRO formulation and neighborhood regularization can be similarly used without the loss of generality as in Equation 2.3-2.8 [27].

In Figure 2.2 exemplary field-mapping results of different methods are illustrated for the above breast scan.
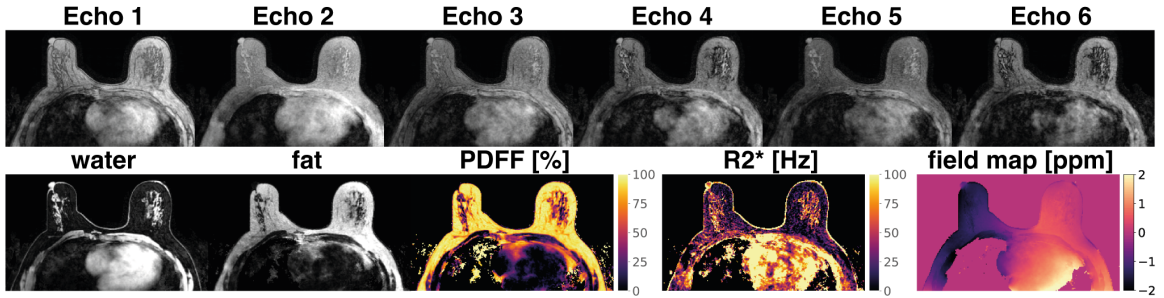
Figure 2.1: Illustrative magnitude echo images and parameter maps of a multi-echo gradient echo experiment with subsequent parameter separation based on Equation 2.2. The first row shows the magnitude of the signal at different echo times. The second row shows the water and fat image, proton density fat fraction, R_2^*- and field map.
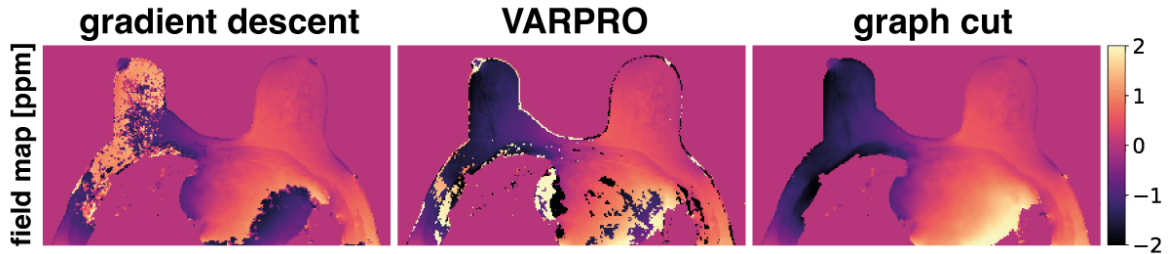

Figure 2.2: Results of different field-mapping algorithms. The gradient descent method, which minimizes Equation 2.4 using conventional gradient-based techniques, struggles to resolve the pronounced field map variations, particularly in the right breast. In contrast, the VARPRO approach from Equation 2.6, which extracts the global minima within a voxel, is capable of resolving much larger field map variations, resulting in substantially improved outcomes in the right breast. Nonetheless, a significant number of wraps can still be observed in the field map. By minimizing a global neighborhood-regularized cost function using a graph cut, as in Equation 2.8, it is possible to obtain a non-wrapped field map. However, this comes at the expense of field map blurring.

11

2.2 Field map unwrapping

From Equation 2.2 it is apparent that the field map parameter f_B is periodic with an period length of

$$f_{\text{period}} = \frac{1}{\Delta \text{TE}} = \frac{1}{t_{n+1} - t_n}, \tag{2.10}$$

in the case of equidistant echo time spacing, which is usually the case. Therefore, the field map parameter is subject to wrapping. When a susceptibility map is sought to estimated, the field map has to be unwrapped as the jumps in the field map are inherently assumed to originate from large susceptibility sources by the field-to-susceptibility inversion algorithms, hence leading to severe artifacts in the resulting map.

Unwrapping itself is an ill posed problem since many values of the true phase lead to the same value in the wrapped phase. Unwrapping algorithms assume the phase to be slowly varying. In a one-dimensional case that means that a wrap is assumed to have occurred when $|\phi(r+1) - \phi(r)| > \pi$ or for the case of the above field map parameter $|f_B(r+1) - f_B(r)| > \frac{f_{\text{period}}}{2}$. This problem is generally solved using path-following methods where a voxel is compared to the adjacent voxel. The difference in the different methods in the literature primarily lies in the path(s) used for unwrapping.

A uniquely different approach to perform the unwrapping is the use of a formulation similar to Equation 2.8. In this case, the first term does not reflect a data consistency term but contains the wrapped possible solutions of the true phase $[\phi(r), \phi(r) + 2\pi, \ldots, \phi(r) + n2\pi], n \in \mathbb{N}$. This approach follows the same inherent assumption of a smooth field map, however using graph cut techniques the unwrapping can be performed simultaneously in the whole three-dimensional FOV and is not dependent on the heuristic optimization of the path in path-following algorithms.

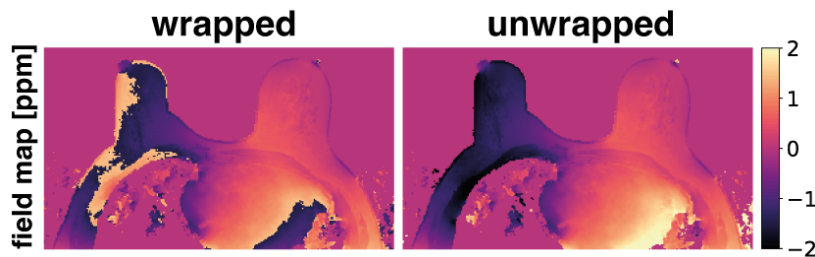In Figure 2.3 the difference between a wrapped and unwrapped field map is illustrated.

Figure 2.3: Illustrative Figure showing a wrapped and unwrapped field map

2.3 Background Field Removal

The field map f_B contains two separable sources of susceptibility. First the so-called internal fields f_{in} originated from susceptibility sources inside the ROI χ_{in} and background fields f_{bg} that originate from susceptibility sources outside the ROI χ_{bg}. Therefore the global susceptibility can be written as

$$\chi(\mathbf{r}) = \begin{cases} \chi_{\text{bg}}(\mathbf{r}) & \forall \mathbf{r} \notin \Omega \\ \chi_{\text{in}}(\mathbf{r}) & \forall \mathbf{r} \in \Omega \end{cases}, \tag{2.11}$$

where Ω contains all voxels inside the ROI. The relation between internal and background field and susceptibility by a dipole approximation reads [13]

$$f_B = f_{\text{bg}} + f_{\text{in}} = d * (\chi_{\text{bg}} + \chi_{\text{in}}), \tag{2.12}$$

where $*$ is the convolution operator and d is the unit dipole kernel

$$d(\mathbf{r}) = \begin{cases} 0 & |\mathbf{r}| = 0 \\ \frac{3\cos^2\Theta - 1}{4\pi|\mathbf{r}|} & \text{otherwise} \end{cases}. \tag{2.13}$$

For efficient calculation of the convolution, the dipole kernel can used in its Fourier space representation

$$D(\mathbf{k}) = \mathcal{F}\big(d(\mathbf{r})\big) = \begin{cases} 0 & |k| = 0 \\ \frac{1}{3} - \frac{k_z^2}{k^2} & \text{otherwise} \end{cases}, \tag{2.14}$$

where $\mathcal{F}$ is the Fourier transform. Equation 2.15 hence reduces to a simple multiplication in k-space

$$f_B = \mathcal{F}^{-1}\big(D * \mathcal{F}(\chi)\big), \tag{2.15}$$

where $\mathcal{F}^{-1}$ is the inverse Fourier transform. For simplicity, the image space formulation of the field-to-susceptibility relation with convolution operator is used throughout the thesis. However, in practice dipole-based methods are predominantly implemented using the Fourier representation.

Now, in order to estimate the parameter of interest χ_{in}, the background field contributions f_{bg} have to be removed from the total field map f_B. The background fields can be uniquely separated from the local fields as the background fields are harmonic in the ROI and the local fields are not [41]. Hence, background field removal techniques

generally aim to remove harmonic components from the total field. As the background fields are harmonic in the ROI, they are a solution to the Laplace equation

$$\nabla^2 f_{\text{bg}} = 0, \quad \mathbf{r} \in \partial\Omega, \tag{2.16}$$

where $\partial\Omega$ is the boundary of Ω, or the equivalent Poisson equation

$$\nabla^2 f_{\text{in}} = \nabla^2 f_B, \quad \mathbf{r} \in \partial\Omega. \tag{2.17}$$

As the background field can be one or two orders of magnitude bigger than the local field, Equation 2.17 is solved with the approximation

$$f_{\text{in}} \ll f_B \iff f_B\big|_{\partial\Omega} = f_{\text{bg}}\big|_{\partial\Omega}. \tag{2.18}$$

Through the definition of the boundary conditions and the inclusion of necessary approximations, the above equations can be solved, allowing for the estimation and subsequent removal of background magnetic field components from the measured total field

$$f_{\text{in}} = f_B - f_{\text{bg}}. \tag{2.19}$$

The method that employs Equations 2.16 through 2.19 is commonly referred to as the Laplacian Boundary Value (LBV, [42]) method. LBV generally yields accurate results, when the conditions in Equation 2.18 are met. However, in body regions the above approximations can be violated when the boundary $\partial\Omega$ includes voxels of strong susceptibility such as subcutaneous fat [43] or bone. The resulting artifacts decrease with an increase in distance from the boundary.

Based on the spherically harmonic nature of the background fields evident from Equation 2.16 and 2.17 and the corresponding mean value property gives basis to a second class of background field removal techniques. The kernel based background field removal:

$$f_{\text{in}} = (\delta - \kappa) *^{-1} \Big((\delta - \kappa) * f_B \Big), \tag{2.20}$$

where δ is the Dirac distribution, κ a spherical convolution kernel and $*^{-1}$ the deconvolution operator. A plethora of methods have been proposed that use the above formulation [41]. However, kernel-based methods suffer from the implicit assumption of no background field sources close to the boundary $\partial\Omega$. Violating this assumption can introduce errors, but some of these errors can be mitigated by selecting a variable kernel size that reduces in size near the boundary. However, even with such adjustments, these
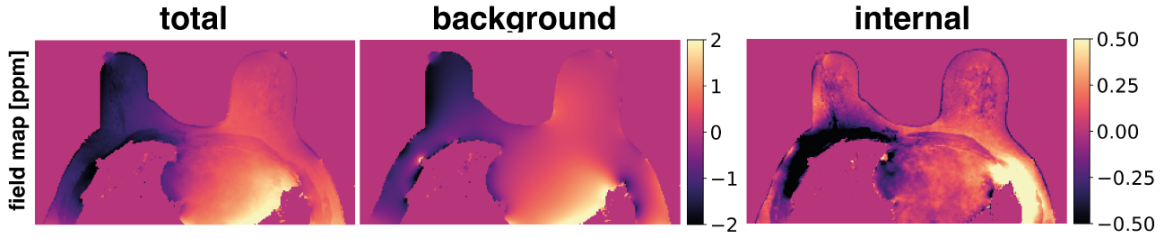
Figure 2.4: Illustrative Figure showing the separation of the total field f_B into the background f_{bg} and internal f_{in} field. The separation is based on the projection onto dipole fields method [44]. While most of the breast tissue shows a proper separation of both fields, strong artifacts are visibile in the posterior direction originating from the lung/tissue interface where the internal field still exhibits significant harmonic contributions from the background field.

methods can still exhibit artifacts near the boundary, which decrease in magnitude with increasing distance from the boundary.

Another method for background field removal is projection onto dipole fields (PDF) [44], which minimizes the following objective function

$$\chi_{\text{bg}} = \underset{\chi_{\text{bg}}'(\mathbf{r}), \, \mathbf{r} \notin \Omega}{\arg \min} \, ||f_B - d * \chi_{\text{bg}}'||. \qquad (2.21)$$

Projection onto dipole fields is based on the Hilbert Projection Theorem [45]. The assumption is that the dipole fields spanned by sources in and outside the ROI are orthogonal. However, this assumption is violated in the proximity to $\partial\Omega$, where in the above unregularized formulation, sources of the local field are erroneously estimated to be based on background sources. When the background susceptibility is successfully estimated, the background field removal contributions can be removed the following

$$f_{\text{in}} = f_B - d * \chi_{\text{bg}}. \qquad (2.22)$$

Figure 2.4 provides a representative example of the separation of the total field into background and internal fields, utilizing the projection onto dipole fields technique. This figure highlights the challenges faced by all individual background field removal methods, as they often achieve only a partial separation of the fields. As a result, harmonic fields may still be present in the purported internal field map, indicating the limitations of these techniques.

As indicated above, all background field removal techniques can exhibit artifacts in proximity to the boundary region with decreasing effect with increasing distance

from the boundary. In body applications the artifacts are generally more prominent, as assumptions of the methods are regularly violated.

2.4 Field-to-susceptibility Inversion

The final step of QSM is the field-to-susceptibility dipole inversion. From Equation 2.15, it is known that the internal susceptibility is directly connected to the internal field.

$$f_{\text{in}} = d * \chi_{\text{in}}. \tag{2.23}$$

In order to estimate χ_{in}, the field-to-susceptibility inversion has to be formulated as an inverse problem. As indicated by Equation 2.14, it is known that the dipole kernel contains zero values in k-space. This not only renders the dipole inversion ill-conditioned, but also precludes the possibility of directly estimating susceptibility by dividing the field map in k-space by the dipole kernel, such as $\chi = \mathcal{F}^{-1}\left(\frac{\mathcal{F}(f_B)}{D}\right)$. However, based on Equation 2.23, an inverse problem can be formulated as follows:

$$\chi_{\text{in}} = \arg\min_{\chi'}||f_{\text{in}} - d * \chi'||_2^2. \tag{2.24}$$

This inverse problem can efficiently be solved using conjugate gradient. However, as previously mentioned, the dipole kernel contains zero elements where $k_z^2 = |\mathbf{k}|^2/3$, specifically a cone-shaped surface consisting solely of zeros, which notably intersects the center of k-space. This leads to three additional implications. Firstly, the mean of the estimated susceptibility map is zero, causing the susceptibility to field relationship to be not a one-to-one problem, but rather a many-to-one problem. This renders the inverse problem ill-posed. Secondly, the estimated susceptibility map serves only as a relative measurement. In order to obtain absolute measurements, reference strategies must be employed. One such strategy is selecting a tissue with well-known susceptibility, which importantly remains unchanged in the presence of pathologies. The tissue of interest can then be referenced to this stable tissue. Thirdly, due to the zero cone surface and surrounding values approaching zero, noise in f_B is substantially amplified, resulting in the notorious streaking artifacts in the estimated susceptibility distribution. The noise amplification is generally addressed by introducing two additional modifications to Equation 2.24. A noise weighting term W is incorporated, which includes information about the reliability of the field map information in specific voxels. Common choices are echo-based magnitude information, such as the maximum intensity projection across

echo times, or the residual error of the parameter separation in the field-mapping step. The second modification entails introducing a regularization term that incorporates additional prior information into the dipole inversion. The resulting minimization problem reads:

$$\chi_{\text{in}} = \arg\min_{\chi'} ||W(f_{\text{in}} - d * \chi')||_2^2 + \lambda R(\chi'), \tag{2.25}$$

where λ is the regularization parameter that balances the data consistency term with the regularization term $R(\chi)$. Numerous methods have been proposed, featuring diverse variations of $R(\chi)$ and W, and employing different minimization algorithms. One particularly notable approach is the smoothness-promoting regularizer $R(\chi) = ||\nabla\chi||_2^2$, for which a closed-form solution exists. The primary advantage of a closed-form solution lies in its remarkably rapid reconstruction time. However, there are some drawbacks, including the resulting oversmoothed susceptibility distributions, limitations in the choice of regularization term, and the constraint to use the ℓ_2-norm, while ℓ_1-norm based regularization has been demonstrated to enhance the dipole inversion.

2.4.1 Morphology enabled dipole inversion

The most popular iterative reconstruction algorithms is the so-called Morphology-Enabled Dipole Inversion (MEDI) [46, 47], where the regularization parameter is

$$R(\chi) = \lambda||M_g\nabla\chi||_1. \tag{2.26}$$

The MEDI regularization parameter integrates additional information from the echo images. Specifically, M_G serves as a weighting term that incorporates edge information from the magnitude image. The underlying assumption in MEDI regularization is that edges in the magnitude image are likely to correspond with edges in the susceptibility map. M_G itself is subject to heuristic optimization; for instance, it can be a binary mask indicating the presence of an edge in the magnitude image or a value on the interval $[0, 1]$ for more nuanced edge occurrence information. Common methods for obtaining M_G include using the total variation of the magnitude images or applying a Sobel or Canny operator. The ℓ_1 norm in the MEDI regularizer promotes sparse susceptibility distributions in the gradient domain, which supports the prior assumption of piecewise constant susceptibility distributions of the total variation-based regularizer.

In addition to the enhanced regularization term, MEDI-based algorithms frequently employ a so-called nonlinear formulation of the data fidelity term, which strengthens the stability of the dipole inversion against noise and errors arising from the unwrapping

step. The nonlinear dipole inversion cost function with MEDI regularizer, which can be considered the state-of-the-art method, reads [47]

$$\chi_{\text{in}} = \arg\min_{\chi'} ||W(e^{id*\chi'} - e^{if_{\text{in}}})||_2^2 + \lambda||M_g\nabla\chi'||_1. \tag{2.27}$$

Although this formulation was introduced over a decade ago, it remains state-of-the-art and is the most widely employed approach across various anatomies and pathologies. While there have been advancements in the formulation of the data fidelity term and the adoption of total generalized variation over total variation for the regularization term, the core concept of edge-based masking continues to be a key component.

Additionally, in MEDI-based methods, the weighting term W is frequently optimized during minimization iterations using a technique called Model Error Reduction through Iterative Tuning (MERIT). MERIT adjusts W at each iteration or after a few iterative steps, based on the evaluation of the residual error in the objective function. This approach assigns less significance to voxels with highly erroneous field map values and effectively reduces the occurrence of shadowing artifacts.

2.4.2 Total field inversion

A significant advancement in the field has been the formulation of the dipole inversion as a total field inversion (TFI) [48]. TFI algorithms directly estimate the global susceptibility distribution χ from the total field map f_B. In doing so, the orthogonality assumption of norm-based background field removal techniques, such as PDF, is not violated, and the internal and background susceptibility can be more effectively separated. However, χ_{in} and χ_{bg} exhibit significant differences in susceptibility magnitudes. To address slow convergence or convergence to an improper separation of internal and background fields, TFI algorithms employ preconditioning. A preconditioner P is constructed based on Ω to implicitly differentiate between internal and background regions, with its simplest variant taking the following form:

$$P(\mathbf{r}) = \begin{cases} P_B & \forall\mathbf{r} \notin \Omega \\ 1 & \forall\mathbf{r} \in \Omega \end{cases}, \tag{2.28}$$

where P_B is chosen such that $P^H P \propto |\chi_{\text{bg}} - \chi_{\text{in}}|$. Additional refinements to P have been proposed, allowing it to automatically adapt to the scanned anatomy and potentially to a manually constructed Ω [49]. In general, the preconditioner can integrate more

nuanced information about tissues with significant susceptibility variations within Ω. This information can primarily be obtained from the field-mapping/parameter estimation step. For example, the R_2^*-map is correlated with susceptibility magnitude. Since the preconditioner only contains information about whether a voxel exhibits strong susceptibility but not its sign, data from the R_2^* map can be directly incorporated into the preconditioner. In body regions where both water and fat are present and a PDFF is estimated during the field-mapping step, this information can be encoded in the preconditioner, as fat exhibits a substantially different susceptibility compared to most predominantly water-containing tissue types.

Including the preconditioner in the inverse problem formulation, the total field inversion cost function can be expressed as [48]

$$y = \arg\min_{y'} ||W(f_B - d * Py')||_2^2 + \lambda ||M_G \nabla Py'||_1, \qquad (2.29)$$

where in the minimization the auxiliary variable y is minimized. After minimization the global susceptibility is obtained by $\chi = Py$. Figure 2.5 illustrates the results obtained minimizing some of the inverse QSM formulations introduced above.

2.4.3 Multi-echo complex total field inversion

Recently, a significant advancement has been made in the data consistency term. Rather than minimizing the difference between the field map and susceptibility, susceptibility can be directly estimated from complex multi-echo data. In the brain, where no fat signal is present, the dipole inversion problem can be reformulated by setting $\rho_W = 0$ and $f_B = d * Py$ into Equation 2.2, resulting in the following minimization problem [50], termed multi-echo complex total field inversion (mcTFI):

$$
\begin{aligned}
\{\rho_W, R_2^*, y\} = \arg\min_{\rho_W', {}_2^{*\prime}, y'} \sum_{j=1}^{N_{\text{echo}}} ||\rho_W' e^{-R_2'^* t_j} e^{i2\pi t_j \, d * Py'} - S_j||_2^2 \\
+ \lambda_1 ||M_g \nabla Py'||_1 + \lambda_2 ||M_C P \left(y' - \overline{y'}^{M_C} \right)||_2^2,
\end{aligned}
\qquad (2.30)
$$

where S_j is the complex echo image at echo time t_j. mcTFI also incorporates a second regularization term λ_2, which enforces homogeneity in regions where a uniform susceptibility is expected. In the brain, the cerebrospinal fluid (CSF) within the ventricles exemplifies such a structure. This approach further diminishes shadowing artifacts, and these homogeneous regions are frequently employed as reference tissue to

determine absolute susceptibility values.

The mcTFI formulation offers two key improvements over field map-based formulations. First, methods such as the previously introduced MERIT are no longer necessary. Since MERIT itself relies on heuristic optimization, eliminating its dependency is advantageous. Second, all above inverse problem formulations inherently assume Gaussian-distributed noise in the observable. While this is not accurate for the field map parameter, it holds true for the real and imaginary parts of the complex signal. Consequently, mcTFI is hypothesized to significantly enhance susceptibility estimation in low SNR regions. Moreover, additionally to the background field removal step, this formulation potentially renders the field map estimation and unwrapping step obsolete if the parameters ρ_W, R_2^*, y can be initialized with zeros or an adequate initialization is otherwise achieved. However, mcTFI is only applicable to regions with a single chemical species, such as the brain, and cannot account for the chemical shift of fat. As a result, it is not directly applicable to regions outside the brain.
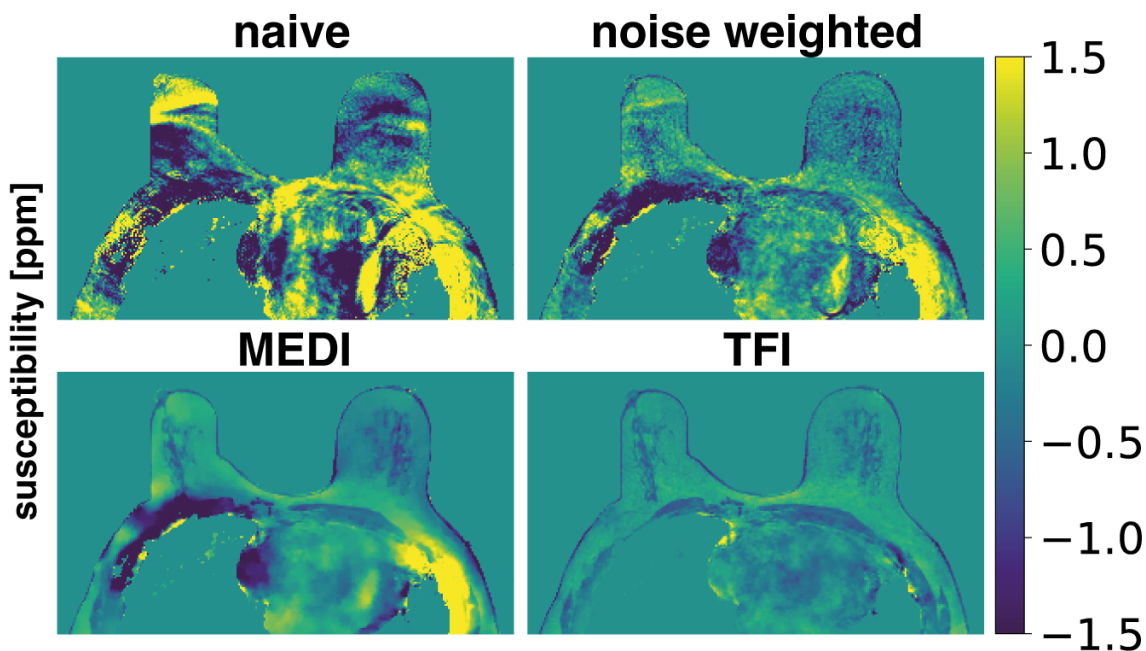
Figure 2.5: Illustrative comparison of the results obtained using various field-to-susceptibility inversion algorithms. The naive method, which minimizes Equation 2.24, yields a susceptibility distribution primarily dominated by artifacts, despite the visibility of some local structures. Introducing a noise weighting term similar to W in Equation 2.25 leads to a substantial enhancement in the results. However, it is only through employing the MEDI method, as described in Equation 2.27, that the local fibrograndular tissue can be effectively resolved. The first three methods, nonetheless, struggle with the inaccurate separation of background and local fields, as depicted in Figure 2.4, which serves as their foundation. By utilizing the TFI method from Equation 2.29, artifacts arising from the background field removal step can be significantly reduced, revealing only the local susceptibility. It is worth noting, though, that this method exhibits a decreased SNR when compared to MEDI.

3 Comprising Journal Publications

This thesis comprises five original first-authored journal publications that cover a novel joint field-mapping and unwrapping method (Section 3.2), a QSM algorithm to remove susceptibility-induced phase-variations in double-echo gradient-echo (DEGRE) acquisition for MR thermometry (Section 3.3), a general purpose body QSM methodology that jointly removes background field contributions and estimates local susceptibility (Section 3.4), a optimized acquisition framework for the fast acquisition of body QSM data (Section 3.5) and a QSM methodology specifically tailored for breast applications with the potential presence of silicone (Section 3.6).

3.1 Compliance with Ethical Standards

All investigations performed in studies involving human participants were in accordance with the ethical standards of the institutional and/or national research committee and with the 1964 Helsinki declaration and its later amendments or comparable ethical standards. Informed consent was obtained from all individual participants included in the studies.

3.2 Journal Publication I:
Improved body quantitative susceptibility mapping by using a variable-layer single-min-cut graph-cut for field-mapping

The publication entitled *Improved body quantitative susceptibility mapping by using a variable-layer single-min-cut graph-cut for field-mapping* was published in Magnetic Resonance in Medicine (ISSN: 0740-3194). The manuscript was authored by Christof Boehm, Maximilian N. Diefenbach, Marcus R. Makowski and Dimitrios C. Karampinos. It is available online (DOI: 10.1002/mrm.28515) as an open access article under the

results were also presented in the conference contribution C1 and C2, where C2 was awarded with an ISMRM Magna Cum Laude Merit Award and selected as an oral presentation at the ISMRM annual meeting 2019. The publication was selected as Editor's pick for March 2021. A summary of the publication is provided in Section 3.2.1, the author contributions are listed in Section 3.2.2 and the full text is included subsequently on the following pages.

3.2.1 Abstract

Purpose

The field map estimation is an important step in the estimation of tissue magnetic susceptibility. This work proposes a methodology based on the variable projection of the water–fat signal model and a neighborhood-regularized spatially global cost function, which is minimized using a graph-cut algorithm with a problem-specific graph construction.

Methods

Variable projection (VARPRO) was used to reduce the parameter estimation of the voxel water–fat signal model to a field map estimation problem. Using an efficient CUDA [51] implementation, all global and local minima of the VARPRO field map cost function were calculated and extracted. Subsequently, all identified minima were encoded in a neighborhood-regularized spatially global cost function. The proposed methodology was tested in numerical simulations, a scanner phantom and in vivo in the head/neck region and the spine.

Results

The simulations showed that accurate, unwrapped and fast field map estimation and water–fat separation are only possible using the proposed methodology. In vivo in the head/neck region, the proposed algorithm is able to resolve a the field map dynamic range of 5430 Hz in a 3T scanner. In the spine scans, susceptibility values based on the field map of the proposed methodology of the cortical bone shell are much closer to literature reference values when compared to other field map estimation algorithms.

Conclusion

Accurate field map estimation especially close to susceptibility interfaces is important for an accurate estimation of tissue magnetic susceptibility. The proposed graph-cut algorithm is superior in the estimation of strong field map variations close to MR signal voids or in regions with high R_2^* values when compared to formerly proposed methods.

3.2.2 Author contributions

The first author developed the problem-specific graph construction for the efficient minimization of the neighborhood-regularized problem formulation; implemented the optimization code in MATLAB; performed the numerical simulations; built the scanner phantom; performed the MR measurements of the scanner phantom and the in vivo spine data sets. With the help and consultation from the coauthors, the first author acquired the head/neck data, analyzed and interpreted the data, and wrote the manuscript.

3.2.3 Original Article

FULL PAPER

Magnetic Resonance in Medicine

Improved body quantitative susceptibility mapping by using a variable-layer single-min-cut graph-cut for field-mapping

Christof Boehm[1] | **Maximilian N. Diefenbach[1,2]** | **Marcus R. Makowski[1]** | **Dimitrios C. Karampinos[1]**

[1]Department of Diagnostic and Interventional Radiology, Technical University of Munich, Munich, Germany

[2]Division of Infectious Diseases and Tropical Medicine, University Hospital, LMU Munich, Munich, Germany

Correspondence
Christof Boehm, Department of Diagnostic and Interventional Radiology, Klinikum rechts der Isar, Ismaninger Str 22, 81675 Munich, Germany.
Email: christof.boehm@tum.de

Purpose: To develop a robust algorithm for field-mapping in the presence of water–fat components, large B_0 field inhomogeneities and MR signal voids and to apply the developed method in body applications of quantitative susceptibility mapping (QSM).

Methods: A framework solving the cost-function of the water–fat separation problem in a single-min-cut graph-cut based on the variable-layer graph construction concept was developed. The developed framework was applied to a numerical phantom enclosing an MR signal void, an air bubble experimental phantom, 14 large field of view (FOV) head/neck region in vivo scans and to 6 lumbar spine in vivo scans. Field-mapping and subsequent QSM results using the proposed algorithm were compared to results using an iterative graph-cut algorithm and a formerly proposed single-min-cut graph-cut.

Results: The proposed method was shown to yield accurate field-map and susceptibility values in all simulation and in vivo datasets when compared to reference values (simulation) or literature values (in vivo). The proposed method showed improved field-map and susceptibility results compared to iterative graph-cut field-mapping especially in regions with low SNR, strong field-map variations and high R_2^* values.

Conclusions: A single-min-cut graph-cut field-mapping method with a variable-layer construction was developed for field-mapping in body water–fat regions, improving quantitative susceptibility mapping particularly in areas close to MR signal voids.

KEYWORDS
chemical shift encoding-based water–fat separation, Dixon imaging, field-mapping, graph-cuts, quantitative susceptibility mapping

[Correction statement: Correction added after online publication November 30, 2020. Due to a publisher error, the article was published online before all corrections were implemented. This version shows the correct figures with the correct captions, corrections to equations 1 and 6, and several minor text edits.]

1 | INTRODUCTION

Quantitative susceptibility mapping (QSM)[1] is an MR technique directly probing a fundamental tissue property, the magnetic susceptibility. QSM is an emerging imaging method in the study of brain physiology,[2] pathology,[3] and function.[4] QSM has been also recently applied in tissues outside the brain, for example, for measuring liver iron overload,[5-7] prostatic calcifications,[8] cartilage degeneration,[9] and bone density.[10,11] The main premise of QSM is that it overcomes limitations of R_2^*-mapping by distinguishing between para- and diamagnetic susceptibility sources, which would similarly result in increased R_2^* values.[12] Furthermore, recent studies have shown that QSM may lead to a reduced dependence on the microscopic distribution of the bone marrow bone microstructure[13] or the microscopic distribution of iron[14] compared to R_2^*-map.

QSM inverts the measured main magnetic field inhomogeneities, the so-called *field-map*, to the magnetic susceptibility map. When applied in body regions, QSM processing needs to particularly address the presence of fat with its chemical shift effect.[5] The first QSM step, the magnetic field-mapping, therefore connects QSM to the sub-domain of chemical shift encoding-based water–fat separation, which also can be reformulated as a field-map estimation problem.[5,11,15] Field-mapping in the body can be challenging for mainly two reasons: (a) the presence of large background fields possibly due to concave geometry of the anatomy or air inclusions in the field of view (FOV),[16] and (b) the presence of signal voids in regions of low signal-to-noise ratio (SNR) due to MR invisible or short-T_2 tissues, for example, bone.[17] Field-mapping in water–fat regions relies on optimizing a least-squares optimization problem due to the nonlinearity of the field-map term.[5,18,19] Most methods previously proposed for solving the above non-convex optimization problem have been investigated in terms of the achieved accuracy on the water- and fat-separated images and not on the field-map. In water–fat imaging, the field-map is typically treated as a nuisance parameter, whereas in QSM the field-map is of central importance.

Most existing approaches proposed to solve the water–fat separation problem have been relying on a smoothness constraint on the field-map[18,20-22] and some of them were incorporated in the 2012 ISMRM fat–water toolbox.[23] Algorithms formulating the water–fat separation problem as a graph search have been particularly successful in solving the constrained optimization problem using either min-cuts iteratively[20] or single-min-cut approaches.[24,25] The formulation of the water–fat separation problem as a graph search was first introduced in the seminal work by Hernando et al.,[20] showing excellent water–fat separation results and was included in the 2012 ISMRM fat–water toolbox. Specifically, for each voxel, only two field-map candidates are taken and

a graph-cut is used to solve the cost function in a so-called jump move. If the cost function decreases, the field-map candidate is taken. This procedure is repeated until a defined convergence criterion is met and the method is therefore labeled as an iterative graph-cut approach (iGC). However, the original iterative graph-cut in[20] does not necessarily converge to the global minimum of its defined cost function, smoothes the field-map by construction and allows for adopting only two-dimensional neighborhood information in the field-map smoothness constraint term (interslice regularization is not possible). A single-min-cut graph-cut can address the above problems of the iterative graph-cut technique and guarantees to find the globally optimal solution. A single-min-cut graph-cut method, labeled as *rapid globally optimal surface estimation* (rGOOSE)[25] was recently introduced and proposed to restrict the field-map candidates to be only local minima of the voxel-wise field-map estimate. However, rGOOSE allows for the same amount of minima per voxel for the whole volume and includes the residual error of each minima in the global cost function similarly to the iterative graph-cut. Therefore, rGOOSE is associated with long computation times and can in some cases miss the optimal solution due to its graph construction.

Therefore, the purpose of the present work is (a) to develop an accelerated single-min-cut graph-cut algorithm for field-mapping in the presence of water–fat using a variable-layer graph construction and (b) to demonstrate the advantages of the developed field-mapping technique when applied for body QSM in the presence of large background fields and signal voids. The ability of the proposed variable-layer graph-cut (vlGC) based algorithm to overcome limitations of current state-of-the-art body field-mapping methods is particularly examined with simulations and in vivo measurements of body QSM.

2 | THEORY

2.1 | Cost function of the water–fat separation problem

Assuming the widely used single-R_2^* multi-fat-peak water–fat voxel signal model,[26,27] the complex signal at the n-th echo is

$$s_{model}(t_n) = (\rho_W + c_n \rho_F) e^{\gamma t_n}, \gamma = i2\pi f_B - R_2^*$$
$$c_n = \sum_{p=1}^{P} a_p e^{i2\pi \Delta f_p t_n}, \text{ with } \sum_{p=1}^{P} a_p = 1, \quad (1)$$

with $t_1, t_2, \ldots, t_N$ the different echo times, f_B the local frequency shift due to static field inhomogeneity and ρ_W and ρ_F the complex signal of the water and fat components assuming to have an equal transverse relaxation rate R_2^*. The fat spectrum

is assumed to have P spectral peaks with corresponding relative amplitudes a_p and chemical shift Δf_p. The above signal model can be rewritten into its matrix representation[24,28]:

$$\underbrace{\begin{pmatrix} e^{\gamma t_1} & e^{\gamma t_1} \sum_{p=1}^{P} a_p e^{i2\pi(\Delta f_p)t_1} \\ \vdots & \vdots \\ e^{\gamma t_n} & e^{\gamma t_n} \sum_{p=1}^{P} a_p e^{i2\pi(\Delta f_p)t_n} \end{pmatrix}}_{\Psi_\gamma} \underbrace{\begin{pmatrix} \rho_W \\ \rho_F \end{pmatrix}}_{\rho} = \underbrace{\begin{pmatrix} y(t_1) \\ \vdots \\ y(t_n) \end{pmatrix}}_{y}. \quad (2)$$

When the fat spectrum and its relative amplitudes are assumed to be known, the remaining unknown parameters are obtained by minimizing the least-squares error between the model and the measured data:

$$\{\rho_W, \rho_F, \gamma\} = \arg\min_{\rho_W, \rho_F, \gamma} \|\Psi_\gamma \rho - y\|_2^2. \quad (3)$$

Since the above voxel-wise minimization problem depends on many parameters the VARPRO[19] approach is used to decouple them. Specifically, the above least-squares error is minimized with respect to some of the variables by assuming the others to be fixed. Minimizing the above cost function with respect to the complex water and fat signal ρ^0 assuming γ to be fixed, the signal estimates as $\rho^0 = (\Psi_\gamma^T \Psi_\gamma)^{-1} \Psi_\gamma^T y$. Substituting ρ^0 back in Equation (3), and solving for γ, we obtain[24]:

$$\gamma(r) = \arg\min_\gamma \underbrace{\|\Psi_\gamma (\Psi_\gamma^T \Psi_\gamma)^{-1} \Psi_\gamma^T y(r) - y(r)\|_2^2}_{\mathcal{D}(r, \gamma)}. \quad (4)$$

To obtain a cost function that is only dependent on f_B the above expression can again be minimized with respect to R_2^{*}[24]:

$$f_B^0 = \arg\min_{f_B} \underbrace{\min_{R_2^*} \mathcal{D}(r, \gamma)}_{\mathcal{C}(f_B(r))}. \quad (5)$$

However, minimizing $\mathcal{C}(f_B)$ voxel by voxel is undesirable, because $\mathcal{C}$ has several local and global minima,[18,29] is non-convex, periodic in the field-map dimension and sensitive to noise. Therefore, a penalized maximum likelihood cost function is employed and minimized allowing to impose spatial smoothness:

$$\widehat{f}_B = \arg\min_{f_B(r)} \sum_r \sum_{s \in N(r)} |f_B(r) - f_B(s)|^2, \quad (6)$$

where $f_B(r)$ is the field-map. At each voxel r, field-map values are restricted to only local minimizers of $\mathcal{C}(f_B(r))$. The restriction to only local minimizers solely enforces the data consistency. $N(r)$ is the voxel neighborhood that has to be selected. Furthermore, the minimization of Equation (6) is restricted to signal only regions by setting:

$$r \in M \text{ and } M = \{(x, y, z) \,|\, \text{MIP}_{TE}(x, y, z) > T\}, \quad (7)$$

where T is a threshold which needs to be chosen appropriately and MIP_{TE} is the the maximum intensity projection of the signal over echo times.

2.1.1 | The sampling interval of the voxel independent field-mapping estimate

The voxel maximum likelihood estimate Equation (5) is periodic in the field-map dimension for equidistant echo times t_n with a period length of:

$$f_{period} = \frac{1}{\Delta TE} = \frac{1}{t_{n+1} - t_n}, \quad (8)$$

where ΔTE is the echo time step. This is the bandwidth of the field-map that should at least be sampled to obtain every existing local and global minima per voxel. The number of minima at each voxel depends on the fat model, the number of recorded echoes and the measured signal.

When two adjacent voxels v_1, v_2 whose signal only differs in their field-map value f_{B_1}, f_{B_2} are considered, the sampling bandwidth of Equation (8) needs to be extended to:

$$f_{total} = f_{period} + |f_{B_1} - f_{B_2}|, \quad (9)$$

to ensure that every minima at each voxel is correctly encoded into the graph without a false value in the penalization term. If the sampling interval was chosen too small, a minima would be wrapped around to the other end of the interval due to the periodicity in the field-map dimension.

The above idea can be generalized to an arbitrary number of voxels:

$$f_{total} = f_{period} + |\max(\widehat{f}_B) - \min(\widehat{f}_B)|, \quad (10)$$

where $\max(\widehat{f}_B)$ and $\min(\widehat{f}_B)$ are the maximum and minimum value of the global field-map estimate, respectively.

The sampling interval is finally defined as the above total bandwidth centered around zero:

$$f_{sampling} = \left[-\frac{f_{total}}{2}, \frac{f_{total}}{2} \right]. \quad (11)$$

3 | METHODS

A novel field-mapping algorithm was first developed based on a variable-layer graph construction concept and the novel formulation of the data consistency as introduced in Equation (6). The developed method was then applied to a numerical

phantom, an experimental phantom, in vivo large FOV head/neck scans and in vivo spine scans and compared to the state-of-the-art iGC method from[20] as included in the ISMRM fat–water toolbox[23] and the previously proposed single-min-cut graph-cut rGOOSE method.[25]

3.1 | Proposed single-min-cut variable-layer graph-cut algorithm

The maximum intensity projection across echoes MIP_{TE}, thresholded at 5% of its maximum value, was used to distinguish between signal and no-signal regions for the mask (see Equation 7). In the calculation of the VARPRO residual, a sampling step size of 2 Hz was used, defined empirically in order to keep the discretization error reasonably small.[19] The residual was computed over the period defined in Equation (8) and replicated until it matched the sampling interval defined in Equation (11). To determine the sampling interval, $\max(\widehat{f}_B)$ and $\min(\widehat{f}_B)$ in Equation (10) needed to be estimated. This was done by choosing the central slice of the volume and using a large sampling interval such that the range of field-map values in the slice lies within this interval. The proposed vlGC was subsequently applied on the central slice with the large sampling interval and $\max(\widehat{f}_B)$ and $\min(\widehat{f}_B)$ were extracted. The voxel-wise residuals were then computed for the whole volume for the sampling interval determined by $\max(\widehat{f}_B)$ and $\min(\widehat{f}_B)$. All local and global minima per voxel were finally extracted using MATLAB (R2017b, MathWorks) built-in functions.

The minimization of the global maximum likelihood cost function defined in Equation (6) can be transformed into a surface estimation problem using the graph-cut algorithm introduced in.[30] The graph-cut algorithm in[30] was designed for graphs with irregularly sampled spacings and a convex regularization term (quadratic distance measure in the present setting) and hence guarantees the convergence to the global

minimum of Equation (6). The ability of the algorithm to incorporate irregularly sampled spacings is necessary since the frequency distance of the extracted local and global minima in the present problem is typically not equidistant. Based on the cost function values for the set of local minima at each voxel, the graph was constructed. Since each node needs to be identifiable, each node was assigned with a distinct identification number (ID). The order x, y, z, frequency was used to create a node index array. Lists with all edges were next calculated and transformed into a equivalent sparse adjacency matrix, which fully defined the graph. Figure 1 shows an example of the constructed graph for two adjacent voxels. Edges between nodes were calculated according to.[30] The MATLAB-implementation of the Boykov-Kolmogorov max-flow algorithm was applied on the constructed graph. The above algorithm was found to be most efficient to solve graph-cut problems like the mapping of a cost function similar to the proposed global cost function.[31] Boykov-Kolmogorov max-flow algorithm returned the max-flow in the network (which was of no further interest) and two lists of node IDs belonging either to the source or to the terminal node. The graph was constructed based on the convention introduced in[30] that the highest ID in a voxel belonging to the subset of the source was the searched solution.

3.2 | Speed comparison

The vlGC was compared to the former proposed single-min-cut graph-cut algorithm rGOOSE.[25] Therefore, the three central slices of a head/neck region were selected (please see below for details). The vlGC was applied to obtain a reference field-map and run-time. The rGOOSE method was repeatedly applied to the dataset while increasing the number of layers at each iteration from 1 to 30. The resulting run-time was normalized with the run-time from the vlGC to increase system comparability. Since the absolute error is
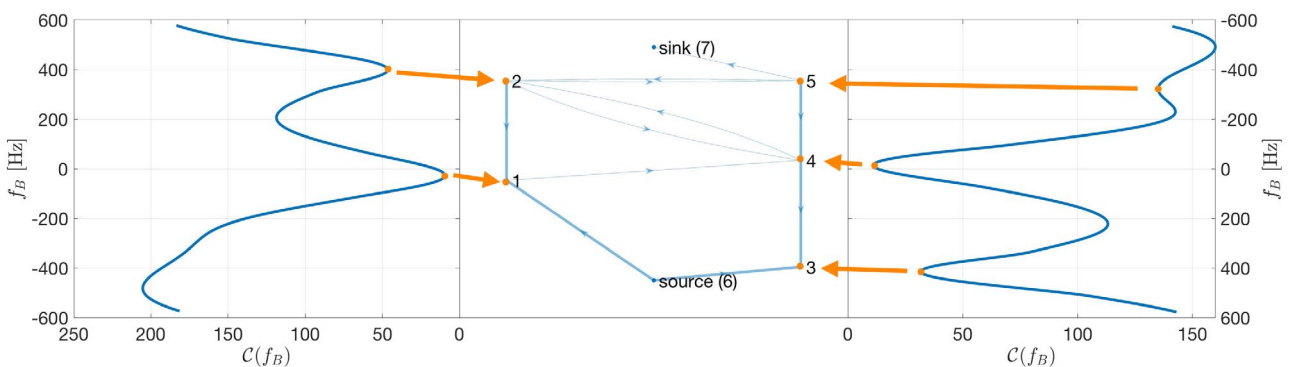

FIGURE 1 Variable-layer graph construction in 2 adjacent voxels arbitrarily extracted from one lumbar spine dataset. The voxel-wise field-mapping estimate $\mathcal{C}(f_B)$ is sampled over the same interval in both voxels, resulting in 2 and 3 minima, respectively, as illustrated in the left and right plots. From $\mathcal{C}(f_B)$ only the local minima are extracted and encoded in the graph as illustraded in the center plot. The edges in the graph are calculated according to[30]

of no interest, the error between the reference and the field-map yielded by rGOOSE was determined by computing the normalized root mean square error (NRMSE) between both and rescaling it into % of its maximum value. The methods were run on a 2017's iMac with a 4.2 GHz CPU (Intel Core i7, 7700, 4 processors) and 32 GiB RAM. Additionally, the run-time of the iGC, the rGOOSE method, and the vlGC were measured for the field-map estimation of the numerical phantom with the sharp air-tissue interface (please see details below).

3.3 | Air bubble phantom: Numerical simulation and experimental measurement

To investigate the behavior of the developed field-mapping method close to signal voids (eg air inclusions), a numerical phantom with an air bubble in the center, surrounded by a tissue with fat fraction of 30% was set up. A FOV = $128 \times 128 \times 60$ mm^3, an isotropic voxel size = $1 \times 1 \times 1$ mm^3 and a single $R_2^* = 40$ Hz for the whole volume were used. The radius of the air bubble was set to $r = 20$ mm. The phantom generation was performed twice: once with a sharp air-tissue interface and once with a smooth air-tissue interface. By applying a Gaussian filter with a standard deviation of $\sigma = 6$ and a mean of $\mu = 0$ the interface from air to tissue was smoothed out to have a continuous transition. A χ-map with $\chi_{air} = 9$ ppm and $\chi_{fat} = 0.6$ ppm in reference to $\chi_{water} = 0$ was created. In the area of the transition, Wiedemanns additive law was used to calculate the χ values accordingly.[32] Wiedemanns additive law states that the overall magnetic susceptibility of a mixture is the weighted sum of the magnetic susceptibilities of the constituents. A corresponding field-map was then forward simulated. With the echo times TE = [2.2, 3.4, 4.6, 5.8, 7.0, 8.2] ms, a field strength of 3 T and a multi-peak fat model specific to bone marrow[33] the signal was also forward simulated using the signal model displayed in Equation (1).

The numerical phantom signal values were used to evaluate the performance of the iGC algorithm and of the developed single-min-cut graph-cut algorithm first for field-mapping. The computed field-maps were subsequently used for QSM processing. The QSM processing used for the dipole inversion a closed-form ℓ_2-regularized algorithm without data weighting as in.[34] Field-mapping and QSM processing were performed for both the phantom with the smooth air-tissue interface and the phantom with the sharp air-tissue interface. The field-mapping results comparison was based on the results from the phantom with the smooth air-tissue interface to especially examine partial volume effects close to signal voids. The QSM comparison was based on the results from the phantom with the sharp air-tissue interface to assure edge preservation.

To validate the numerical simulation, an air bubble phantom was built consisting of an air-containing ball with a thin plastic shell and a radius of $r = 20$ mm placed in the center of a large water reservoir. Scanning was performed on a 3 T scanner (Ingenia, Philips Healthcare, Release 5.4, Best, The Netherlands) using a monopolar time-interleaved multi-echo gradient echo sequence,[35] acquiring 6 echoes with 3 echoes per interleave. TE$_{min}$ = 1.12 ms, ΔTE = 0.98 ms, orientation = coronal, readout direction = feet-head, and an isotropic acquisition voxel size of 1.5 mm in every dimension. The phantom was repeatedly scanned varying the shimming parameters from no shimming to only a linear shimming field in z-direction of $B_{0,shimming(z)}$ = [0.2, 0.4, 0.6] mT/m. To obtain susceptibility maps the pipeline of the numerical simulation was used in addition to the Laplacian boundary value method[36] to remove the background fields.

3.4 | In vivo measurements

The vlGC was applied to in vivo scans of both healthy volunteers and patients. Approval by the institutional review board (Klinikum Rechts der Isar, Technical University of Munich, Munich, Germany) was granted beforehand and informed written consent was obtained from all scanned volunteers and patients. Scanning was performed on the aforementioned 3 T scanner.

Specifically, 14 scans of the head/neck region of healthy volunteers, scans of the lumbar spine of 4 healthy volunteers and scans of the lumbar spine of two osteoporotic patients were evaluated.

The head/neck region was selected as a region with large B_0 inhomogeneities to assess the performance of the vlGC in field-mapping of regions with a rapidly spatially varying field-map. A monopolar multi-echo gradient echo sequence with 3 echoes acquired in a single TR was used[35] with TE$_{min}$ = 1.06 ms, ΔTE = 1.59 ms, orientation = coronal, readout direction = feet-head, FOV = $480 \times 480 \times 224$ mm^3 and acquisition voxel size = $2 \times 2 \times 4$ mm^3.

The lumbar spine was selected to assess the performance of the vlGC on field-mapping used for subsequent QSM processing. For the spine scans, the aforementioned monopolar time-interleaved multi-echo gradient echo sequence was used. For the osteoporotic spine, imaging parameters were set to TE$_{min}$ = 1.33 ms, ΔTE = 1.08 ms, orientation = sagittal, readout direction = anterior-posterior, FOV = $220 \times 220 \times 79.2$ mm^3, acquisition voxel size of 1.8 mm^3 isotropic and for the healthy spines to TE$_{min}$ = 1.12 ms, ΔTE = 0.87 ms, orientation = sagittal, readout direction = anterior-posterior, FOV = $220 \times 220 \times 79.2$ mm^3 and acquisition voxel size of 1.8 mm^3 isotropic. For QSM processing
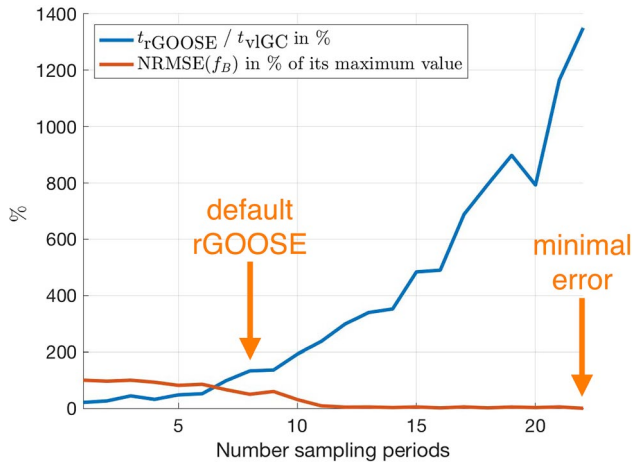
FIGURE 2 Speed comparison of the vlGC to a previously proposed single-min-cut graph-cut method (rGOOSE).[25] The underlying dataset is one of the head/neck datasets. With increasing layers in rGOOSE the resulting field-map converges to the field-map of the vlGC. When the difference between the two methods becomes minimal, rGOOSE takes 14 times as long as the vlGC. In[25] it was suggested to use 8 layers in the graph, this point is indicated in the plot and represents a suboptimal solution

in the lumbar vertebral column region, an algorithm with joint background field removal and dipole inversion was used solving the following ℓ_1 total-variation regularized optimization problem[37]:

$$\chi = \arg\min_{\chi'} \left\| W\Delta \left(f_B - \frac{\gamma}{2\pi} B_0 d * \chi' \right) \right\|_2 + \lambda \left\| M\nabla \chi' \right\|_1, \quad (12)$$

where f_B is the field-map estimate, the Larmor frequency $\frac{\gamma}{2\pi} B_0$, dipole kernel d, magnitude weighting W, and a MEDI-like edge regularization damping M.[1] The joint background field and dipole inversion method has been chosen since it does not require the definition of a background and foreground region-of-interest in order to perform the background field removal. To evaluate the quantitative performance of the performed QSM, the susceptibility values of the spinous process cortical bone region were determined in all subjects. Specifically, the ROIs were manually drawn in the cortical bone sites of the spinous process at the level of the L3 lumbar vertebral body. In addition, one subject was re-positioned and re-scanned to assess the repeatability of the estimated spinous process magnetic susceptibility.

3.5 | In vivo field-mapping consistency check

An obvious challenge while comparing the performance of different field-mapping methods in vivo is the absence of an established gold-standard measurement of the field-map. A heuristic method to verify correct field-mapping is the

examination of the water–fat separated images, as applied in previous works. Given anatomical prior knowledge, it should be known which anatomy is mainly water- or fat-containing. Based on the above knowledge, the corresponding water–fat images were checked if the separation has correctly worked. All head/neck datasets processed with both the iGC and the vlGC were visually rated and categorized in results with and without water–fat swaps, where regions in the heart and only a few voxels close to the object boundaries were not regarded. The overall counts of datasets with and without residual water–fat swaps served as a more global metric on how the vlGC performed in a challenging anatomy across all 14 datasets.

4 | RESULTS

4.1 | Speed comparison

Figure 2 compares the computational speed of the rGOOSE method to the speed of the vlGC. The three central slices of one head/neck region were selected for the speed comparison. With increasing number of layers the run-time of rGOOSE drastically increases and the difference between the field-map obtained by the rGOOSE compared to the field-map obtained by the vlGC decreases. The difference between the two methods becomes minimal from 22 layers, where the computational time for the rGOOSE is 14 times longer than the computational time for the vlGC. In absolute time units, the rGOOSE requires 1 hr 31 mins and the vlGC requires 7 mins.

4.2 | Air bubble phantom: Numerical simulation and experimental measurement

Figure 3 compares the field-mapping accuracy of the different methods in the numerical phantom. The field-map obtained by the iGC shows significant errors particular close to the signal void in the center of the volume (region with a small MR signal due to the simulated partial voluming effect) and a strong ring-shaped artifact reaching to the borders of the volume. The field-map from the iGC shows primarily larger errors in regions with small MR signal. The field-map obtained by the vlGC shows errors smaller than the field-map discretization step throughout the volume. The field-mapping errors propagate into the water–fat separated images. The error maps of the water–fat separated images from the iGC show a ring-shaped artifact, similar to the field-map, and largest errors close to the signal void. The above errors of the iGC lead to a significant false estimation of the water and fat components and to partial swaps, whereas the vlGC shows negligible errors and no swaps.

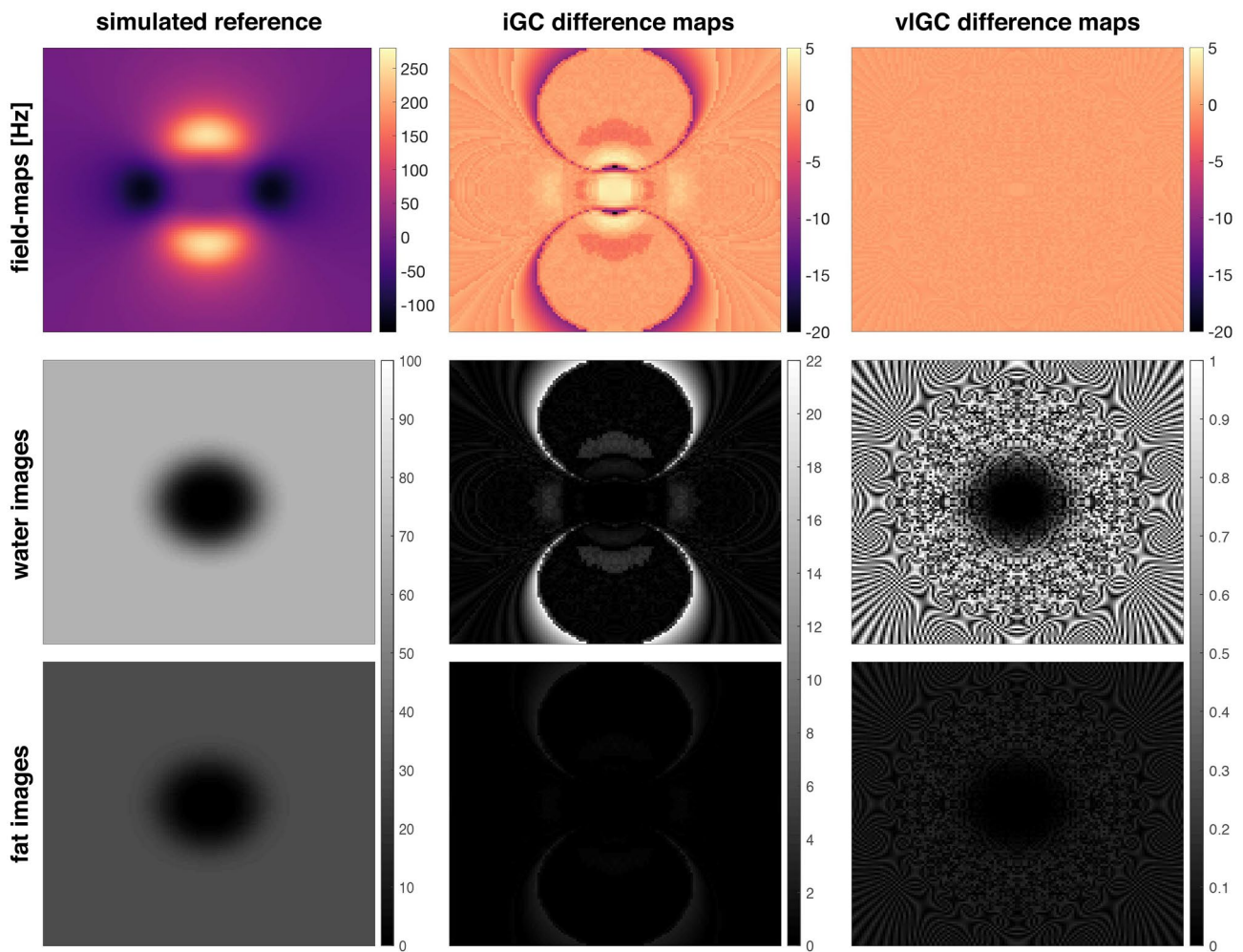The first row of Figure 4 shows the field-maps of the iGC, rGOOSE and the vlGC in the sharp boundary numerical

FIGURE 3 Field-mapping (first row), water- (second row) fat (third row) separation results of the numerical phantom with smooth air-tissue interface at the central slice using the iGC and the vlGC. The first column shows the reference water and fat images, the second column shows the difference of the results from the iGC to the reference, and the third column shows difference of the results from the vlGC to the reference. The field-mapping errors in the numerical phantom propagate into water–fat separation, where the error in the iGC method becomes up to 61%, while for the proposed vlGC it stays below 1.4% in the whole volume

phantom. The field-map of the iGC method follows the reference starting at the periphery of the volume until a certain point close to the boundary with the signal void and the errors become then significant until the center of the volume. The field-map of rGOOSE follows the reference for a wider spatial extent but also fails very close to the signal void on one side of the air-tissue interface. Only the field-map of the vlGC follows the reference for the whole volume.

The second row of Figure 4 shows the closed-form ℓ_2-regularized dipole inversion results for the different field-maps plotted in the first row of Figure 4. The magnetic susceptibility results based on the vlGC are much closer to the ground truth and show greatly reduced streaking artifacts. The corresponding line plot show that the χ-maps based on the iGC method drastically overshoot outside and inside the air-containing signal void. While there is still a significant underestimation of χ values outside the signal void, the results based on rGOOSE already show a significant improvement

over the iGC. However, the field-map jump close to the interface clearly introduces artifacts in the susceptibility map. The vlGCs χ-maps are closest to the reference, compared to the iGC and the rGOOSE method. Figure 5 shows that the simulation depicted in Figure 4 are in close agreement with the experimental measurements of the air bubble phantom. Furthermore, the vlGC is significantly more robust to the strong background field variations introduced by the shiming fields and yields comparable susceptibility values at different shimming settings. The QSM results based on the iGC significantly overestimate the susceptibility of air and include large errors at strong background fields

4.3 | In vivo results

Figure 6 shows the field-mapping results and the corresponding water–fat separated images in one large-FOV
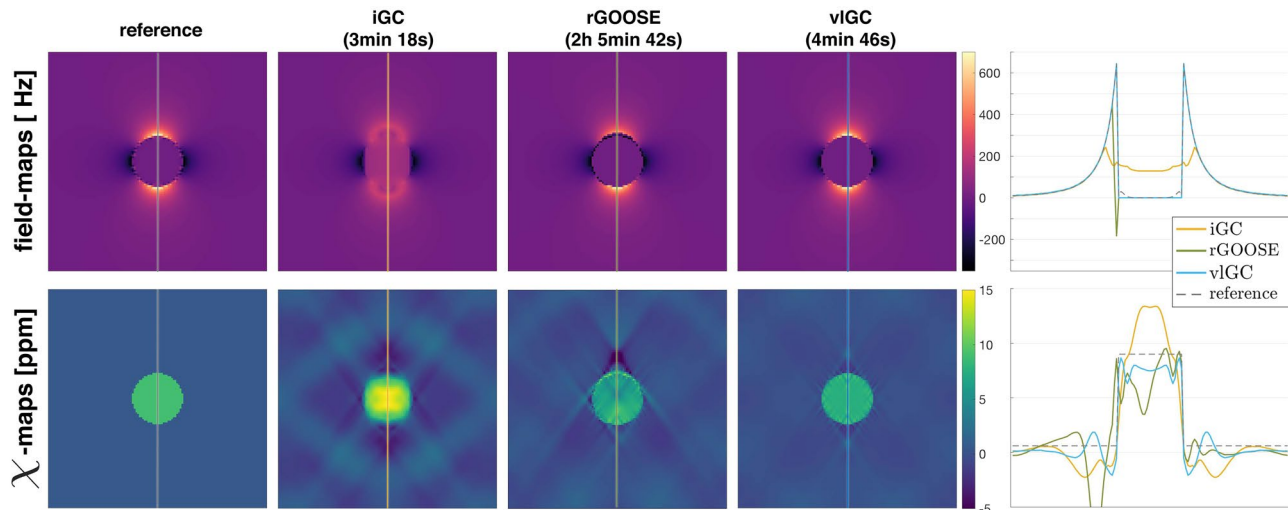
FIGURE 4 Field-mapping (first row) and QSM (second row) results of the numerical simulation with sharp air-tissue interface of an MR-invisible air bubble in an environment with 30% fat fraction using a simple closed-form ℓ_2-regularized dipole inversion. The time given below each method's name represents the run-time of the respective method. The first column shows the reference field- and susceptibility-map, the second column shows the results from the iGC, the third column shows the results from the rGOOSE and the fourth column the results from the vlGC and the fifth column shows line plots for the field-mapping and susceptibility-map for all methods. Compared to the iGC the vlGC is able to greatly reduce streaking by correctly estimating field-map values close to the signal void and the shape of the sphere is preserved while the computational cost is only reasonably increased. The rGOOSE is already performing significantly better in the parameter estimation than the iterative graph-cut. However, it suffers from its graph construction leading to a long run-time and a accidental rejection of the correct field-map solution close the signal void in the algorithms default settings

head/neck scan. The vlGC is able to resolve the large dynamic range of 5340 Hz on the shown field-map, without an additional unwrapping step, resolving even the very rapid field-map variation at the bottom of the FOV. The volumetric field-mapping data from the head/neck region of 14 subjects are provided as Supporting Information Video S1-S14. The visual reading of the 14 head/neck datasets yields swaps in the results by the iGC in all subjects obtained by the iGC. Furthermore, the location of the swaps changes significantly along the slice direction. The vlGC shows water–fat swaps in 3 subjects.

Figure 7 shows a lumbar spine with an intradiscal air inclusion. The derived χ-map based on the field-map of the vlGC reveals the true underlying paramagnetic property of the air-like gas (of the order of 9.4 ppm). The χ-map based on the field-map of the iGC indicates a paramagnetic susceptibility source. The presence of the air-inclusion was verified on a computed tomography (CT) scan. The CT scan showed an additional calcification on the top of the FOV, which also results in an MR signal void in the corresponding image of the magnitude of the first echo. QSM based on both field-mapping methods is able to correctly estimate the diamagnetic property of the calcification.

Figure 8 shows field-mapping and QSM results of a second lumbar spine scan with the trabecular bone structure of a spinous process as the region-of-interest (arrow). The estimated QSM maps show first that the field-map estimated by the iGC was very smooth when compared to the vlGC and

second that the smoothed field-map translated to a significant underestimation of the susceptibility values of the cortical bone structure in the ROI.

Figure 9 shows the results of the mean magnetic susceptibility value analysis of the spinous process cortical bone region of the L3 vertebra in the lumbar spine of the 4 scanned volunteers. QSM based on the vlGC yields susceptibility values that are significantly closer to the literature value of cortical bone than QSM based on the iGC. Furthermore, in a repeatability experiment in one subject the mean susceptibility value within the ROI was stable when using the field-map from the vlGC.

5 | DISCUSSION

The present work aimed to develop a method for improved field-mapping in challenging anatomical water–fat regions and to particularly apply the developed method in body applications of QSM. Specifically, this work first proposed a global penalized maximum likelihood cost function with a novel formulation to enforce the data consistency and then introduced the solution of the cost function using a single-min-cut graph-cut on a variable-layer graph that allows to select the same field-map range for each voxel. The work then examined the effect of the field-mapping accuracy on the estimated magnetic susceptibility in particular close to MR signal voids and applied the developed field-mapping method in body QSM of regions enclosing water, fat, and MR signal voids.
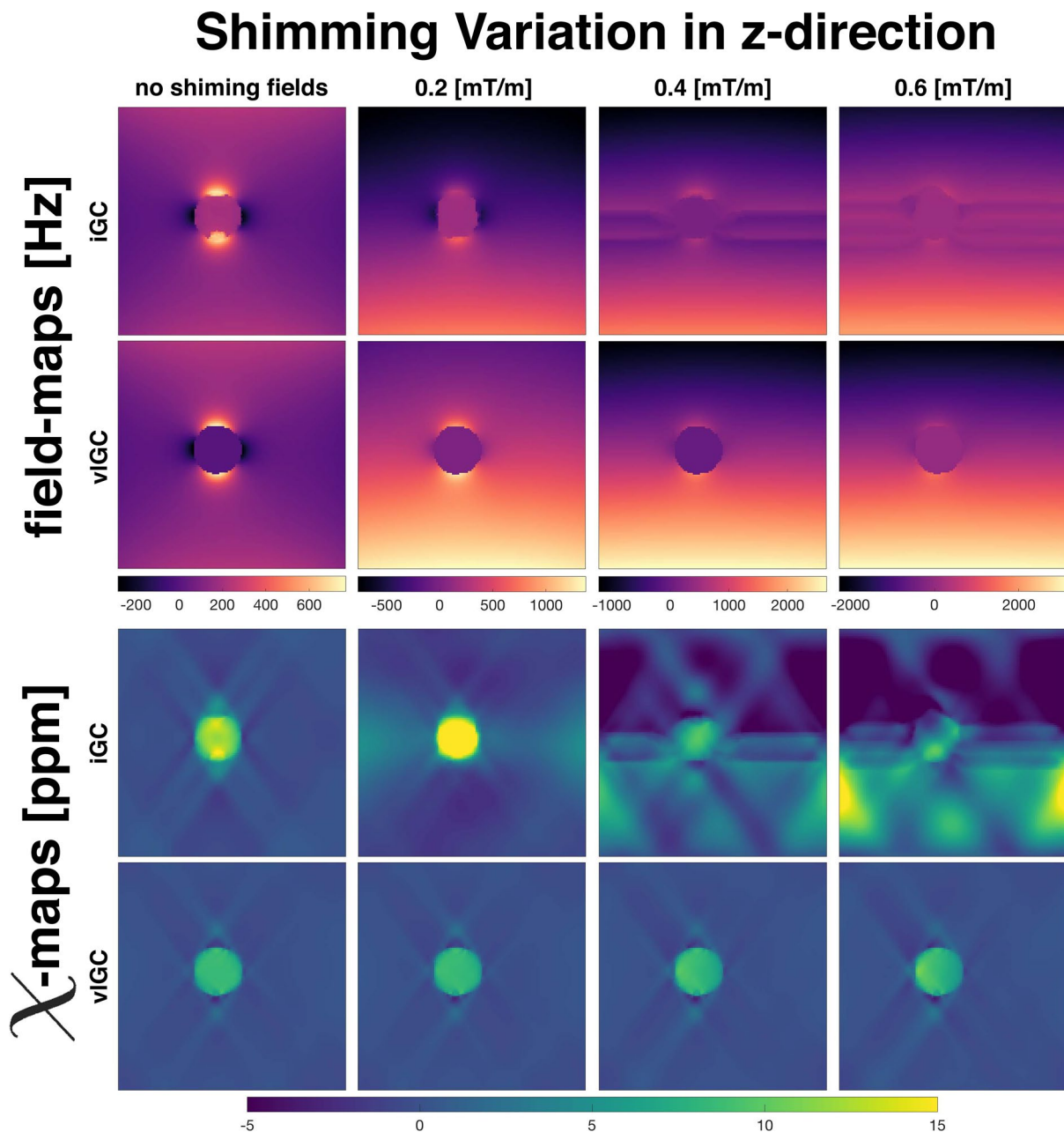
FIGURE 5 Field-mapping (first two rows) and QSM (last two rows) results of the experimental air bubble phantom with sharp air-water interface and varying shim fields. The iGC is challenged in estimating the sharp boundary of the phantom estimating non-physical values within the signal void. Furthermore, the iGC is only able to pick up the background field variation for the first shim field setting of 0.2 mT/m and is showing wraps at higher shim field settings. The difference of the vlGC field-map and of the iGC field-map for the first shim setting is in the order of 440 Hz and refers to a total swap for the iGC. QSM based on the vlGC yields homogeneous and robust results for all shim field strengths while slightly underestimating the susceptibility within the air inclusion. QSM based on the iGC shows a strong dependence on the underlying shim field strength

Since the vlGC will always find the global minimum of the cost function,[30] the correct estimation of the field-map and the occurrence of resulting water–fat swaps only depend on the design of the cost function. Consequently, the proposed field-mapping method introduces some important novel features for solving the water–fat problem using graph-cuts. First, the vlGC algorithm enforces the data consistency solely by the extraction of the minima from the voxel-wise

estimates. In the iGC and in the rGOOSE methods,[20,25] the voxel-wise residual is used for data consistency. The presently proposed enforcement of the data consistency by extracting only the local minima equalizes the significance of all voxels in the volume in reference to the smoothness constraint. The ability of the vlGC to find the global minimum of the cost function potentially comparing a manifold of voxel-wise solutions is a strong advantage when compared
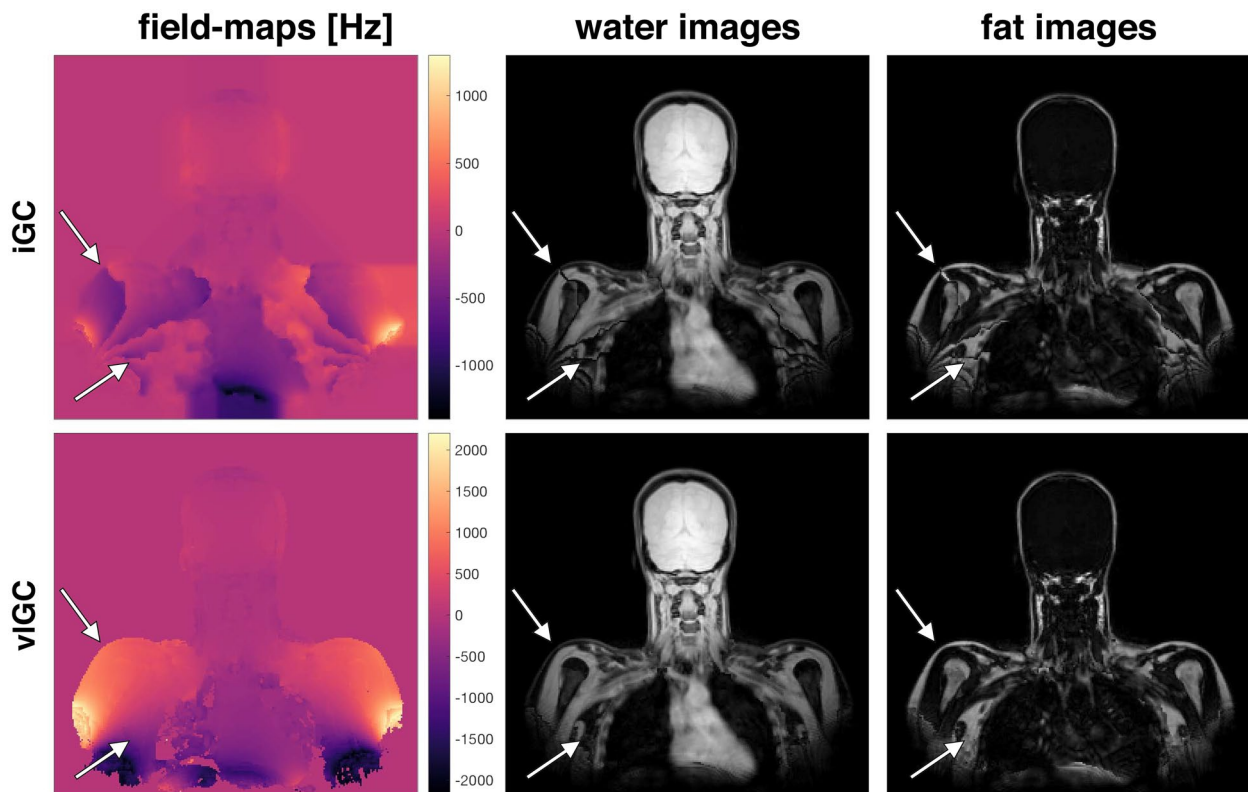
FIGURE 6 Field-mapping (first column) and water- (second column) fat (third column) separation results in a large FOV head/neck region scan. The first row shows the results from the iGC and the second row the results from the vlGC. The vlGC is able to resolve the large dynamic range of 5340 Hz on the shown field-map resolving even the very rapid field-map variation at the bottom of the FOV. The iGC yields a significantly reduced dynamic range and shows phase-wraps. The phase-wraps propagate into the water–fat separated images (arrows). Similar datasets are provided in the supplementary material as videos showing the methods comparison across slices

to the iGC. In the iGC, for each voxel only two field-map candidates are taken and a graph-cut is used to solve the cost function value in a so-called jump move. If the cost function decreases, the field-map candidate is taken. This procedure is repeated until a defined convergence criterion is met. In contrast to the vlGC, the iGC needs to perform several graph-cuts in several jump move steps. While each graph-cut is guaranteed to find the globally optimal solution to the corresponding binary sub-problem, this is not necessarily true for the global cost function. Furthermore, since in the iGC the candidates are not restricted to be only local minima of the voxel-wise field-map estimate, the field-map estimation is inherently dependent on the use of an additional data consistency term.

Second, the vlGC requires an a priori defined field-map sampling interval. Specifically, the present work first defined an optimal sampling interval over which the voxel-wise cost function Equation (5) needs to be sampled in order to obtain phase unwrapped field-map solutions in the whole volume. Overestimating the size of the field-map sampling interval still leads to the global minimum of the cost function, but with a longer run-time of the graph routine. Since $\widehat{f}_B$ is unknown, $f_{\text{interval}} = |\max(\widehat{f}_B) - \min(\widehat{f}_B)|$ must be estimated with prior

knowledge. Since overestimating the size of the sampling interval f still leads to the global minimum of the cost function, one can choose the sampling interval in this first step arbitrarily large. For $f > f_{\text{interval}} + n \cdot f_{\text{period}}$, $n \in \mathbb{N}$, Equation (6) becomes periodic with $n+1$ solutions. Since the graph-cut algorithm will yield only one solution, the graph-cut solution can lead to field-maps not centered around zero but in a different period of the field-map estimate. Which exact solution is yielded simply depends on rounding and numerical errors. However, all above solutions are correct and can be brought into the same period centered around zero by computing the mean of the field-map estimate modulo the period length.

Third, the vlGC uses a graph construction enabling accelerated computations. The introduced advancements in the graph construction related to the variable-layer architecture and the inclusion to the graph of signal-only regions lead to the smallest possible size of the graph for a given a priori known sampling interval f_{total}. After the field-map sampling interval is defined, it is important to point out that the variable-layer graph architecture significantly reduces the number of nodes per voxel compared to formerly proposed single-min-cut graph-cut algorithms. Usually, in regions with high SNR there are only two minima per period
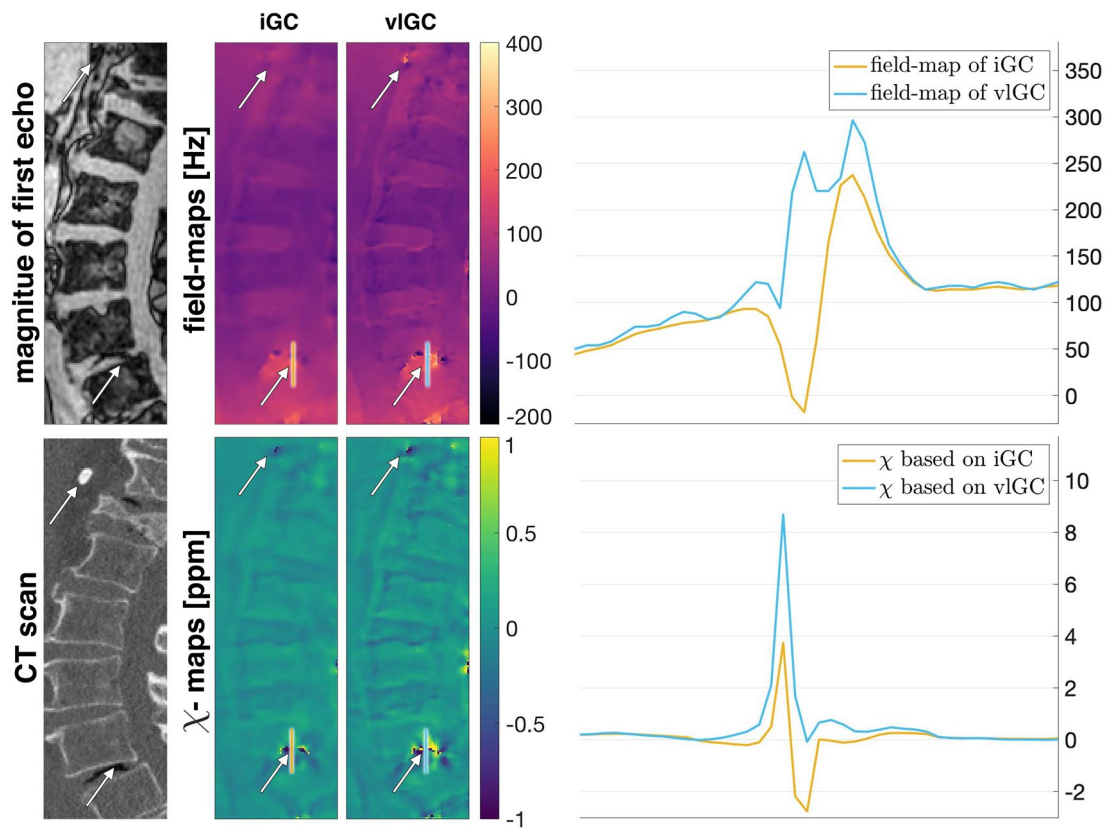
FIGURE 7 Field-mapping (first row) and susceptibility (second row) results in a pathological lumbar spine with a calcification at the top of the FOV and a intradiscal gas inclusion at the bottom leading to an MR signal void region, both highlighted by arrows. The first column shows the magnitude of the first echo , the second column shows the results from the iGC, the third column shows the result from the vlGC, and the last column shows line plots over the intradiscal gas inclusion. All susceptibility maps can correctly estimate the calcification to be diamagnetic. The line profiles over the intradiscal gas inclusion illustrate the significantly different values yielded by the iGC and the vlGC in this region. Only the vlGC is able to reveal the true underlying paramagnetic property of the air-like gas (of the order of 9.4 ppm). The susceptibility map based on the field-maps of the iGC falsely indicates the air inclusion to be mainly diamagnetic. The result is verified by the CT scan

in C. Only in voxels with low SNR there are commonly more. Compared to GOOSE[24] and rGOOSE,[25] the size of the graph using the vlGC can be reduced by approximately a factor of 50 and 4 for voxels with high SNR, respectively, and by factor of 200 and 16 for voxels with low SNR, respectively. Such a reduction in the graph size results in a decrease of the required run-time by an order of magnitude. However, in the case of strong background field-map variations as shown in Figure 6 the vlGC could potentially be combined with a phase-unwrapping methods such as[38] or coarse to fine grid approaches as used in[39] in order to further reduce the run-time. The variable-layer graph construction is also a significant advantage over the rGOOSE method that only allows for the same amount of minima per voxel for the whole volume. However, when the same field-map range is sampled for the voxel-wise field-map estimate, the number of minima in a voxel depends on the SNR and can consequently vary voxel by voxel. Although rGOOSE guarantees convergence to its global minimum, the restriction in the graph-construction can lead either to an accidental

miss of the correct voxel field-map estimate or to a significant increase in run-time making the method infeasible for clinical datasets of large sizes. Furthermore, the vlGC has been demonstrated to be able to directly yield non-wrapped field-maps. An accurate and inherently non-wrapped field-map is particularly important for quantitative susceptibility mapping. Field-map errors and wraps are expected to translate in strong susceptibility artifacts.[16] Since QSM is based on the field-map estimate, errors in the field-map estimation propagate into the susceptibility maps as demonstrated in Figures 4 and 5. Using the proposed method, an erroneous algorithmic step in the QSM processing pipeline can be circumvented. It has also been demonstrated that despite the long-range effect of the dipole field and the corresponding kernel,[1] field-map values at the border to an MR signal void containing a strong susceptibility source like air are important to map correctly in order to obtain correct susceptibility values. Correct field-map values at a certain distance to the signal void and data weighting are not sufficient. Therefore, it becomes essential to accurately estimate field-map values
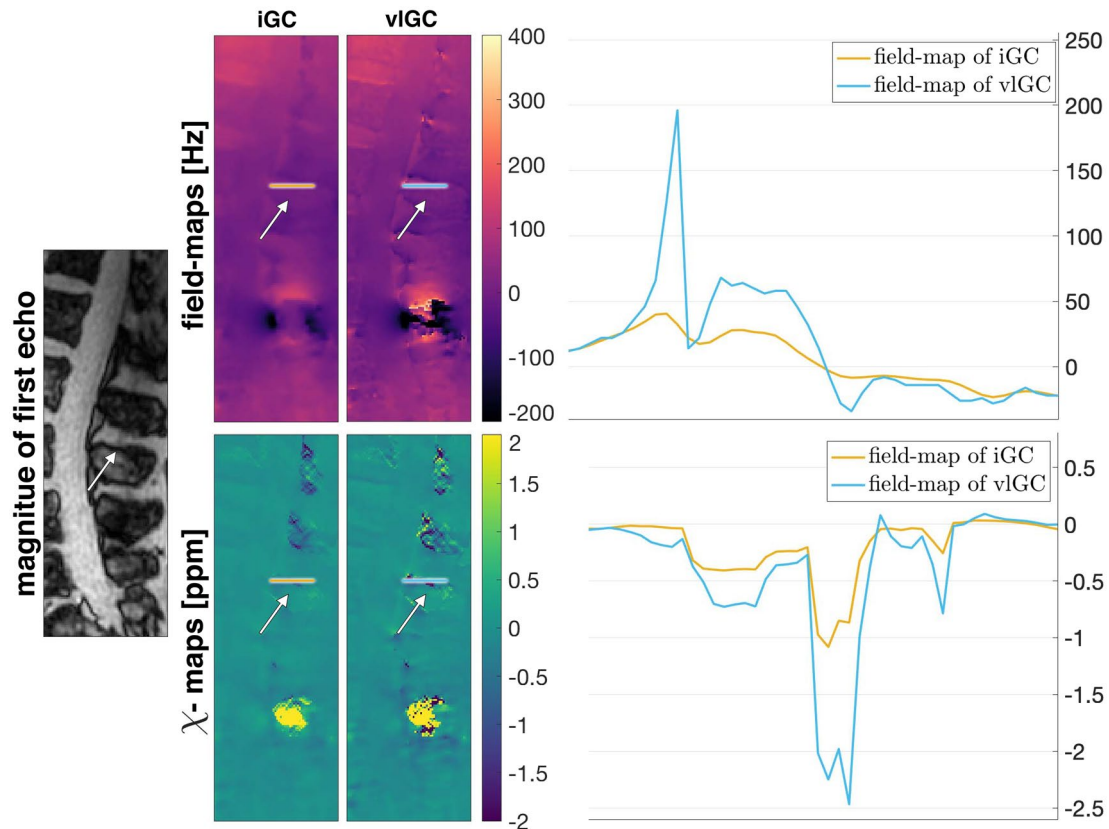
FIGURE 8 Field-mapping (first row) and susceptibility (second row) results in the spinous process cortical bone region-of-interest (arrows). The first column shows the magnitude of the first echo, the second column shows the results from the iGC, the third column shows the result from the vlGC, and the last column shows line plots over the cortical bone region. QSM based on the vlGC is able to estimate the literature susceptibility value of bone of approximately -2 ppm at the spinous process while the QSM based on the iGC yields significantly reduced susceptibility values of only −1 ppm
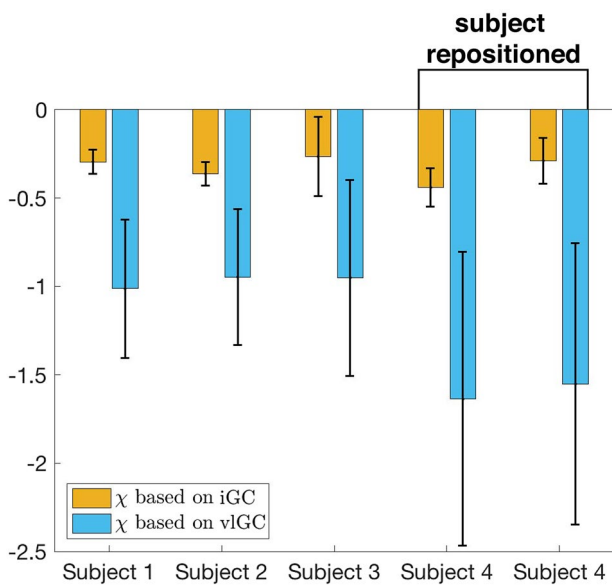
FIGURE 9 Mean magnetic susceptibility value analysis of the spinous process cortical bone region-of-interest at the L3 in 4 subjects as well as a repeatability test of the fourth subject by re-positioning and re-scanning the subject. QSM based on the iGC yields in all subjects a significant underestimation of susceptibility values of cortical bone while susceptibility values based on the vlGC are significantly closer to the literature value

as close as possible to an MR signal void. This conclusion is supported by the spine with an intradiscal air inclusion. QSM based on the vlGC is able to reveal the strong paramagnetic susceptibility value of the air-like gas. The correct estimation of the air inclusion magnetic susceptibility was not achieved with the field-maps of the iGC. Furthermore, the vlGC is able to estimate susceptibility values much closer to the literature value in a cortical bone region-of-interest in several subjects as shown in Figures 8 and 9.

The present work has some limitations. In order to benefit from the full 3D neighborhood information, the graph for the whole volume needs to be loaded into the RAM, which can be in the order of several 10 GiB. Furthermore the graph-cut itself is intrinsically not parallelizable without the loss of accuracy[40-42] and the run-time drastically scales with the number of nodes. Due to possible computation time restrictions with big datasets, a chunked minimization can be applied, which does not only minimize partial volumes (eg, slices) independently, but applies the smoothness constraint from Equation (6) from one chunk to the adjacent. A more detailed description of the chunked minimization is provided in the supplementary material. However, the run-time for a clinical relevant dataset like in the presented lumbar

spine is in the reasonable order of 5 minutes. Second, the selection of the size of the neighborhood $N(\mathbf{r})$ of the global cost function has not been optimized. The 6-connected von Neumann voxel neighborhood including the adjacent voxel in x-, y-, z-direction was presently used but a 26-neighborhood would be also possible. A larger neighborhood translates into an increased importance of the spatial smoothness term in Equation (6), which has to be considered. Since only local minima that have a predefined distance in frequency are extracted, the global optimal field-map is piece-wise constant with respect to the size of the penalization term and therefore the global minimum might not be effected. Third, studies on field-map and QSM generally have the limitations that results can only heuristically be evaluated in the water–fat domain or be compared to literature values for susceptibility values. The present work showed that the present methodology yields robust field-map and susceptibility results in numerical simulations of air-tissue geometries, in a phantom scanned at different settings and in vivo spine measurements. However, the present methodology would strongly benefit from a large scale validation of its performance in estimating magnetic susceptibility in further body QSM applications.

6 | CONCLUSION

A single-min-cut graph-cut field-mapping method with a variable-layer construction was proposed for field-mapping in body water–fat regions. The proposed method shows the following significant improvements over an iterative graph-cut field-mapping method: (a) it can resolve strong field-mapping variations close to MR signal voids, (b) it performs significantly better in regions with strong field-map variation and high R_2^* values, (c) it can directly yield non-smooth field-maps like a voxel-wise method, and (d) it significantly improves subsequently performed quantitative susceptibility mapping particularly in areas close to MR signal voids.

ORCID
Christof Boehm https://orcid.org/0000-0003-1321-5804
Maximilian N. Diefenbach https://orcid.org/0000-0002-5581-885X

TWITTER
Christof Boehm @BoehmChristof

REFERENCES

1. Wang Y, Liu T. Quantitative susceptibility mapping (QSM): decoding MRI data for a tissue magnetic biomarker. *Magn Reson Med*. 2014;73:82-101.
2. Liu C, Li W, Tong KA, Yeom KW, Kuzminski S. Susceptibility-weighted imaging and quantitative susceptibility mapping in the brain. *J Magn Reson Imaging*. 2014;42:23-41.
3. EskreisWinkler S, Zhang Y, Zhang J, et al. The clinical utility of qsm: disease diagnosis, medical management, and surgical planning. *NMR Biomed*. 2016;30:e3668.
4. Sun H, Seres P, Wilman A. Structural and functional quantitative susceptibility mapping from standard FMRI studies. *NMR Biomed*. 2016;30:e3619.
5. Sharma SD, Hernando D, Horng DE, Reeder SB. Quantitative Susceptibility mapping in the abdomen as an imaging biomarker of hepatic iron overload. *Magn Reson Med*. 2014;74:673-683.
6. Lin H, Wei H, He N, et al. Quantitative susceptibility mapping in combination with water–fat separation for simultaneous liver iron and fat fraction quantification. *Eur Radiol*. 2018;28:3494-3504.
7. Jafari R, Sheth S, Spincemaille P, et al. Rapid automated liver quantitative susceptibility mapping. *J Magn Reson Imaging*. 2019;50:725-732.
8. Straub S, Laun FB, Emmerich J, et al. Potential of quantitative susceptibility mapping for detection of prostatic calcifications. *J Magn Reson Imaging*. 2016;45:889-898.
9. Wei H, Lin H, Qin L, et al. Quantitative susceptibility mapping of articular cartilage in patients with osteoarthritis at 3t. *J Magn Reson Imaging*. 2018;49:1665-1675.
10. Dimov AV, Liu Z, Spincemaille P, Prince MR, Du J, Wang Y. Bone quantitative susceptibility mapping using a chemical species-specific R_2^* signal model with ultrashort and conventional echo data. *Magn Reson Med*. 2017;79:121-128.
11. Diefenbach MN, Meineke J, Ruschke S, Baum T, Gersing A, Karampinos DC. On the sensitivity of quantitative susceptibility mapping for measuring trabecular bone density. *Magn Reson Med*. 2019;81:1739-1754.
12. Wang Y, Spincemaille P, Liu Z, et al. Clinical quantitative susceptibility mapping (qsm): biometal imaging and its emerging roles in patient care. *J Magn Reson Imaging*. 2017;46:951-971.
13. Diefenbach MN, Van A, Meineke J, et al. On the sensitivity of bone marrow magnetic susceptibility and R_2^* on trabecular bone microstructure. In Proceedings 26th Annual Meeting International Society for Magnetic Resonance in Medicine, Paris, France; 2018:0533.
14. Colgan TJ, Knobloch G, Reeder SB, Hernando D. Sensitivity of quantitative relaxometry and susceptibility mapping to microscopic iron distribution. *Magn Reson Med*. 2020;83:673-680.

15. Dimov AV, Liu T, Spincemaille P, et al. Joint estimation of chemical shift and quantitative susceptibility mapping (chemical Qsm). *Magn Reson Med*. 2014;73:2100-2110.

16. Bechler E, Stabinska J, Wittsack H. Analysis of different phase unwrapping methods to optimize quantitative susceptibility mapping in the abdomen. *Magn Reson Med*. 2019;82:2077-2089.

17. Fortier V, Levesque IR. Phase processing for quantitative susceptibility mapping of regions with large susceptibility and lack of signal. *Magn Reson Med*. 2018;79:3103-3113.

18. Yu H, Reeder SB, Shimakawa A, Brittain JH, Pelc NJ. Field map estimation with a region growing scheme for iterative 3-point water–fat decomposition. *Magn Reson Med*. 2005;54:1032-1039.

19. Hernando D, Haldar JP, Sutton BP, Ma J, Kellman P, Liang ZP. Joint estimation of water/fat images and field inhomogeneity map. *Magn Reson Med*. 2008;59:571-580.

20. Hernando D, Kellman P, Haldar JP, Liang ZP. Robust water/fat separation in the presence of large field inhomogeneities using a graph cut algorithm. *Magn Reson Med*. 2009;63:NA-NA.

21. Tsao J, Jiang Y. Hierarchical ideal: fast, robust, and multiresolution separation of multiple chemical species from multiple echo times. *Magn Reson Med*. 2012;70:155-159.

22. Berglund J, Johansson L, Ahlström H, Kullberg J. Three-point Dixon method enables whole-body water and fat imaging of obese subjects. *Magn Reson Med*. 2010;63:1659-1668.

23. Hu HH, Börnert P, Hernando D, et al. Ismrm workshop on fat-water separation: insights, applications and progress in MRI. *Magn Reson Med*. 2012;68:378-388.

24. Cui C, Wu X, Newell JD, Jacob M. Fat water decomposition using globally optimal surface estimation (goose) algorithm. *Magn Reson Med*. 2014;73:1289-1299.

25. Cui C, Shah A, Wu X, Jacob M. A rapid 3d fat-water decomposition method using globally optimal surface estimation (R-GOOSE). *Magn Reson Med*. 2017;79:2401-2407.

26. Yu H, Shimakawa A, McKenzie CA, Brodsky E, Brittain JH, Reeder SB. Multiecho water–fat separation and simultaneous R_2^* estimation with multifrequency fat spectrum modeling. *Magn Reson Med*. 2008;60:1122-1134.

27. Bydder M, Yokoo T, Hamilton G, et al. Relaxation effects in the quantification of fat using gradient echo imaging. *Magn Reson Imaging*. 2008;26:347-359.

28. Hernando D, Kellman P, Haldar J, Liang ZP. Estimation of water/fat images, B_0 field map and T_2^* map using VARPRO. In *ISMRM 16th Scientific Meeting & Exhibition, Toronto, Canada*, 2008:1517.

29. Lu W, Hargreaves BA. Multiresolution field map estimation using golden section search for water–fat separation. *Magn Reson Med*. 2008;60:236-244.

30. Shah A, Abramoff MD, Wu X. Optimal surface segmentation with convex priors in irregularly sampled space. *Med Image Anal*. 2019;54:63-75.

31. Boykov Y, Kolmogorov V. An experimental comparison of min-cut/max- flow algorithms for energy minimization in vision. *IEEE Trans Pattern Anal Mach Intelligence*. 2004;26:1124-1137.

32. Griffiths DJ. *Introduction to electrodynamics*, 4th ed. Boston, MA: Pearson, 2013. Re-published by Cambridge University Press in 2017.

33. Ren J, Dimitrov I, Sherry AD, Malloy CR. Composition of adipose tissue and marrow fat in humans by 1 h Nmr at 7 Tesla. *J Lipid Res*. 2008;49:2055-2062.

34. Bilgic B, Chatnuntawech I, Fan AP, et al. Fast image reconstruction With L2-regularization. *J Magn Reson Imaging*. 2013;40:181-191.

35. Ruschke S, Eggers H, Kooijman H, et al. Correction of phase errors in quantitative water–fat imaging using a monopolar time-interleaved multi-echo gradient echo sequence. *Magn Reson Med*. 2016;78:984-996.

36. Zhou D, Liu T, Spincemaille P, Wang Y. Background field removal by solving the Laplacian boundary value problem. *NMR Biomed*. 2014;27:312-319.

37. Diefenbach MN, Van A, Meineke J, et al. Vertebral column quantitative susceptibility mapping using joint background field removal and dipole inversion. In Proceedings 26th Annual Meeting International Society for Magnetic Resonance in Medicine, Paris, France; 2018:0191.

38. Dong J, Chen F, Zhou D, Liu T, Yu Z, Wang Y. Phase unwrapping with graph cuts optimization and dual decomposition acceleration for 3d high-resolution MRI data. *Magn Reson Med*. 2016;77:1353-1358.

39. Berglund J, Skorpil M. Multi-scale graph-cut algorithm for efficient water–fat separation. *Magn Reson Med*. 2016;78:941-949.

40. Vineet V, Narayanan PJ. CUDA cuts: fast graph cuts on the GPU. In *2008 IEEE Computer Society Conference on Computer Vision and Pattern Recognition Workshops, Anchorage, USA*, 2008;6:1-8.

41. Strandmark P, Kahl F. Parallel and distributed graph cuts by dual decomposition. In *2010 IEEE Computer Society Conference on Computer Vision and Pattern Recognition, San Francisco, CA, USA*, 2010;6:2085-2092.

42. Yu M, Shen S, Hu Z. Dynamic parallel and distributed graph cuts. *IEEE Trans Image Process*. 2016;25:5511-5525.

SUPPORTING INFORMATION

Additional supporting information may be found online in the Supporting Information section.

VIDEO S1. Volunteer 1: Field-mapping (first column) and water– (second column) fat (third column) separation results in large FOV head/neck region scan. The first row shows the results from the iGC and the second row the results from the vlGC. The vlGC is able to resolve the large dynamic range of the field-map in the subject resolving even the very rapid field-map variation at the bottom of the FOV. The iGC yields a significantly reduced dynamic range of the field-map and shows water–fat swaps. The location of water–fat swaps in the iGC results strongly varies along slice direction

VIDEO S2. Volunteer 2: Field-mapping (first column) and water– (second column) fat (third column) separation results in large FOV head/neck region scan. The first row shows the results from the iGC and the second row the results from the vlGC. The vlGC is able to resolve the large dynamic range of the field-map in the subject resolving even the very rapid field-map variation at the bottom of the FOV. The iGC yields a significantly reduced dynamic range of the field-map and shows water–fat swaps. The location of water–fat swaps in the iGC results strongly varies along slice direction

VIDEO S3. Volunteer 3: Field-mapping (first column) and water– (second column) fat (third column) separation results

in large FOV head/neck region scan. The first row shows the results from the iGC and the second row the results from the vlGC. The vlGC is able to resolve the large dynamic range of the field-map in the subject resolving even the very rapid field-map variation at the bottom of the FOV. The iGC yields a significantly reduced dynamic range of the field-map and shows water–fat swaps. The location of water–fat swaps in the iGC results strongly varies along slice direction

VIDEO S4. Volunteer 4: Field-mapping (first column) and water– (second column) fat (third column) separation results in large FOV head/neck region scan. The first row shows the results from the iGC and the second row the results from the vlGC. The vlGC is able to resolve the large dynamic range of the field-map in the subject resolving even the very rapid field-map variation at the bottom of the FOV. The iGC yields a significantly reduced dynamic range of the field-map and shows water–fat swaps. The location of water–fat swaps in the iGC results strongly varies along slice direction

VIDEO S5. Volunteer 5: Field-mapping (first column) and water– (second column) fat (third column) separation results in large FOV head/neck region scan. The first row shows the results from the iGC and the second row the results from the vlGC. The vlGC is able to resolve the large dynamic range of the field-map in the subject resolving even the very rapid field-map variation at the bottom of the FOV. The iGC yields a significantly reduced dynamic range of the field-map and shows water–fat swaps. The location of water–fat swaps in the iGC results strongly varies along slice direction

VIDEO S6. Volunteer 6: Field-mapping (first column) and water– (second column) fat (third column) separation results in large FOV head/neck region scan. The first row shows the results from the iGC and the second row the results from the vlGC. The vlGC is able to resolve the large dynamic range of the field-map in the subject resolving even the very rapid field-map variation at the bottom of the FOV. The iGC yields a significantly reduced dynamic range of the field-map and shows water–fat swaps. The location of water–fat swaps in the iGC results strongly varies along slice direction

VIDEO S7. Volunteer 7: Field-mapping (first column) and water– (second column) fat (third column) separation results in large FOV head/neck region scan. The first row shows the results from the iGC and the second row the results from the vlGC. The vlGC is able to resolve the large dynamic range of the field-map in the subject resolving even the very rapid field-map variation at the bottom of the FOV. The iGC yields a significantly reduced dynamic range of the field-map and shows water–fat swaps. The location of water–fat swaps in the iGC results strongly varies along slice direction

VIDEO S8. Volunteer 8: Field-mapping (first column) and water– (second column) fat (third column) separation results in large FOV head/neck region scan. The first row shows the results from the iGC and the second row the results from the vlGC. The vlGC is able to resolve the large dynamic range

of the field-map in the subject resolving even the very rapid field-map variation at the bottom of the FOV. The iGC yields a significantly reduced dynamic range of the field-map and shows water–fat swaps. The location of water–fat swaps in the iGC results strongly varies along slice direction.

VIDEO S9. Volunteer 9: Field-mapping (first column) and water– (second column) fat (third column) separation results in large FOV head/neck region scan. The first row shows the results from the iGC and the second row the results from the vlGC. The vlGC is able to resolve the large dynamic range of the field-map in the subject resolving even the very rapid field-map variation at the bottom of the FOV. The iGC yields a significantly reduced dynamic range of the field-map and shows water–fat swaps. The location of water–fat swaps in the iGC results strongly varies along slice direction

VIDEO S10. Volunteer 10: Field-mapping (first column) and water– (second column) fat (third column) separation results in large FOV head/neck region scan. The first row shows the results from the iGC and the second row the results from the vlGC. The vlGC is able to resolve the large dynamic range of the field-map in the subject resolving even the very rapid field-map variation at the bottom of the FOV. The iGC yields a significantly reduced dynamic range of the field-map and shows water–fat swaps. The location of water–fat swaps in the iGC results strongly varies along slice direction

VIDEO S11. Volunteer 11: Field-mapping (first column) and water– (second column) fat (third column) separation results in large FOV head/neck region scan. The first row shows the results from the iGC and the second row the results from the vlGC. The vlGC is able to resolve the large dynamic range of the field-map in the subject resolving even the very rapid field-map variation at the bottom of the FOV. The iGC yields a significantly reduced dynamic range of the field-map and shows water–fat swaps. The location of water–fat swaps in the iGC results strongly varies along slice direction

VIDEO S12. Volunteer 12: Field-mapping (first column) and water– (second column) fat (third column) separation results in large FOV head/neck region scan. The first row shows the results from the iGC and the second row the results from the vlGC. The vlGC is able to resolve the large dynamic range of the field-map in the subject resolving even the very rapid field-map variation at the bottom of the FOV. The iGC yields a significantly reduced dynamic range of the field-map and shows water–fat swaps. The location of water–fat swaps in the iGC results strongly varies along slice direction

VIDEO S13. Volunteer 13: Field-mapping (first column) and water– (second column) fat (third column) separation results in large FOV head/neck region scan. The first row shows the results from the iGC and the second row the results from the vlGC. The vlGC is able to resolve the large dynamic range of the field-map in the subject resolving even the very rapid field-map variation at the bottom of the FOV. The iGC yields a significantly reduced dynamic range of the field-map and

shows water–fat swaps. The location of water–fat swaps in the iGC results strongly varies along slice direction. The vlGC and the iGC show a water–fat swap in the upper part of the brain

VIDEO S14. Volunteer 14: Field-mapping (first column) and water– (second column) fat (third column) separation results in large FOV head/neck region scans. The first row shows the results from the iGC and the second row the results from the vlGC. The vlGC is able to resolve the large dynamic range of the field-map in the subject resolving even the very rapid field-map variation at the bottom of the FOV. The iGC yields a significantly reduced dynamic range of the field-map and

How to cite this article: Boehm C, Diefenbach MN, Makowski MR, Karampinos DC. Improved body quantitative susceptibility mapping by using a variable-layer single-min-cut graph-cut for field-mapping. *Magn Reson Med*. 2021;85:1697–1712. https://doi.org/10.1002/mrm.28515

3.3 Journal Publication II: Susceptibility artifact correction in MR thermometry for monitoring of mild radiofrequency hyperthermia using total field inversion

The publication entitled *Susceptibility artifact correction in MR thermometry for monitoring of mild radiofrequency hyperthermia using total field inversion* was published in Magnetic Resonance in Medicine (ISSN: 0740-3194). The manuscript was authored by Christof Boehm, Marianne Goeger-Neff, Hendrik T. Mulder, Benjamin Zilles, Lars H. Lindner, Gerard C. van Rhoon, Dimitrios C. Karampinos, and Mingming Wu. It is available online (DOI: 10.1002/mrm.29191) as an open access article under the terms of the Creative Commons Attribution-NonCommercial License. Preliminary results were also presented in the conference contribution C15, which was awarded with an ISMRM Magna Cum Laude Merit Award and selected as an oral presentation at the ISMRM annual meeting 2021. A summary of the publication is provided in Section 3.3.1, the author contributions are listed in Section 3.3.2 and the full text is included subsequently on the following pages.

3.3.1 Abstract

Purpose

Mild radiofrequency hyperthermia (RF-HT) of cancerous tissue during chemotherapy has shown to significantly increase the survival rate. Exact measurement of the tissue temperature is critical in the procedure to prevent tissue damage by overheating. Conventionally, sensor probes are placed invasively inside the tumor before therapy starts. However, this method has a few drawbacks, including the invasive nature of the probe placement during which cancer cells could be spread outside the tumor and the only localized temperature measurement. MRI can theoretically record 3D relative temperature maps non-invasively due to the proton resonance frequency shift of water with temperature. However, susceptibility artifacts often dominate the temperature changes by several orders of magnitude. In this work the use of a TFI algorithm for susceptibility contribution estimation and removal is proposed and applied to overcome limitations of previously proposed susceptibility removal methods.

Methods

A ℓ_1-norm-based TFI algorithm was developed and compared to the Laplacian boundary value and projection onto dipole fields background field removal techniques. The comparison encompassed a simulation, a phantom scan, four volunteer scans, and patient scans from four individuals—one with cervical cancer, two with sarcoma, and one with seroma—undergoing mild RF-HT treatment.

Results

The simulation revealed that both TFI and the BFR methods remove the susceptibility induced background fields while preserving the phase of temperature. In the phantom heating experiment TFI yields the most accurate results, while PDF tends to underestimate the temperature at air tissue interfaces and LBV removes valuable pixel layers. In the 4 volunteers scans, TFI resulted in the least cumulative error. In the patient scans, the temperature estimated via correction with TFI correlated best with the temperature probe inside the tumor.

Conclusion

The proposed ℓ_1-norm based TFI algorithm outperforms previously suggested BFR method for susceptibility artifact correction in terms of accuracy and robustness.

3.3.2 Author contributions

The first author developed the problem specific inverse model for the susceptibility source removal and implemented the optimization code in Python. The data were acquired with help from the coauthors. The first author furthermore analyzed and interpreted the data, and wrote the manuscript.

3.3.3 Original Article

RESEARCH ARTICLE

Magnetic Resonance in Medicine

Susceptibility artifact correction in MR thermometry for monitoring of mild radiofrequency hyperthermia using total field inversion

Christof Boehm[1] | **Marianne Goeger-Neff**[2] | **Hendrik T. Mulder**[3] | **Benjamin Zilles**[2] | **Lars H. Lindner**[2] | **Gerard C. van Rhoon**[3] | **Dimitrios C. Karampinos**[1] | **Mingming Wu**[1]

[1]Department of Diagnostic and Interventional Radiology, School of Medicine, Technical University of Munich, Munich, Germany

[2]Department of Medicine III, University Hospital, LMU Munich, Munich, Germany

[3]Erasmus MC Cancer Institute, Rotterdam, The Netherlands

Correspondence
Mingming Wu, Department of Diagnostic and Interventional Radiology, School of Medicine, Ismaninger Str. 22, 81675 Munich, Germany.
Email: mingming.wu@tum.de; @MingmingWu10

Funding information
H2020 European Research Council, Grant/Award Number: 677661, ProFatMRI

Purpose: MR temperature monitoring of mild radiofrequency hyperthermia (RF-HT) of cancer exploits the linear resonance frequency shift of water with temperature. Motion-induced susceptibility distribution changes cause artifacts that we correct here using the total field inversion (TFI) approach.

Methods: The performance of TFI was compared to two background field removal (BFR) methods: Laplacian boundary value (LBV) and projection onto dipole fields (PDF). Data sets with spatial susceptibility change and B_0-drift were simulated, phantom heating experiments were performed, four volunteer data sets at thermoneutral conditions as well as data from one cervical cancer, two sarcoma, and one seroma patients undergoing mild RF-HT were corrected using the proposed methods.

Results: Simulations and phantom heating experiments revealed that using BFR or TFI preserves temperature-induced phase change, while removing susceptibility artifacts and B_0-drift. TFI resulted in the least cumulative error for all four volunteers. Temperature probe information from four patient data sets were best depicted by TFI-corrected data in terms of accuracy and precision. TFI also performed best in case of the sarcoma treatment without temperature probe.

Conclusion: TFI outperforms previously suggested BFR methods in terms of accuracy and robustness. While PDF consistently overestimates susceptibility contribution, and LBV removes valuable pixel information, TFI is more robust and leads to more accurate temperature estimations.

KEYWORDS
interventional, mild hyperthermia, motion artifact, MR thermometry, proton resonance frequency shift, susceptibility artifact, total field inversion

1 | INTRODUCTION

Mild hyperthermia (HT) treatment (40-44°C) of various cancer types has shown to sensitize tumors to radio- and chemotherapy, thus increasing the survival rate.[1] Regional heating of tissue can be induced with radiofrequency (RF) antennas that create a focus in the target area. This treatment modality has become part of clinical practice for the treatment of various cancer types, including the treatment of sarcoma patients and patients with cervical cancer.[2-4] To prevent tissue damage by overheating, many procedures rely on temperature probes that are placed intraluminally or superficially onto the skin. Sometimes, a catheter is inserted into the tumor. In addition to these limited local temperature information, the only feedback originates from the patient's complaint to feeling local heat. MR temperature mapping can provide the required tissue coverage to detect unwanted hot-spots, and to monitor whether the desired thermal dose is applied to the tumor.

MR temperature monitoring of aqueous tissue exploits the linear proton resonance frequency shift (PRFS) of water with temperature, that can detect relative temperature changes with regards to a reference image.[5-7] Using PRFS of water can lead to accurate temperature readings when other phase confounders are accounted for.[8]

The conductivity change of tissue with temperature leads to different phase offsets at different time points and thus to significant temperature estimation errors.[9] This becomes especially important in the context of mild regional heating as the heated volume is large and as a high accuracy of temperature estimation is important for the small temperature change. The double echo gradient echo (DEGRE)[9] scheme or a phase-cycled fast spin echo (FSE) sequence[10] can correct for the conductivity bias.

Spatiotemporal drift of the main magnetic field B_0 as a result of hardware heating and hardware instabilities may be misinterpreted as temperature change if not corrected for.[11] The installation of additional reference tubes in the scanned field of view (FOV) containing substances with negligible PRFS with temperature, such as oil or silicone, allows to detect the B_0-drift in these areas.[12] Signal outside the heated area had been used as a reference as well.[13] The field drift is subsequently extrapolated onto the scanned FOV and subtracted from the phase difference map. The concept of B_0-drift correction using magnetic field probes was shown previously[14] and applied more recently to evaluate the specific absorption rate using MR thermometry.[15] However, this setup requires additional hardware. Another approach suggested the acquisition of free induction decay (FID) signals across multiple channels and the use of coil sensitivity profiles to generate B_0-drift maps.[16]

Monitoring organs affected by periodic respiratory motion requires a high temporal resolution and thus oftentimes only allow for two-dimensional (2D) slice coverage.[17] Motion compensation techniques in the context of tissue ablation and mild HT using MR-guided high-intensity focused ultrasound (MRgHIFU) include the multi-baseline approach, which acquires a dictionary of images at different respiratory states that can be used as the best matching reference.[18-20] This addresses periodic tissue displacement during ablation using MRgHIFU in abdominal organs[21] as well as periodic B_0-fluctuations during mild HT using MRgHIFU in the head and neck region.[22]

Another approach used during MRgHIFU is referred to as the "referenceless" approach.[23] It uses the phase of the current image outside the heated area as reference and interpolates a smooth function for the phase distribution into the heated area.[24] It resolves both the motion problem from reference images acquired at a different motion state and B_0-drift simultaneously, but only works if the heating is spatially confined, which is not the case during mild regional RF-HT.

It has been shown previously, that respiratory-induced B_0-fluctuations are negligible during PRFS-based MR thermometry of mild RF-HT in the pelvic region.[25] The predominant artifact source here originates from dynamic changes of susceptibility distribution leading to dipole artifacts that propagate to neighboring tissues.[26] Due to intestinal motion, the paramagnetic gases and diamagnetic water tissue exchange position, and cause large susceptibility distribution changes during treatment. The observed field perturbation equals the susceptibility change map convoluted with a dipole kernel. Furthermore, moving air bubbles inside a cooling water bolus during MR temperature monitoring of thermal therapies lead to strong susceptibility artifacts.[25]

Recently, it was proposed to correct for both the susceptibility artifacts and the B_0-drift up to a spatially first-order phase distribution in PRFS-based MR thermometry by solving the Laplacian boundary value problem (LBV)[27] or by projection onto dipole fields (PDF).[25,28] These two methods are well known in the context of quantitative susceptibility mapping (QSM) for separating the foreground from the background fields and were demonstrated to be advantageous in comparison to other background field removal (BFR) methods.[29,30] PDF is formulated as an optimization problem where the magnetic field inside the foreground mask is minimized by placing origins of dipole fields into a background mask. LBV solves the Laplace operator at the interface between foreground and background under the assumption that the field contributions at this layer of pixels originate only from the background field. However, PDF is known to overestimate the

background field, especially at air–tissue interfaces.[29,31] The LBV-based BFR method removes at least one pixel layer at the air–tissue border in order to calculate the Laplace operator, resulting in a loss of valuable temperature information.

Total field inversion was introduced for QSM and improves the quality of the QSM maps by incorporating background and local field estimation in one single step.[31-33] In this paper we applied TFI to DEGRE data acquired during mild RF-HT to correct for motion-induced susceptibility artifacts and resolve B_0-drift. We show that TFI can overcome the problem of PDF to overfit the background phase contribution as well as the problem of LBV to erase one pixel layer.

2 | METHODS

2.1 | MR thermometry

The phase difference from DEGRE was extracted as given in formula 1 in Reference 10. The resulting phase difference map to the reference time point was then unwrapped using the *unwrap_phase* method of the scikit-image python library (https://scikit-image.org/). The TFI and the BFR were then applied to the unwrapped phase as described in Reference 25. TFI and both BFR remove a spatially linear and constant phase distribution. This rendered the B_0-drift correction using the signal from reference tubes obsolete. However, as we observed a spatially constant temperature increase within the sarcoma and seroma patient, and a spatially linear temperature increase in the phantom experiment, we used the signal within the reference tubes to discern temperature and B_0-drift, as shown in Supporting Information Figure S1 of Reference 25. A polynomial function of first order was fit over the three-dimensional (3D) volume using the signal from all four vials for that purpose. In the following, we used the notation "B0-drift corrected" for this approach.

2.2 | Total field inversion

The total field inversion method consists of minimizing the following cost function:

$$y = \arg\min_{y'} = ||W(f - d * Py')||_1 + \lambda ||M_G \nabla Py'||_1, \quad (1)$$

where $|| \cdot ||_1$ is the ℓ_1-norm, W is the magnitude weighting, f is the unwrapped phase, d is the dipole kernel, $*$ denotes a convolution, P is the preconditioner, λ is the regularization parameter, M_G is the MEDI-like edge mask[34] and ∇ is the gradient operation.[35] The final QSM map was

computed as $\chi = Py$. The estimated susceptibility distribution χ was forward simulated to a phase map and subsequently demodulated from the original phase map. By design, the preconditioner P implicitly distinguishes between regions of background and local susceptibility sources.[31] To distinguish between background and local regions (region-of-interest [ROI]), a binary mask M_i per time point was calculated based on the maximum intensity projection (MIP) across echo times thresholded at 10% of its maximum value. A foreground mask per time point was subsequently defined where both the aforementioned thresholded MIP and the MIP at the reference time point had enough signal. For the LBV method three pixel layers were eroded from the foreground mask to obtain robust results through subjects and anatomies. Outside M_i, the preconditioner was calculated as a continuous cubic decay fitted to background susceptibility values obtained by the PDF method[28] as proposed in Reference 36. Inside M_i, the preconditioner was set to 1. Consequently, the preconditioner was automatically adapted to the ROI. To obtain the edge mask M_G, the Sobel filter in all three spatial dimensions was applied on the MIP. The regularization parameter λ was determined by a normalized root mean square error (RMSE) analysis of the numerical simulation (see below) and set to 1 for all datasets. For the normalization the averaged Euclidean norm of the reference map was used. The processing was mainly performed in Python 3.8 and CuPy 8.3.0[37] on a NVIDIA GeForce GTX 1080 Ti. Only for LBV the Matlab implementation available from Cornell University (http://pre.weill.cornell.edu/mri/pages/qsm.html) was used. The Matlab function was called from Python using the Matlab Engine API for Python.

2.3 | Materials

The phantom heating experiment, the volunteer data sets as well as the cervical cancer RF-HT treatment were acquired on a 1.5T GE system (GE Discovery MR450w) in combination with a BSD2000-3D Sigma Eye MR-compatible RF applicator (PYREXAR Medical). The RF applicator consisted of 24 dipole antennas arranged in three rings of eight antennas. Water circulation was not turned on during the phantom measurement nor the volunteer study. Water was circulated during the patient treatment, but stopped during MR measurements to avoid flow artifacts as described in Reference 38. The sarcoma patients were monitored in a 1.5T Philips system (Philips Ingenia 1.5T) and treated using a Sigma Eye MR Universal, or the Sigma 30 MR (PYREXAR Medical) in case of the single-leg treatment. RF-immune thermistors with high-impedance carbon wires ("Bowman" temperature

probes[39]) with an accuracy of 0.1°C were used to validate MR thermometry data.

2.4 | Simulations

The effect of motion-induced susceptibility changes on the phase distribution by field disturbances were simulated with a numerical water phantom. A spherical change of susceptibility values from water to air was simulated in the image center. This corresponds to a temporal field difference between an air-filled sphere at a reference time point and a water-filled sphere at the current time point. A FOV = $150 \times 150 \times 150$ mm, an isotropic voxel size = $1 \times 1 \times 1$ mm^3 and a susceptibility of 9.44 ppm[40] for air in reference to water was used. A 3D temperature increase following a Gaussian profile with a peak value of 10°C and a standard deviation of 5 voxels was added to the image. Furthermore, a spatially variant 1st order phase was added to imitate B_0-drift.

2.5 | Phantom measurements

A 2D multislice DEGRE with slice-interleaved acquisition scheme was used to monitor temperature. Using the phase signal at both TEs compensated for conductivity change-induced phase offsets[9] (TR = 620 ms, 25 slices, total scan time = 83 s, TE_1 = 4.8 ms, TE_2 = 19.1 ms, matrix size = 128×128, FOV = 50 cm × 50 cm, flip angle = 40°, slice thickness = 10 mm, bandwidth = 325.5 Hz/px). A cylindrical phantom (with a diameter of 30 cm and a depth of 40 cm) consisting of demineralized water, "super stuff" (TX-151), a hydrophilic organic polymer solidifying powder, and NaCl, to mimic the electrical properties of human tissue was used, for details see Reference 10. The phantom temperature started at 20°C and 400 W heating was performed for 25 min. This was repeated twice to show repeatability. Within the phantom, temperature sensors were placed which served as a reference measurement for the MR-based temperature maps. The mean MR temperature and standard deviation at the sensors' tips was estimated within a region of interest with the size of 8 voxels.

2.6 | Volunteers

Single echo datasets were acquired in the pelvic region of four volunteers at constant temperature (three male, one female) adhering to local ethics regulations (TE/TR = 15 ms/21 ms, 20 slices, matrix size = 128×160, FOV = 50 cm × 50 cm, flip angle = 14°, slice thickness = 10 mm). As no temperature change was expected, the conductivity bias did not need to be considered, and thus, a double echo acquisition scheme was not required. Between the acquisition of the reference baseline scan and the second scan for calculating the temperature difference map we waited for 30 min. Any temperature change would result purely from motion-induced susceptibility artifacts.

2.7 | Patients

Patient treatment scans were performed with the approval of the respective local ethics board at two hospitals with specialization on the treatment of cervical tumors and sarcoma patients, respectively. The cervical tumor was treated with the aforementioned BSD2000-3D Sigma Eye applicator inside a 1.5T GE system. One patient with a sarcoma, and one with a seroma after surgical removal of the sarcoma in the thigh, were treated with a Sigma Eye MR Universal inside a 1.5T Philips system. Temperature probes were inserted within catheters into the tumor. Every 5 or 10 min the temperature probe was retracted and reinserted within the catheter to map the temperature distribution along the catheter. Another sarcoma patient was treated using a single-leg applicator (Sigma 30 MR) and no invasive temperature probe was inserted into the tumor. A DEGRE acquisition corrected for the conductivity bias. In the GE system the echo times were set to TE = [4.8, 19.1] ms, and TE = [4.60, 18.41] ms in the Philips scanner, respectively. Other sequence parameters were identical to the ones used for the phantom heating experiment. The total RF-HT treatment duration was about 90 min with an initial ramp-up time of 30 min and subsequent maintenance of the temperature of about 60 min. Depending on the scanning protocol, DEGRE scans were acquired. A detailed summary of the patient treatment scans is given in Table 1.

2.8 | L1 versus L2 norm

To compare the presently adopted ℓ_1 data consistency term to the previously proposed ℓ_2-based TFI,[31] both approaches were applied and compared with each other in two of the volunteer scans at constant temperature, one treatment of a sarcoma, and a treatment of a cervical tumor.

2.9 | Cumulative distribution function analysis

For the detailed analysis of the error distribution for cases where no or small temperature changes are expected, the cumulative distribution function can serve as the cumulative error and can be calculated as

TABLE 1 Overview on mild radiofrequency hyperthermia treatment details on patient data. One cervix cancer patient, two sarcoma patients and one seroma patient were included in this paper. Three out of four patients had a temperature probe placed inside the tumor that was matched with MR thermometry data. The retraction frequency describes how frequently the temperature probe was retracted and reinserted in order to map a one-dimensional temperature distribution. The respective echo times for the double echo gradient echo sequence are also given.

Tumor type	Applicator	MR system	Probes + retraction frequency	TE_1/TE_2 (ms)
Cervical tumor Figure 6	BSD2000-3D Sigma Eye applicator	1.5 T GE Discovery MR450w	1 (tumor) every 10 min	4.8/19.1
Seroma Figure 7	BSD2000-3D Universal applicator	1.5 T Philips Ingenia	1 (tumor) every 5 min	4.6/18.41
Sarcoma Figure 8	BSD2000-3D Universal applicator	1.5 T Philips Ingenia	1 (tumor) every 5 min	4.6/18.41
Sarcoma Supporting Information Figure S1	Sigma 30 MR Single leg applicator	1.5 T Philips Ingenia	none	4.6/18.41

$$\mathrm{cdf}(\Delta T) = \frac{1}{N}\sum_{i=0}^{N} n(\Delta T_i), \quad n(\Delta T_i) = \begin{cases} 1, & \Delta T_i \leq \Delta T \\ 0, & \text{else} \end{cases},$$

where N is the number of voxels and ΔT_i the estimated temperature at voxel i.

3 | RESULTS

3.1 | Simulations

The comparison of the three aforementioned susceptibility artifact correction methods in a numerical simulation revealed that all three methods can eliminate both the linear phase as well as the dipole, while preserving the simulated Gaussian heat distribution (Figure 1). The LBV method led to the least cumulative error and performed best. PDF and TFI performed similarly, as seen in the cumulative error plot and the cross-sectional slice. However, TFI performed best close to the air inclusion in the center while LBV eroded valuable pixel information, PDF showed residual artifacts at the air–water interface. However, the TFI-corrected map showed diagonal streaks of over-estimated temperatures originating from the simulated heating spot.

3.2 | Phantom measurements

Temperature difference maps of the phantom heating experiment are shown in Figure 2. In addition, the local temperature estimation around two temperature sensor tips are plotted against the reference temperature probe
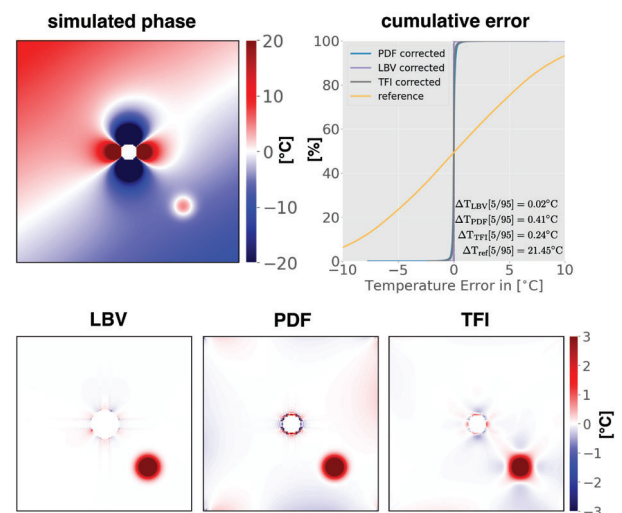

FIGURE 1 Results of temperature mapping in numerical simulations. The simulated phase included a Gaussian-shaped temperature change, as well as a dipole field caused by a moving air inclusion within surrounding water, and a first-order B_0-drift. The second row illustrates the corrected temperature difference maps, where B_0-drift and the susceptibility artifact have been removed, but the temperature was preserved. The Laplacian boundary value-based temperature map showed the least residual artifacts at the cost of a reduced region-of-interest, especially around the air inclusion in the center. Projection onto dipole fields and total field inversion (TFI) performed similarly, while the TFI-based temperature map showed less artifacts especially at the air–water interface in the center of the field of view. However, streaking could be observed for TFI. On the top right, the cumulative error is plotted for all cases.

data in Figure 3. In the beginning, as observed in the temperature maps, PDF overestimated the background field effect, which is particularly prominent at the border of the phantom (arrow). This was also reflected in

FIGURE 2 Results of temperature mapping in a gel phantom heating experiment. In general, all methods showed the highest temperature in the center of the phantom which was the selected target area for the heating microwaves. However, before correction, the temperature map was heterogeneous and showed unphysical negative temperature values, while the projection onto dipole fields-corrected temperature map showed decreased temperature values at air/phantom interfaces (arrow). Laplacian boundary value and total field inversion correction performed similarly and yielded homogeneous temperature maps.
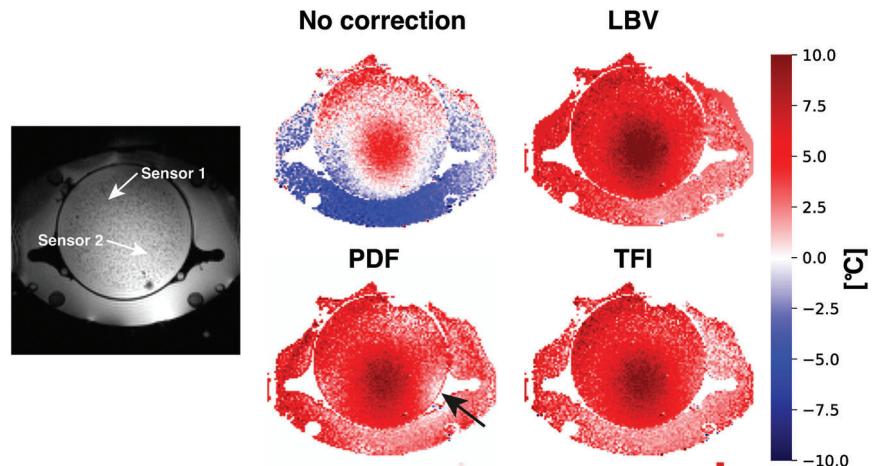
FIGURE 3 Correlation between sensors and MR temperature in the phantom depicted in Figure 2. Sensors 1 and 2 refer to the sensor position indicated in the magnitude image in Figure 2. A root mean square error analysis between MR temperature and sensor data yielded 0.61, 0.81, 0.69, 0.68 for Laplacian boundary value, the projection onto dipole fields method, total field inversion, and the B_0-drift corrected data in sensor 1, respectively, and 1.31, 0.59, 0.82, 0.88 in sensor 2. As seen, MR temperature mapping with susceptibility correction or B_0-drift correction was able to follow the trend of an increasing temperature for the phantom heating experiment.
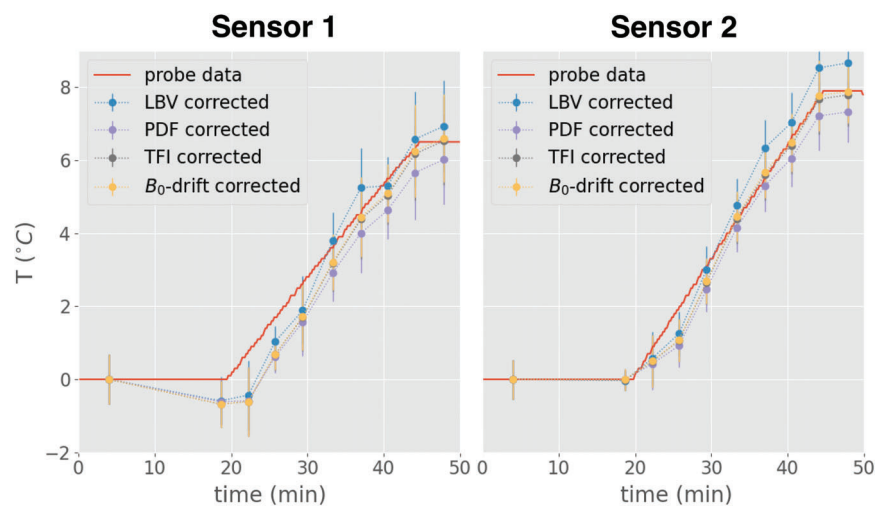
the sensor matching data, where PDF-corrected MR data predominantly underestimated the temperature increase (Figure 2). At the same time, TFI underestimated the temperature, however, it followed the probe data more closely. At early time points, the LBV-corrected temperature was underestimated in reference to the probe data while overestimating at later timepoints. A RMSE analysis between MR data and probe data yielded 0.61, 0.81, 0.69, 0.68 for LBV, PDF, TFI, and the B_0-drift corrected data in sensor 1, respectively, and 1.31, 0.59, 0.82, 0.88 in sensor 2. It is to be noted, that the small RMSE differences between the methods remain difficult to interpret due to both a high spatial temperature distribution gradient and a residual uncertainty of the exact probe location. Yet, the phantom measurement has proven that all three methods successfully removed the B_0-drift effect while largely preserving the temperature-induced phase change, as the maps were in good agreement with the sensor probe data. However, when calculating the standard deviation inside the region of interest around the sensor probe, a smaller value could be observed for the BFR and TFI-corrected maps compared to the B_0-corrected

maps, which can be explained by a subvoxel sinking of the phantom during the heating experiment and creation of small local dipoles that were corrected by both BFR and TFI.[25]

3.3 | Volunteers

The temperature difference maps of four volunteers at constant temperature showed strong susceptibility artifacts before correction (Figure 4). The artifacts were significantly reduced in the LBV- and PDF-corrected maps, but residual artifacts, especially in the water bolus at the posterior part of the image were visible. TFI was able to further reduce these artifacts and performs best in terms of cumulative error in all four volunteers (Figure 5). Furthermore, the TFI-corrected maps contained less noise. The characteristic of noise can best be assessed in the cumulative error plots, in which TFI showed the smallest interval between the 5 and 95 percentile for all subjects. The LBV-corrected maps showed a reduced remaining ROI due to the inherent need for erosion.
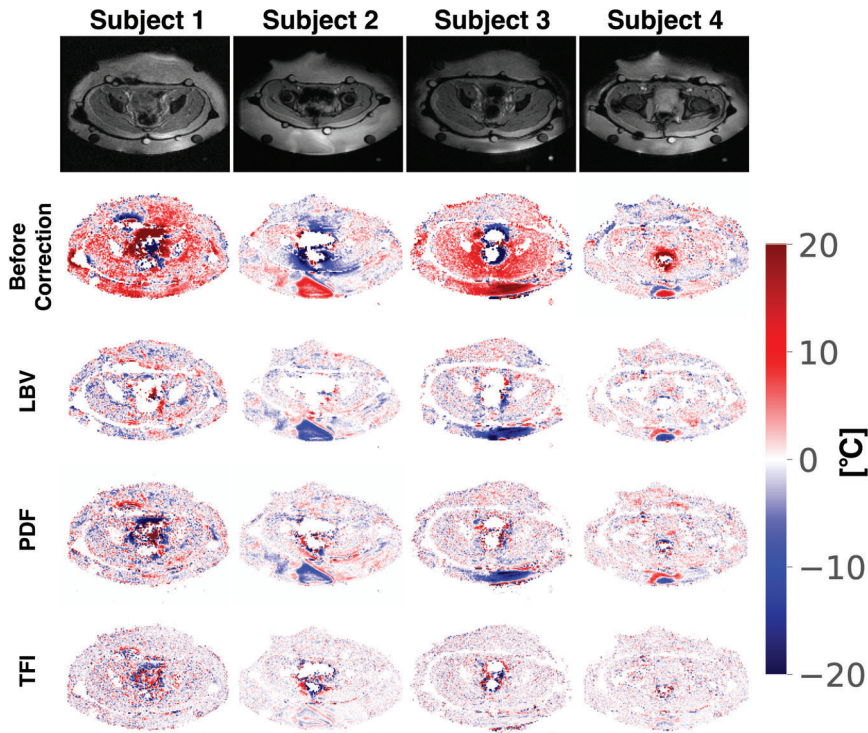
FIGURE 4 Results of temperature mapping in four volunteers at constant temperature. The temperature maps before correction showed strong bowel motion-induced susceptibility artifacts. While in subjects 2–4 residual artifacts remained especially in the posterior region, the total field inversion method was able to remove them.
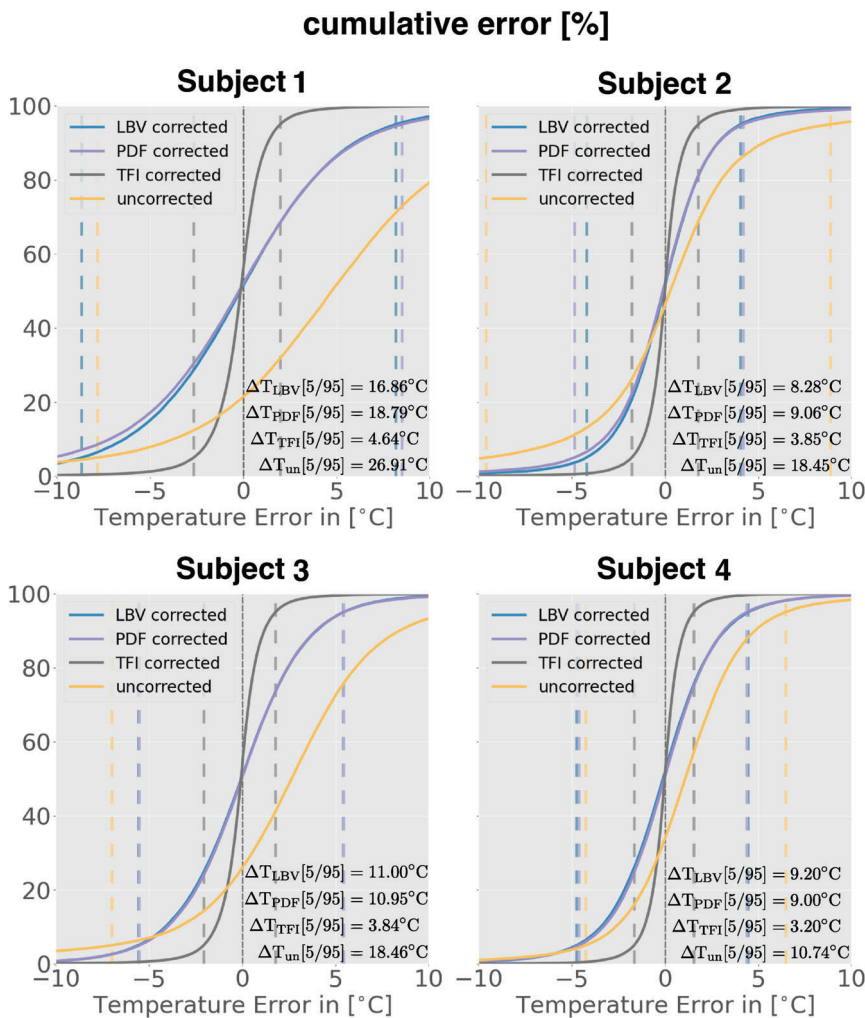

FIGURE 5 The cumulative error plots were calculated including all pixels within a common foreground mask. The plots indicate that total field inversion results in the least residual phase error in all four volunteer datasets. For subjects 3 and 4, the projection onto dipole fields and Laplacian boundary value (LBV) method performed similarly and are thus displayed on top of each other. In contrast to the cumulative error plot from the simulated data (Figure 1), LBV was here more vulnerable to noise.
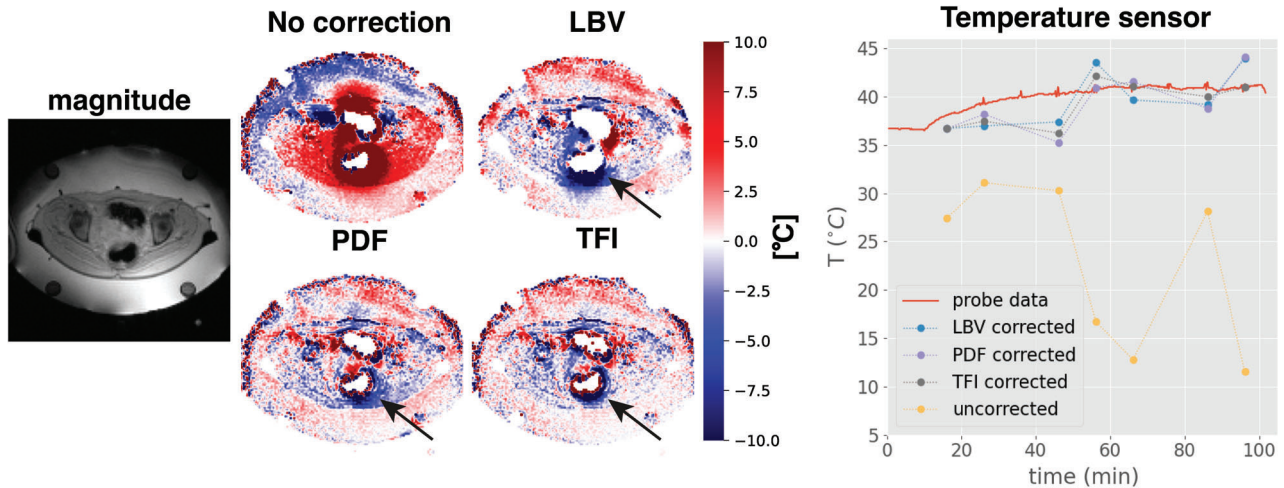
FIGURE 6 Results of temperature mapping for a cervical cancer patient during mild radiofrequency hyperthermia of the tumor. In the uncorrected temperature map strong susceptibility artifacts close to the intestines can be observed, caused by inter-scan gas motion. After correction the residual phase errors were reduced (arrows). However, the Laplacian boundary value (LBV) method was challenged with the removal of the error and dipole phase propagates into the surrounding tissue. While projection onto dipole fields could further reduce the range of the phase error it was minimal in the total field inversion-corrected map. Furthermore, the LBV method resulted in the loss of valuable pixels. The comparison of the corrected temperature with a sensor illustrates how severe the susceptibility artifacts were in the uncorrected DEGRE.

3.4 | Patients

The performance of the methods was evaluated for a mild RF-HT treatment of a patient with cervical cancer (Figure 6). Before susceptibility artifact correction, motion-induced temperature errors led to dipole-shaped artifacts amounting to more than 130°C and below −80°C locally. LBV could reduce the susceptibility artifacts at the cost of eroding pixel layers. PDF and TFI preserved the pixel information close to the air tissue interface, while TFI showed the smallest residual dipole artifact (arrow). Particularly noteworthy is that due to the spatial extension of the susceptibility artifact it propagated inside the silicone reference tubes. Hence, B_0-drift correction using the signal inside the reference tubes was not possible.

The temperature mapping results of the treatment of a patient with a seroma in the right thigh are shown in Figure 7. B_0-drift correction, LBV, PDF, and TFI yielded apparent sufficiently corrected temperature change maps and followed the trend of temperature increase over time compared to a temperature sensor inside the sarcoma. However, the coronal and sagittal view revealed two susceptibility artifacts (arrows) in proximity to the tumor and thus influencing temperature mapping accuracy. The dipole visible in the head direction of the FOV originated from bowel motion including gas and the dipole visible in the anterior part of the image in the sagittal views was introduced by a moving gas bubble inside the water bolus. In case of the LBV method, the axial and sagittal view revealed the estimation of unrealistic negative

temperature values in the water bolus. PDF and TFI appear to remove all susceptibility artifacts and yielded a similar temperature map. On the right-hand side of Figure 7 the mean temperature is calculated over the tumor mask delineated with black lines in the views for the B_0-drift corrected maps. When correlating the mean temperature estimated via MR with the temperature sensor inside the tumor over time, the B_0-drift correction, PDF, and LBV yielded unstable results across time points, while the TFI-corrected temperature map followed the temperature sensor most accurately and robustly. A mean difference analysis of the the MR-based temperature with the sensor yielded −0.01°C for B_0-drift correction, −0.11°C for LBV, −0.21°C for PDF, and −0.40°C for TFI, while a RMSE analysis yielded 0.71°C for B_0-drift correction, 0.56°C for LBV, 0.57°C for PDF, and 0.49°C for TFI.

Figure 8 shows the temperature mapping results of the last time point of a patient with a sarcoma in the left thigh. B_0-drift correction, LBV and PDF were challenged in this subject and show a poor correlation with the temperature sensor. However, the TFI-corrected data is in good agreement with the temperature sensor. A mean difference analysis of the MR-based temperature with the sensor yielded 0.42°C for B_0-drift correction, −3.41°C for LBV, −3.57°C for PDF, and 0.09°C for TFI while a root mean square error analysis yielded 1.61°C for B_0-drift correction, 3.80°C for LBV, 4.05°C for PDF, and 0.21°C for TFI.

The significance of correcting for susceptibility artifacts also for regions distant to the intestines becomes apparent in another mild RF-HT of a sarcoma in the left
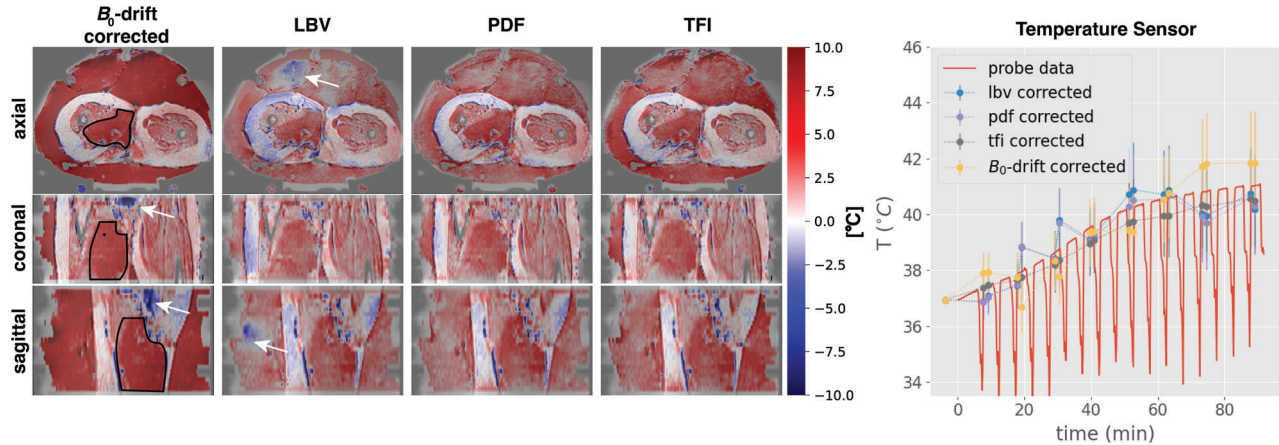
FIGURE 7 Temperature change maps derived from the last time point of a mild radiofrequency hyperthermia in a seroma patient after different correction schemes are shown on the left. The black line in the first column depicts the contours of the tumor in the right thigh. In the B_0-drift corrected temperature maps, a susceptibility artifact could be observed in the coronal and sagittal view (arrows). This susceptibility artifact was successfully removed in Laplacian boundary value (LBV)-, projection onto dipole fields (PDF)-, and total field inversion (TFI)-based maps. However, negative temperature value could be observed in the water bolus in the LBV-corrected maps. In the correlation between a temperature sensor within the seroma and the mean temperature in the tumor estimated by the different methods, the B_0-drift, LBV, and PDF corrected temperature values showed strong fluctuations and outliers between time points while the trend of temperature increase was picked up. Only the TFI-based temperature map correlated continuously across time points.
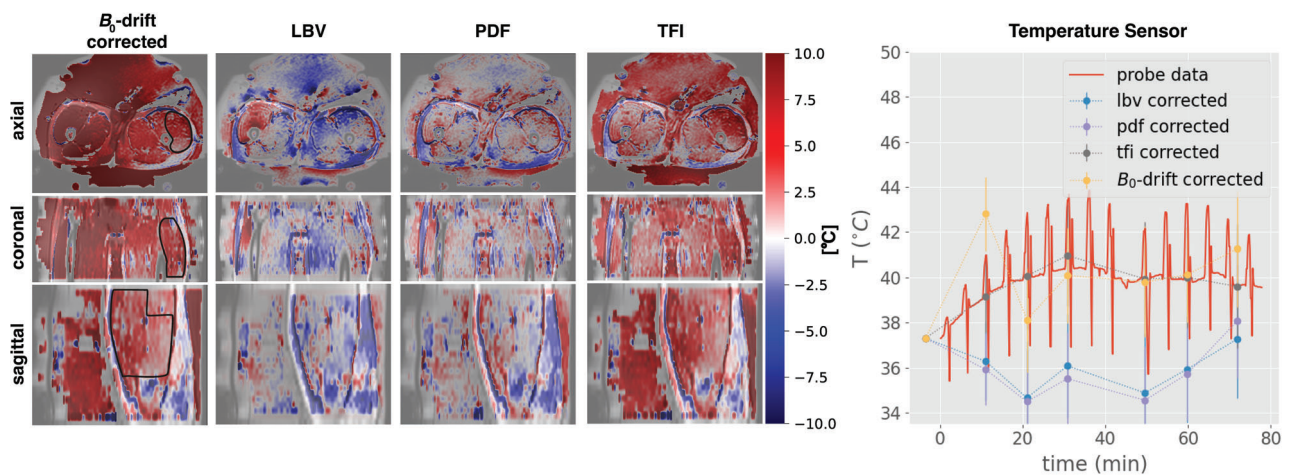

FIGURE 8 Temperature change maps derived from the last time point of a mild radiofrequency hyperthermia (RF-HT) targeting a sarcoma in the left thigh are shown. The contour of the tumor is depicted in the first column, on the B_0-drift corrected maps. The B_0-drift corrected map showed a residual first order variation in the right-left direction, while projection onto dipole fields (PDF) and especially Laplacian boundary value (LBV) showed predominantly negative temperature values in the entire FOV. Total field inversion (TFI) correction yielded consistently positive temperature values. The same was reflected in the probe matching evaluation on the right that reflect the temperature evolution over the time of the entire mild RF-HT. The mean temperature inside the tumor estimated with MR was compared to a reference temperature sensor using the mean value from signal inside the tumor region. In the correlation with a temperature sensor in the thigh, B_0-drift, LBV, and PDF correction showed heterogeneous values across time points, while TFI-corrected temperature points were in good agreement with the sensor.

thigh (Supporting Information Figure S1). The B_0-drift correction using the silicon reference tube signal failed to remove the first-order drift visualized in the axial view (arrow), as the susceptibility effects dominated the signal. Furthermore, strong susceptibility artifacts could be observed in the sagittal plane (arrows), originating from

gas motion in the anterior part of the water bolus. LBV, PDF, and TFI successfully removed both the B_0-drift and the susceptibility artifacts. However, one susceptibility artifact remained across all method revealed in the coronal plane at the hollow of the knee (arrows). Furthermore, the PDF method yielded negative temperature at the air-bolus

FIGURE 9 Results of temperature mapping in two volunteers (first two columns) and two patients (last two columns). Magnitude images (first row), corrected temperature maps based on the total field inversion method with an ℓ_2-based data consistency term (second row), and a ℓ_1-based data-consistency term (last row), are shown. In subject 1, the ℓ_1-based method was able to reduce the noise artifacts. In subject 2, the ℓ_1-based method reduced the noise artifacts as well as artifact in the posterior of the field of view (arrow). In subject 3, the ℓ_1-based method yielded positive temperature values within the right leg (arrow), while the ℓ_2-based map showed negative values. In subject 4, both methods performed similarly.
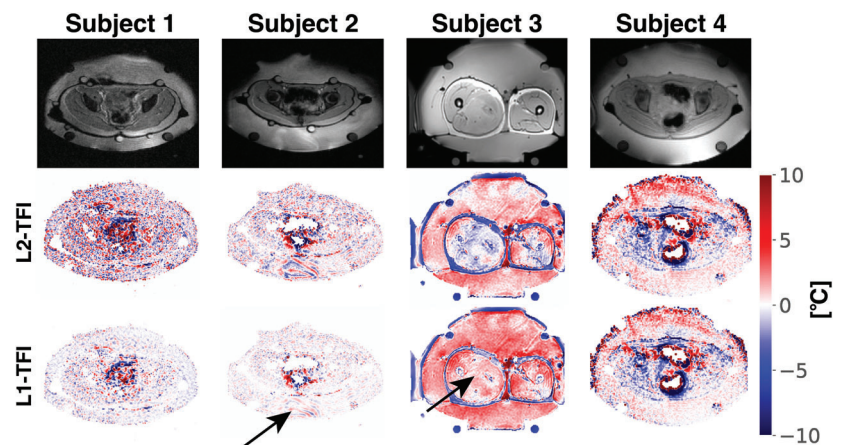
interface (axial view arrows), while TFI yielded the most homogeneous temperature map.

3.5 | L1 versus L2 norm

Figure 9 compares the performance of a ℓ_2 and the presently employed ℓ_1 data consistency term in the TFI cost function equation (1). In subjects 1 and 2 the ℓ_1 TFI reduced the background noise. In subject 2 the ℓ_1 TFI reduced the artifact in the posterior region almost to noise level (arrow). In subject 3, the ℓ_2 TFI-corrected temperature map showed nonphysical negative temperature values, which are estimated to be positive in the ℓ_1 TFI-corrected map (arrow). In subject 4 the two methods yielded almost the same temperature map.

4 | DISCUSSION

TFI-correction of MR thermometry data hampered by motion-induced susceptibility artifacts were superior to conventional B_0-drift corrected temperature maps and outperformed the recently proposed susceptibility artifact correction methods LBV and PDF in all examined data sets, except for the simulation data, where LBV revealed the least cumulative error after correction.

A TFI algorithm with a ℓ_1 norm data consistency term was proposed as it has proven to be more robust against phase inconsistencies and to perform better in low signal-to-noise ratio (SNR) regions in the domain of susceptibility mapping.[41] Furthermore, the proposed ℓ_1-based TFI algorithm was proven to perform more robustly in the presence of noise, as seen in the phantom and volunteer measurements and is thus in agreement with susceptibility mapping literature. This is advantageous in the context of mild RF hyperthermia treatments, as the heating device precludes the use of MR receive coils

other than the body coil and thus suffers from low SNR. In contrast to LBV, TFI-corrected maps preserved all pixels. This is particularly useful in tumors that are located next to intestinal gas, and thus at the edge of the foreground mask, as it is the case for cervical or rectal cancer. Furthermore, TFI is known to be robust against the selection of a foreground mask[33] and enables a robust automatic mask generation based on a magnitude threshold across subjects and anatomies. The PDF method also preserves all pixels, however, it can suffer from its tendency to overfit, especially at air-tissue interfaces.

A B_0-drift with a spatial distribution following a first order polynomial is robustly removed using the proposed methods, as seen in the simulated data, the volunteer, and the pelvic tumor treatment. However, we observed a temperature rise following a spatially first-order polynomial for the phantom measurement and a spatially zeroth order polynomial (i.e., a constant temperature offset) for the patient heating data in the leg. To discern the contribution of temperature and the contribution of B_0-drift, we could use the signal within the silicon reference tubes (Supporting Information figure S1 in Reference 25). It is important to note that in presence of large susceptibility artifacts it becomes impossible to correct for B_0-drift by using the signal inside the reference tubes, which was the case both for the presented volunteer and patient scans in the pelvis. As the dipole-shaped artifact propagated to the reference tubes, fitting a first-order polynomial to only the reference tubes worsened the phase error. It is to be noted that a more efficient cooling during the cervical tumor treatment (water of around 20°C was used in comparison to 33°C in the sarcoma treatment) likely prevented a zeroth-order temperature rise in the data. B_0-drift correction methods for MR thermometry were proposed recently by acquiring additional FIDs[16] or using nuclear MR field probes.[15] In the absence of susceptibility change-induced dipole fields, both BFR and TFI can also remove a

spatially first-order B_0-drift, rendering aforementioned methods obsolete. Furthermore, the aforementioned methods would falsely identify the susceptibility change-induced dipole fields as B_0-drift, and a wrong field model would be applied, as neither the coil sensitivity profiles, in case of the FID acquisitions, nor the spherical harmonics functions, in case of the field probe approach, represent the dipolar field change correctly. The slow temperature increase during mild RF-HT allows for a low temporal resolution of the MR sequence, compared to MR monitoring sequences during ablation therapies. Thus, a large volume can be covered during imaging. This is needed to detect unintended hot-spots outside of the heating target. Moreover, it provides the phase distribution in 3D that is necessary to remove the susceptibility artifacts with high accuracy. Removing susceptibility artifacts from 2D data had been shown using PDF during ablation therapy, but is less robust.[17]

Crucial to PRFS-based MR thermometry that uses phase information are correctly represented phase maps. Influences from breathing-induced B_0 fluctuations in the pelvis were excluded in a previous study that showed the stabilizing effect of the water bolus on the phase signal.[25] This is partly explained by the restricting effects of the water bolus on respiratory motion, but mainly with the absence of susceptibility distribution changes: In absence of a surrounding water bolus, breathing would imply periodic susceptibility distribution change of tissue with air, causing periodic field perturbations. In the presence of the water bolus, tissue moves within the water bolus, leading to much smaller susceptibility distribution changes with time and thus the elimination of B_0-fluctuation inside the pelvis.

Certain limitations remain: GPU with at least 6GiB of RAM is needed for the processing to finish in a reasonable time frame. The processing of one time point took around 13, 6, and 25 s for TFI, PDF, and LBV, respectively, while only TFI and PDF used the GPU. Furthermore, intra-scan motion artifacts originating from bulk motion and intestinal gas motion affect image quality. These scans can be seen as outliers in the temperature quantification maps and need to be discarded or repeated. Inter-scan bulk motion occurs as neither the pelvis nor the legs are externally fixed. This leads to misalignment of the current phase map with the reference map. It was not observed in the datasets we presented in this paper, but can be solved by using the image after bulk motion as the reference for subsequent images and performing nonrigid image registration of the temperature maps as suggested in Reference 42. In our study, we did not optimize the MR sequence details for speed or temperature-to-noise ratio,[10] but evaluated data obtained with clinically established standard sequences.

5 | CONCLUSION

Susceptibility artifacts hamper MR temperature estimation during mild RF-HT in the pelvis and the legs due to motion of gas, inside the bowel due to digestion, or inside the cooling water bolus. These susceptibility distribution changes superimpose the temperature-induced phase change of 0.01 ppm/°C. LBV, PDF, and TFI successfully remove susceptibility artifacts while preserving the temperature-induced phase change, as seen in the simulation and the phantom heating experiment. For in vivo data however, TFI performed more robustly. In contrast to the PDF algorithm, TFI did not show the tendency to overestimate the background field contribution, and in contrast to the LBV method, TFI preserved all pixels, which was expected. Apart from the simulated dataset, TFI consistently outperformed both BFR methods. It resulted in the least cumulative error for the volunteer scans, and matched best to the reference temperature probe for all three patient treatments with a temperature sensor. TFI can thus be used for gaining accurate temperature maps during mild RF-HT treatments.

ORCID
Christof Boehm https://orcid.org/0000-0003-1321-5804
Hendrik T. Mulder https://orcid.org/0000-0003-2165-8840
Lars H. Lindner https://orcid.org/0000-0003-3708-8264
Gerard C. van Rhoon https://orcid.org/0000-0002-7365-5783
Dimitrios C. Karampinos https://orcid.org/0000-0003-4922-3662
Mingming Wu https://orcid.org/0000-0002-8593-7091

REFERENCES
1. Kampinga HH. Cell biological effects of hyperthermia alone or combined with radiation or drugs: a short introduction to newcomers in the field. *Int J Hyperth*. 2006;22:191-196.
2. Issels RD, Lindner LH, Verweij J, et al. Effect of neoadjuvant chemotherapy plus regional hyperthermia on long-term outcomes among patients with localized high-risk soft tissue sarcoma: the EORTC 62961-ESHO 95 randomized clinical trial. *JAMA Oncol*. 2018;4:483-492.
3. Bucklein V, Limmroth C, Kampmann E, et al. Ifosfamide, Carboplatin, and Etoposide (ICE) in combination with regional hyperthermia as salvage therapy in patients with locally advanced nonmetastatic and metastatic soft-tissue sarcoma. *Sarcoma*. 2020;2020:6901678.
4. Franckena M, Fatehi D, de Bruijne M, et al. Hyperthermia dose-effect relationship in 420 patients with cervical cancer

treated with combined radiotherapy and hyperthermia. *Eur J Cancer*. 2009;45:1969-1978.

5. Ishihara Y, Calderon A, Watanabe H, et al. A precise and fast temperature mapping using water proton chemical shift. *Magn Reson Med*. 1995;34:814-823.

6. Gellermann J, Hildebrandt B, Issels R, et al. Noninvasive magnetic resonance thermography of soft tissue sarcomas during regional hyperthermia: correlation with response and direct thermometry. *Cancer*. 2006;107:1373-1382.

7. Gellermann J, Wlodarczyk W, Hildebrandt B, et al. Noninvasive magnetic resonance thermography of recurrent rectal carcinoma in a 1.5 tesla hybrid system. *Cancer Res*. 2005;65:5872-5880.

8. Winter L, Oberacker E, Paul K, et al. Magnetic resonance thermometry: methodology, pitfalls and practical solutions. *Int J Hyperth*. 2016;32:63-75.

9. Peters RD, Henkelman RM. Proton-resonance frequency shift MR thermometry is affected by changes in the electrical conductivity of tissue. *Magn Reson Med*. 2000;43:62-71.

10. Wu M, Mulder HT, Zur Y, et al. A phase-cycled temperature-sensitive fast spin echo sequence with conductivity bias correction for monitoring of mild RF hyperthermia with PRFS. *MAGMA*. 2019;32(3):369-380.

11. ElSharkawy AM, Schär M, Bottomley PA, Atalar E. Monitoring and correcting spatio-temporal variations of the MR scanner's static magnetic field. *MAGMA*. 2006;19:223-236.

12. Poorter JD. Noninvasive MRI thermometry with the proton resonance frequency method: study of susceptibility effects. *Magn Reson Med*. 1995;34:359-367.

13. Bing C, Staruch RM, Tillander M, et al. Drift correction for accurate PRF-shift MR thermometry during mild hyperthermia treatments with MR-HIFU. *Int J Hyperth*. 2016;32:673-687.

14. Hernandez D, Kim KS, Michel E, Lee SY. Correction of B0 drift effects in magnetic resonance thermometry using magnetic field monitoring technique. *Concepts Magn Reson B Magn Reson Eng*. 2016;46B:81-89.

15. Ster CL, Mauconduit F, Mirkes C, et al. RF heating measurement using MR thermometry and field monitoring: methodological considerations and first in vivo results. *Magn Reson Med*. 2021;85:1282-1293.

16. Ferrer CJ, Bartels LW, van der Velden TA, et al. Field drift correction of proton resonance frequency shift temperature mapping with multichannel fast alternating nonselective free induction decay readouts. *Magn Reson Med*. 2020;83(3):962–973.

17. Tan J, Mougenot C, Pichardo S, Drake JM, Waspe AC. Motion compensation using principal component analysis and projection onto dipole fields for abdominal magnetic resonance thermometry. *Magn Reson Med*. 2019;81:195-207.

18. Vigen KK, Daniel BL, Pauly JM, Butts K. Triggered, navigated, multi-baseline method for proton resonance frequency temperature mapping with respiratory motion. *Magn Reson Med*. 2003;50:1003-1010.

19. Grissom WA, Rieke V, Holbrook AB, et al. Hybrid referenceless and multibaseline subtraction MR thermometry for monitoring thermal therapies in moving organs. *Med Phys*. 2010;37:5014-5026.

20. Wu M. *MR Thermometry for Monitoring mild Radio-Frequency Hyperthermia*. Dissertation. Technische Universität München, München; 2020.

21. Köhler MO, de Senneville BD, Quesson B, Moonen CT, Ries M. Spectrally selective pencil-beam navigator for motion compensation of MR-guided high-intensity focused ultrasound therapy of abdominal organs. *Magn Reson Med*. 2011;66:102-111.

22. Pichardo S, Köhler M, Lee J, Hynnyen K. In vivo optimisation study for multi-baseline MR-based thermometry in the context of hyperthermia using MR-guided high intensity focused ultrasound for head and neck applications. *Int J Hyperth*. 2014;30:579-592.

23. Rieke V, Vigen KK, Sommer G, Daniel BL, Pauly JM, Butts K. Referenceless PRF shift thermometry. *Magn Reson Med*. 2004;51:1223-1231.

24. Salomir R, Viallon M, Kickhefel A, et al. Reference-free PRFS MR-thermometry using near-harmonic 2-D reconstruction of the background phase. *IEEE Trans Med Imaging*. 2012;31:287-301.

25. Wu M, Mulder HT, Baron P, et al. Correction of motion-induced susceptibility artifacts and B0 drift during proton resonance frequency shift-based MR thermometry in the pelvis with background field removal methods. *Magn Reson Med*. 2020;84:2495-2511.

26. Dadakova T, Gellermann J, Voigt O, et al. Fast PRF-based MR thermometry using double-echo EPI: in vivo comparison in a clinical hyperthermia setting. *MAGMA*. 2015;28:305-314.

27. Zhou D, Liu T, Spincemaille P, Wang Y. Background field removal by solving the Laplacian boundary value problem. *NMR Biomed*. 2014;27:312-319.

28. Liu T, Khalidov I, de Rochefort L, et al. A novel background field removal method for MRI using projection onto dipole fields (PDF). *NMR Biomed*. 2011;24:1129-1136.

29. Schweser F, Robinson SD, de Rochefort L, Li W, Bredies K. An illustrated comparison of processing methods for phase MRI and QSM: removal of background field contributions from sources outside the region of interest. *NMR Biomed*. 2017; 30:(e3604).

30. Ozbay PS, Deistung A, Feng X, Nanz D, Reichenbach JR, Schweser F. A comprehensive numerical analysis of background phase correction with V-SHARP. *NMR Biomed*. 2017;30:e3550.

31. Liu Z, Kee Y, Zhou D, Wang Y, Spincemaille P. Preconditioned total field inversion (TFI) method for quantitative susceptibility mapping. *Magn Reson Med*. 2016;78:303-315.

32. Wen Y, Spincemaille P, Nguyen T, et al. Multiecho complex total field inversion method (mcTFI) for improved signal modeling in quantitative susceptibility mapping. *Magn Reson Med*. 2021;86(4):2165–2178.

33. Boehm C, Sollmann N, Meineke J, et al. Preconditioned water-fat total field inversion: application to spine quantitative susceptibility mapping. *Magnet Reson Med*. 2022;87(1):417-430.

34. Liu T, Liu J, de Rochefort L, et al. Morphology enabled dipole inversion (MEDI) from a single-angle acquisition: comparison with cosmos in human brain imaging. *Magn Reson Med*. 2011;66:777-783.

35. Wang Y, Liu T. Quantitative susceptibility mapping (QSM): decoding MRI data for a tissue magnetic biomarker. *Magn Reson Med*. 2014;73:82-101.

36. Liu Z, Wen Y, Spincemaille P, et al. Automated adaptive preconditioner for quantitative susceptibility mapping. *Magn Reson Med*. 2020;83:271-285.

37. Okuta R, Unno Y, Nishino D, Hido S, Loomis C. CuPy: a NumPy-compatible library for NVIDIA GPU calculations. Proceedings of the 31st Annual Conference on Neural Information Processing Systems (NIPS) Workshop on Machine Learning Systems (LearningSys); 2017.

38. Allen SP, Steeves T, Fergusson A, et al. Novel acoustic coupling bath using magnetite nanoparticles for MR-guided transcranial focused ultrasound surgery. *Med Phys*. 2019;46:5444-5453.

39. Bowman R. A probe for measuring temperature in radio-frequency-heated material (short papers). *IEEE Trans Microw Theory Techn*. 1976;24:43-45.

40. Collins CM, Yang B, Yang QX, Smith MB. Numerical calculations of the static magnetic field in three-dimensional multi-tissue models of the human head. *Magn Reson Imaging*. 2002;20:413-424.

41. Milovic C, Lambert M, Langkammer C, Bredies K, Tejos C, Irarrazaval P. QSM streaking suppression with L1 data fidelity terms. Proceedings of the 29th Annual Meeting International Society for Magnetic Resonance in Medicine; 2020:3257.

42. de Zwart JA, Vimeux FC, Palussiere J, et al. On-line correction and visualization of motion during MRI-controlled hyperthermia. *Magn Reson Med*. 2001;45:128-137.

SUPPORTING INFORMATION

Additional supporting information may be found in the online version of the article at the publisher's website.

Figure S1 Temperature change maps of the last time point of a patient treatment targeting a sarcoma using a single-leg applicator. The B_0-drift corrected map shows a residual first-order temperature change in AP direction and strong susceptibility artifacts at the anterior edge of the image originating from moving air inside the water bolus (see arrow in sagittal view). Laplacian boundary value (LBV)-, projection onto dipole fields (PDF)-, and total field inversion (TFI)-corrected maps show no B_0-drift artifact and removed the susceptibility artifacts in the anterior part of the image. However, some smaller residual dipole artifacts remain after correction (arrows in the coronal view) in all correction schemes. Again, an overestimation of the background field can be observed for PDF at the edge of the field of view (arrows in the axial view). The LBV-corrected maps also led to large areas with a negative temperature inside the water bolus and the fat.

How to cite this article: Boehm C, Goeger-Neff M, Mulder HT, et al. Susceptibility artifact correction in MR thermometry for monitoring of mild radiofrequency hyperthermia using total field inversion. *Magn Reson Med*. 2022;88:120-132. doi: 10.1002/mrm.29191

3.4 Journal Publication III: Preconditioned water-fat total field inversion: Application to spine quantitative susceptibility mapping

The publication entitled *Preconditioned water-fat total field inversion: Application to spine quantitative susceptibility mapping* was published in Magnetic Resonance in Medicine (ISSN: 0740-3194). The manuscript was authored by Christof Boehm, Nico Sollmann, Jakob Meineke, Stefan Ruschke, Michael Dieckmeyer, Kilian Weiss, Claus Zimmer, Marcus R. Makowski, Thomas Baum, and Dimitrios C. Karampinos. It is available online (DOI: 10.1002/mrm.28903) as an open access article under the terms of the Creative Commons Attribution-NonCommercial License and Figure 6 of the manuscript was the cover image of the journal in January 2022 (DOI: 10.1002/mrm.29087). Preliminary results were presented in the conference contribution C14, which was awarded with an ISMRM Summa Cum Laude Merit Award and selected as an oral presentation at the ISMRM annual meeting 2021. Furthermore, the abstract made the 3rd place of the best trainee abstracts on susceptibility technology issued by ISMRM's Electro-Magnetic Tissue Properties Study Group. A summary of the publication is provided in Section 3.4.1, the author contributions are listed in Section 3.4.2 and the full text is included subsequently on the following pages.

3.4.1 Abstract

Purpose

The single-orientation dipole-based susceptibility estimation is a ill-posed and ill-conditioned minimization problem. Conventionally, the susceptibility estimation consists of four main steps: field map estimation, field map unwrapping, background field removal and local field-to-susceptibility inversion. This work proposes the use of a preconditioned water–fat total field inversion (wfTFI) algorithm to estimate tissue susceptibility directly from complex multi-echo gradient-echo images in regions where both water and fat are present. wfTFI allows to simultaneously perform the previously four independent steps of QSM.

Methods

The tissue magnetic susceptibility estimation was formulated as and IDEAL-like minimization problem, where the only searched parameter was the susceptibility. To compare the proposed method to formerly proposed disjoint background field removal and local field inversion methods, a numerical simulation and the data from 1 healthy volunteer and 10 patients with metastatic bone disease were included in the analysis. In the 10 patients scans, the ability of QSM-based differentiation of osteoblastic and osteolytic changes in reference to computed tomography was evaluated.

Results

The proposed wfTFI method reduces the normalized root mean square error in the numerical simulation when compared to formerly proposed susceptibility estimation methods. In vivo, wfTFI results show reduced BFR artifacts, better noise performance and reduced streaking artifacts. In the differentiation of osteoblastic from osteolytic changes, the proposed wfTFI method provided a significantly higher diagnostic confidence compared to formerly proposed methods.

Conclusion

The proposed wfTFI is able to increase the accuracy of tissue magnetic susceptibility estimation in water–fat regions and can thus improve the delineation between osteoblatic and osteolytic bone changes.

3.4.2 Author contributions

The first author developed the problem formulation; implemented the minimization code in Python; performed the numerical simulation; performed the MR measurement for the healthy volunteer data set. With the help and consultation from the coauthors, the first author evaluated, analyzed and interpreted the data from the patient cohort and wrote the manuscript.

3.4.3 Original Article

RESEARCH ARTICLE

Magnetic Resonance in Medicine

Preconditioned water-fat total field inversion: Application to spine quantitative susceptibility mapping

Christof Boehm[1] | **Nico Sollmann[2,3,4]** | **Jakob Meineke[5]** | **Stefan Ruschke[1]** | **Michael Dieckmeyer[2]** | **Kilian Weiss[6]** | **Claus Zimmer[2,3]** | **Marcus R. Makowski[1]** | **Thomas Baum[2]** | **Dimitrios C. Karampinos[1]**

[1]Department of Diagnostic and Interventional Radiology, School of Medicine, Klinikum rechts der Isar, Technical University of Munich, Munich, Germany

[2]Department of Diagnostic and Interventional Neuroradiology, School of Medicine, Klinikum rechts der Isar, Technical University of Munich, Munich, Germany

[3]TUM-Neuroimaging Center, Klinikum rechts der Isar, Technical University of Munich, Munich, Germany

[4]Department of Diagnostic and Interventional Radiology, University Hospital Ulm, Ulm, Germany

[5]Philips Research, Hamburg, Germany

[6]Philips Healthcare, Hamburg, Germany

Correspondence
Christof Boehm, Department of Diagnostic and Interventional Radiology, Klinikum rechts der Isar, Ismaninger Str 22, Munich 81675, Germany.
Email: christof.boehm@tum.de

Twitter: @BoehmChristof

Funding information
Philips Healthcare; H2020 European Research Council, Grant/Award Number: 677661

Purpose: To (a) develop a preconditioned water-fat total field inversion (wfTFI) algorithm that directly estimates the susceptibility map from complex multi-echo gradient echo data for water-fat regions and to (b) evaluate the performance of the proposed wfTFI quantitative susceptibility mapping (QSM) method in comparison with a local field inversion (LFI) method and a linear total field inversion (TFI) method in the spine.

Methods: Numerical simulations and in vivo spine multi-echo gradient echo measurements were performed to compare wfTFI to an algorithm based on disjoint background field removal (BFR) and LFI and to a formerly proposed TFI algorithm. The data from 1 healthy volunteer and 10 patients with metastatic bone disease were included in the analysis. Clinical routine computed tomography (CT) images were used as a reference standard to distinguish osteoblastic from osteolytic changes. The ability of the QSM methods to distinguish osteoblastic from osteolytic changes was evaluated.

Results: The proposed wfTFI method was able to decrease the normalized root mean square error compared to the LFI and TFI methods in the simulation. The in vivo wfTFI susceptibility maps showed reduced BFR artifacts, noise amplification, and streaking artifacts compared to the LFI and TFI maps. wfTFI provided a significantly higher diagnostic confidence in differentiating osteolytic and osteoblastic lesions in the spine compared to the LFI method ($p = .012$).

Conclusion: The proposed wfTFI method can minimize BFR artifacts, noise amplification, and streaking artifacts in water-fat regions and can thus better differentiate

between osteoblastic and osteolytic changes in patients with metastatic disease compared to LFI and the original TFI method.

KEYWORDS

MEDI, osteoblastic, osteolytic, spine, QSM, TFI, vertebral metastases

1 | INTRODUCTION

The spine is the most frequent skeletal site for bone metastases.[1,2] In clinical routine, bone metastases are categorized to be either predominantly osteoblastic or osteolytic. Osteoblastic changes are characterized by the formation of new bone structures that might be weak and deformed while osteolytic meastastases are associated with bone destruction. The detection of bone metastases and their categorization into osteoblastic/osteolytic can be clinically important for several reasons, including the assessment of therapy response,[3] fracture risk,[4] or to support the search for an unknown primary tumor.[1,5] Due to its excellent soft tissue contrast, MRI is routinely used for assessing metastatic spread in vertebral bone marrow.[6] However, the delineation of osteoblastic and osteolytic metastases based on standard T1- and T2-weighted images cannot be achieved reliably.[6,7] Therefore, computed tomography (CT) remains the clinical standard for the osteoblastic/osteolytic categorization of bone metastases.

Susceptibility-weighted imaging (SWI) has been proposed and successfully applied for the MR-based differentiation of osteolytic and osteoblastic bone metastases at the spine.[7] Specifically, spine SWI has used the magnetic susceptibility to visualize the more diamagnetic properties of osteoblastic lesions (with locally increased mineralization) than osteolytic lesions (with locally decreased mineralization).[7] However, SWI only allows the qualitative assessment of bone mineralization changes and is also affected by changes in water-fat composition. Quantitative susceptibility mapping (QSM)[8] has been proposed to overcome the qualitative limitation of SWI. QSM is an MR technique that directly estimates the magnetic susceptibility and has been extensively used in the study of cerebral brain physiology,[9] pathology,[10] and function.[11] QSM has recently also been combined with water-fat separation techniques and has been applied in body regions outside the brain, for example, for measuring liver iron overload,[12-14] prostatic calcifications,[15] cartilage degeneration,[16] and bone density.[17-20]

QSM inverts the measured main magnetic field inhomogeneities, called the "field map," to the magnetic susceptibility map. The field map is thought to originate from two main sources: (1) the local field map that originates from MR-visible susceptibility sources within the region-of-interest (ROI) and (2) background field map contributions originating from MR-visible susceptibility sources outside the ROI, the concave geometry of the anatomy, the large susceptibility difference at the borders between tissue and air, flow, or breathing. In most imaging situations, the background field dominates the local field map by one or two orders of magnitude. Consequently, the background field map contributions need to be accounted for in order to estimate the local susceptibility map. A plethora of methods have been proposed to remove the background field contributions in a separate preprocessing step[21-25] before the local field inversion (LFI) is performed. However, background field removal (BFR) methods often suffer from an improper separation of background and local fields introduced by the assumptions of the adopted method. The improper separation of background and local fields can be particularly problematic at tissue-air boundaries.[8,12,21] Single-step methods have been proposed to simultaneously perform the steps of BFR and LFI to overcome the limitations associated with performing separately the two steps.[26,27] Most of the single-step methods implicitly remove the background field by a Laplacian operation. However, Laplacian-based single-step methods have shown to yield significantly reduced contrast in the finally estimated susceptibility maps in the applications also including spine QSM.[28-30]

A linear TFI algorithm has been proposed to perform the background field removal and estimate local susceptibility sources.[28] The proposed TFI algorithm reportedly overcomes the limitations of disjoint BFR and LFI and is able to robustly remove background field contributions. In addition, the adoption of a nonlinear QSM model has been proven to reduce streaking artifacts, particularly in regions with strong susceptibility sources and low SNR.[31] Strong susceptibility differences in the ROI are particularly common in body regions at the border of soft tissue and air (9.44 ppm)[32] or between tissue and the cortical bone shell (−2 ppm).[33] However, neither the linear TFI method nor the nonlinear QSM model can totally eliminate streaking artifacts in the presence of strong susceptibility differences. Therefore, the use of an iterative re-weighting method (MERIT)[31] was proposed and applied in both methods to alleviate remaining artifacts. In methods that use the Gauss-Newton approach for the minimization of the cost function, MERIT re-weights the voxels in the data

consistency term according to their residual error at each Gauss-Newton step. Voxels with high model mismatch are weighted down to reduce the influence of outliers in otherwise normally distributed data. However, MERIT can be subject to heuristic optimization and it can deteriorate the depiction of strong susceptibility sources.[34]

A recently proposed TFI method that directly estimates the susceptibility map from complex multi-echo gradient echo data (mcTFI)[34] combines the advantages of a nonlinear QSM model and a total field inversion method by reducing noise amplification and BFR artifacts. Additionally, mcTFI is able to reduce streaking artifacts without the use of the MERIT method. However, the original mcTFI can only be applied to regions with one chemical species and cannot account for the chemical shift of fat. Therefore, a new method is required to estimate the susceptibility map from complex multi-echo gradient echo data outside of the brain where both water and fat species are present.

Therefore, the purpose of this study is to (a) develop a water-fat total field inversion (wfTFI) method that directly estimates the susceptibility map from complex multi-echo gradient echo data in water-fat regions, and (b) to demonstrate the advantages of the developed method when applied in spine QSM of patients with metastatic bone disease where the the chemical shift of fat, large background fields, signal voids, and large susceptibility differences are present.

2 | METHODS

2.1 | Proposed preconditioned water-fat total field inversion algorithm

The proposed water-fat total field inversion (wfTFI) algorithm consists of 3 main steps (Figure 1). First, the water and fat image, field map, and R_2^*-map were estimated using a recently proposed graph-cut algorithm[35] and a water-fat signal model accounting for a single R_2^* decay and employing a multi-peak fat model specific to bone marrow.[36] Second, an initial susceptibility map in the background and local region (see below regarding the determination of the background and local region) was estimated using a linear preconditioned TFI algorithm.[28] Finally, the susceptibility map was computed by estimating the susceptibility distribution directly from the complex multi-echo data by using a single-R_2^* multi-fat-peak water-fat signal model minimizing the following preconditioned water-fat total field inversion cost function:

$$y = \arg\min_{y'} = \sum_{j=1}^{N_{echo}} || (\rho_W + c_n \rho_F) \, e^{-R_2^* t_j} e^{i t_j \, d \, *Py'} - S_j ||_2^2 + \lambda ||M_g \nabla Py'||_1 \tag{1}$$

$$c_n = \sum_{p=1}^{N_p} a_p e^{i2\pi \Delta f_p t_j}, \quad \text{with} \quad \sum_{p=1}^{N_p} a_p = 1, \tag{2}$$
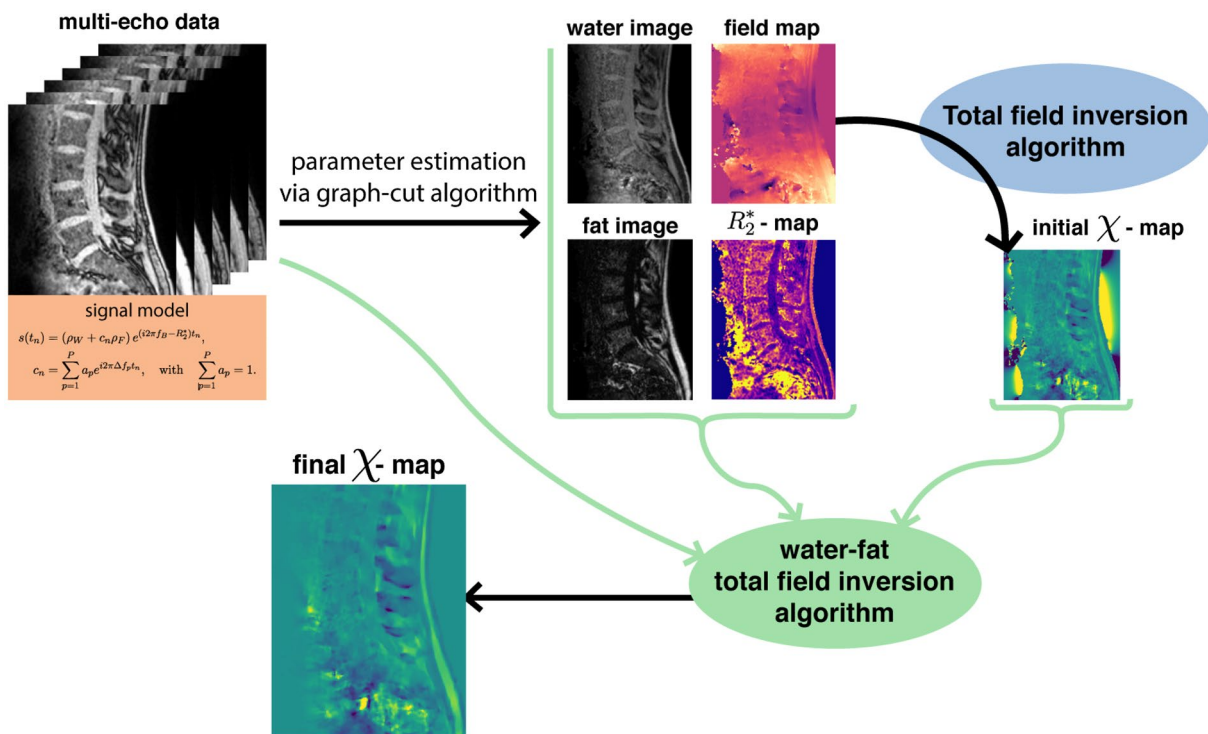

FIGURE 1 Pipeline of the proposed water-fat TFI algorithm. The acquired multi-echo data are separated into water and fat image, field-, and R_2^* −map using a variable-layer single-min-cut graph-cut algorithm.[35] An initial χ-map is estimated based on the field-map using the original TFI method.[28] Finally, the water-fat total field inversion algorithm is initiated with the initial χ-map, water and fat image, and R_2^*-map. The final χ-map is directly estimated from the multi-echo data

where $t_1, t_2, \ldots, t_N$ are the different echo times, d is the dipole kernel, P is the preconditioner, M_G is the MEDI-like edge mask, [37] and ∇ is the gradient operation,[8] ρ_W and ρ_F are the complex signal of the water and fat components assumed to have an equal transverse relaxation rate R_2^*. The fat spectrum was assumed to have N_p spectral peaks with corresponding relative amplitudes a_p and chemical shift Δf_p. The final QSM map was computed as $\chi = Py$.

By design, the preconditioner P implicitly distinguishes between regions of background and local susceptibility sources.[28] To distinguish between background and local regions (region-of-interest (ROI)), a binary mask M was calculated based on the maximum intensity projection (MIP) across echo times thresholded at 5% of its maximum value. Outside M, the preconditioner was calculated as a continuous cubic decay fitted to background susceptibility values obtained by the projection onto dipole fields method[22] as proposed in Ref. [38]. Inside M, the preconditioner was set to 1. Consequently, the preconditioner was automatically adapted to the ROI.

To obtain the edge mask M_G, the Sobel filter in all 3 spatial dimensions was applied on the MIP. The regularization parameter λ was via L-curve analysis of a numerical simulation (see below) and was set to 100 for all data sets. The cost function in Equation (1) was minimized using the iterative Gauss-Newton algorithm with a conjugate gradient solver at each step. In total, 30 Gauss-Newton steps were performed.

2.2 | Comparison methods

The proposed wfTFI method was applied and compared to (1) a methodology combining the Laplacian boundary value (LBV)[21] method for BFR and MEDI for LFI (labeled as LBV+MEDI),[31] (2) a methodology combining the projection onto dipole fields (PDF)[22] for BFR and MEDI for LFI (labeled as PDF+MEDI), and (3) the original TFI methodology with MERIT (labeled as TFI).[28] All methods were initialized with a field map obtained by the aforementioned graph-cut method.[35]

The presently employed MEDI-regularized LFI used the following nonlinear formulation of the field to susceptibility inversion[31]:

$$\chi = \arg\min_{\chi'} = ||W(e^{id*\chi'} - e^{if_l})||_2^2 + \lambda||M_g \nabla \chi'||_1, \quad (3)$$

where W is the magnitude weighting and f_l is the local field map. The cost function was minimized with the aforementioned Gauss-Newton algorithm.

The original TFI algorithm was used as the third comparison method. The original TFI minimizes the following preconditioned linear formulation of the field to susceptibility inversion[28]:

$$y = \arg\min_{y'} = ||W(f_B - d*Py')||_2^2 + \lambda||M_g \nabla Py'||_1, \quad (4)$$

where the final QSM map was computed as $\chi = Py$. The same preconditioner P was used as in the proposed wfTFI method. Due to the nonlinearity of the regularization term, the above cost-function was again minimized with the above Gauss-Newton algorithm. At each Gauss-Newton step, MERIT re-weighting was applied to the magnitude weighting W, where each voxel was re-weighted according to their residual error.[31]

The regularization parameter λ was determined via L-curve analysis of a numerical simulation (see below) and was set to 1/250 for MEDI and 1/2500 for TFI, respectively. The stopping criterion for both methods was a relative residual of < 0.01. The edge mask M_G in the regularization term, represented by the second term in Equations (1), (3), and (4), was the same for all methods, including the proposed wfTFI. All processing was performed in Python 3.8 and CuPy 8.0.0[39] on a NVIDIA GeForce GTX 1080 Ti.

2.3 | Numerical simulation in the thoracolumbar spine

To investigate the difference between the presently proposed wfTFI method, the separate BFR and LFI methods and the formerly proposed TFI method, a numerical simulation based on the Duke phantom was performed using the annotated geometrical data from.[40] All of the body mesh data was converted into a three-dimensional volume corresponding to maps of 1.5 mm isotropic resolution. In order to assign bone marrow and the cortical bone shell with their respective susceptibility values, the binary erosion operation was applied on the bone mask and the difference between the original bone mask and the eroded mask was used as the mask for the cortical bone region. Each tissue was assigned with either their literature value or values extracted from in vivo scans as listed in Supporting Information Table S1. Based on the values in Supporting Information Table S1, fat fraction, R_2^*- and χ-maps were generated. Additionally, SimpleITK[41] was used to manually add regions of air into the gastrointestinal system. To reduce the artificial piece-wise constant property of the generated maps, an independent Gaussian-filtered white noise distribution was added to each of the maps. The χ-map was forward simulated to a field map f_B using the dipole kernel in k-space. The widely used single-R_2^* multi-fat-peak water-fat voxel signal model [42,43] was used to forward simulate the fat fraction f_f, R_2^*, and field maps to complex multi-echo data:

$$s(t_n) = \left((1-f_f) + c_n f_f\right) e^{\gamma t_n}, \quad \gamma = i2\pi f_B - R_2^*$$
$$c_n = \sum_{p=1}^{P} a_p e^{i2\pi \Delta f_p t_n}, \quad \text{with} \quad \sum_{p=1}^{P} a_p = 1. \quad (5)$$

The echo times were set to $TE_{min} = 1.1$ ms, $\Delta TE = 1.1$ ms. A field strength of 3 T and the aforementioned fat model specific to bone marrow were used. An additional parabolic signal drop in posterior-anterior direction was added to account for the signal drop observed in the in vivo spine scans due to the common lack of surface coils placed on top of patients (anterior body region). Independent Gaussian noise was added to the real and imaginary part of the echo data with an signal-to-noise ratio (SNR) of 50. The SNR was defined as the maximum signal amplitude of the first echo divided by the standard deviation. To obtain water- and fat-separated images, field map and R_2^*-map from the simulated multi-echo data, the aforementioned graph-cut based field-mapping method was used. Based on the maps estimated by the graph-cut method, the proposed wfTFI method was applied and compared to the aforementioned comparison methods (LBV+MEDI, PDF+MEDI, TFI). The estimated χ-maps were visually examined for BFR and streaking artifacts and noise amplification.

2.4 | In vivo measurements

The aforementioned processing of graph-cut based field mapping and water-fat separation followed by LBV + MEDI, PDF + MEDI, TFI, and wfTFI QSM methods was applied to in vivo scans of a healthy volunteer and patients. Approval by the institutional review board (Klinikum rechts der Isar, Technical University of Munich, Munich, Germany) was granted for the patient scans and informed consent was received. The scanning was performed on a 3 T scanner (Ingenia, Philips Healthcare, Release 5.4, Best, The Netherlands) using a monopolar time-interleaved multi-echo gradient echo sequence,[44] acquiring 6 echoes in 2 interleaves with 3 echoes per interleave. For all subjects, the imaging parameters were set to $TE_{min} = 1.12$ ms, $\Delta TE = 0.96$ ms, orientation = sagittal, readout direction = anterior-posterior, FOV $= 219.6 \times 219.6 \times 79.2$ mm^3, and an isotropic acquisition voxel size of 1.8 mm.

In the patient study, only data were included from patients who received a CT and MRI examination, including T_1-weighted turbo spin echo (T1w TSE), T_2-weighted Dixon in-phase (T2w IP), and water (T2w water) from the standard clinical routine protocol. The CT scans were acquired within 30 days before or after the MRI due to clinically indicated reasons, including sagittal reformations of the spine (slice thickness of 3 mm). Specifically, 1 scan of the lumbar spine of a healthy volunteer and 10 scans of the spine of patients with osteolytic/osteoblastic changes due to metastatic disease were evaluated. The scans covered the lumbar spine in 7 patients, the cervical spine in 2 patients, the thoracic spine in one patient, and the lumbar spine in the volunteer.

The scans derived from the 10 scans in patients were evaluated and graded by two radiologists (a board-certified radiologist with 11 years of experience and a resident with 8 years of experience in neuroradiological imaging). The scans were read in a consensus-like setting and the readers were strictly blinded to the reports created during the clinical routine and to the characteristics of the metastases (osteolytic/osteoblastic) similiar to.[7] First, the CT images were evaluated via consensus reading in order to provide the reference standard for osteolytic and osteoblastic metastases. After an interval of about four weeks to avoid recall bias, the conventional MR sequences (T1w TSE, T2w IP, T2w water) and the QSM sequence results were separately evaluated for differentiating metastases between osteolytic and osteoblastic. In the reading of the conventional MR sequences, metastases that were predominantly hypointense on T1-weighted images and hyperintense on T2-weighted images were classified as osteolytic, and, conversely, metastases that were predominantly hypointense on T1- and T2-weighted images were classified as predominantly osteoblastic.[7] In the reading of the QSM maps, metastases were graded as osteoblastic if they were hypointense on MIP across echo times and hypointense on the QSM map, and, conversely, metastases that were hyperintense in the MIP and neutral on the QSM map (values around zero) were classified as osteolytic. The diagnostic confidence of the QSM methods to distinguish between osteolytic and osteoblastic changes was graded as 1 (low confidence), 2 (medium confidence), or 3 (high confidence). Additionally, the three χ-maps estimated by the PDF+MEDI, TFI, and wfTFI QSM methods were graded for the overall image quality on a scale from 1 (low quality) to 3 (high quality). A Wilcoxon test was employed for comparing the diagnostic confidence and the image quality of the susceptibility maps derived with the wfTFI method and the PDF+MEDI method.

3 | RESULTS

3.1 | Numerical simulation in the thoracolumbar spine

Figure 2 compares the aforementioned QSM methods with respect to BFR artifacts, noise amplification, and susceptibility values. The first row of Figure 2 shows that the employed graph-cut based field mapping and water-fat separation method is able to yield a non-wrapped field- and fat fraction map. LBV+MEDI and PDF+MEDI show BFR artifacts in the whole ROI and significantly reduced susceptibility values of the vertebral bodies and the fat region surrounding the spinous processes. The TFI method does not suffer from BFR artifacts but shows noise amplification and further reduced susceptibility values in the spinous process fat region. The proposed wfTFI appears less noisy and shows reasonable susceptibility values in the vertebral bodies and spinous process fat region. Additionally, the wfTFI method shows
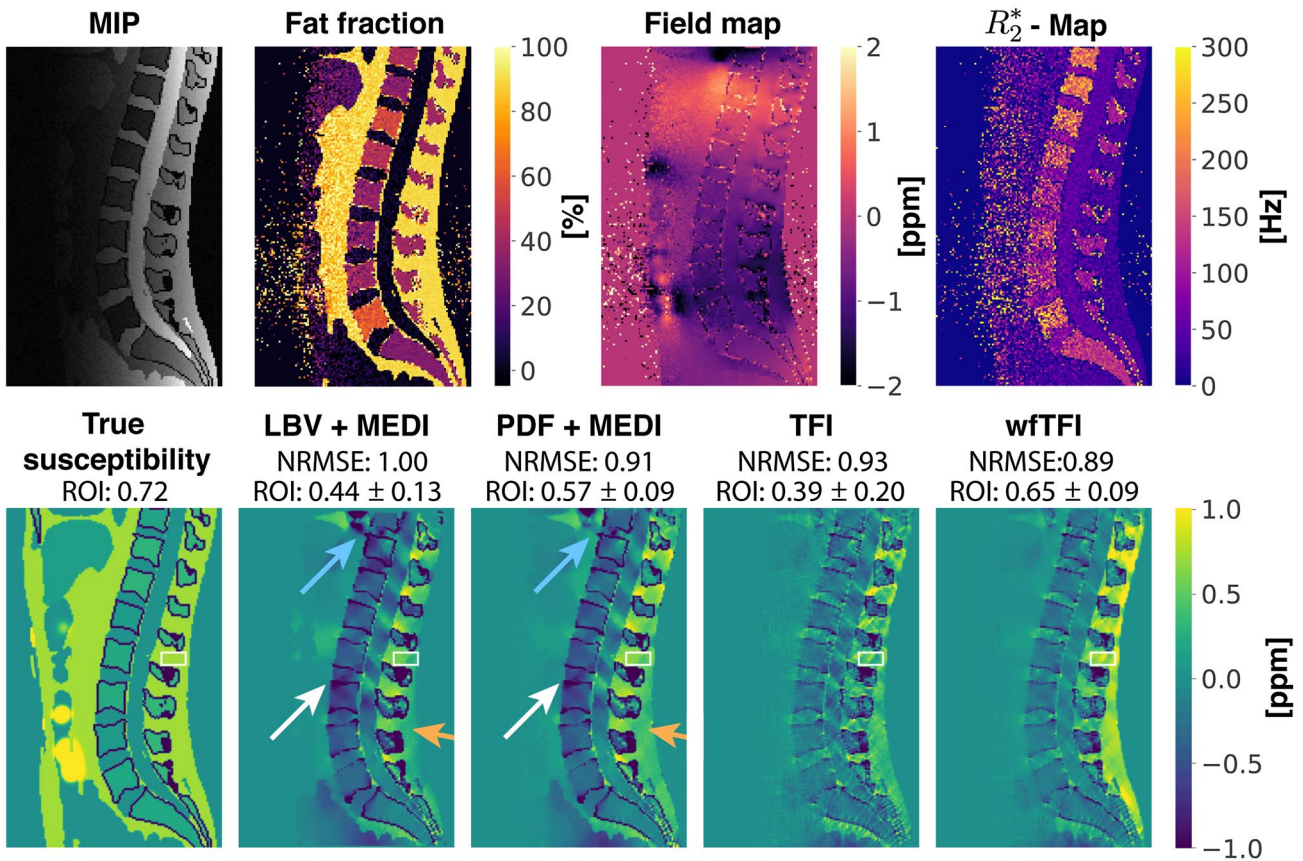
FIGURE 2 Results of water-fat imaging (first row) and QSM (second row) results in the numerical multi-echo lumbar spine simulation. The first row shows the maximum intensity projection over echo times (MIP) of the 6 simulated echos and reveals the simulated cubic signal drop in posterior-anterior direction. Furthermore, the estimated fat fraction, field map, and R_2^*-map are shown in the first row. The graph-cut based field mapping is able to estimate a non-wrapped field map and fat fraction. In the LBV + MEDI and the PDF + MEDI method, BFR artifacts appear in the whole ROI. Both methods indicate an artifactual diamagnetic source present at the air-tissue interface to the lungs (blue arrow). Decreased susceptibility values can be observed in the center of the spine (white arrow) and inside all vertebral bodies. The simulated susceptibility of fat around the spinous processes (orange arrow) is significantly reduced in comparison to the true susceptibility. The TFI method does not show BFR artifacts but shows strongly elevated noise and reduced susceptibility values in the spinous process region. The wfTFI does not show BFR artifacts, yields reasonable susceptibility values inside the vertebral bodies and shows significantly reduced streaking, especially in cerebrospinal fluid. Furthermore, the susceptibility of fat surrounding the spinous processes is closer to the reference values when estimated by the wfTFI method in comparison to the other methods (susceptibility ROI values within the white box reported within the Figure)

significantly decreased streaking artifacts in comparison to all other methods, which can be best illustrated within in the cerebrospinal fluid region. A normalized root mean square error analysis (NRMSE) of the QSM maps yields an error of 0.89 for the proposed wfTFI method, 0.93 for TFI, 0.91 for PDF+MEDI, and 1.00 for LBV+MEDI.

3.2 | In vivo measurements

Figure 3 compares the QSM methods with respect to BFR artifacts, noise amplification, and streaking artifacts in a healthy volunteer. The first row shows that the employed graph-cut based field-mapping method is able to estimate water-fat-swap-free field-, fat fraction-, and R_2^*-map in an in vivo scan. The different QSM methods show the same

behavior as in the numerical simulation shown in Figure 2. LBV+MEDI and PDF+MEDI show severe BFR artifacts. Furthermore, they show strong streaking artifacts around air inclusions in the bowel at the bottom of the FOV. The TFI method significantly reduces the BFR artifacts while elevating the noise level. However, the TFI method still shows significant streaking around the air inclusion in the bowel. The proposed wfTFI method shows no noise amplification and the weakest streaking artifact from the air inclusion in the bowel, compared to the other methods.

Among the 10 patients (4 females and 6 males, mean age: 71.5 ± 10.9 years, age range: 49.2-83.3 years), 3 patients suffered from metastasized prostate cancer, 2 patients each from breast cancer and lung cancer. The other patients suffered from mouth floor carcinoma, kidney cancer, and a neuroendocrine tumor, respectively. Figure 4 compares the QSM
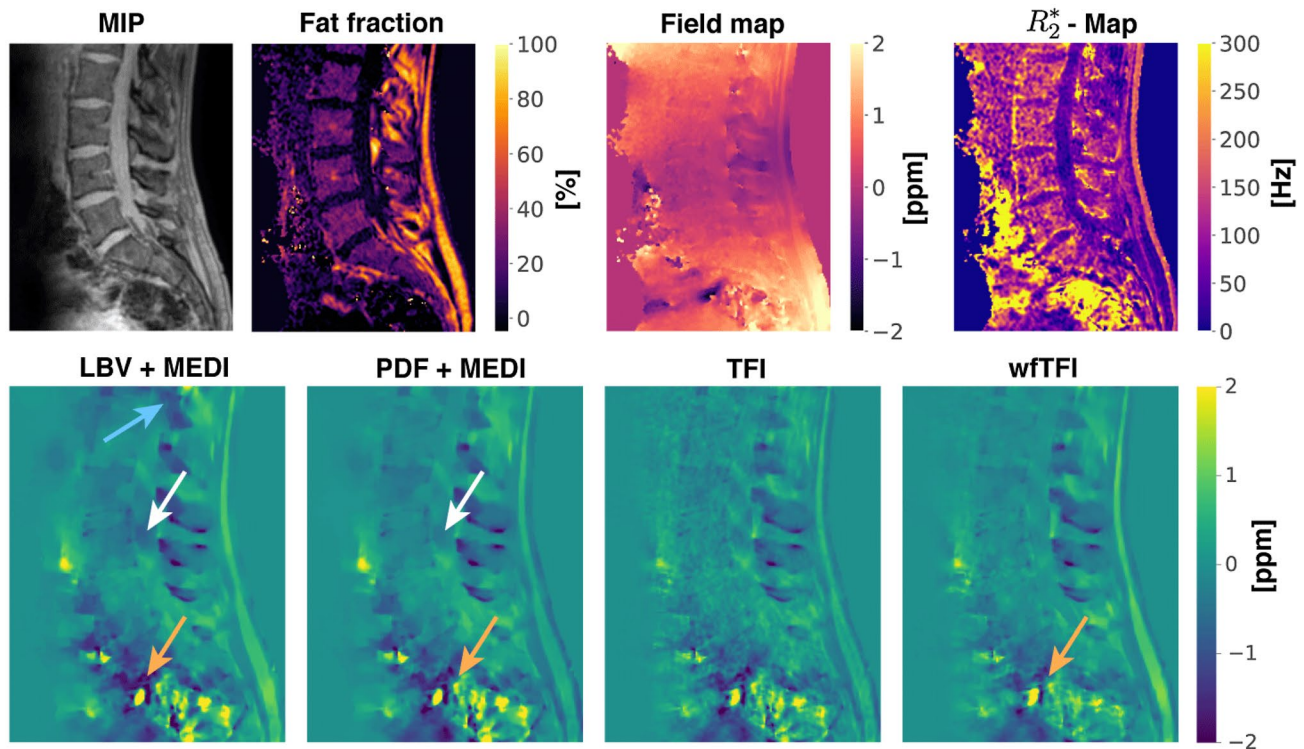
FIGURE 3   Results of water-fat imaging (first row) and QSM (second row) in a healthy volunteer. The first row shows that the graph-cut based field mapping method is able to estimate a non-wrapped field map and fat fraction. In both QSM methods where BFR and LFI are independent steps, BFR artifacts appear in the whole ROI. In the LBV + MEDI method, there is an artifactual strong paramagnetic susceptibility source present in the spinous process region (blue arrow). In both BFR + LFI methods, a systematic underestimation of susceptibility values in the cerebrospinal fluid can be observed (white arrow). Air in the bowel causes strong streaking artifacts in the surrounding tissue (orange arrow). The streaking artifacts of the air in bowel are reduced when the original TFI method is used but the artifacts are still present. BFR artifacts are greatly reduced in the TFI method. However, the noise in the vertebral body region is elevated. The wfTFI method does not show BFR artifacts, shows no noise amplifications in the vertebral bodies, and shows the weakest streaking artifacts around the air inclusion in the bowel

methods in a subject with metastatic disease and mainly osteoblastic changes of the spine. The MIP shows that the vertebral bodies have almost no signal. Despite the low signal in the vertebral bodies, all QSM methods are able to pick up the strong diamagnetic property of the calcified vertebral bodies. However, the LBV + MEDI method shows a strong artifactual paramagnetic susceptibility source in the spinous process region of the T10 vertebra and the fat region at the L5 level (arrows). The PDF + MEDI shows a BFR artifact in the subcutaneous fat region of the T11 vertebra and the same BFR artifact as the LBV + MEDI method posterior to the L5 vertebra (white arrows). The TFI method yields a map without BFR artifacts. However, the noise in the TFI method is significantly elevated and it shows an artifactual increase of susceptibility values in the intervertebral discs (IVD). The proposed wfTFI method shows no BFR artifacts, minimal noise amplification, and reduced artifactual paramagnetic elevation in the IVDs.

Figure 5 plots the TFI susceptibility maps at different regularization parameters. When the regularization parameter λ is increased in the TFI method in order to decrease the noise, the overall susceptibility contrast quickly degrades (Figure 5). Furthermore, increasing the regularization parameter induces paramagnetic susceptibility values in the IVDs.

Figure 6 shows the water-fat imaging, clinical T1w TSE, T2w IP, T2w water, CT, and wfTFI results in a female patient diagnosed with breast cancer and both osteoblastic and osteolytic bone metastases at the lumbar spine. The osteoblastic components in the vertebrae L3-L5 according to CT show T1- and T2-hypointense correlates. The osteoblastic components are in good agreement with the results of the wfTFI QSM methods. The wfTFI QSM method is able to pick up intravertebral variations as present in the L2 vertebra, where a localized increased bone deposition can be observed in the posterior inferior part of the vertebra. This directly translates to diamagnetic values in the same region in the susceptibility of the wfTFI method.

Figure 7 shows the water-fat imaging, clinical T1w TSE, T2w IP, T2w water, CT, and wfTFI results in a female patient diagnosed with renal cancer and mainly osteolytic bone metastases of the T4 and T5 vertebral body. However, the clinical sequences suggest an osteoblastic lesion, since the lesion appears as T1- and T2-hypointense. The MIP together with
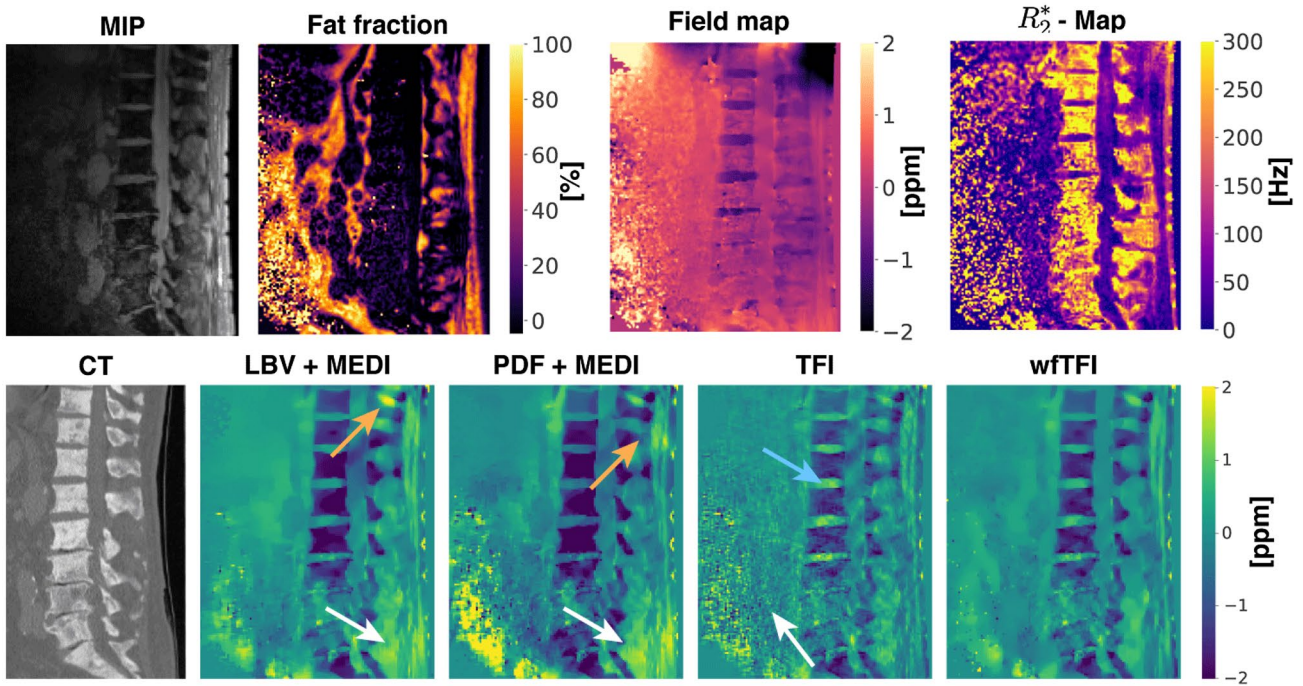
FIGURE 4 Results of water-fat imaging (first row), CT (bottom left image), and QSM (second row) in a subject with mainly osteoblastic bone metastases. The fat fraction and R_2^*-map indicate a pathological change of the vertebral bodies by showing significantly reduced fat fraction and elevated R_2^* values, respectively. In the estimation of the vertebral body susceptibility, all 4 QSM methods agree very well with the CT scan. However, the BFR + LFI methods show severe BFR artifacts, especially in the spinous process region of the T10 and T11 vertebra (orange arrows) in the LBV and PDF based maps, respectively, and the fat region in the height of the L5 vertebra (white arrow). The TFI method shows significant noise amplification in the anterior to the spinal cord (white arrow) and artifactual strong paramagnetic susceptibility values in all IVDs (blue arrow). The wfTFI shows no noise amplification, no BFR artifacts, and reduced artifactual paramagnetic elevation in the IVDs
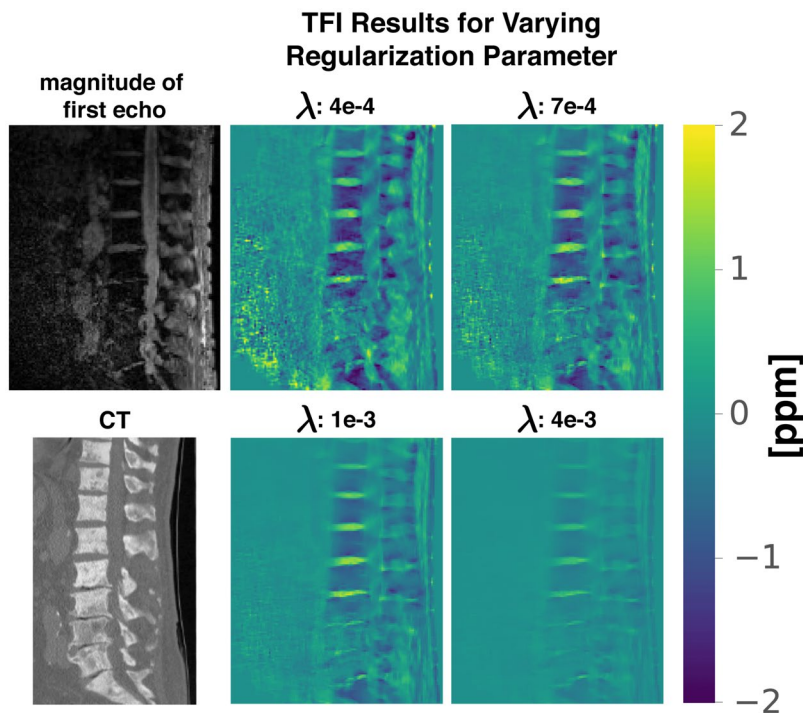
FIGURE 5 TFI results for varying the regularization parameter λ. When increasing the regularization parameter, the overall susceptibility contrast decreases while the noise artifacts are only slightly reduced. The artifactual paramagnetic estimation of the IVD regions remain strong for high regularization parameters

wfTFI suggests an osteolytic lesion, thus being in agreement with CT. Figure 8 shows the water-fat imaging, clinical T1w TSE, T2 IP, T2 water, CT, and wfTFI results in a male patient

diagnosed with prostate cancer and mainly osteoblastic bone metastases. The QSM map estimated by the proposed wfTFI method is in good agreement with the CT scan. It reveals
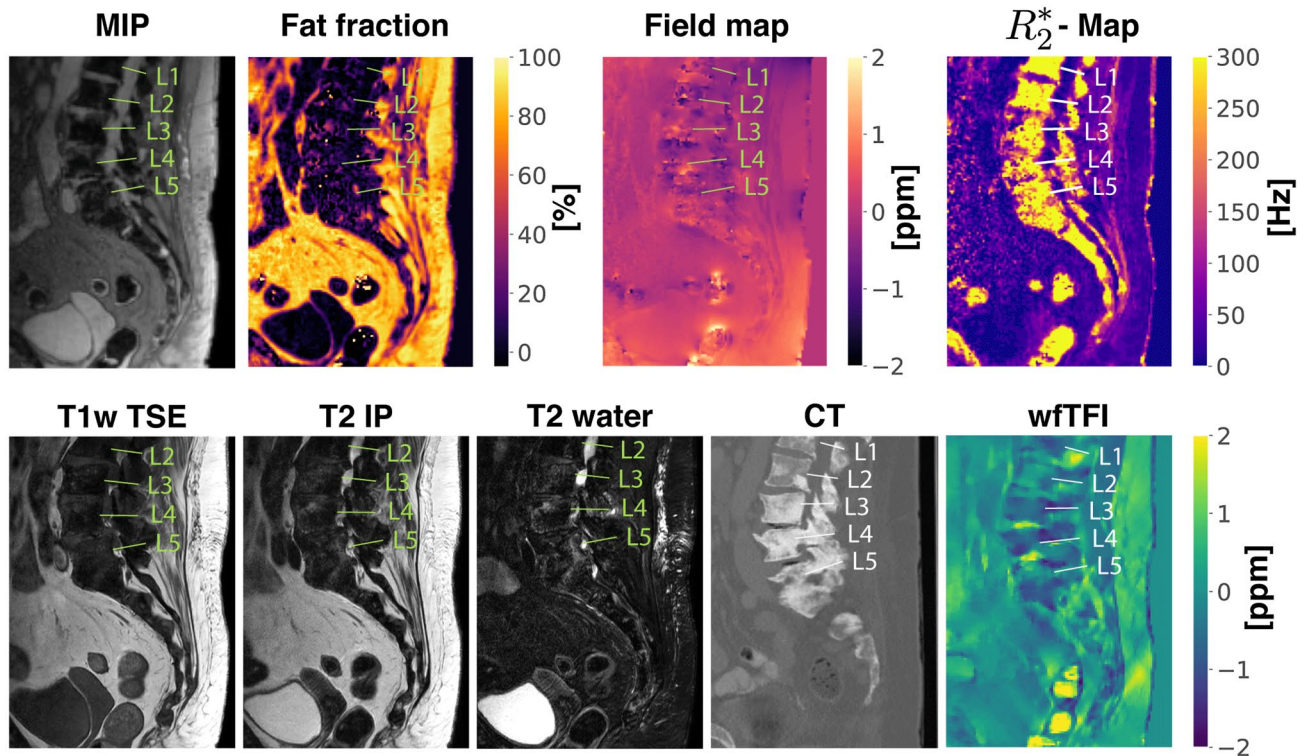
FIGURE 6 Results of water-fat imaging (first row), clinical T1w TSE, T2 IP, T2 water, CT, and QSM (second row) in a female patient diagnosed with breast cancer and mainly osteoblastic bone metastases along the displayed lumbar spine. In detail, the osteoblastic components in the vertebrae L3-L5 according to CT show T1- and T2-hypointense correlates, which are in good agreement with the results of the wfTFI QSM method that show diamagnetic values in the specific regions

the T12-L3 vertebra to be mainly osteoblastic and L4 and L5 to be mainly osteolytic. Additionally, the susceptibility map reveals the intradiscal air inclusions between sacrum-L5, L5-L4, L4-L3, and L3-L2, as verified by the CT scan. The detection of the air inclusion is not possible in conventional MRI sequences, MIP, or R_2^*-map.

The results of the reading of 10 subjects showed a mean diagnostic confidence of 2.1 ± 0.7 for PDF+MEDI, 2.6 ± 0.66 for TFI, and 2.8 ± 0.4 for wfTFI. The diagnostic confidence was significantly higher with the wfTFI method compared to the PDF+MEDI method ($p = .012$). The wfTFI method showed higher diagnostic confidence rating compared to the TFI method in 2 patient scans and equal diagnostic confidence to the TFI method in the rest. Furthermore, the image quality was estimated to be 1.1 ± 0.3 for PDF+MEDI, 2.4 ± 0.66 for TFI and 2.8 ± 0.4 for wfTFI. The image quality was also significantly higher with the wfTFI method compared to the PDF+MEDI method ($p < .001$). The wfTFI method increased the image quality rating compared to the TFI method in 3 patient scans and showed equivalent image quality to the TFI method in the rest. Within the reading of conventional sequences, only in 8/10 patients could the bone metastases correctly be identified as predominantly osteoblastic/osteolytic, while within the reading of the χ-maps of the wfTFI method a correct classification in relation to CT was possible in all patients.

4 | DISCUSSION

The present study aimed to develop a method for improved QSM in water-fat regions. Specifically, the present study proposed to use a preconditioned water-fat TFI algorithm that directly estimates the susceptibility map from complex multi-echo gradient echo data. The study then examined the performance of the proposed wfTFI method in comparison to PDF + MEDI, LBV + MEDI, and a formerly proposed preconditioned linear TFI method in a numerical simulation, a healthy volunteer, and 10 patients with metastatic bone disease. The wfTFI results of the patients were graded by two senior radiologists with (a) respect to diagnostic confidence to distinguish osteolytic from osteoblastic bone metastases and (b) overall image quality. The proposed wfTFI method yielded a high diagnostic confidence and image quality for data derived from the patients, which may be due to the combination of advantages of formerly proposed methods, including the reduction of BFR artifacts, noise amplification, and streaking artifacts.

First, QSM based on the LBV and PDF both show BFR artifacts at the air-tissue interface of the lungs, the fat, and areas of hypointense values at some distance to convex geometry. In general, BFR artifacts appear as a slowly varying susceptibility distribution or as streaking artifacts at the local/background region interface. In the present study, the
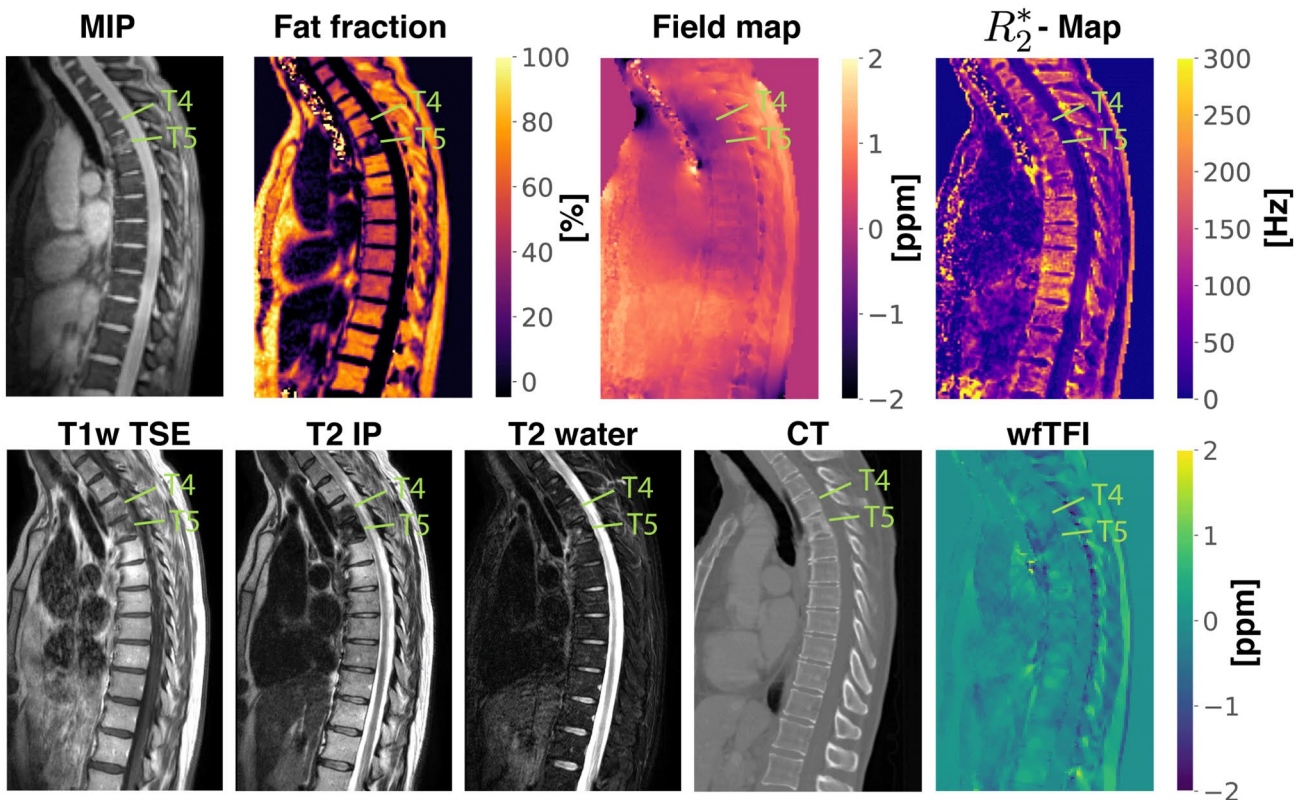
FIGURE 7 Results of water-fat imaging (first row), clinical T1w TSE, T2w IP, T2w water, CT, and QSM (second row) in a female patient diagnosed with renal cancer and mainly osteolytic bone metastases of the vertebrae T4 and T5 according to CT. The metastatic lesion appears T1- and T2-hypointense, thus suggesting an osteoblastic mass. The results of the wfTFI QSM method and the MIP, however, suggest an osteolytic pattern, therefore being in agreement with CT as the reference standard

BFR artifacts in LBV+MEDI are more dominant than in PDF+MEDI. The BFR artifacts within LBV can be reduced by optimizing the local region mask at the cost of reduced visible tissue. However, it has been shown that the LBV method is problematic in body applications when the edges of the region mask contain strong susceptibility sources such as subcutaneous fat.[45] When the edges of the ROI mask contain strong susceptibility sources, the approximative assumption of the LBV method is violated: the local field in the selected boundary voxels is not much smaller than the local field. Hence, values close to the boundary are shifted towards zero. This limitation of the LBV can cause strong artifacts in body regions, when the ROI mask is not adjusted manually. A similar decrease in susceptibility values close to the ROI mask can be observed in the susceptibility map based on PDF BFR. However, in the PDF method, the underestimation of susceptibility in the ROI originates from the tendency of the PDF algorithm to overfit at the local/background region interface.[22,38] Consequently, susceptibility originating from the ROI is falsely estimated to originate from the background region. The significant reduction of BFR artifacts in the proposed wfTFI method originates from the simultaneous estimation of background and local susceptibility and was described in Ref. [28]. Furthermore,

in Ref. [28] the use of a preconditioner is proposed to increase the speed of convergence and is presently adapted in self-adapting variant similar to.[38] However, in the original TFI, the use of a preconditioner was mainly proposed to improve the rate of convergence and the use of the preconditioner was assumed to be optional. However, in the present study, the preconditioner has proven to be essential. When the preconditioner was removed, the estimation of local susceptibility was not possible and the result was dominated by artifacts. The preconditioner therefore contains the remaining necessary implicit assumption to distinguish regions of local and background susceptibility based on prior knowledge. However, the method was robust to the selection of the binary mask that distinguishes the above regions. The MIP across echo times thresholded at 5% of its maximum value has been proven to be robust across subjects and regions and was applied in all subjects and the simulation. In general, the results in the ROI have proven to be robust against the selection of the threshold. Furthermore, the BFR performance and susceptibility value estimation were robust against variations of the above binary mask selection.

Second, using a linear QSM model can (1) lead to the amplification of noise and (2) wraps in the field-map cannot be accounted for. While wraps in the field map can be
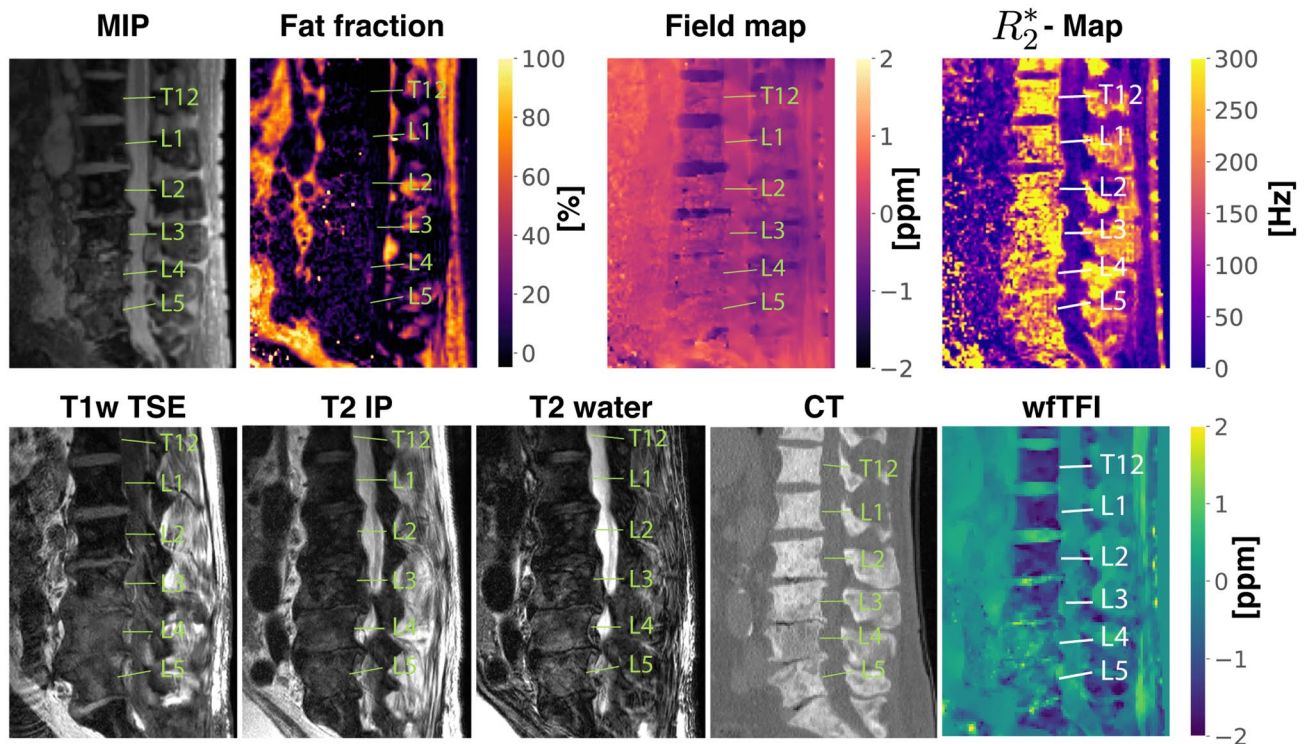
FIGURE 8 Results of water-fat imaging (first row), clinical T1w TSE, T2w IP, T2w water, CT, and QSM (second row) results in a male patient diagnosed with prostate cancer and mainly osteoblastic bone metastases along the displayed thoracolumbar spine. The osteoblastic components in the vertebrae T12-L5 according to CT show T1- and T2-hypointense correlates that are in good agreement with the results of the wfTFI QSM method

eliminated by the correct parameter selection in the field mapping and water-fat separation method employed,[35] the noise amplification can be accounted for by an improved problem formulation. A nonlinear formulation of the field-to-source relation can be used to alleviate the abovementioned noise amplification problem.[31] The proposed wfTFI explicitly formulates the susceptibility estimation as a non-linear problem by fitting the nonlinear water-fat signal model to the multi-echo gradient echo data. Additionally, the direct use of echo data benefits from the fact that the assumption of Gaussian noise is well justified in all voxels in contrast to the linear TFI model, where this assumption is only true in voxels with high SNR.[31] In body regions, voxels with low SNR frequently occur for different reasons, including (1) short T_2 tissues such as cortical bone in the ROI,[46] (2) air within in the ROI, for example, the lungs, air in the bowel or intraspinal air,[35] or (3) the general low signal strength due to coil sensitivity effects in standard clinical body MR protocols.[29] The estimation of susceptibility values within the original linear TFI method was not possible in regions with very low signal eg, anterior to the spine. QSM based on the linear TFI was not able to depict structures in this region while PDF+MEDI and the wfTFI method did. Furthermore, the linear TFI showed a significant overestimation in the IVDs in Figure 4. The proposed wfTFI showed that the formulation used in the present study can significantly reduce the noise

in QSM in regions with low SNR voxels that arise for the above reasons.

Third, the direct estimation of the susceptibility map from multi-echo has proven to reduce streaking artifacts originating from large susceptibility differences in the ROI. In QSM a plethora of methods have been proposed to reduce streaking artifacts originating from the zero-cone surface of the dipole kernel in k-space and many of them are based on regularization. One of the most well-established QSM regularization methods MEDI.[37] The assumption in MEDI regularization is that edges occurring in magnitude images are also likely to occur in the susceptibility map and was presently implemented in the wfTFI method. Despite the effectiveness of the MEDI regularization to reduce streaking artifacts, they still appear in many imaging situations. To further reduce streaking artifacts, the use of MERIT was proposed to alleviate remaining artifacts.[31] However, this method can lead to an artifactual distortion of regions with strong susceptibility sources[34] and the method itself requires appropriate optimization. A previous method ,called mcTFI, which directly estimates susceptibility from multi-echo data in the brain could reduce streaking artifacts, while the depiction of strong susceptibility sources was improved without the need for the MERIT method.[34] The proposed wfTFI shows the same reduction in streaking artifacts as shown in Figure 3 close to the air in the bowel and in all depicted spine regions in the

cerebrospinal fluid region. However, noteworthy is that the proposed wfTFI only optimizes over the susceptbility map after an initialization with the complex water and fat image and R_2^*-map, while mcTFI additionally optimizes over the complex signal and R_2^*.

Finally, the proposed wFTFI method shows improved diagnostic confidence in the particular application setting: the assessment of metastatic bone disease in order to distinguish between osteolytic and osteoblastic changes. It is clinically important to distinguish between osteolytic and osteoblastic metastases for several reasons: (1) vertebral bodies with osteolytic metastases have a higher probability of pathological fractures compared to osteoblastic metastases,[4] (2) osteolytic metastases can be subject to a sclerotic transformation after therapy,[3] and (3) the differentiation can support the search for an unknown primary tumor. The search for an unknown primary tumor is supported because osteolytic metastases are predominantly associated with renal, thyroid, colorectal, lung, and breast cancer in contrast to osteoblastic metastases that are predominantly associated with breast and prostate cancer.[1,5] The sensitivity to detect osteoblastic and osteolytic changes in standard T1- and T2-weighted spine MRI sequences has been estimated to be 89% and 73%, respectively.[7] In the present small patient study, the metastases in all patients could be correctly classified as predominantly osteolytic or osteoblastic based on the QSM maps of the proposed wfTFI method.

The present study has some limitations. First, in order to solve the proposed minimization problem in a reasonable timeframe a GPU with enough RAM is necessary. The depicted spine data sets needed approximately 6 GiB of RAM and the runtime for graph-cut based field-mapping and QSM was around 40 seconds on a NVIDIA GeForce GTX 1080 Ti consumer GPU used in the study. Second, the present wfTFI methodology would strongly benefit from a large-scale validation of its performance in more patients with bone metastases and other body QSM applications. Third, the improvement in the susceptibility value estimation was only evaluated in a qualitative setting. Therefore, the proposed method would benefit from a more quantitative validation. However, despite the fact that the proposed method is able to significantly reduce artifacts commonly present in the comparison methods and yields robust results across the present in vivo measurements, the aforementioned artifacts may still appear in some imaging situations.

In conclusion, the present study proposed a preconditioned water-fat total field inversion method for QSM in water-fat regions. The proposed method shows the following significant improvements over former proposed QSM methods: (1) it significantly reduces background field removal artifacts, (2) noise amplification, and (3) streaking artifacts, and thereby (4) improves the depiction of local susceptibility in water-fat regions.

5 | CONCLUSION

A preconditioned water-fat total field inversion method was proposed for QSM in water-fat regions. The proposed method shows the following significant improvements over former proposed QSM methods: (1) it significantly reduces background field removal artifacts, (2) noise amplification and (3) streaking artifacts while (4) improving the accuracy of the local susceptibility estimation

CONFLICT OF INTEREST
Jakob Meineke is an employee of Philips Research and Kilian Weiss is an employee of Philips Healthcare. Dimitrios Karampinos receives grant support from Philips Healthcare.

DATA AVAILABILITY STATEMENT
The Python implementation of all QSM methods as well as an example lumbar spine data set will be made freely available for download at https://github.com/BMRRgroup/wfTFI.

ORCID
Christof Boehm http://orcid.org/0000-0003-1321-5804

TWITTER
Christof Boehm @BoehmChristof

REFERENCES
1. Yochum T, Rowe L. *Rowe's Essentials of Skeletal Radiology*. Philadelphia: Lippincott/Williams & Wilkins; 2005.
2. Kirchhoff SB, Becker C, Duerr HR, Reiser M, BaurMelnyk A. Detection of osseous metastases of the spine: comparison of high resolution multi-detector-CT with MRI. *Eur J Radiol*. 2009;69:567-573.
3. Kesavadas C, Santhosh K, Thomas B, et al. Signal changes in cortical laminar necrosis-evidence from susceptibility-weighted magnetic resonance imaging. *Neuroradiology*. 2009;51:293-298.
4. Freeman A, Sumathi V, Jeys L. Metastatic tumours of bone. *Surgery (Oxford)*. 2017;36.
5. Freyschmidt J. *Skeletterkrankungen: Klinisch-Radiologische Diagnose und Differenzialdiagnose*. Berlin, Germany: Springer; 2008.
6. Lange MB, Nielsen ML, Andersen JD, Lilholt HJ, Vyberg M, Petersen LJ. Diagnostic accuracy of imaging methods for the diagnosis of skeletal malignancies: a retrospective analysis against a pathology-proven reference. *Eur J Radiol*. 2016;85:61-67.

7. Böker SM, Adams LC, Bender YY, et al. Differentiation of predominantly osteoblastic and osteolytic spine metastases by using susceptibility-weighted MRI. *Radiology*. 2019;290:146-154.

8. Wang Y, Liu T. Quantitative susceptibility mapping (QSM): decoding MRI data for a tissue magnetic biomarker. *Magn Reson Med*. 2014;73:82-101.

9. Liu C, Li W, Tong KA, Yeom KW, Kuzminski S. Susceptibility-weighted imaging and quantitative susceptibility mapping in the brain. *J Magn Reson Imaging*. 2014;42:23-41.

10. EskreisWinkler S, Zhang Y, Zhang J, et al. The clinical utility of QSM: disease diagnosis, medical management, and surgical planning. *NMR Biomed*. 2016;30.e3668

11. Sun H, Seres P, Wilman A. Structural and functional quantitative susceptibility mapping from standard fMRI studies. *NMR Biomed*. 2016;30.e3619

12. Sharma SD, Hernando D, Horng DE, Reeder SB. Quantitative susceptibility mapping in the abdomen as an imaging biomarker of hepatic iron overload. *Magn Reson Med*. 2014;74:673-683.

13. Lin H, Wei H, He N, et al. Quantitative susceptibility mapping in combination with water-fat separation for simultaneous liver iron and fat fraction quantification. *Eur Radiol*. 2018;28:3494-3504.

14. Jafari R, Sheth S, Spincemaille P, et al. Rapid automated liver quantitative susceptibility mapping. *J Magn Reson Imaging*. 2019;50:725-732.

15. Straub S, Laun FB, Emmerich J, et al. Potential of quantitative susceptibility mapping for detection of prostatic calcifications. *J Magn Reson Imaging*. 2016;45:889-898.

16. Wei H, Lin H, Qin L, et al. Quantitative susceptibility mapping of articular cartilage in patients with osteoarthritis at 3T. *J Magn Reson Imaging*. 2018;49:1665-1675.

17. Dimov AV, Liu Z, Spincemaille P, Prince MR, Du J, Wang Y. Bone quantitative susceptibility mapping using a chemical species-specific R_2^* signal model with ultrashort and conventional echo data. *Magn Reson Med*. 2017;79:121-128.

18. Diefenbach MN, Meineke J, Ruschke S, Baum T, Gersing A, Karampinos DC. On the sensitivity of quantitative susceptibility mapping for measuring trabecular bone density. *Magn Reson Med*. 2019;81:1739-1754.

19. Bray TJ, Karsa A, Bainbridge A, et al. Association of bone mineral density and fat fraction with magnetic susceptibility in inflamed trabecular bone. *Magn Reson Med*. 2019;81:3094-3107.

20. Jerban S, Lu X, Jang H, et al. Significant correlations between human cortical bone mineral density and quantitative susceptibility mapping (QSM) obtained with 3D cones ultrashort echo time magnetic resonance imaging (UTE-MRI). *Magn Reson Imaging*. 2019;62:104-110.

21. Zhou D, Liu T, Spincemaille P, Wang Y. Background field removal by solving the laplacian boundary value problem. *NMR Biomed*. 2014;27:312-319.

22. Liu T, Khalidov I, de Rochefort L, et al. A novel background field removal method for mri using projection onto dipole fields (PDF). *NMR Biomed*. 2011;24:1129-1136.

23. Özbay PS, Deistung A, Feng X, Nanz D, Reichenbach JR, Schweser F. A comprehensive numerical analysis of background phase correction with V-SHARP. *NMR Biomed*. 2016;30.e3550

24. Li W, Avram AV, Wu B, Xiao X, Liu C. Integrated laplacian-based phase unwrapping and background phase removal for quantitative susceptibility mapping. *NMR Biomed*. 2013;27:219-227.

25. Schweser F, Deistung A, Lehr BW, Reichenbach JR. Quantitative imaging of intrinsic magnetic tissue properties using MRI signal phase: an approach to in vivo brain iron metabolism? *NeuroImage*. 2011;54:2789-2807.

26. Langkammer C, Bredies K, Poser BA, et al. Fast quantitative susceptibility mapping using 3D EPI and total generalized variation. *NeuroImage*. 2015;111:622-630.

27. Chatnuntawech I, McDaniel P, Cauley SF, et al. Single-step quantitative susceptibility mapping with variational penalties. *NMR Biomed*. 2016;30:e3570.

28. Liu Z, Kee Y, Zhou D, Wang Y, Spincemaille P. Preconditioned total field inversion (TFI) method for quantitative susceptibility mapping. *Magn Reson Med*. 2016;78:303-315.

29. Diefenbach MN, Van A, Meineke J, et al. Vertebral column quantitative susceptibility mapping using joint background field removal and dipole inversion. *Proceedings 26*. Paris, France: Annual Meeting International Society for Magnetic Resonance in Medicine; 2018:0191.

30. Böhm C, Diefenbach MN, Meineke J, Haase A, Karampinos DC. Improved body quantitative susceptibility mapping by using a variable-layer single-min-cut graph-cut algorithm for field-mapping. *Proceedings 27*. Montreal, Canada: Annual Meeting International Society for Magnetic Resonance in Medicine; 2019:0693.

31. Liu T, Wisnieff C, Lou M, Chen W, Spincemaille P, Wang Y. Nonlinear formulation of the magnetic field to source relationship for robust quantitative susceptibility mapping. *Magn Reson Med*. 2012;69:467-476.

32. Collins CM, Yang B, Yang QX, Smith MB. Numerical calculations of the static magnetic field in three-dimensional multi-tissue models of the human head. *Magn Reson Imaging*. 2002;20:413-424.

33. Hopkins JA, Wehrli FW. Magnetic susceptibility measurement of insoluble solids by NMR: magnetic susceptibility of bone. *Magn Reson Med*. 1997;37:494-500.

34. Wen Y, Spincemaille P, Nguyen T, et al. Multiecho complex total field inversion method (mcTFI) for improved signal modeling in quantitative susceptibility mapping. *Magn Reson Med*. 2021;86:2165-2178.

35. Boehm C, Diefenbach MN, Makowski MR, Karampinos DC. improved body quantitative susceptibility mapping by using a variable-layer single-min-cut graph-cut for field-mapping. *Magn Reson Med*. 2021;85:1697-1712.

36. Ren J, Dimitrov I, Sherry AD, Malloy CR. Composition of adipose tissue and marrow fat in humans By1h Nmr At 7 Tesla. *J Lipid Res*. 2008;49:2055-2062.

37. Liu T, Liu J, de Rochefort L, et al. Morphology enabled dipole inversion (MEDI) from a single-angle acquisition: comparison with cosmos in human brain imaging. *Magn Reson Med*. 2011;66:777-783.

38. Liu Z, Wen Y, Spincemaille P, et al. Automated adaptive preconditioner for quantitative susceptibility mapping. *Magn Reson Med*. 2020;83:271-285.

39. Okuta R, Unno Y, Nishino D, Hido S, Loomis C. CuPy: a NumPy-compatible library for NVIDIA GPU calculations. In: Proceedings of Workshop on Machine Learning Systems (LearningSys) in The Thirty-first Annual Conference on Neural Information Processing Systems (NIPS). 2017.

40. Gosselin MC, Neufeld E, Moser H. Development of a new generation of high-resolution anatomical models for medical device evaluation: the virtual population 3.0. *Phys Med Biol*. 2014;59:5287-5303.

41. Yaniv Z, Lowekamp BC, Johnson HJ, Beare R. Simpleitk image-analysis notebooks: a collaborative environment for education and reproducible research. *J Digital Imaging*. 2017;31:290-303.

42. Yu H, Shimakawa A, McKenzie CA, Brodsky E, Brittain JH, Reeder SB. Multiecho water-fat separation and simultaneous R_2^* estimation with multifrequency fat spectrum modeling. *Magn Reson Med*. 2008;60:1122-1134.

43. Bydder M, Yokoo T, Hamilton G, et al. Relaxation effects in the quantification of fat using gradient echo imaging. *Magn Reson Imaging*. 2008;26:347-359.

44. Ruschke S, Eggers H, Kooijman H, et al. Correction of phase errors in quantitative water-fat imaging using a monopolar time-interleaved multi-echo gradient echo sequence. *Magn Reson Med*. 2016;78:984-996.

45. Van AT, Diefenbach MN, Meineke J, Kooijman H, Haase A, Karampinos DC. Background field removal in the presence of subcutaneous fat in body QSM. In: 4th International Workshop on MRI Phase Contrast & QSM, Graz, Austria. 2016.

46. Fortier V, Levesque IR. Phase processing for quantitative susceptibility mapping of regions with large susceptibility and lack of signal. *Magn Reson Med*. 2018;79:3103-3113.

SUPPORTING INFORMATION

Additional Supporting Information may be found online in the Supporting Information section.

Table S1 Fat fraction, R_2^* and χ values of different body structures used for the numerical simulation of multi-echo lumbar spine data. The values were taken from either the literature or extracted from in vivo scans of the specific anatomical structure

3.5 Journal Publication IV:
On the water–fat in-phase assumption for quantitative susceptibility mapping

3.5.1 Abstract

Purpose

Conventionally, multiple echoes are recorded for the estimation of quantitative susceptibility maps in regions where both water and fat are present. This is necessary to remove the phase contributions induced by the chemical shift of fat. However, this leads to long acquisition times, a limited resolution and introduces the need for sophisticated field-mapping techniques that either might simply not be available or have long computation time. Therefore, this work proposes *effective* in-phase echo times to allow for body QSM acquisitions with less then 3 echoes and simplified field map estimation.

Methods

A single-voxel simulation was performed to estimate the echo times where the phase contributions of fat are zero. The echo times were estimated for different fat models including the in vivo liver, in vivo bone marrow and ex vivo peanut oil. The estimated *effective* in-phase echo times were validated in a Monte Carlo simulation, a liver simulation, in an peanut oil phantom and in vivo in the liver, spine and breast.

Results

QSM based on the proposed *effective* multipeak in-phase echo times achieve the same quantitative accuracy as QSM based on conventional water–fat separation based echo acquisition and parameter separation.

Conclusion

QSM based on the proposed *effective* multipeak in-phase echo times has the same quantitative performance as water–fat separation based QSM. *Effective* multi-peak echo times hence allow for a much faster acquisition of QSM maps when compared to water–fat separation based acquisitions by reducing the required number of recorded echoes. Furthermore, the computational cost of the field map estimation is significantly reduced.

3.5.2 Author contributions

The hypothesis of the existence of zeros in the phase of the water-fat signal evolution function for physiological multi-peak fat models was devised by the first author. In support of this hypothesis, the first author developed all necessary code for the manuscript, including single voxel simulations, Monte Carlo simulations, numerical liver simulations, as well as the field-mapping and QSM methods. The scanner phantom was constructed by the first author, who also collected all experimental data. With the guidance and input of coauthors, the first author analyzed and interpreted the data, and authored the manuscript.

3.5.3 Original Article

Magnetic Resonance in Medicine

On the water–fat in-phase assumption for quantitative susceptibility mapping

Christof Boehm[1] | **Sarah Schlaeger[2]** | **Jakob Meineke[3]** | **Kilian Weiss[4]** | **Marcus R. Makowski[1]** | **Dimitrios C. Karampinos[1]**

[1]Department of Diagnostic and Interventional Radiology, School of Medicine, Klinikum rechts der Isar, Technical University of Munich, Munich, Germany

[2]Department of Diagnostic and Interventional Neuroradiology, School of Medicine, Klinikum rechts der Isar, Technical University of Munich, Munich, Germany

[3]Philips Research, Hamburg, Germany

[4]Philips GmbH Market DACH, Hamburg, Germany

Correspondence
Christof Boehm, Department of Diagnostic and Interventional Radiology, Klinikum rechts der Isar, Ismaninger Str 22, 81675 Munich, Germany.
Email: christof.boehm@tum.de

Funding information
H2020 European Research Council, Grant/Award Number: 677661; Philips Healthcare

Purpose: To (a) define multi-peak fat model-based *effective* in-phase echo times for quantitative susceptibility mapping (QSM) in water–fat regions, (b) analyze the relationship between fat fraction, field map quantification bias and susceptibility bias, and (c) evaluate the susceptibility mapping performance of the proposed *effective* in-phase echoes in comparison to single-peak in-phase echoes and water–fat separation for regions where both water and fat are present.

Methods: *Effective* multipeak in-phase echo times for a bone marrow and a liver fat spectral model were derived from a single voxel simulation. A Monte Carlo simulation was performed to assess the field map estimation error as a function of fat fraction for the different in-phase echoes. Additionally, a phantom scan and in vivo scans in the liver, spine, and breast were performed and evaluated with respect to quantification accuracy.

Results: The use of single-peak in-phase echoes can introduce a worst-case susceptibility bias of 0.43 ppm. The use of *effective* multipeak in-phase echoes shows a similar quantitative performance in the numerical simulation, the phantom and in all in vivo anatomies when compared to water–fat separation-based QSM.

Conclusion: QSM based on the proposed *effective* multipeak in-phase echoes can alleviate the quantification bias present in QSM based on single-peak in-phase echoes. When compared to water–fat separation-based QSM the proposed *effective* in-phase echo times achieve a similar quantitative performance while drastically reducing the computational expense for field map estimation.

KEYWORDS
field map, in phase, quantitative susceptibility mapping, susceptibility

1 | INTRODUCTION

Quantitative susceptibility mapping (QSM)[1] has been applied in tissues outside the brain, for example, to distinguish osteolytic/osteoblastic bone changes in the spine,[2] to characterize lesions and calcifications in breast disease,[1,3] to measure bone density,[4-7] or liver iron overload.[8-10] However, QSM in the body remains challenging for several reasons including the large susceptibility difference between bone, soft tissue, and air and the presence of fat. To obtain a field map without fat phase contributions, multi-echo acquisitions and subsequent extraction of the water–fat model parameters such as the water- and fat-images, R_2^*- and field map[11] are commonly performed. However, water–fat separation-based field-mapping itself is a large field of research and subject to a variety of restrictions and limitations.

First, the echo times have to be carefully selected for a robust separation of water and fat and consequently for the correct estimation of the field map parameter.[12,13] At 3T, optimal echo time step for a 6 echo acquisition has been estimated by Cramer–Rao analysis to be of the order of 1ms.[13] However, such a short echo time step either limits the achievable resolution or the echoes cannot be recorded in a single repetition time (TR), especially while using monopolar gradients. A possible solution to the trade off between echo time selection and resolution is a time interleaved sequence[14] and has successfully been applied to QSM in water–fat regions.[2,5,11] However, such an acquisition comes at the cost of an increased scan time since the echo times are not acquired in a single TR. Therefore, typically a low number of echoes is used resulting in a comparably short maximum echo time. Longer maximum echo times can be desirable for QSM due to the increased phase weighting and the associated increase in sensitivity for the field map parameter.

Second, the separation of water–fat images and the field map is challenging due to the nonconvex inverse problem, where the solution space is known to include several local and global minima.[15,16] A plethora of field-mapping methods have been proposed to solve the field map estimation problem and many of them rely on a spatial smoothness constraint on the field map.[17-19] Graph-cut-based field-mapping methods have been particularly successful in solving the constraint optimization problem. However, graph-cut-based methods are notoriously computationally intensive and can show processing times of up to hours for scans with either a high resolution or a large field of view.[11]

To sidetrack the above problems of water–fat separation-based field-mapping in body regions, gradient echo imaging using only in-phase echoes has been proposed for the estimation of susceptibility and has primarily been used in the spine.[6,7] By definition, in-phase echoes are acquired when water and fat are in phase. Conventionally, a single-peak fat model is assumed for the definition of in-phase echo times. When using in-phase echo times, the signal model is convex within the period of the phasor and thus the field map can robustly be estimated using gradient descent-based nonlinear least squares techniques. However, physiological fat spectra are known to be spectrally complex rendering the definition of single-peak in-phase echo times problematic.[20] The use of single-peak in-phase echo times has been shown to introduce significant susceptibility quantification bias[21] in regions where the fat spectrum is spectrally complex.

Therefore, the purpose of this work is to (a) generalize the approach of single-peak in-phase echoes to the use of *effective* multipeak in-phase echo times, (b) to investigate the correlation between fat fraction, field map estimation bias and susceptibility bias and to (c) demonstrate the feasibility of *effective* multipeak in-phase echo times to successfully alleviate the quantification bias of single-peak in-phase echoes. Therefore, susceptibility mapping based on *effective* multipeak in-phase echoes, conventional single-peak in-phase echoes and water–fat separation were compared in a numerical liver simulation, a phantom and in vivo in the liver, the spine, and the breast.

2 | METHODS

Multipeak effective in-phase echo times

In regions where water and fat are present, the well-established single-R_2^* multipeak water–fat signal model can be used to describe the voxel signal evolution with time as follows:[22]

$$\boldsymbol{s}(t_n) = (\rho_W + c_n\rho_F)\, e^{\gamma t_n}, \quad \gamma = i2\pi f_B - R_2^*,$$
$$c_n = \sum_{p=1}^{P} a_p e^{i2\pi\Delta f_p t_n}, \quad \text{with} \quad \sum_{p=1}^{P} a_p = 1, \tag{1}$$

where t_n are the echo time points, ρ_W and ρ_F are the complex signal of the water and fat components with an equal transverse relaxation rate R_2^* and f_B is the field map. The fat spectrum is assumed to have P spectral peaks with corresponding relative amplitudes a_p and chemical shift Δf_p. Conventionally, for the definition of in-phase echo times, the fat spectrum is assumed to have only one spectral peak $P = 1$. Thus, Equation (1) can be simplified to

$$\boldsymbol{s}(t_n) = \left(\rho_W + \rho_F e^{i2\pi f_p t_n}\right) e^{\gamma t_n}, \quad \gamma = i2\pi f_B - R_2^*, \tag{2}$$

where f_p is the chemical shift of a single fat peak. Under the above assumption of only one spectral peak, the water and fat signal are in-phase when the following condition $e^{i2\pi f_p t_n} = 1 \Leftrightarrow f_p \cdot t_n = b, b \in \mathbf{N}$ for the fat-phasor is met. Often, the methylene peak is set as f_p[23] due to its predominant amplitude in different fat compositions and has a chemical shift of -3.4 ppm relative to water[24] and is presently employed.

In case of the more accurate multipeak signal model in Equation (1), the definition of in-phase echo times is not possible due to the complexity of the fat-phasor where at any time after $t = 0$ the different fat constituents are never simultaneously aligned again. However, *effective* in-phase echoes can be defined, meaning the time points, where the fat-phasor in Equation (1) meets the condition $\angle c_n = 0$, representing the time points where the phase of the fat-phasor is zero.

2.1 | Field map estimation

For the field map estimation from complex multi-echo data a graph-cut algorithm was used.[11] In the case of water–fat separation based field map estimation, the graph-cut method was used as described in Reference 11. In the case of single-peak and multipeak in-phase echoes, the signal model in the graph-cut was reduced to a single species estimation. Specifically, the term describing the contributions of fat was removed since both the single-peak and the multipeak in-phase echoes are hypothesized to contain no phase contributions of fat.

2.2 | Numerical simulations

2.2.1 | Single voxel simulation

For the estimation and visualization of the difference between conventional single-peak and *effective* multipeak fat-model and to find the *effective* multipeak echo times, a single voxel simulation was performed using Equation (1) with either a single-peak fat spectral model using the above chemical shift frequency, a fat-model specific to bone marrow[25] or fat spectral model specific to the liver,[26] a fat fraction of 70%, $R_2^* = 30$ (Hz) and $f_B = 0$. The bone marrow and the liver spectral fat model both have nine fat peaks. The position of the fat peaks is $\Delta f = [-3.8, -3.4, -3.1, -2.68, -2.46, -1.95, -0.5, 0.49, 0.59]$ ppm for both models. The relative amplitude of the fat peak is $a = [0.09, 0.583, 0.06, 0.085, 0.06, 0.015, 0.04, 0.01, 0.057]$ ppm for the bone marrow model and $a = [0.088, 0.642, 0.058, 0.062, 0.058, 0.006, 0.039, 0.01, 0.037]$

ppm for the liver model, respectively. The two spectral models were selected based on the evidence that liver and adipose tissue have different triglyceride composition. The fat fraction and R_2^* were selected for a realistic and clear visualization of the signal evaluation. The variation of both parameters do not influence the zero crossings of the fat phasor.

2.2.2 | Monte Carlo simulation

A Monte Carlo simulation was performed for assessing the field map estimation error at different fat fractions using both conventional single-peak or *effective* multipeak in-phase echo times. The fat fraction values were varied from 0% to 100%, $R_2^* = 30$(Hz) and $f_B = 0$ were used. Independent Gaussian noise was added to the real and imaginary part of the echo data with an signal-to-noise ratio (SNR) of 100. The SNR was defined as the maximum signal amplitude of the first echo divided by the SD of noise. Based on the above values, the signal at different time points was simulated using Equation (1) with the single-peak fat model, the multipeak fat liver model or the multipeak bone marrow fat model. Subsequently, the field map from the three different signals were estimated for each fat fraction using each, the single-peak in-phase echoes and the *effective* multipeak in-phase echoes based on the liver and bone fat-model. Based on the above simulation, the accuracy of field map estimation choosing the echo times in accordance to the underlying fat model as well as cross-model correlation were estimated.

2.2.3 | Correlation between field map estimation error and susceptibility quantification bias

In order to quantify how the field map estimation error translates into susceptibility error without the potential bias of a selected inversion method, a simulation of a sphere with varying susceptibility difference from outside to inside and of an infinite flat surface of two materials with a susceptibility difference was performed. The susceptibility map was forward simulated to a field map and the field map difference was measured at the surface.

2.2.4 | Numerical liver simulation

In order to assess the quantification bias induced by the in-phase assumption in a realistic anatomy, a numerical

simulation based on the Duke phantom was performed using the annotated geometrical data from Reference 27. Each tissue was assigned with either their literature value or values extracted from in vivo scans and forward simulated using Equation (1). To account for the significantly different fat-models of the liver and other fatty tissues, the above liver fat-model was used within the liver and in all other fatty tissues the bone marrow model was used. In the simulation, either conventional water–fat separation echo times with six echoes, $TE_{min}/\Delta TE = 1.0$ ms, conventional single-peak in-phase echo times or *effective* in-phase echo times for the two above-mentioned fat-models were used. In the case of in-phase echo times the first three echo times were used due to there equidistant nature (see below in Results). A background field was simulated based on air outside the subject (9.94 ppm[28]) and in the lungs (13.36 ppm[29]). An SNR of 50 was added similar to the above Monte Carlo simulation. The field map, water(–fat)-images and R_2^*-map were estimated using a graph-cut algorithm.[11] The field maps were inverted to a susceptibility map using a linear total field inversion algorithm.[30] Since the linear total field inversion algorithm method only obtains relative susceptibility maps, the susceptibility maps were referenced using the subcutaneous fat layer. Within the subcutaneous fat layer the susceptibility distribution is assumed to mainly originate from fatty tissue and not altered by diseases such as hepatic iron overload.[8] Normalized root mean square errors (NRMSE) were calculated in reference to the ground truth.

2.2.5 | Phantom measurements

To validate the numerical results, a scan of a vial filled with peanut oil in the center of a water reservoir was performed. Scanning was performed on a 3 T scanner (Ingenia Elition, Philips Healthcare) using a monopolar time-interleaved multi-echo gradient echo sequence[14] for reference water–fat separation, acquiring six echoes with 3 echoes per interleave. An isotropic voxel size of 1.5 mm, a field of view =[120,120, 141], $TE_1 = 1.23$ ms and $\Delta TE = 0.99$ ms were used. For the *effective* in-phase echo times a fat model specific to peanut oil was used.[31] Both the single peak in-phase echo times and the *effective* in-phase echo times were temperature corrected[32] to 23°C and were recorded with $TE_{single\ peak} = [2.21, 4.42, 6.63]$ ms and $TE_{peanut\ oil} = [2.29, 4.44, 6.59]$ ms, respectively. The above processing of graph-cut-based field-mapping and linear total field inversion algorithm dipole inversion was used and the difference susceptibility between an region-of-interest (ROI) in the vial and the water reservoir was measured.

2.3 | In vivo measurements

The aforementioned processing of graph-cut-based field-mapping followed by linear total field inversion algorithm QSM was applied in in vivo scans of the spine, the breast and the liver of 10 volunteers, where in six volunteers only the spine was acquired, in three volunteers the spine and liver were acquired and in one subject only the breast was acquired. Approval by the institutional review board (Klinikum rechts der Isar, Technical University of Munich) was granted for the scans and informed consent was received by all subjects. Scanning was performed on the aforementioned scanner. Reference field maps were estimated using the above monopolar time-interleaved multi-echo gradient echo sequence, where the liver fat model was used for the liver scan and the bone marrow model for the scan of the spine and breast, respectively. In all anatomies scans based on conventional single-peak in-phase echoes were performed. Additionally, the liver was scanned once with *effective* multi-peak echo times based on the liver model and once based on the bone marrow model. The spine and breast were scanned once with *effective* multipeak in-phase echo times based on the bone marrow model. The scanning parameters for each anatomy are given in Table 1. For a quantitative assessment of the results, a difference measurement within the susceptibility map was performed between different tissue types. Fat[8] and paraspinal muscles[33] have previously been used for referencing of susceptibility maps and hence were presently adopted. For the liver scan, the difference between subcutaneous fat and a ROI in the liver of the size of ~ 12 cm^3 and an ROI in the paraspinal muscle of the size of ~ 4 cm^3 and the ROI in the liver were measured (see Figure 5). For the subcutaneous fat layer mask, all voxels with a fat fraction greater than 75% were selected. In the lumbar spine scans, the difference between the posterior subcutaneous fat layer (orange arrow in Figure 6) and the spinal canal between the upper plate of the L3 vertebra and the base plate of the L5 vertebra was measured. Since in healthy adults the spinal cord ends at the height of the L1/L2 vertebrae, the segmented part of the spinal canal is predominantly filled with cerebrospinal fluid (CSF, white arrow) which is often used in brain QSM for referencing.[34] The subcutaneous fat layer mask was generated as for the liver scan. The CSF region was manually segmented. In the breast scan, the difference between fatty and fibroglandular tissue in the right breast was measured. First, the right breast was segmented using the deep neural network and weights from Reference 35. Within the right breast, the fat mask was again based on all voxels with a fat fractions greater than 75%. The fibroglandular tissue mask was based on all voxels with a fat fraction from 0%–20%.

TABLE 1 MR scan parameters for the in vivo acquisitions for the respective anatomy

Parameter	Liver	Spine	Breast
Field of view	$400 \times 320 \times 180$ mm^3	$220 \times 220 \times 79.2$ mm^3	$220 \times 382 \times 192.4$ mm^3
Voxel size	$2 \times 2 \times 5$ mm^3	1.8 mm isotropic	1.3 mm isotropic
Flip angle	3°	3°	3°
Acceleration	Compressed sensing ($R = 4$)	None	Compressed sensing ($R = 6$)
Acquisition for water–fat separation			
Type	Interleaved (2)	Interleaved (2)	Interleaved (2)
TE	$N_{TE} = 4$ TE$_{min} = 1.09$ ms ΔTE $= 0.80$ ms	$N_{TE} = 6$ TE$_{min} = 1.33$ ms ΔTE $= 1.05$ ms	$N_{TE} = 6$ TE$_{min} = 1.58$ ms ΔTE $= 1.28$ ms
TR	4.7 ms	8.1 ms	10 ms
Scan time	0:16 min	3:12 min	4:15 min
Acquisition of *effective* multipeak in-phase echoes			
Type	Single acquisition (all echoes in one TR)	Single acquisition (all echoes in one TR)	Interleaved (2)
TE	(Liver model) $N_{TE} = 3$ TE$_{min} = 2.35$ ms ΔTE $= 2.24$ ms	(Bone marrow model) $N_{TE} = 3$ TE$_{min} = 2.38$ ms ΔTE $= 2.22$ ms	(Bone marrow model) $N_{TE} = 4$ (3 used) TE$_{min} = 2.38$ ms ΔTE $= 2.22$ ms
TR	8.5 ms	8.3 ms	11 ms
Scan time	0:17 min	1:52 min	3:21 min

Note: All acquisitions used monopolar gradients.

On the fibroglandular tissue mask, binary erosion was applied once in order to remove the skin layer from the mask. All manual segmentations namely, the drawing of the ROI in the subcutaneous fat, the ROI in the liver, the ROI in the paraspinal muscle and the spinal chanel between L3 and L5 were performed by a radiologist (with 6 years experience).

3 | RESULTS

3.1 | Numerical simulations

3.1.1 | Single voxel simulation

Figure 1 shows the signal evolution of a voxel containing both water and fat for different fat models. The dashed lines in gray indicate the time points where water and fat are in-phase in the case of the single-peak assumption (TE$_{min}$/ΔTE $= 2.3$ ms). The dashed lines in green indicate the time points, where the phase is zero and refer to the *effective* in-phase echo times The first six *effective* in-phase echoes are TE $= [2.38, 4.6, 6.81, 9.17, 11.62, 13.92]$ and TE $= [2.35, 4.59, 6.83, 9.2, 11.6, 13.89]$ for the bone marrow and the liver model, respectively. In the case of the bone marrow model the first three echoes are

almost equidistant. Echo times of TE $= [2.38, 4.6, 6.82]$ (TE$_{min}$/ΔTE $= 2.38/2.22$ ms) were subsequently used as the *effective* in-phase echo times for the bone marrow fat model. In the case of the liver model the first three echo times are exactly equidistant with TE$_{min}$/ΔTE $= 2.35/2.24$ ms and are subsequently referred to as *effective* in-phase echo times for the liver fat model.

3.1.2 | Monte Carlo simulation

Figure 2 shows the quantification bias of the field map as a function of the fat fraction for different fat models. The plots in the first column show the quantification bias of the single-peak in-phase assumption. For the single-peak assumption and a voxel with a fat fraction of 100% the field map error is almost -0.1 ppm for the liver fat model and -0.13 ppm for the bone marrow fat model, respectively (yellow background). The plots on the diagonal (blue background) reveal that the use of *effective* multi-peak in-phase echoes can reduce the field map quantification bias down to the noise level for both multipeak fat models. Measuring with *effective* in-phase echo times cross model (green background), the field map quantification bias for voxel with a fat fraction of 100% is significantly smaller than
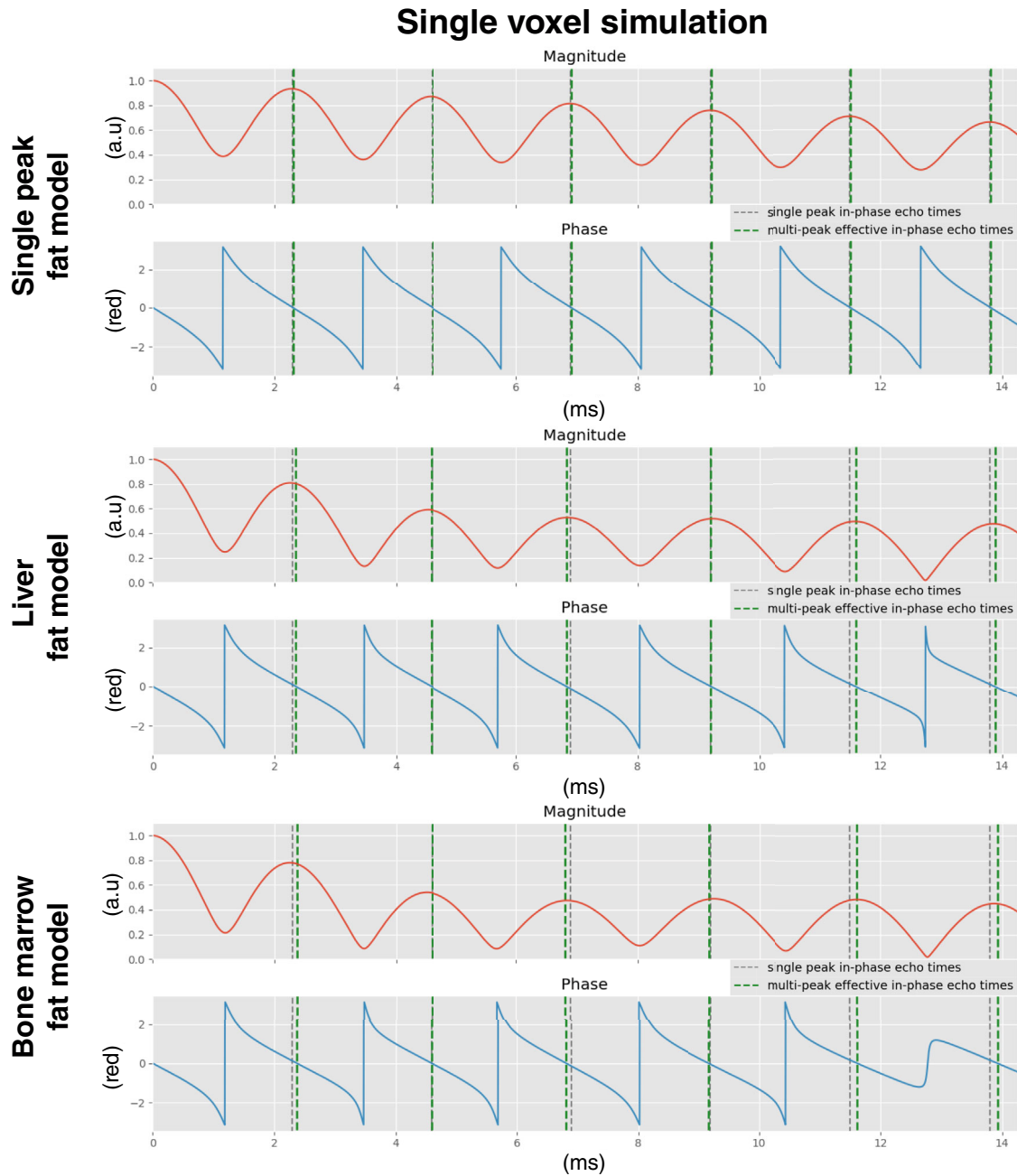
FIGURE 1 Magnitude and phase evolution for different fat models in a voxel containing both water and fat. The dashed line in gray refer to the time points at which the phase of fat in the single-peak assumption is zero ($TE_{min}/\Delta TE = 2.3$ ms). The dashed lines in green refer to the time points, where the fat phase is generally zero. For the single-peak fat model both time points coincide. In case of both the multi-peak liver and the bone marrow model the green and gray lines generally do not coincide and are shifted in both directions around the single-peak in-phase time points. Most importantly, in both multipeak fat models the time points where the fat phasor is zero are not equidistant and read TE = [2.38, 4.6, 6.81, 9.17, 11.62, 13.92] and TE = [2.35, 4.59, 6.83, 9.2, 11.6, 13.89] for the bone marrow and the liver fat spectrum model, respectively. While the first three echo times for liver model are equidistant this is not true for the bone marrow fat model. However, in the case of the bone marrow model either the first or the third echo time can be shifted by 0.01 ms to obtain three equidistant echoes

for the single-peak assumption and is 0.03 ppm. The plots with the red background show the correlation for the case of fatty tissue with only a single-fat peak estimated with *effective* multipeak in-phase echo times. Fatty tissue with only a single-fat peak is nonphysiological and is given for completeness. Noteworthy is that the correlation for physiological meaningful combinations (second and third row) are nonlinear. The correlations are well approximated using a second-order polynomial (see χ^2-test in each subplot's legend).
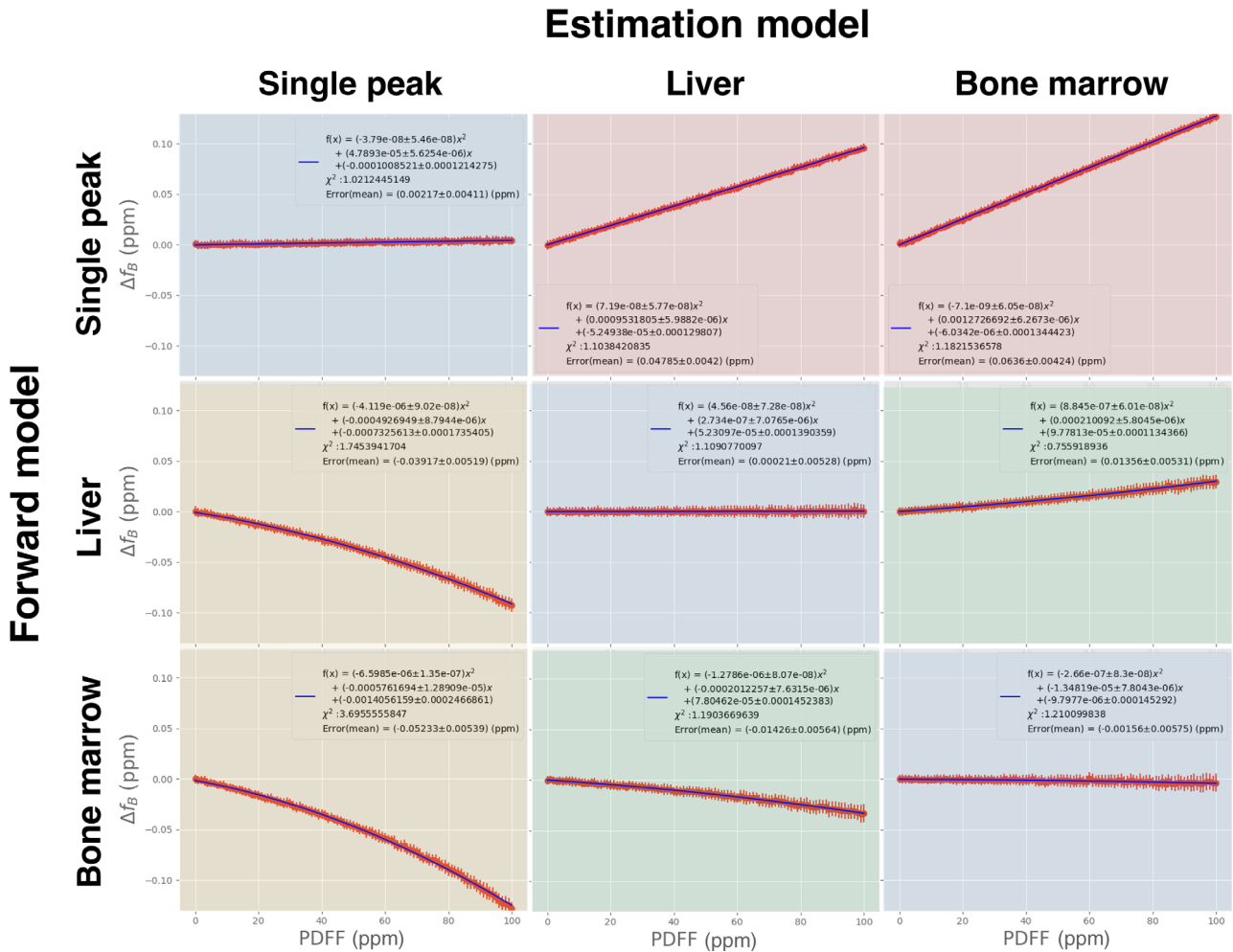
FIGURE 2 Analysis of the quantification bias of the field map in dependence of the fat fraction for different in-phase models. Each row shows the bias for the different fat model which were used to forward simulate the signal, while each column shows the bias for the different fat models which were used to define the (*effective multi-peak*) in-phase echo times used for the field map estimation. On the diagonal (blue background) plots, the results are shown when for a fat model the corresponding (*effective*) in-phase echo times were used. Using the correct in-phase echoes, the field map quantification bias can be alleviated for each fat model. When single-peak in-phase echo times are used to measure in the liver or the bone marrow (yellow background). The field map quantification bias correlates quadratically with fat fractions and reaches up to −0.1 ppm for the liver model and −0.13 ppm for the bone marrow model, respectively. Measuring with *effective* in-phase echo times cross model (green background), the field map quantification bias also correlates quadratically with fat fraction. In a voxel with a fat fraction of 100% the field map quantification bias in a cross-model measurement is significantly smaller than for the single-peak assumption and is 0.03 ppm. The case where the voxel only contains a single species, but are estimated with a multipeak fat model (red background) is only given for completeness.

3.1.3 | Correlation between field map estimation error and susceptibility quantification bias

Figure S1 shows how the field map quantification error propagates into susceptibility mapping error without the bias of the selected dipole inversion method. The field map quantification error correlation for a spherical surface and an infinite surface is −0.304 and −0.332 when the surface is parallel to B_0 and 0.608 and 0.664 when the surface is perpendicular to B_0, respectively. The difference between both surface types is 9.2%. The field map error in a

voxel with a fat fraction of 100% measured with single-peak in-phase echoes hence translates into worst-case susceptibility estimation error of $\frac{-0.1\text{ppm}}{-0.304} = 0.33$ ppm in the liver and $\frac{-0.13\text{ppm}}{-0.304} = 0.43$ ppm in bone marrow, respectively.

3.1.4 | Numerical liver simulation

Figure 3 shows field- and susceptibility-mapping results in a numerical liver simulation. The second row shows the reference field map and the difference between reference
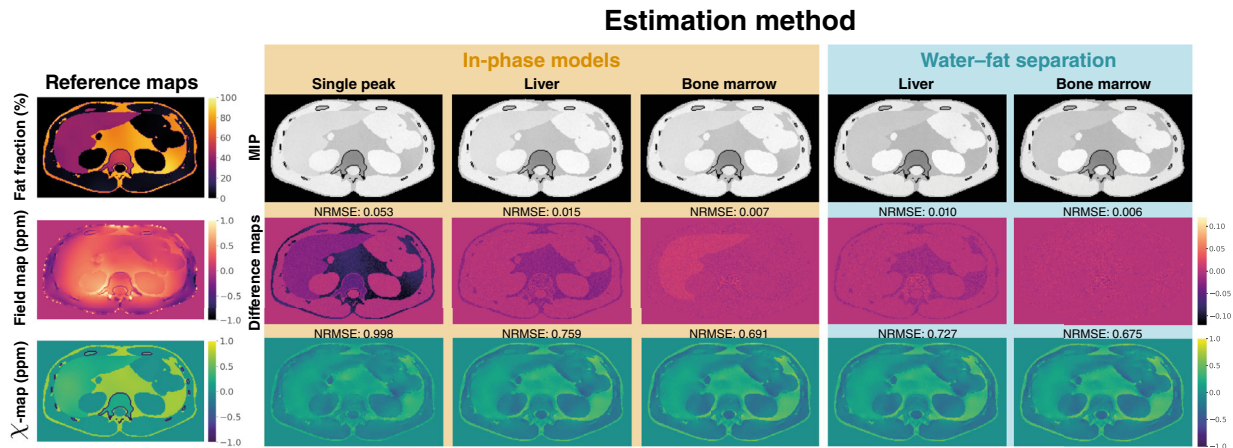
FIGURE 3 Results of field- and susceptibility-mapping in a numerical liver simulation. The first column shows the reference fat fraction, field map and susceptibility map used in the forward simulation. The rest of columns show the maximum intensity projection across echo times, the difference field maps with respect to the reference map and the susceptibility maps. The in-phase models (yellow background) refer to an acquisition based on the respective echo times specific to the fat model. For the water–fat separation-based estimation (blue background), the same echo times were used while in the separation the respective fat models were employed. The field map quantification bias correlates (i) with the fat fraction and (ii) with the employed estimation method. The use of single-peak in-phase echoes shows the largest field- and susceptibility-mapping error. Results based on *effective* bone marrow in-phase echoes (i) perform better than the liver model echo times and (ii) the normalized root mean square errors is comparable to water–fat separation-based results. However, general underestimation of susceptibility in all methods can be observed.

field map and estimated field map for each method. The difference map for the single-peak in-phase assumption yields the largest NRMSE of 0.053 ppm. The offset is dependent on the fat fraction and is always negative. The field map difference map of the liver *effective* in-phase model yields a NRMSE of 0.015 ppm. Using *effective* in-phase echoes based on the liver fat model, no field map quantification bias can be observed within the liver. However, a negative correlation with the fat fraction in other fatty tissue can be observed which is significantly smaller than in the single-peak in-phase echo-based map. The field map difference map based on the bone marrow model has an NRMSE of 0.007 ppm and quantification bias only within the liver. The quantification bias in the case of the bone marrow model has a positive correlation with the fat fraction. The correlations observed in the numerical liver simulation are in good agreement with the cross-model correlations shown in Figure 2. The error of the referenced susceptibility maps directly correlates with the error of the underlying field map. The higher the field map error, the higher the susceptibility error. However, a general overestimation of susceptibility values can be observed even in the method with the lowest NRMSE.

3.1.5 | Phantom measurements

In the phantom scan shown in Figure 4 the difference between the ROI in the vial and the water reservoir

yielded −0.068 ppm for single-peak in-phase echoes, 0.035 for *effective* in-phase echoes and −0.039 for water–fat separation-based susceptibility mapping. The use of conventional single-peak in-phase echo times shows a underestimation of field map and susceptibility values in the vial. Furthermore, in the susceptibility map based on single-peak in-phase echoes strong streaking artifacts around the oil-filled vial can be observed. Field-mapping and QSM results based on *effective* multipeak in-phase echoes show similar results to water–fat separation-based estimation. Mean, SD, and ROI size of the water reservoir and the oil vial can be found in Table S1.

3.2 | In vivo measurements

In a exemplary scan of the liver shown in Figure 5 the used ROIs in the paraspinal muscle and the liver for the difference measurements are depicted. The mean difference across all subject between the subcutaneous fat layer and the ROI in the liver yielded (0.15 ± 0.01) ppm for single-peak in-phase echoes, (0.24 ± 0.06) ppm and (0.28 ± 0.08) ppm for *effective* multipeak in-phase echoes based on the liver and bone marrow fat model, respectively, and (0.29 ± 0.05) ppm based on water–fat separation-based susceptibility mapping. The mean difference across all subject between the ROI in the back muscle and the ROI in the liver yielded $(−0.03 \pm 0.04)$ ppm for single-peak in-phase echoes, $(−0.08 \pm 0.05)$ ppm and

FIGURE 4 First echo (first row), field-mapping (second row) and susceptibility mapping (last row) results in the scan of a oil filled vial in a water reservoir. The in-phase models (yellow background) refer to an acquisition based on the respective echo times specific to the model. Both the in-phase and the water–fat separation fat model used fat spectracs temperature corrected to 23°C. For comparison, the difference susceptibility between an region-of-interest in the vial (white circle) and the water reservoir was measured. The single-peak in-phase estimation shows an underestimation in field map and susceptibility value and strong streaking artifacts around the vial in the susceptibility map. The use of peanut oil model-based *effective* in-phase echoes shows similar results to reference water–fat separation-based estimation. Specifically, the differences measurement between the vial and the water reservoir yield −0.068 ppm for the single-peak in-phase estimation, −0.035 ppm for the *effective* multi-peak in-phase echoes and −0.039 ppm for water–fat separation-based estimation.
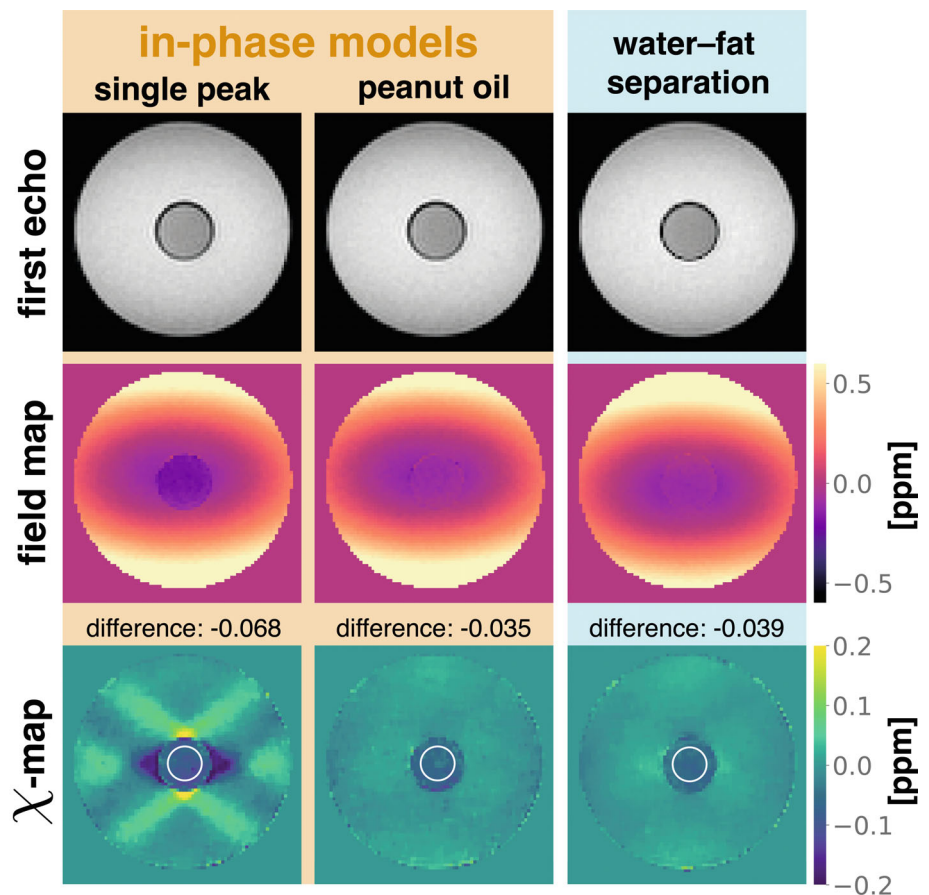
(-0.10 ± 0.06) ppm for *effective* multipeak in-phase echoes based on the liver and bone marrow fat model, respectively, and (-0.12 ± 0.09) ppm based on water–fat separation-based susceptibility mapping.

Using *effective* bone marrow in-phase echo times in the spine (exemplary Figure 6), similar susceptibility values in the anterior subcutaneous fat (orange arrows) can be observed as in the susceptibility map based on a water–fat separation-based field map. The use of single-peak in-phase echoes significantly underestimate regions with high fat fractions. Particularly noteworthy is the CSF region in the susceptibility map based on single-peak in phase echoes (white arrow) that shows strong streaking artifacts. The CSF region in the susceptibility map based on water–fat separation and on *effective* multipeak in-phase echoes is less effected by streaking artifacts. Furthermore, the susceptibility map based on water–fat separation shows the highest SNR and hence minimal noise compared to both in-phase maps. The mean susceptibility difference across the nine subjects between the subcutaneous fat layer and the CSF yielded (0.07 ± 0.07) ppm for single-peak in-phase echoes, (0.30 ± 0.09) ppm for *effective* multipeak in-phase echoes based on the bone marrow model and (0.31 ± 0.08) ppm

for water–fat separation-based susceptibility mapping, respectively.

The in vivo breast scan shown in Figure 7 yielded comparable results. The water–fat separation-based susceptibility allowed for a good delineation between fatty and dense breast tissue (arrow) and showed the least noisy image. A lot of contrast between the tissue types was lost in the single-peak-based map and noise was increased. The susceptibility map based on *effective* in-phase echo times showed a similar contrast between the tissue types at the arrow position. However, also an increase in residual background field removal artifacts was observed especially in proximity to the sternum and thoracic bones. The susceptibility difference measurement between fatty breast tissue and fibrograndular tissue yielded 0.22 ppm for single-peak in-phase echoes, 0.29 ppm for *effective* multipeak in phase echoes based on the bone marrow model and 0.30 ppm for water–fat separation-based susceptibility mapping, respectively.

The correlation of the difference measurements between reference water–fat separation-based susceptibility estimation and an estimation based on (*effective*) in-phase echoes yields a strong correlation between *effective* in-phase echoes based on the bone marrow fat model.
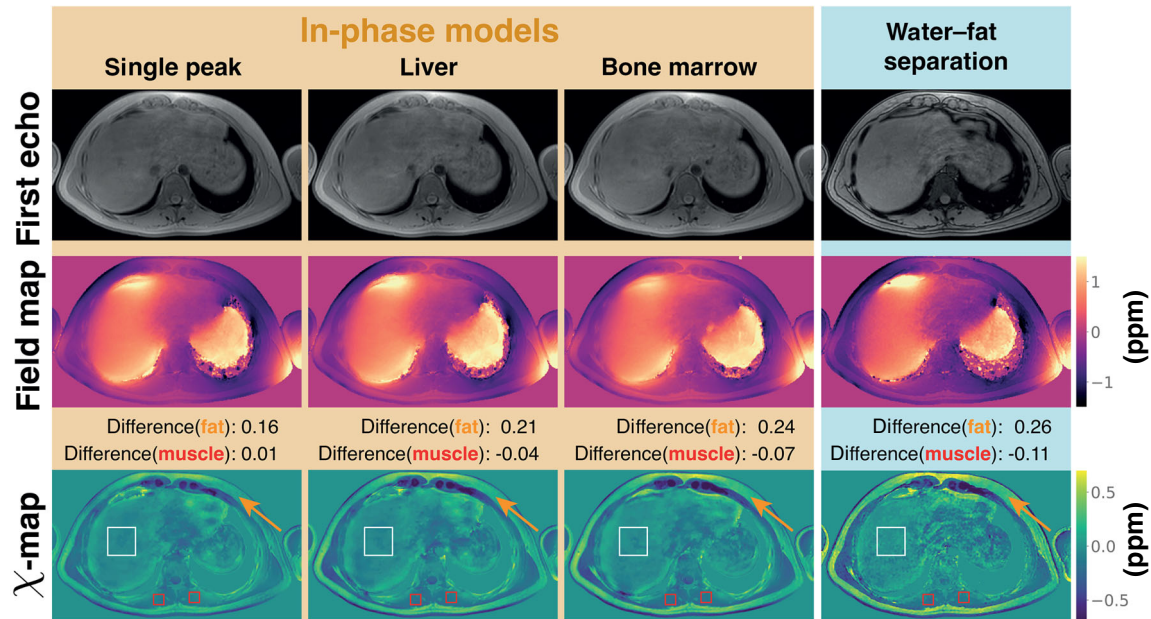
FIGURE 5 First echo (first row), field-mapping (second row) and susceptibility-mapping (last row) results in the liver scan of a volunteer. The in-phase models (yellow background) refer to an acquisition based on the respective echo times specific to the model. The field map quantification bias correlates (i) with the fat fraction and (ii) with the employed estimation method. For comparison of the different susceptibility estimation methods, the difference between the subcutaneous fat layer (orange arrow) and an region-of-interest in the liver (white box) was measured and is given above the susceptibility maps. The susceptibility maps based on single-peak and on *effective* in-phase echoes based on the liver model show a significant underestimation of the difference when compared to water–fat separation-based susceptibility estimation. Susceptibility mapping based on *effective* in-phase echoes based on the bone marrow modal only show a small deviation water–fat separation-based result.

Using single-peak in-phase echoes results in a significant underestimation of susceptibility and an increase in variability (Figure 8). *effective* in-phase echoes based on the liver fat model shows a moderate underestimation of susceptibility values. Mean, SD, and ROI size for each subject, anatomy and ROI can be found in Table S1.

4 | DISCUSSION

The present study aimed to enable the field map estimation and subsequent susceptibility mapping in water–fat regions without the need of the often computational intensive water–fat separation. First, the concept of *effective* multipeak in-phase echo times was introduced which generalizes single fat peak in-phase echo times to the more physiological meaningful multipeak fat models. Specifically, for a in vivo liver, a in vivo bone marrow and a ex vivo peanut oil multipeak fat spectral model the *effective* multipeak in-phase echo times were defined as the time points, where the sum of the individual fat phasors is zero. These time points have the same *effect* in the multipeak water–fat signal model as in-phase echoes in the single-peak model, meaning the nulling of fat phase contributions by echo time selection. The study then quantified the field map

estimation error for single-peak in-phase echoes and multipeak *effective* in-phase echoes for the above in vivo multipeak fat models at different fat fractions. Next, the study estimated how field map quantification bias translates into susceptibility map based on a forward simulation at an infinite surface and a sphere. The different echo times were then tested in a numerical simulation of the liver and in vivo measurements in the liver, spine, and breast. In the simulation, multipeak *effective* in-phase echo times based on the bone marrow model was able to achieve a significantly reduced NRMSE when compared to conventional single-peak-based in-phase echo times. In a phantom scan, QSM based on *effective* in-phase echoes yielded the same results as water–fat separation-based estimation while single-peak in-phase echo estimation showed a underestimation of susceptibility of the oil vial and strong streaking artifacts. In vivo, multipeak *effective* in-phase echo times showed comparable results to water–fat separation-based field- and susceptibility-mapping and was able to especially alleviate the quantification bias of the single-peak in-phase echoes-based estimation in regions with high fat fraction such as the subcutaneous fat layer or fatty breast tissue. Furthermore, the study showed that the bone marrow fat model yields improved susceptibility mapping results in the liver when compared to the use of a fat
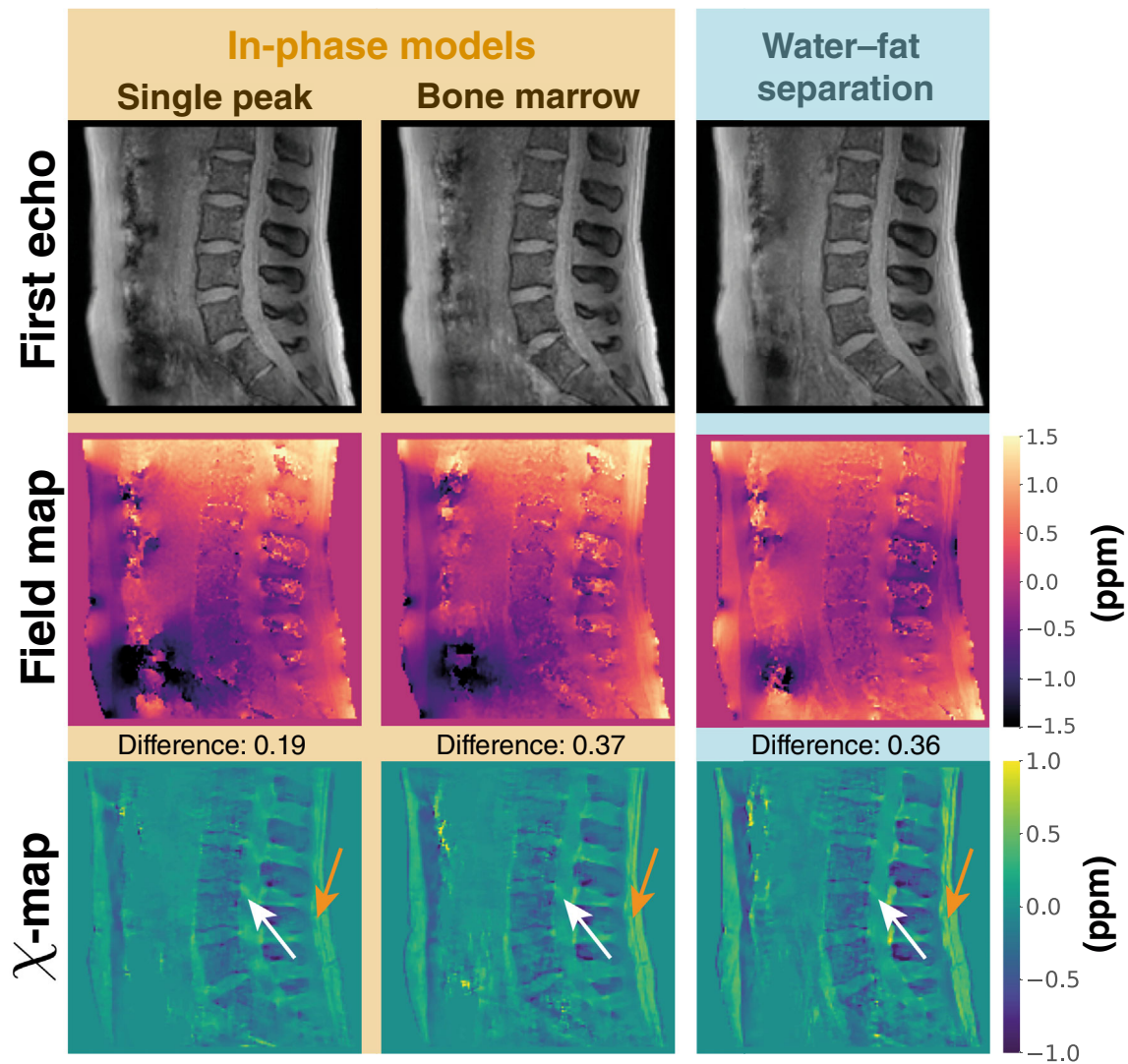
FIGURE 6 First echo (first row), field-mapping (second row) and susceptibility-mapping (last row) results in the scan of the lumbar spine in a volunteer. The in-phase models (yellow background) refer to an acquisition based on the respective echo times specific to the model. For comparison of the different susceptibility estimation methods, the difference between the posterior subcutaneous fat layer (orange arrow) and the cerebrospinal fluid (CSF, white arrow) was measured and is displayed above the susceptibility maps. The susceptibility map based on single-peak in-phase echoes shows a significant underestimation in the subcutaneous fat layer and strong streaking artifacts in the CSF when compared to both *effective* multipeak in phase echo times and water–fat separation-based susceptibility-mapping. The susceptibility map based on the water–fat separation shows the highest signal-to-noise ratio due to the acquisition of twice as many echo time points compared to in-phase acquisition. The differences measurement between the CSF and subcutaneous fat yield 0.38 ppm for the single-peak in-phase estimation, 0.61 ppm for the *effective* multipeak in-phase echoes and 0.68 ppm for water–fat separation-based estimation.

model specific to the liver fat composition. The use of (*effective*) in-phase echoes can be advantageous for several reasons including (a) the simplified signal model, (b) reduced scan time, and (c) the selection of larger echo time steps compared to water–fat separation-based sequences.

First, the simplified signal model allows for the robust estimation of the field map parameter by using least squares techniques followed by an unwrapping step that are both generally computationally inexpensive when compared to water–fat separation-based techniques

such as IDEAL[36] or generalized IDEAL-like methods,[37] which iteratively alternate between linear and nonlinear terms, or graph-cut-based methods[11,18,19,38] that are known to yield a high accuracy in field map quantification at the cost of long-run times of several minutes up to hours.[11] Although the presently employed field-mapping technique for the in-phase echoes is based on a graph-cut algorithm introduced in Reference 11, the reduction of computational cost within the graph-cut method is significant in the case of a convex cost function within one period. The underlying graph-cut algorithm
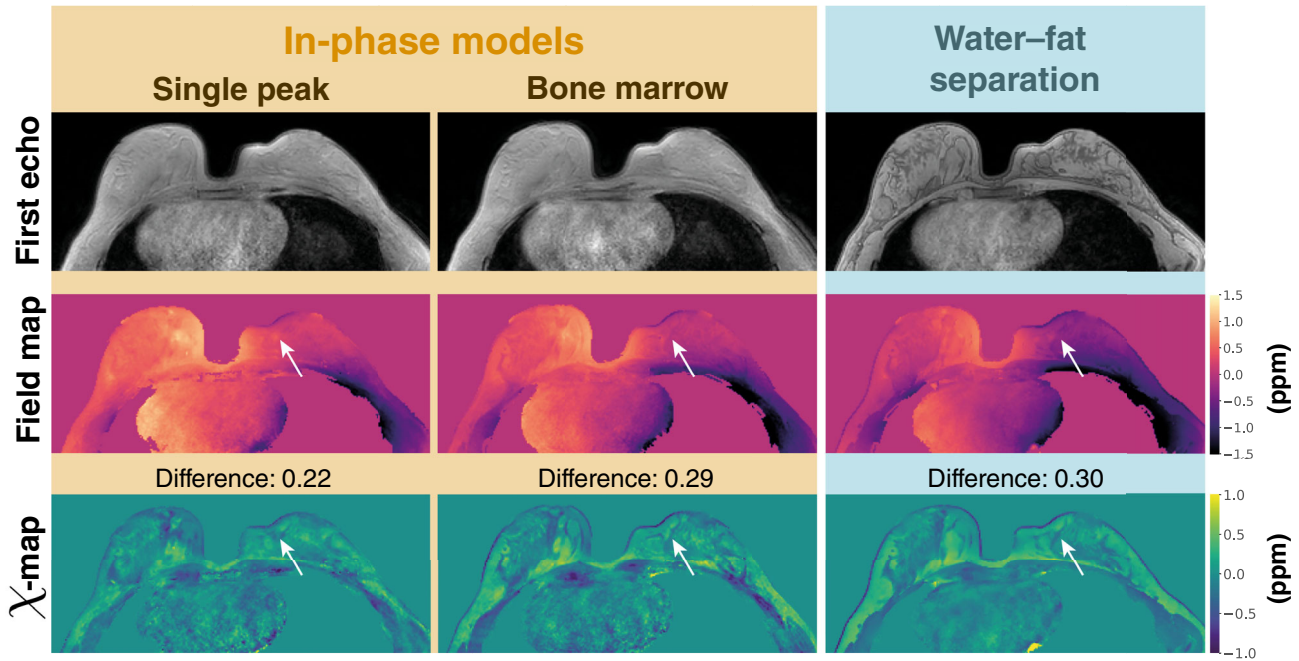
FIGURE 7 First echo (first row), field-mapping (second row) and susceptibility-mapping (last row) results in the scan of the breast in a volunteer. The in-phase models (yellow background) refer to an acquisition based on the respective echo times specific to the model. For comparison of the different susceptibility estimation methods, in the righ breast (white arrow) the difference between fatty and nonfatty breast tissue was measured and is given above the susceptibility maps. The susceptibility map based on in-phase echoes (first column) shows a underestimation of the fatty breast tissue when compared to the water–fat separation-based susceptibility estimation (third column). The results based on *effective* multipeak in-phase echo times (second column) shows a similar difference to the water–fat separation based. However, the bone marrow in-phase susceptibility map shows strong residual susceptibility variations especially between the breast and close to the lungs originating from an improper removal of the background field. Additionally, an increase in noise can be observed in the in-phase-based susceptibility maps.

(boykov-kolmogorov) has a worst case complexity of $\mathcal{O}(n^2m|C|)$, where n are the number of nodes, m the number of edges and C the cost of the minimum cut.[39] The number of nodes n scales with the complexity of the signal model and unwrapping range needed while m also scales quadratically with the number of nodes n.[11,40] The achieved estimation times per in-phase field map in the present work was below 10 s for all cases, while water–fat separation-based field-mapping in a similar breast scan can take up to 1 h using the same graph-cut method.[13]

Second, although the selection of echo times for water–fat separation seems more flexible when compared to single-peak or *effective* multipeak in-phase echo times, this is generally not true. Echo times for water–fat separation have to be carefully selected and are itself subject to optimization. For example, the first echo time and the echo time step has to be chosen for robust species separation and high SNR,[13] and are both of the order of 1 ms at 3T. To achieve a reasonable resolution while acquiring the above echo times and using monopolar gradients, sequences such as a time-interleaved multi-echo gradient echo sequence[14] are necessary, which was presently

adopted. However, the above sequence comes at the cost of increased scan time. When two shots are employed only half of the echo times are recorded per TR hence approximately doubling the scan time. In order to achieve a reasonable total scan time the maximum echo time is reduced to reduce the TR. However, a late maximum echo time can be desirable in the realm of susceptibility mapping due to the increased susceptibility weighting of the later echoes.

Finally, susceptibility mapping is well known to only estimate relative susceptibility maps, since the dipole kernel is zero at the center of k − space. Therefore, a reference strategy is needed to compare different dipole inversion method within one subject, and, more importantly, to allow for cross-subject comparison. In the liver, the subcutaneous fat and the paraspinal muscle were used for referencing since they are both known to not accumulate iron, which is important for the assessment of iron accumulation in the liver.[8] Referencing was also employed for the numerical liver simulation for the comparison of the different methods and was based on the subcutaneous fat. In the spine, the difference between the posterior subcutaneous fat and the CSF was measured and in the breast
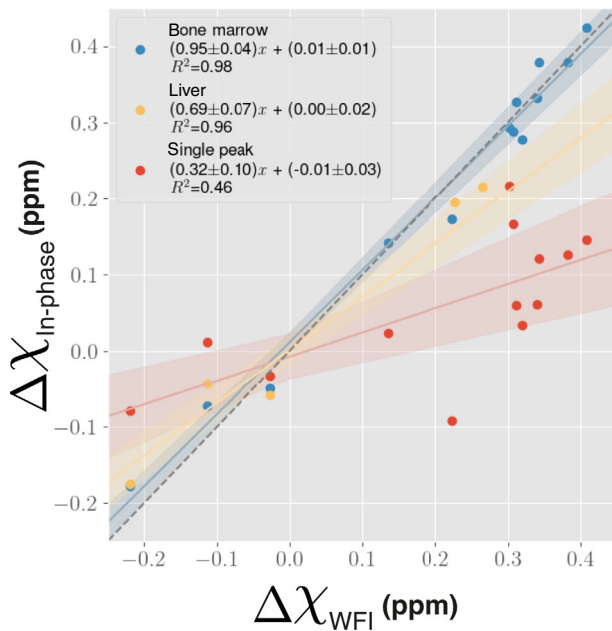
FIGURE 8 Correlation between reference water–fat separation-based susceptibility difference measurements and difference measurements based on (*effective*) in-phase acqusitions of all volunteer scans. The correlation based on single-peak in-phase echoes shows a significant underestimation of susceptibility and strong variability. Effective *in-phase* echoes based on the liver model shows a better correlation with the reference while *effective* in-phase echoes based on the bone marrow model is almost identical with the reference with the smallest variability.

the difference between fatty breast tissue and fibrograndular tissue was measured. In the spine, only the posterior subcutaneous fat was chosen since the anterior part of the body is affected by motion due to the free breathing nature of the acquisition protocol. In the brain, the CSF is often used as a reference and is assumed to have a susceptibility of zero.[34] Therefore the difference between subcutaneous fat and CSF in the spine region should be constant for different methods and even between subjects. When using *effective* multipeak in-phase echo times based on the bone marrow model, the measured susceptibility difference in all three anatomies is similar to the water–fat separation-based difference. The water–fat separation-based susceptibility maps can serve as a reference measurement for the removal of phase contributions of fat in the field map, since water–fat separation-based field maps are not prone to erroneous fat phase contributions. Particularly noteworthy is that field- and susceptibility mapping in the numerical simulation based on the bone marrow model achieved lower NRMSE in both multipeak *effective* in-phase echoes acquisition and water–fat separation when compared to the liver model. The same can be observed in the in vivo liver, where the difference measurements based on the liver fat model shows a larger deviation

in reference to water–fat separation than when based on the bone marrow model. In the case of referencing in the subcutaneous fat, this can be explained by the employed referencing strategy and the different fat fractions in the liver and subcutaneous fat. The subcutaneous fat has a fat fraction of above 80% and is significantly higher than for fatty livers which can have up to 40%. In the cross-model field map quantification bias simulation with fat fraction shown in Figure 2 it was shown that the error correlates quadratically with the fat fraction. Therefore, when the relative susceptibility between subcutaneous fat and liver is tried to be measured, the error is smaller when the error in the subcutaneous fat is minimized. In the case of referencing the liver to the paraspinal muscle the improved results based on the bone marrow model may originate from the reduction of the total field map estimation error. The paraspinal muscle is close to subcutaneous fat and field map estimation error in the fat potentially propagates nonlocally into the susceptibility map.

The use of *effective* multipeak in-phase echoes still has one apparent limitation. The presently adopted liver and bone marrow signal model used for the definition of the respective *effective* multipeak in phase echoes only represent a fraction of fatty tissue compositions. In fact, most of the different adipose tissue types show a different fat composition including abdominal superficial subcutaneous adipose tissue, deep subcutaneous adipose tissue, visceral adipose tissue and the aforementioned bone marrow and liver fat compositions.[24] For all the above fat models different *effective* multipeak in-phase echo times can be defined. However, based on the tissue of interest and the employed referencing strategy, one set of *effective* multipeak in-phase echo times has to be selected. However, only the liver spectral fat model shows a significantly different composition when compared to all other fat models. In this work it was shown that field- and susceptibility-mapping based on *effective* multipeak in-phase echoes derived from the bone marrow fat model show less quantification bias then in-phase echoes based on the liver fat model. This is also true, when the liver is the tissue of interest and, more importantly, the referencing strategy is based in nonfatty regions such as the paraspinal muscle. Arguably, the in-phase echoes based on the bone marrow fat model might be the best choice for all fat-containing anatomies.

5 | CONCLUSION

The use of of *effective* multipeak in-phase echo times was proposed for QSM in water–fat regions. The proposed in-phase echoes successfully remove the field map quantification bias of single-peak based in-phase echoes and show similar results to water–fat separation based field-

and susceptibility-mapping. The use of *effective* multipeak in-phase echoes allows for a rapid field map estimation due to the simplified signal model and can reduce the scan time compared to a time interleaved multi-echo gradient echo sequence.

CONFLICT OF INTEREST
Jakob Meineke is employee of Philips Research, Kilian Weiss is employee of Philips GmbH Market DACH, Dimitrios Karampinos receives grant support from Philips Healthcare.

ORCID
Christof Boehm https://orcid.org/0000-0003-1321-5804
Jakob Meineke https://orcid.org/0000-0001-8663-1468

TWITTER
Christof Boehm @BoehmChristof

REFERENCES
1. Wang Y, Liu T. Quantitative susceptibility mapping (QSM): decoding MRI data for a tissue magnetic biomarker. *Magn Reson Med*. 2014;73:82-101. doi:10.1002/mrm.25358
2. Boehm C, Sollmann N, Meineke J, et al. Preconditioned water-fat total field inversion: application to spine quantitative susceptibility mapping. *Magn Reson Med*. 2022;87:417-430. 10.1002/mrm.28903
3. Schweser F, Hermann KH, Deistung A, et al. Quantitative magnetic susceptibility mapping (QSM) in breast disease reveals additional information for mr-based characterization of carcinoma & calcification. Proceedings 19 Annual Meeting International Society for Magnetic Resonance in Medicine, Montreal; 2011:1014.
4. Dimov AV, Liu Z, Spincemaille P, Prince MR, Du J, Wang Y. Bone quantitative susceptibility mapping using a chemical species-specific R2* signal model with ultrashort and conventional echo data. *Magn Reson Med*. 2017;79:121-128. doi:10.1002/mrm.26648
5. Diefenbach MN, Meineke J, Ruschke S, Baum T, Gersing A, Karampinos DC. On the sensitivity of quantitative susceptibility mapping for measuring trabecular bone density. *Magnet Reson Med*. 2018;81:1739-1754. doi:10.1002/mrm.27531

6. Chen Y, Guo Y, Zhang X, Mei Y, Feng Y, Zhang X. Bone susceptibility mapping with MRI is an alternative and reliable biomarker of osteoporosis in postmenopausal women. *Eur Radiol*. 2018;28:5027-5034. doi:10.1007/s00330-018-5419-x
7. Guo Y, Chen Y, Zhang X, et al. Magnetic susceptibility and fat content in the lumbar spine of postmenopausal women with varying bone mineral density. *J Magn Reson Imaging*. 2018;49:1020-1028. doi:10.1002/jmri.26279
8. Sharma SD, Hernando D, Horng DE, Reeder SB. Quantitative susceptibility mapping in the abdomen as an imaging biomarker of hepatic iron overload. *Magn Reson Med*. 2014;74:673-683. doi:10.1002/mrm.25448
9. Lin H, Wei H, He N, et al. Quantitative susceptibility mapping in combination with water–fat separation for simultaneous liver iron and fat fraction quantification. *Eur Radiol*. 2018;28:3494-3504. doi:10.1007/s00330-017-5263-4
10. Jafari R, Sheth S, Spincemaille P, et al. Rapid automated liver quantitative susceptibility mapping. *J Magn Reson Imaging*. 2019;50:725-732. doi:10.1002/jmri.26632
11. Boehm C, Diefenbach MN, Makowski MR, Karampinos DC. Improved body quantitative susceptibility mapping by using a variable-layer single-min-cut graph-cut for field-mapping. *Magn Reson Med*. 2020;85:1697-1712. doi:10.1002/mrm.28515
12. Pineda AR, Reeder SB, Wen Z, Pelc NJ. Cramér-rao bounds for three-point decomposition of water and fat. *Magn Reson Med*. 2005;54:625-635. doi:10.1002/mrm.20623
13. Stelter JK, Boehm C, Ruschke S, et al. Hierarchical multi-resolution graph-cuts for water-fat-silicone separation in breast MRI. *IEEE Trans Med Imaging*. 2022;41:1. doi:10.1109/TMI.2022.3180302
14. Ruschke S, Eggers H, Kooijman H, et al. Correction of phase errors in quantitative water–Fat imaging using a monopolar time-interleaved multi-echo gradient echo sequence. *Magn Reson Med*. 2016;78:984-996. doi:10.1002/mrm.26485
15. Hernando D, Haldar JP, Sutton BP, Ma J, Kellman P, Liang ZP. Joint estimation of water/fat images and field inhomogeneity map. *Magn Reson Med*. 2008;59:571-580. doi:10.1002/mrm.21522
16. Lu W, Hargreaves BA. Multiresolution field map estimation using golden section search for water–fat separation. *Magn Reson Med*. 2008;60:236-244. doi:10.1002/mrm.21544
17. Yu H, Reeder SB, Shimakawa A, Brittain JH, Pelc NJ. Field map estimation with a region growing scheme for iterative 3-point water–Fat decomposition. *Magn Reson Med*. 2005;54:1032-1039. doi:10.1002/mrm.20654
18. Cui C, Shah A, Wu X, Jacob M. A rapid 3D fat-water decomposition method using globally optimal surface estimation (R-GOOSE). *Magn Reson Med*. 2017;79:2401-2407. doi:10.1002/mrm.26843
19. Cui C, Wu X, Newell JD, Jacob M. Fat water decomposition using globally optimal surface estimation (goose) algorithm. *Magn Reson Med*. 2014;73:1289-1299. doi:10.1002/mrm.25193
20. Hernando D, Kühn JP, Mensel B, et al. R2* estimation using "in-phase" echoes in the presence of fat: the effects of complex spectrum of fat. *J Magn Reson Imaging*. 2012;37:717-726. doi:10.1002/jmri.23851
21. Boehm C, Diefenbach MN, Kronthaler S, Meineke J, Weiss K, Makowski MR, Karampinos DC. Quantitative susceptibility mapping in water-fat regions using in-phase echoes introduces

significant quantification bias. Proceedings of the Annual Meeting International Society for Magnetic Resonance in Medicine; 2021:3972.

22. Yu H, Shimakawa A, McKenzie CA, Brodsky E, Brittain JH, Reeder SB. Multiecho water–Fat separation and simultaneous r2* estimation with multifrequency fat spectrum modeling. *Magn Reson Med*. 2008;60:1122-1134. doi:10.1002/mrm.21737

23. Guo Y, Liu Z, Wen Y, et al. Quantitative susceptibility mapping of the spine using in-phase echoes to initialize inhomogeneous field and R2* for the nonconvex optimization problem of fat-water separation. *NMR Biomed*. 2019;32:e4156. doi:10.1002/nbm.4156

24. Hamilton G, Schlein AN, Middleton MS, et al. In vivo triglyceride composition of abdominal adipose tissue measured by 1 H Mrs At 3T. *J Magn Reson Imaging*. 2016;45:1455-1463. doi:10.1002/jmri.25453

25. Ren J, Dimitrov I, Sherry AD, Malloy CR. Composition of adipose tissue and marrow fat in humans By1h Nmr At 7 tesla. *J Lipid Res*. 2008;49:2055-2062. doi:10.1194/jlr.d800010‐jlr200

26. Hamilton G, Yokoo T, Bydder M, et al. In vivo characterization of the liver fat 1h Mr spectrum. *NMR Biomed*. 2010;24:784-790. doi:10.1002/nbm.1622

27. Gosselin MC, Neufeld E, Moser H, et al. Development of a new generation of high-resolution anatomical models for medical device evaluation: the virtual population 3.0. *Phys Med Biol*. 2014;59:5287-5303. doi:10.1088/0031-9155/59/18/5287

28. Collins CM, Yang B, Yang QX, Smith MB. Numerical calculations of the static magnetic field in three-dimensional multi-tissue models of the human head. *Magn Reson Imaging*. 2002;20:413-424. doi:10.1016/s0730-725x(02)00507-6

29. Maril N, Collins CM, Greenman RL, Lenkinski RE. Strategies for shimming the breast. *Magn Reson Med*. 2005;54:1139-1145. doi:10.1002/mrm.20679

30. Liu Z, Kee Y, Zhou D, Wang Y, Spincemaille P. Preconditioned total field inversion (TFI) method for quantitative susceptibility mapping. *Magn Reson Med*. 2016;78:303-315. doi:10.1002/mrm.26331

31. Bydder M, Girard O, Hamilton G. Mapping the double bonds in triglycerides. *Magn Reson Imaging*. 2011;29:1041-1046.

32. Muller N, Reiter RC. Temperature dependence of chemical shifts of protons in hydrogen bonds. *J Chem Phys*. 1965;42:3265-3269. doi:10.1063/1.1696408

33. Dong J, Liu T, Chen F, et al. Simultaneous phase unwrapping and removal of chemical shift (SPURS) using graph cuts: application in quantitative susceptibility mapping. *IEEE Trans Med Imaging*. 2015;34:531-540. doi:10.1109/tmi.2014.2361764

34. Liu Z, Spincemaille P, Yao Y, Zhang Y, Wang Y. Medi+0: morphology enabled dipole inversion with automatic uniform cerebrospinal fluid zero reference for quantitative susceptibility mapping. *Magn Reson Med*. 2017;79:2795-2803. doi:10.1002/mrm.26946

35. Somasundaram A, Wu M, Borde T. Automated breast segmentation using deep-learning in water-fat breast MRI: application to breast density assessment. Proceedings of the 30th International Society for Magnetic Resonance in Medicine, London, UK; 2022:1683.

36. Tsao J, Jiang Y. Hierarchical ideal: fast, robust, and multiresolution separation of multiple chemical species from multiple echo times. *Magn Reson Med*. 2012;70:155-159. doi:10.1002/mrm.24441

37. Diefenbach MN, Liu C, Karampinos DC. Generalized parameter estimation in multi-echo gradient-echo-based chemical species separation. *Quant Imaging Med Surg*. 2020;10:554-567. doi:10.21037/qims.2020.02.07

38. Hernando D, Kellman P, Haldar JP, Liang ZP. Robust water/fat separation in the presence of large field inhomogeneities using a graph cut algorithm. *Magn Reson Med* 2009; 22177; 63:doi:10.1002/mrm.22177

39. Boykov Y, Kolmogorov V. An experimental comparison of min-cut/max- flow algorithms for energy minimization in vision. *IEEE Trans Pattern Anal Mach Intell*. 2004;26:1124-1137. doi:10.1109/tpami.2004.60

40. Shah A, Abámoff MD, Wu X. Optimal surface segmentation with convex priors in irregularly sampled space. *Med Image Anal*. 2019;54:63-75.

SUPPORTING INFORMATION

Additional supporting information may be found in the online version of the article at the publisher's website.

Figure S1. Correlation between susceptibility and field map based on a forward simulation at a sphere and an infinite surface. The correlation for a spherical surface and an infinite surface is -0.304 and -0.332 when the surface is parallel to B_0 and 0.608 and 0.664 when the surface is perpendicular to B_0, respectively. Based on the results in Figure 2, the field map quantification bias in a voxel with a fat fraction of 100% measured with single-peak in phase echo translates into a susceptibility estimation error of $\frac{-0.1\text{ppm}}{-0.304} = 0.33$ ppm in the liver and $\frac{-0.13\text{ppm}}{-0.304} = 0.43$ ppm in bone marrow, respectively.

Table S1: Mean susceptibility, standard deviation and size of all ROIs for all scans. In brackets the region of the ROI is given (fat, muscle, fibroglandular, etc.). The subscripted text refers to the estimation method, hence $\overline{\chi}(\text{fibroglandular})_{\text{WFI}}$ refers to the mean susceptibility and standard deviation of fibroglandular tissue based on waterŰfat separation field map estimation.

3.6 Journal Publication V:
Robust quantitative susceptibility mapping in the breast in the presence of silicone

The publication entitled *Robust quantitative susceptibility mapping in the breast in the presence of silicone* was published in Magnetic Resonance in Medicine (ISSN: 0740-3194). The manuscript was authored by Christof Boehm, Jonathan K. Stelter, Jakob Meineke, Kilian Weiss, Zimmer, Alexander Komenda, Tabea Borde, Marcus R. Makowski, Eva M. Fallenberg, and Dimitrios C. Karampinos. It is available online (DOI: 10.1002/mrm.29694) as an open access article under the terms of the Creative Commons Attribution-NonCommercial License. Preliminary results were also presented in the conference contribution C29. A summary of the publication is provided in Section 3.6.1, the author contributions are listed in Section 3.6.2 and the full text is included subsequently on the following pages.

3.6.1 Abstract

Purpose

Breast microcalcifications (MCs) constitute a marker of malignant early stage breast tumors. X-ray based mammography is routinely used due to the excellent contrast of calcified structures. However, an MR based screening method is desirable for target sub-cohorts at high risk or young patients to reduce radiation dose. QSM is an established MR technology to visualize and quantify calcified structures. After skin sparing mastectomy, the residual breast tissue is routinely monitored for recurrent cancer. Therefore, an MR-based methodology needs to address the presence of silicone with its chemical shift and strong susceptibility. Hence, this work proposes a QSM methodology specifically tailored for breast applications in the presence of silicone breast implants.

Methods

A recently proposed graph-cut algorithm is employed to obtain water-, fat-, and silicone-separated images from multi-echo gradient-echo images. From these separated images, a silicone fraction map is derived. Utilizing the silicone fraction map, a silicone implant mask is generated. An additional term, based on the silicone implant mask, is introduced in the dipole inversion to enforce homogeneous susceptibility within

regions of silicone. This approach is combined with a data consistency term that directly estimates susceptibility from complex multi-echo images. The proposed method was applied to a numerical breast simulation and in vivo for five patient scans. The method was compared to previously proposed QSM approaches that do not explicitly or implicitly account for the presence of silicone.

Results

In the simulation, the proposed method successfully reduces the normalized root mean squared error by 62% compared to previously proposed QSM methods. Both the simulation and in vivo maps exhibit reduced artifacts in the residual breast tissue adjacent to silicone implants when employing the proposed methodology.

Conclusion

In contrast to previously proposed QSM methods, the proposed method accounts for the strong susceptibility and the chemical shift of silicone and consequently allows for the visualization of local susceptibility values in proximity to silicone breast implants.

3.6.2 Author contributions

The first author developed the problem-specific inverse problem formulation; implemented the optimization code in Python; performed the numerical simulation; enrolled the patients and acquired the patient data with help of the coauthors; analyzed and interpreted the data, and wrote the manuscript.

3.6.3 Original Article

Magnetic Resonance in Medicine

Robust breast quantitative susceptibility mapping in the presence of silicone

Christof Böhm[1] | **Jonathan K. Stelter[1]** | **Kilian Weiss[2]** | **Jakob Meineke[3]** |
Alexander Komenda[1] | **Tabea Borde[1]** | **Marcus R. Makowski[1]** |
Eva M. Fallenberg[1] | **Dimitrios C. Karampinos[1]**

[1]Department of Diagnostic and Interventional Radiology, School of Medicine, Klinikum rechts der Isar, Technical University of Munich, Munich, Germany

[2]Philips GmbH Market DACH, Hamburg, Germany

[3]Philips Research, Hamburg, Germany

Correspondence
Christof Boehm, Department of Diagnostic and Interventional Radiology, Klinikum rechts der Isar, Ismaninger Str 22, 81675 Munich, Germany.
Email: christof.boehm@tum.de

Purpose: To (a) develop a preconditioned water–fat–silicone total field inversion (wfsTFI) algorithm that directly estimates the susceptibility map from complex multi-echo data in the breast in the presence of silicone and to (b) evaluate the performance of wfsTFI for breast quantitative susceptibility mapping (QSM) in silico and in vivo in comparison with formerly proposed methods.

Methods: Numerical simulations and in vivo multi-echo gradient echo breast measurements were performed to compare wfsTFI to a previously proposed field map-based linear total field inversion algorithm (lTFI) with and without the consideration of the chemical shift of silicone in the field map estimation step. Specifically, a simulation based on an in vivo scan and data from five patients were included in the analysis.

Results: In the simulation, wfsTFI is able to significantly decrease the normalized root mean square error from lTFI without (4.46) and with (1.77) the consideration of the chemical shift of silicone to 0.68. Both the in silico and in vivo wfsTFI susceptibility maps show reduced shadowing artifacts in local tissue adjacent to silicone, reduced streaking artifacts and no erroneous single voxels of diamagnetic susceptibility in proximity to silicone.

Conclusion: The proposed wfsTFI method can automatically distinguish between subjects with and without silicone. Furthermore wfsTFI accounts for the presence of silicone in the QSM dipole inversion and allows for the robust estimation of susceptibility in proximity to silicone breast implants and hence allows the visualization of structures that would otherwise be dominated by artifacts on susceptibility maps.

KEYWORDS
breast disease, cancer, chemical shift encoding, field map, QSM, quantitative susceptibility mapping, silicone, susceptibility

1 | INTRODUCTION

Breast cancer is the most common malignancy in women worldwide.[1] To provide an adequate and successful treatment, early detection and correct size estimation is necessary.[2] Breast calcifications are common and mostly benign, but certain distributions of especially microcalcifications constitute a marker of malignancy.[3] Microcalcifications detected by mammographic screening account for the detection of 30%–50% of nonpalpable breast tumors.[4] X-ray-based mammography examinations are routinely used for screening and provide excellent contrast of calcified structures but is limited in detecting masses in dense breasts.[5,6] However, this technique is not ideal for imaging young patients, particularly women with a genetic predisposition to breast cancer, who may require screening as early as the age of 25–30 years[7-9] as these young patients are more sensitive to radiation.[10] Nevertheless, a portion of these patients are presenting with microcalcifications as the only sign of malignancy. Another patient population for whom mammography is limited is those with silicone implants. Due to the two-dimensional nature of mammography, silicon can obscure significant portions of breast tissue, masking masses or calcifications. As a result, implants are better imaged using MRI or ultrasound.[11,12] Therefore, the use of an MR-based technique to detect calcified structures would be desirable especially for young patients receiving repeated examinations.[13] Existing clinical breast MRI examinations cannot detect and characterize breast calcifications due to the invisibility of calcified structures caused by their short T2 components. Quantitative susceptibility mapping (QSM)[14,15] is a common methodology to assess calcified structures and has been used to depict brain calcifications[16-18] and prostatic calcifications,[19,20] to quantify calcium changes in the fetal spine,[21] to measure bone density[22-25] and to categorize osteoblastic bone metastases which are characterized by the formation of new bone structures.[26] QSM is able to overcome the limitations of routine MRI protocols in measuring the susceptibility of short T2 components due to the long range effect of susceptibility-induced phase changes into MR visible tissues around the MR invisible structure. Some early works have reported on the ability to detect breast calcifications with QSM.[27-29] However, QSM in the breast remains challenging by the presence of multiple species such as water, fat, and potentially silicone. Specifically silicone has to be addressed due to its chemical shift and its strong susceptibility when compared to local breast tissue. If not accounted for, silicone induces strong susceptibility artifacts that dominate the local tissue around it.[30] In patients with a history of breast cancer and subsequent skin sparing mastectomy and reconstruction with implants, the regular check of the residual breast tissue around the implant for cancer formation and distributions of microcalcifications is of high clinical relevance.[31,32]

Total field inversion (TFI) algorithms[33] that directly estimate the susceptibility map from complex multi-echo data[26,34] have been particularly successful in removing background field effects and solving the ill-posed and ill-conditioned dipole inversion problem and yield susceptibility maps with reduced artifacts. However, all of them rely on an robust initialization based on the field map parameter. To obtain a bias free field map, an optimal experimental design (especially echo times) has to be performed and all parameters have to be separated. In the case of water–fat regions, optimal experimental design[35] and echo data-based TFI-based dipole inversion[26] have successfully been applied. However, the above methods do not account for the chemical shift of silicone in breasts with silicone implants. Therefore, a new method is required to estimate the susceptibility map from complex multi-echo gradient echo data in the breast where water, fat and silicone may be present. Recently, a graph-cut based field-mapping algorithm has been proposed for the robust and automatic water–fat–silicone separation with optimized echo time selection[36] that allows for the bias free field map estimation in the breast. The field-mapping algorithm in Reference 36 would result in an accurate estimation of the field map in the breast, which could subsequently used to generate an initial susceptibility map. The susceptibility map can be then refined by estimation the susceptibility map from the complex multi-echo data.

Therefore, the purpose of the present work is to (a) develop a preconditioned water–fat–silicone TFI (wfsTFI) method that directly estimates the susceptibility map from complex multi-echo gradient echo data in the breast, and to (b) demonstrate the advantages of the developed method in silico and in vivo.

2 | METHODS

The proposed wfsTFI algorithm consists of three main steps (Figure 1). First, the water-, fat- and silicone-separated images, field map, and R_2^*-map were estimated using a recently proposed hierarchical multiresolution graph-cut algorithm[36] employing a water–fat–silicone signal model accounting for a single R_2^* decay and employing a multipeak fat model specific to adipose tissue.[37] Second, an initial global susceptibility map was estimated using a linear preconditioned TFI algorithm (see below).[33] Finally, the susceptibility map was computed by estimating the susceptibility distribution directly from the complex multi-echo data by using a single-R_2^* multi-fat-peak water–fat–silicone signal
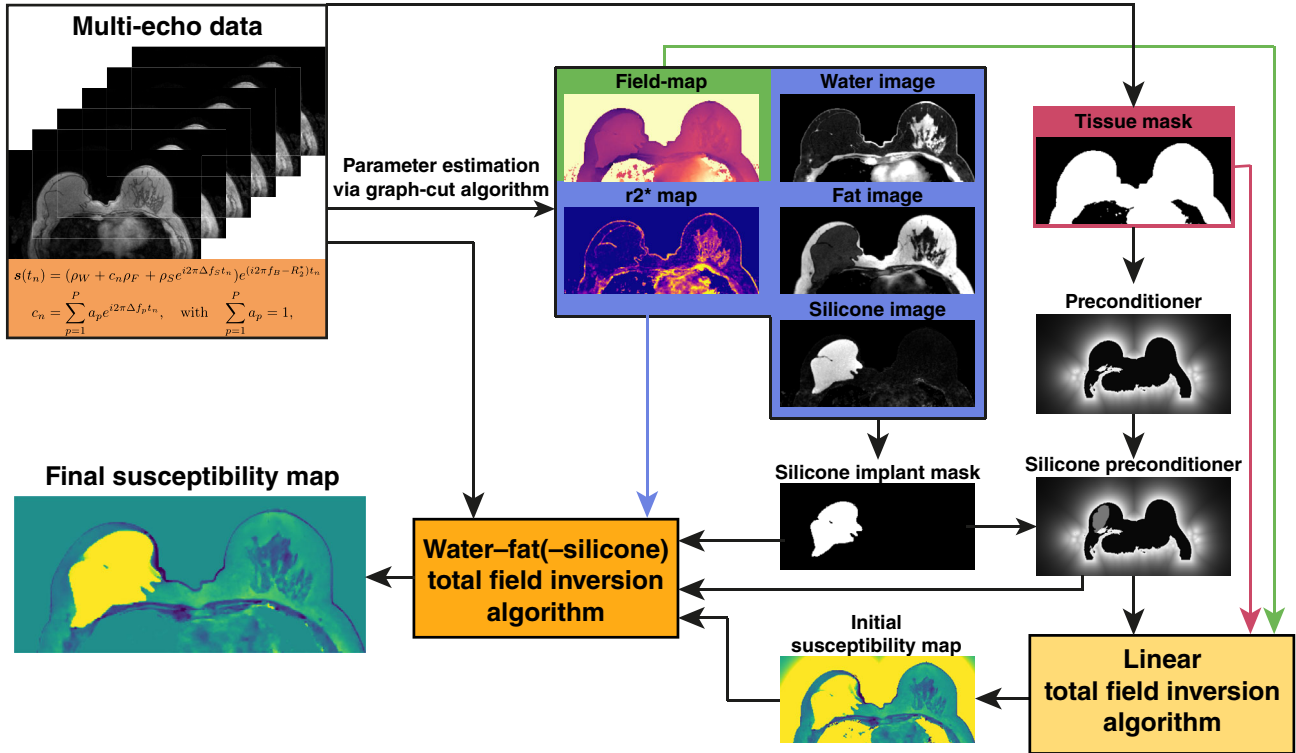
FIGURE 1 Pipeline of the proposed water–fat–silicone total field inversion (wfsTFI) algorithm. Water-, fat-, and silicone-separated images, field- and R_2^*-map are estimated using a graph-cut algorithm. Additionally a tissue mask is derived from the magnitude data and an initial preconditioner is calculated. When silicone is detected, a silicone implant mask is generated and added to the preconditioner. Based on the field map an initial susceptibility map is calculated. Next, the wfsTFI is initialized with the initial susceptibility map and the water-, fat-, silicone-separated images R_2^*-map and silicone implant mask are added as constant parameters. Finally, the susceptibility distribution is directly estimated from the complex multi-echo data.

model minimizing the following preconditioned TFI cost function:

$$
y = \arg\min_{y'} \sum_{j=1}^{N_{echo}} || \left(\rho_W + c_n\rho_F + \rho_s e^{i2\pi\Delta f_S t_j} \right)
$$
$$
\times e^{-R_2^* t_j} e^{i2\pi t_j d * Py'} - S_j||_2^2
$$
$$
+ \lambda_1||M_g \nabla Py'||_1 + \lambda_2||M_S P\left(y' - \overline{y'}^{M_S}\right)||_2^2,
$$
$$
c_n = \sum_{p=1}^{N_p} a_p e^{i2\pi\Delta f_p t_j}, \quad \text{with} \quad \sum_{p=1}^{N_p} a_p = 1, \tag{1}
$$

where ρ_W, ρ_F, and ρ_S are the complex signal of the water, fat, and silicone components, t_j are the echo times, Δf_S is the chemical shift of silicone, R_2^* is the transverse relaxation rate, d is the dipole kernel, P is the preconditioner, S_j are the echo time data, λ_1 is the regularization parameter and M_G is an edge mask,[38] λ_2 is the silicone regularization parameter, M_S is the silicone implant mask and $\overline{y'}^{M_S}$ is the mean susceptibility within the silicone implant mask M_S. The fat spectrum is assumed to have N_p spectral peaks with corresponding relative amplitudes a_p and chemical shift Δf_p. The final QSM map is computed as $\chi = Py$.

To generate the binary silicone implant mask M_S, the proton density silicone fraction map (determined as in Reference 36) was thresholded at 60%. The two largest continuous areas with a volumetric size larger than 10 cm^3 were assigned as silicone implants. Based on the above silicone implant mask, a scan can be automatically categorized to contain either (i) no, (ii) one, or (iii) two silicone implants. The silicone implant mask was subsequently included in the preconditioner, to account for the strong susceptibility of silicone of around 2 ppm with respect to tissue.

The preconditioner was automatically adapted to the region-of-interest following[26] for the background region and was set to 1 in the local tissue region. For the preconditioner and the initial linear TFI algorithm a binary mask M was calculated to distinguish between background and local regions (region-of-interest). The binary mask M was calculated based on the maximum intensity projection across echo times thresholded at 15% of its maximum value.

The regularization parameters λ_1 and λ_2 were based on a grid parameter sweep in a numerical breast simulation (see below) and were set to $\lambda_1 = 10$ and $\lambda_2 = 100$. The cost

function in Equation (1) was minimized using the iterative Gauss–Newton algorithm with a conjugate gradient solver at each step. In total, 25 Gauss-Newton steps were performed.

2.1 | Comparison methods

The proposed wfsTFI with silicone regularization was applied and compared to (a) linear TFI (lTFI) based on a field map estimation that does not account for the chemical shift of silicone,[39] (b) lTFI using the field map of the hierarchical multiresolution water–fat–silicone graph-cut algorithm,[36] and (c) wfsTFI without silicone regularization.[30]

The lTFI method minimizes the following cost function:

$$y = \arg\min_{y'} ||W(f_B - d * Py')||_2^2 + \lambda ||M_G \nabla Py'||_1, \quad (2)$$

where f_B is the field map parameter. The regularization parameter λ for the above lTFI cost-function was set to 1/2500 based on Reference 26. Since the field map parameter is in unitless ppm, the same regularization parameter can be applied across subjects and anatomies. Due to the nonlinearity of the regularization term, the above cost-function was again minimized with the above Gauss–Newton algorithm. The stopping criterion was a relative residual of <0.01. All processing was performed in Python 3.8 and CuPy 9.1.0[40] on a NVIDIA GeForce RTX 3060.

2.2 | Numerical breast simulation

To investigate the difference between the presently proposed wfsTFI with silicone regularization and the aforementioned comparison methods, a numerical simulation based on the water–fat–silicone separated images of an in vivo scan was performed. An artificial susceptibility map was generated from the fat fraction and the silicone fraction, where fatty voxels were weighted with a susceptibility of 0.8 ppm and silicone voxels with 2.0 ppm. Additionally, a single voxel in close proximity to the silicone breast implant and within residual breast tissue was assigned with a negative susceptibility of −2 ppm to mimic the appearance of a calcification. The χ-map was forward simulated to a field map f_B using the dipole kernel in k-space. The water–fat–silicone single-R_2^* signal model[36] was used to forward simulate the fat fraction f_f, R_2^*, field map and silicone image to complex multi-echo data:

$$s(t_n) = \left((1 - f_f) + c_n f_f + \rho_s e^{i2\pi\Delta f_S t_j}\right) e^{\gamma t_n}, \quad \gamma = i2\pi f_B - R_2^*$$

$$c_n = \sum_{p=1}^{P} a_p e^{i2\pi\Delta f_p t_n}, \quad \text{with} \quad \sum_{p=1}^{P} a_p = 1. \quad (3)$$

The echo times were based of the in vivo acquisition of the data (see below). A field strength of 3T and the a fat model specific to adipose tissue were used.[37] Independent Gaussian noise was added to the real and imaginary part of the echo data with a signal-to-noise ratio of 100. The signal-to-noise ratio was defined as the maximum signal amplitude of the first echo divided by the SD of the noise. A normalized root mean square error analysis with respect to the reference susceptibility maps was performed for all methods within the local tissue region (excluding the silicone implants).

2.3 | In vivo measurements

The processing of graph-cut-based field-mapping and water–fat(–silicone) separation followed by the proposed method and the above comparison methods was applied to IRB-approved in vivo scans of five patients with silicone implants (two unilateral, three bilateral). The scanning was performed on a 3 T scanner (Ingenia, Philips Healthcare, Release 5.6) using a monopolar time-interleaved multi-echo gradient echo sequence,[41] acquiring six echoes in two interleaves with 3 echoes per TR. For all subjects, the imaging parameters were set to $TE_{min} = 1.58$ ms, $\Delta TE = 1.28$ ms, orientation = axial, readout direction = anterior-posterior, FOV = $220 \times 382.6 \times 192.4 \text{mm}^3$, and an isotropic acquisition voxel size of 1.3 mm. The in vivo measurements were evaluated visually with regard to susceptibility artifacts originating from (i) erroneous field-mapping when silicone is not accounted for, (ii) the strong difference between local tissue susceptibility and silicone, and (iii) the ability to visualize calcifications in proximity to silicone breast implants.

3 | RESULTS

3.1 | Numerical breast simulation

A large field map error can be observed in the field map of the numerical breast simulation when the chemical shift of silicone is not accounted for (Figure 2, second row). The field-mapping error propagates into the susceptibility map where the silicone implants are falsely identified to be diamagnetic. Furthermore, the error propagates non-locally and strong artifacts can be observed in the surrounding breast tissue limiting the visualization of the calcification (white arrow). When the chemical shift of silicone is accounted for in the parameter separation, the estimated field map is comparable to the reference field map (third row). However, the susceptibility map still shows a significant underestimation of silicone susceptibility
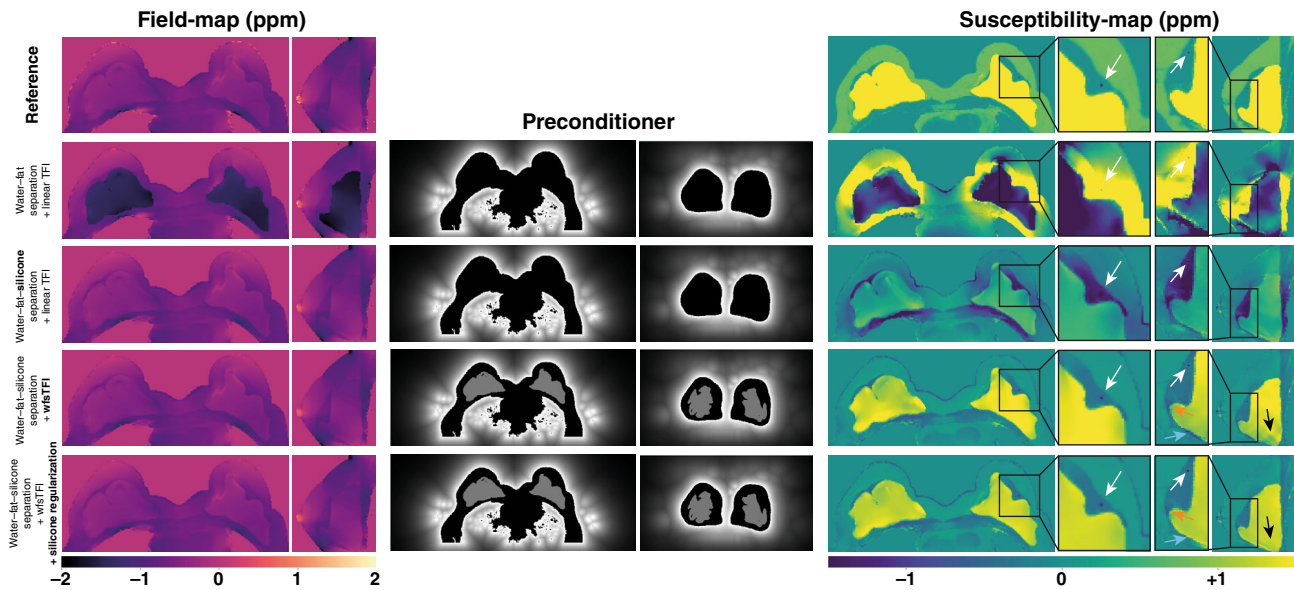
FIGURE 2 Field- and susceptibility mapping result in a numerical breast simulation with bilateral silicone implants and a calcification in the breast tissue of the left breast. When the chemical shift of silicone is not accounted for (second row), the field map within the silicone is significantly underestimated while the susceptibility map falsely estimates the implants to be diamagnetic. Most importantly, strong artifacts are present in the whole breast tissue making the visualization of the calcification impossible (white arrow). When the chemical shift of silicone is accounted for (third row), the field map is correctly estimated. However, there are strong diamagnetic artifacts around the silicone implant and the susceptibility of silicone is underestimated. Susceptibility mapping based on water–fat–silicone total field inversion (wfsTFI) without regularization (fourth row) is able to reveal the calcification in the local breast tissue. However, erroneous voxels of diamagnetic susceptibility values occur close to the silicone implant potentially limiting the visualization of calcifications in the region (blue and orange arrows). The proposed wfsTFI with silicone regularization (last row) alleviates the remaining artifacts and increases the homogeneity of the susceptibility distribution within the silicone (black arrow).

and artifacts in the adjacent breast tissue. While the artifacts are reduced, the calcification is dominated by artifacts and cannot be identified. Using wfsTFI without silicone regularization (fourth row) the silicone is correctly estimated to be strongly paramagnetic and the calcification has a good delineation from residual breast tissue. However, some diamagnetic artifacts remain in close proximity to the implant (orange and blue arrow) potentially limiting the visualization of calcifications in both regions. The proposed wfsTFI with silicone regularization (fifth row) is able to alleviate the remaining artifacts in the residual breast tissue and yields a more homogeneous susceptibility within the implant (black arrow). The results of the normalized root mean square error analysis yield values of 4.46 for water–fat separation and lTFI, 1.77 for water–fat–silicone separation and lTFI, 0.70 for water–fat–silicone separation and wfsTFI without silicone regularization, and 0.68 for the proposed wfsTFI with silicone regularization.

3.2 | In vivo measurements

Figure 3 shows field-mapping and susceptibility mapping results for the different methods in a patient with a silicone

implant and a significant amount of residual breast tissue in the left breast. When the chemical shift of silicone is not accounted for in the parameter separation (first row), strong artifacts can be observed in the susceptibility map dominating almost the whole breast tissue of interest while silicone is falsely estimated to be diamagnetic. When the chemical shift of silicone is accounted for in the parameter separation (second row), the artifacts in the susceptibility map are strongly reduced. However, the breast tissue closer to the implant is still significantly underestimated. When using the wfsTFI without silicone regularization (third row) most of the artifacts in the breast tissue are alleviated. However, single voxels with strong diamagnetic susceptibility (orange arrows), an paramagnetic increase close to the implant (blue arrow) and a strong streaking artifact can only be reduced using the presently proposed wfsTFI with silicone regularization. Furthermore, the homogeneity of the susceptibility is strongly increased when using the presently proposed wfsTFI with silicone regularization, while without the silicone regularization the implant shows diamagnetic values in some regions. The in vivo scan is thus in very good agreement with the simulation in Figure 2.

Figure 4 yields similar results in a patient with silicone implants in both breasts. In the left breast, a significant
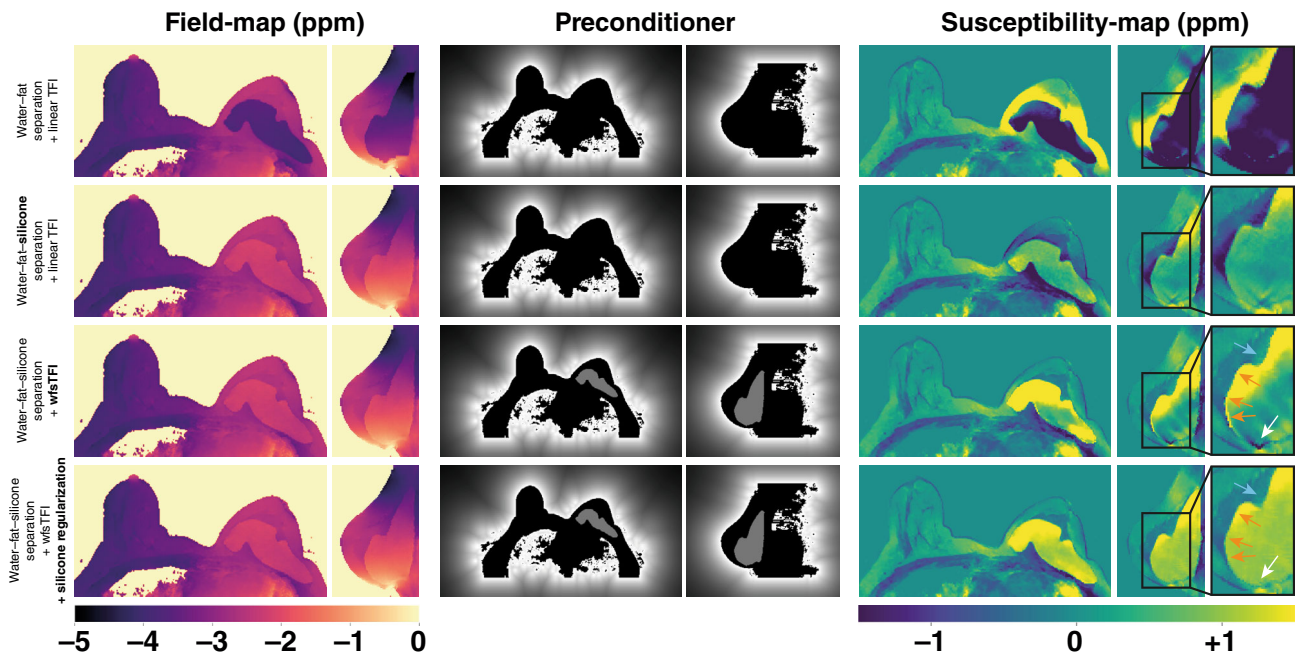
FIGURE 3 Field- and susceptibility mapping results in the scan of a patient with a history of breast cancer and subsequent mastectomy in the left breast. Both field- and susceptibility-map results agree very well with the simulation shown in Figure 2. When the chemical shift is not accounted for (first row), the field map of silicone is underestimated which propagates into the susceptibility map wherein silicone is falsely estimated to be diamagnetic and the susceptibility of the surrounding breast tissue is affected by strong artifacts. When silicone is accounted for in the parameter separation, the artifacts in the susceptibility map are reduced but are still to strong to allow for a robust detection of potential calcifications. Using water–fat–silicone total field inversion (wfsTFI) without silicone regularization (third row) yields almost artifact-free residual breast tissue susceptibility maps. However an shadowing-like paramagnetic increase (blue arrow), single voxels of strong diamagnetic susceptibility (orange arrow) and a streaking artifact at the bottom of the silicone implant can only be alleviated by using the proposed wfsTFI with silicone regularization (last row).
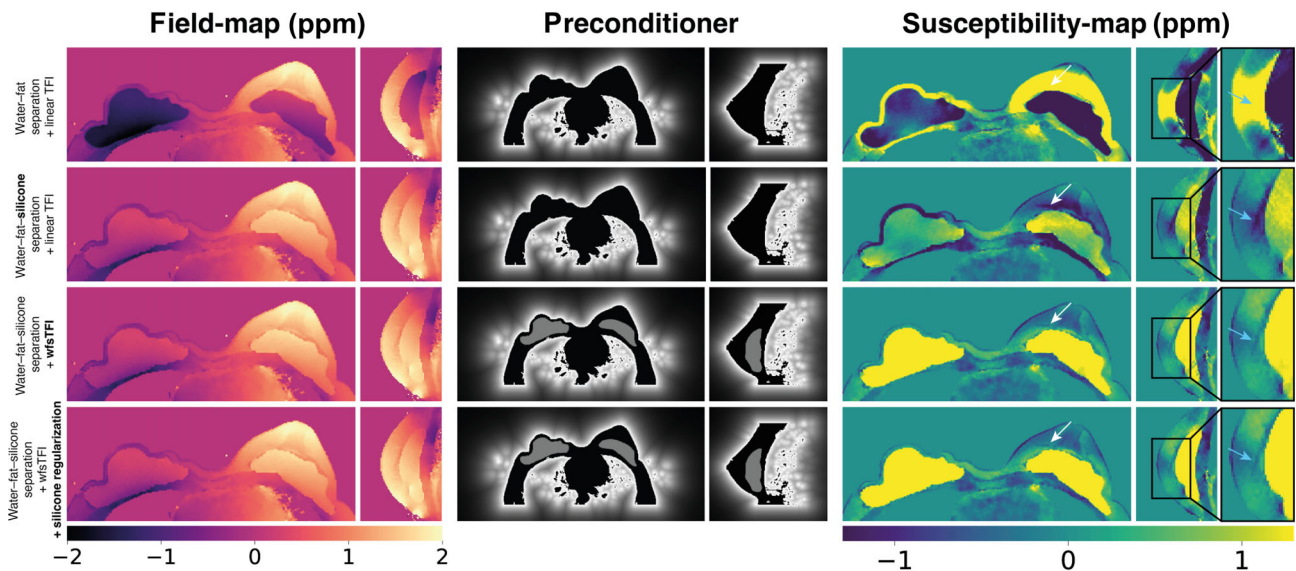

FIGURE 4 Field- and susceptibility mapping results in the scan of a patient with a history of breast cancer, subsequent mastectomy in the left breast and the formation of calcifications in the residual breast tissue (see mammography in Figure S1). Using water–fat separation and linear total field inversion (lTFI; first row), the visualization of the calcification is not possible (white and blue arrow). Using water–fat–separation and lTFI (second row), susceptibility artifacts are reduced, however an overall diamagnetic artifact still dominates the calcification. Only water–fat–silicone total field inversion (wfsTFI) with and without silicone regularization (third and last row) are able to reveal the presence of the calcification.

amount of residual breast tissue is present which includes the formation of several calcifications. Only wfsTFI with and without silicone regularization (rows three and four in Figure 4) yield a susceptibility map with sufficiently reduced artifacts such that the calcification can be identified (white and blue arrow). The appearance of the calcification is verified by the corresponding mammography scan (see Figure S1).

4 | DISCUSSION

An MR-based screening technique to delineate between malignant and benign breast calcifications is of high clinical interest, especially for targeted subcohorts at high-risk or young patients. Previous work on the visualization of breast calcifications with QSM have shown the feasibility of the technique, however, only in subjects without silicone implants.[27,28,30] The visualization of calcifications in proximity to silicone breast implants is important in cases of skin and/or nipple spearing mastectomies with the risk of cancer recurrence in the residual breast tissue.[31] Consequently, the present study aimed to develop a method for robust QSM in the breast where three chemical species, namely water, fat and potentially silicone, are present. Specifically, the present study proposes to use a preconditioned water–fat–silicone TFI algorithm with silicone regularization that directly estimates the susceptibility map from complex multi-echo data. The study examined the performance of the proposed wfsTFI method in comparison to (i) a method that neither accounts for chemical shift of silicone nor the strong susceptibility of silicone, (ii) a method that accounts for the chemical shift of silicone but not for its strong susceptibility, and (iii) a method that accounts for the chemical shift of silicone and uses a water–fat–silicone TFI algorithm without silicone regularization. To examine the performance of the different methods, a numerical breast simulation was performed and five patients with a history of breast cancer and subsequent mastectomy were scanned and evaluated. The proposed wfsTFI with silicone regularization yielded the best normalized root mean square error in the numerical simulation and the least artifacts in regions close to silicone implants. The improvements of the proposed wfsTFI method is based on three main factors.

First, the chemical shift of silicone needs to be accounted for in the parameter separation in order to obtain a bias-free field map. Although wfsTFI ultimately estimates the susceptibility directly from complex multi-echo data, it relies on proper initialization. The proper initialization is a characteristic known for TFI algorithms that directly estimate susceptibility from complex

multi-echo data.[26,34] A field map-based linear total field inversion algorithm is presently employed to generate an initial susceptibility. Therefore a bias-free field map is an important prerequisite. Hence, a recently proposed hierarchical multiresolution graph-cut algorithm specifically tailored for water–fat–silicone separation was presently adopted which is able to robustly yield unwrapped and swap-free field maps.[36]

Second, the large silicone difference between breast tissue and silicone needs to be accounted for in the dipole inversion in order to obtain artifact-free susceptibility values in tissue in close proximity to silicone. Dipole inversion algorithms are well known to yield shadowing-like susceptibility artifacts around strong susceptibility sources as well as streaking artifacts.[17,18,26,33,42] In case of preconditioned QSM algorithms, the inclusion of strong susceptibility regions within the preconditioner has been shown to alleviate artifacts in such regions and was presently adopted.[42] Based on the water-, fat-, and silicone-separated image estimated by the graph-cut algorithm, a silicone fraction map was derived and subsequently served for the robust and automatic generation of a silicone implant mask. The silicone mask was then added to the preconditioner. Particularly noteworthy is that the preconditioner does not only improve convergence speed as suggested in Reference 33 but also changes and potentially improves results as presently shown in normalized root mean square error analysis of the numerical phantom and previously in the work by Liu et al.[42]

Finally, the homogeneity of silicone implants can be exploited to include additional prior information in the dipole inversion. The dipole inversion problem is well-known to be ill-posed and ill-conditioned. To improve the conditioning of the dipole inversion problem, an additional regularization term that enforces the susceptibility within the silicone to be homogeneous is adopted. Similar regularization terms have been successfully employed in other regions such as in the cerebrospinal fluid[43] when the cerebrospinal fluid was used for improved referencing of the susceptibility map, in the carotid artery for the better delineation of calcified plaque and intraplaque hemorrhage,[44] or in subcutaneous fat.[45] The additional silicone regularization is able to reduce shadowing artifacts around silicone implants, streaking artifacts and, most importantly, single voxel of strong diamagnetic susceptibility in close proximity to the silicone implant. These voxel of strong diamagnetic susceptibility can potentially be misinterpreted as calcifications, which are of particular interest in the early detection of malignant breast tumor formation. As of now, silicone cannot be used for referencing as in the above methods, since there are no studies investigating whether silicone breast implants exhibit

consistent magnetic susceptibility across different models and vendors.

Nevertheless, the present study some limitation. First, only macrocalcifications were visualized in the patients due to the limited spatial resolution. Second, only a limited number of patients were scanned and a larger patient study would be required for clinical evaluation.

In conclusion, the present study proposes a preconditioned water–fat–silicone TFI QSM method that allows for the robust and automatic estimation of breast susceptibility in the potential presence of silicone implants.

CONFLICTS OF INTEREST
Kilian Weiss is employee of Philips GmbH Market DACH, Jakob Meineke is employee of Philips Research, Dimitrios Karampinos receives grant support from Philips Healthcare.

DATA AVAILABILITY STATEMENT
The Python implementation of all QSM methods as well as the simulation data will be made freely available at https://github.com/BMRRgroup/wfsTFI.

ORCID
Christof Böhm https://orcid.org/0000-0003-1321-5804
Jakob Meineke https://orcid.org/0000-0001-8663-1468

TWITTER
Christof Böhm @BoehmChristof

REFERENCES
1. Siegel RL, Miller KD, Fuchs HE, Jemal A. Cancer statistics, 2022. *CA Cancer J Clin*. 2022;72:7-33. doi:10.3322/caac.21708
2. Tirada N, Aujero M, Khorjekar G, et al. Breast cancer tissue markers, genomic profiling, and other prognostic factors: a primer for radiologists. *Radiographics*. 2018;38:1902-1920. doi:10.1148/rg.2018180047
3. Mordang JJ, GubernMérida A, Bria A, et al. The importance of early detection of calcifications associated with breast cancer in screening. *Breast Cancer Res Treat*. 2017;167:451-458. doi:10.1007/s10549-017-4527-7
4. Logullo AF, Prigenzi KCK, Nimir CCBA, Franco AFV, Campos MSDA. Breast microcalcifications: past, present and future (review). *Mol Clin Oncol*. 2022;16:81.
5. Weigel S, Heindel W, Heidrich J, Hense HW, Heidinger O. Digital mammography screening: sensitivity of the programme dependent on breast density. *Eur Radiol*. 2016;27:2744-2751. doi:10.1007/s00330-016-4636-4
6. Mann RM, Athanasiou A, Baltzer PAT, et al. Breast cancer screening in women with extremely dense breasts recommendations of the european society of breast imaging (EUSOBI). *Eur Radiol*. 2022;32:4036-4045. doi:10.1007/s00330-022-08617-6
7. Wanders JOP, Holland K, Karssemeijer N, et al. The effect of volumetric breast density on the risk of screen-detected and interval breast cancers: a cohort study. *Breast Cancer Res*. 2017;19:67. doi:10.1186/s13058-017-0859-9
8. Saadatmand S, Obdeijn IM, Rutgers EJ, et al. Survival benefit in women with *BRCA1* mutation or familial risk in the Mri screening study (MRISC). *Int J Cancer*. 2015;137:1729-1738. doi:10.1002/ijc.29534
9. Guindalini RSC, Zheng Y, Abe H, et al. Intensive surveillance with biannual dynamic contrast-enhanced magnetic resonance imaging downstages breast cancer in *BRCA1* mutation carriers. *Clin Cancer Res*. 2019;25:1786-1794. doi:10.1158/1078-0432.ccr-18-0200
10. Colin C, Foray N, Leo GD, Sardanelli F. Radiation induced breast cancer risk in BRCA mutation carriers from low-dose radiological exposures: a systematic review. *Radioprotection*. 2017;52:231-240. doi:10.1051/radiopro/2017034
11. Juanpere S, Perez E, Huc O, Motos N, Pont J, Pedraza S. Imaging of breast implants-a pictorial review. *Insights Imaging*. 2011;2:653-670. doi:10.1007/s13244-011-0122-3
12. Stivala A, Rem K, Leuzzi S, et al. Efficacy of ultrasound, mammography and magnetic resonance imaging in detecting breast implant rupture: a retrospective study of 175 reconstructive and aesthetic sub-pectoral breast augmentation cases. *J Plast Reconstr Aesthet Surg*. 2017;70:1520-1526. doi:10.1016/j.bjps.2017.05.051
13. Cooney CS, Khouri NF, Tsangaris TN. The role of breast Mri in the management of patients with breast disease. *Adv Surg*. 2008;42:299-312. doi:10.1016/j.yasu.2008.03.003
14. de Rochefort L, Liu T, Kressler B, et al. Quantitative susceptibility map reconstruction from MR phase data using Bayesian regularization: validation and application to brain imaging. *Magn Reson Med*. 2009;63:194-206. doi:10.1002/mrm.22187
15. Wang Y, Liu T. Quantitative susceptibility mapping (QSM): decoding MRI data for a tissue magnetic biomarker. *Magn Reson Med*. 2014;73:82-101. doi:10.1002/mrm.25358
16. Deistung A, Schweser F, Wiestler B, et al. Quantitative susceptibility mapping differentiates between blood depositions and calcifications in patients with glioblastoma. *PLoS One*. 2013;8:e57924. doi:10.1371/journal.pone.0057924
17. Chen W, Zhu W, Kovanlikaya I, et al. Intracranial calcifications and hemorrhages: characterization with quantitative susceptibility mapping. *Radiology*. 2014;270:496-505. doi:10.1148/radiol.13122640
18. Sun H, Klahr A, Kate M, et al. Quantitative susceptibility mapping for following intracranial hemorrhage. *Radiology*. 2018;288:171918. doi:10.1148/radiol.2018171918

19. Straub S, Laun FB, Emmerich J, et al. Potential of quantitative susceptibility mapping for detection of prostatic calcifications. *J Magn Reson Imaging*. 2016;45:889-898. doi:10.1002/jmri.25385

20. Kan H, Tsuchiya T, Yamada M, Kunitomo H, Kasai H, Shibamoto Y. Delineation of prostatic calcification using quantitative susceptibility mapping: spatial accuracy for magnetic resonance-only radiotherapy planning. *J Appl Clin Med Phys*. 2021;23:e13469. doi:10.1002/acm2.13469

21. Sun C, Ghassaban K, Song J, et al. Quantifying calcium changes in the fetal spine using quantitative susceptibility mapping as extracted from stage imaging. *Eur Radiol*. 2022;33:606-614. doi:10.1007/s00330-022-09042-5

22. Dimov AV, Liu Z, Spincemaille P, Prince MR, Du J, Wang Y. Bone quantitative susceptibility mapping using a chemical species-specific R2* signal model with ultrashort and conventional echo data. *Magn Reson Med*. 2017;79:121-128. doi:10.1002/mrm.26648

23. Diefenbach MN, Meineke J, Ruschke S, Baum T, Gersing A, Karampinos DC. On the sensitivity of quantitative susceptibility mapping for measuring trabecular bone density. *Magn Reson Med*. 2018;81:1739-1754. doi:10.1002/mrm.27531

24. Chen Y, Guo Y, Zhang X, Mei Y, Feng Y, Zhang X. Bone susceptibility mapping with MRI is an alternative and reliable biomarker of osteoporosis in postmenopausal women. *Eur Radiol*. 2018;28:5027-5034. doi:10.1007/s00330-018-5419-x

25. Guo Y, Chen Y, Zhang X, et al. Magnetic susceptibility and fat content in the lumbar spine of postmenopausal women with varying bone mineral density. *J Magn Reson Imaging*. 2018;49:1020-1028. doi:10.1002/jmri.26279

26. Boehm C, Sollmann N, Meineke J, et al. Preconditioned water–fat total field inversion: application to spine quantitative susceptibility mapping. *Magn Reson Med*. 2022;87:417-430. doi:10.1002/mrm.28903

27. Dimov AV, Liu T, Spincemaille P, et al. Joint estimation of chemical shift and quantitative susceptibility mapping (chemical QSM). *Magn Reson Med*. 2014;73:2100-2110. doi:10.1002/mrm.25328

28. Schweser F, Hermann KH, Deistung A, et al. Quantitative magnetic susceptibility mapping (QSM) in breast disease reveals additional information for MR-based characterization of carcinoma & calcification. Paper presented at: Proceedings 19. Annual Meeting International Society for Magnetic Resonance in Medicine; 2011; Montreal, Canada:1014.

29. FatemiArdekani A, Boylan C, Noseworthy MD. Identification of breast calcification using magnetic resonance imaging. *Med Phys*. 2009;36:5429-5436. doi:10.1118/1.3250860

30. Boehm C, Stelter JK, Meineke J, et al. Mammography-like MR images using a preconditioned water-fat-silicone total field inversion QSM algorithm. Paper presented at: Proceedings 30. Annual Meeting International Society for Magnetic Resonance in Medicine; 2022; London, UK:1588.

31. Heaney R, Sweeney L, Flanagan F, O'Brien A, Smith C. Ipsilateral microcalcifications after breast-conserving surgery: is it possible to differentiate benign from malignant calcifications? *Clin Radiol*. 2022;77:216-223. doi:10.1016/j.crad.2021.12.005

32. Sen LQC, Ko A, Patel MM, Leung JWT. Time to development and imaging features of new calcifications in the treated breast after breast-conserving therapy. *Breast J*. 2021;27:761-767. doi:10.1111/tbj.14277

33. Liu Z, Kee Y, Zhou D, Wang Y, Spincemaille P. Preconditioned total field inversion (TFI) method for quantitative susceptibility mapping. *Magn Reson Med*. 2016;78:303-315. doi:10.1002/mrm.26331

34. Wen Y, Spincemaille P, Nguyen T, et al. Multiecho complex total field inversion method (mcTFI) for improved signal modeling in quantitative susceptibility mapping. *Magn Reson Med*. 2021;86:2165-2178. doi:10.1002/mrm.28814

35. Diefenbach MN, Liu C, Karampinos DC. Generalized parameter estimation in multi-echo gradient-echo-based chemical species separation. *Quant Imaging Med Surg*. 2020;10. doi:10.21037/qims.2020.02.07

36. Stelter JK, Boehm C, Ruschke S, et al. Hierarchical multi-resolution graph-cuts for water-fat-silicone separation in breast MRI. *IEEE Trans Med Imaging*. 2022;41:3253-3265. doi:10.1109/tmi.2022.3180302

37. Ren J, Dimitrov I, Sherry AD, Malloy CR. Composition of adipose tissue and marrow fat in humans By1h NMR at 7 Tesla. *J Lipid Res*. 2008;49:2055-2062. doi:10.1194/jlr.d800010-jlr200

38. Liu T, Liu J, de Rochefort L, et al. Morphology enabled dipole inversion (MEDI) from a single-angle acquisition: comparison with cosmos in human brain imaging. *Magn Reson Med*. 2011;66:777-783. doi:10.1002/mrm.22816

39. Boehm C, Diefenbach MN, Makowski MR, Karampinos DC. Improved body quantitative susceptibility mapping by using a variable-layer single-min-cut graph-cut for field-mapping. *Magn Reson Med*. 2020;85:1697-1712. doi:10.1002/mrm.28515

40. Okuta R, Unno Y, Nishino D, Hido S, Loomis C. CuPy: a NumPy-compatible library for NVIDIA GPU calculations. Paper presented at: Proceedings of Workshop on Machine Learning Systems (LearningSys) in The Thirty-first Annual Conference on Neural Information Processing Systems (NIPS), Long Beach, CA, USA; 2017.

41. Ruschke S, Eggers H, Kooijman H, et al. Correction of phase errors in quantitative water–fat imaging using a monopolar time-interleaved multi-echo gradient echo sequence. *Magn Reson Med*. 2016;78:984-996. doi:10.1002/mrm.26485

42. Liu Z, Wen Y, Spincemaille P, et al. Automated adaptive preconditioner for quantitative susceptibility mapping. *Magn Reson Med*. 2019;83:271-285. doi:10.1002/mrm.27900

43. Liu Z, Spincemaille P, Yao Y, Zhang Y, Wang Y. Medi+0: morphology enabled dipole inversion with automatic uniform cerebrospinal fluid zero reference for quantitative susceptibility mapping. *Magn Reson Med*. 2017;79:2795-2803. doi:10.1002/mrm.26946

44. Nguyen TD, Wen Y, Du J, et al. Quantitative susceptibility mapping of carotid plaques using nonlinear total field inversion: initial experience in patients with significant carotid stenosis. *Magn Reson Med*. 2020;84:1501-1509. doi:10.1002/mrm.28227

45. Sharma SD, Hernando D, Horng DE, Reeder SB. Quantitative susceptibility mapping in the abdomen as an imaging biomarker of hepatic iron overload. *Magn Reson Med*. 2014;74:673-683. doi:10.1002/mrm.25448

SUPPORTING INFORMATION

Additional supporting information may be found in the online version of the article at the publisher's website.

Figure S1. Mammography image of the left breast showing the formation of calcifications in the residual breast tissue between skin and silicone implant. The highlighted calcification (white arrow) is the same as the one depicted in the susceptibility maps in Figure 4.

4 Discussion

This dissertation addresses a multitude of technical challenges for QSM in regions with several chemical species, such as water, fat, or silicone, laying the foundation for QSM applications outside the brain using *off the shelf* MRI scanners. Specifically, no additional pulse sequences or post-processing are required beyond the QSM estimation algorithm itself.

Furthermore, this work advances all four major steps of quantitative susceptibility mapping: i) estimating the susceptibility-induced B_0 field inhomogeneities, ii) unwrapping the field map, iii) removing the background field, and iv) performing the field-to-susceptibility inversion. This is accomplished through the joint problem formulation of field mapping and unwrapping, as well as background field removal and field-to-susceptibility inversion. Consequently, the necessary steps are reduced to two, minimizing artifact amplification of errors from previous stages.

4.1 Review of Existing Literature

4.1.1 Field-mapping

The field map parameter has historically posed a significant challenge, requiring estimation or approximation in order to attain robust water and fat separation. In the well-established single-R_2^* multi-fat-peak water–fat voxel signal model [35, 52], the field map parameter is a periodic and nonlinear parameter with several local minima. Gradient descent methods are challenging to apply when large B_0 field inhomogeneities are present, as conventional multi-echo gradient-echo sequences do not provide an initial estimate other than zero. The use of a zero-initialized gradient descent method can lead to water–fat swaps, where water is identified as fat and vice versa. This poses two issues. First, when the water and fat images are intended to use, the diagnostic value might be limited [53]. Second, the estimated field map contains artifactual field map jumps of approximately 3.4ppm that propagate into the susceptibility map, thereby rendering the latter useless. When the field map is known, the estimation of all other parameters

in the above signal model are convex and in the case of known nonlinear parameters reduces to solving an over-determined system of linear equations. Therefore, accurate field-mapping is the foundation of both, body quantitative susceptibility mapping and water–fat separation. To overcome the voxelwise ambiguity of several local minima, a variable projection method (VARPRO) has been proposed to enable the brute-force residual calculation of the cost function in dependence on the field map parameter thus revealing all local minima and enabling the determination of the global voxel minima [54]. This approach can substantially alleviate water/fat swaps. However, the voxel-wise VARPRO formulation is sensitive to noise and prone to water-fat swaps when the voxel consists primarily of water or fat [55] or in the case of low SNR.

To stabilize the field map estimation, the use of spatial neighborhood information has extensively been explored. Many of the developed methods rely on a smoothness constraint on the field map. The assumption of a smooth field map only holds true for background field contributions which follow a Laplace/Poisson equation. On the other hand, local tissue field maps deviate from this assumption. Nevertheless, the approximation of a smooth total field map can be considered valid due to the background field contributions being significantly larger (1-2 orders of magnitude) than the local field contributions. A variety of algorithms have been developed to enforce a smoothness constraint on the field map including region-growing [53, 56], cellular automata [57–59], message passing [60, 61] and global estimation [62] especially using graph cuts [19, 38–40, 63]. However, all of the above methods focus on accurate water/fat separation and the estimated field maps being subject to varying degrees of blurring. Only the graph cut-based R-GOOSE method [40] is able to estimate a high-resolution field map as a by-product of efforts to enhance processing efficiency. Some of the above water–fat separation/field-mapping methods can be used as an initialization for a voxelwise refinement of the field map using methods that minimize the voxel signal model by alternating between linear and nonlinear parameters [31, 35]. However, the intensity of field map blurring is often proportional to the gradient of the field map, resulting in a stronger effect at edges in the field map. The edges in the field map are of particular interest for susceptibility mapping since they define the bulk susceptibility differences between different tissue types. Hence, field map blurring can have the same effect as low resolution averaging of edge voxels [64].

A fundamentally different approach to obtain accurate field map results without the need to use neighborhood regularization in conjunction with a computational expensive global minimization problem was presented in [65] and was developed further in [66]. In [65] the use of an objects-based field map estimate was proposed derived from the

segmentation of magnitude images, the creation of an artificial susceptibility map assigned with literature values of water, fat and air, the forward simulation to a field map and the subsequent demodulation of the field map from the echo time data. In addition to the demodulation of the object-based field map estimate, in [66] it was proposed to incorporate the information about the inhomogeneities of the scanner magnet, the shim field and residual fields caused by the approximation of susceptibility sources outside the FOV. This approach is able to significantly reduce the occurrence of water/fat swaps and hence also yields increased field map accuracy.

There has also been efforts to simplify the field map estimation in water/fat regions by means of optimal echo time selection. Specifically, the use of in-phase echoes have been proposed. This approach removes the need to model fat contributions to the signal model as only echoes are acquired at timepoints where the phasor of water and fat are aligned and the remaining phase is assumed to originate only from susceptibility [24, 25]. For the definition of in-phase echoes a single fat peak has to be assumed. However, it is well known that physiological fat spectra are spectrally complex and they vary across different fatty tissue types [32, 34]. Therefore, it can be expected that using in-phase echoes for QSM in body regions is associated with systematic bias correlated with fatty voxel content.

4.1.2 Field map unwrapping

The process of unwrapping the field map in QSM is related to the vast domain of phase unwrapping, which itself is a highly researched area. The need to unwrap the field map stems from the often used linear problem formulation of the field-to-susceptibility relation [46, 48, 67]. In the linear problem formulation, the potential wrapping in the field map is not accounted for. This results in large quantification bias as a jump in the field map is considered to originate from susceptibility differences. There have been efforts to formulate the dipole inversion problem such that field map wraps are accounted for in the dipole inversion. However, none of the proposed methods work without the initialization with an unwrapped field map [47, 50, 68, 69]. Therefore, accurate unwrapping is needed for accurate susceptibility estimation. There are three categories of unwrapping methods, so-called Laplacian unwrapping, path-following methods and graph-cut methods. Laplacian unwrapping minimizes the difference between the derivatives of the wrapped and the unwrapped phase and finally the unwrapped phase is obtained by solving the corresponding Poisson equation [70]. Laplacian-based methods are known for their robustness, especially in low SNR cases,

and are the predominant choice in studies focused on the brain region. Laplacian-based phase unwrapping techniques offer a convenient and efficient solution that can effectively handle noise. This resilience, however, comes at the cost of only approximately estimating the actual phase. This can be addressed to a certain extent by refining the discretization process, utilizing appropriate weighting and linear solution methods, and implementing heuristics and congruence operations [71]. In general, these Laplacian-methods are recommended for data sets with moderate to low SNR, where obtaining precise quantitative values is not of utmost importance. However, that inability to estimate accurate phase maps might limit the usability of Laplacian-based methods when used for quantitative susceptibility estimation.

Path-following methods, on the other hand, determine that a wrap has occurred when the phase change between two voxels along a path exceeds π. A plethora of methods have been proposed that apply the above assumption on various ways in one, two or three dimensions. Some of them are guided by quality of the voxel [72, 73] or by branch cut lines which impose barriers to paths [74]. Some of the often used path-following methods in quantitative susceptibility mapping are PRELUDE [75], BEST-PATH [76], QGU [73], SEGUE [77] or ROMEO [78].

Graph-cut methods have mainly been developed to improve water–fat separation by enforcing the field map to be smooth (see section 4.1.1). However, all of them rely on a predefined interval of the field map in which a solution is searched for. Theoretically, this interval can be as large as the unwrapped field map. In that case, these algorithms work similar as the path-following methods in a way that phase jumps larger than π are recognized as wraps. However, this approach has a few limitations. First, some graph cut algorithms iteratively compare the current field map solution with a potential better candidate. These candidates however have to be chosen heuristically. Hence, these algorithms are not guaranteed to converge to the global minimum of their defined cost function and struggle with an increased unwrapped field map range [19, 38, 39]. A second type of graph-cut algorithms employs distinct graph constructions that guarantee the global optimal solution with a single graph cut. However, these graph cuts can be computationally expensive due to the large number of nodes per voxel [63] or a suboptimal graph construction that results in either excessively long processing times or the rejection of the correct solution [40].

4.1.3 Background Field Removal

The terms "background field" and "external field" have traditionally been used interchangeably, referring to magnetic inhomogeneities generated outside the ROI. On the other hand, "internal fields" or "local fields" are caused by sources within the ROI and result from the material-related demagnetization fields of dipole moments. Although the main magnetic field is typically considered homogeneous, small inhomogeneities may arise due to imperfections in the magnet geometry and shim coils. These factors contribute to the background field. However, including magnet geometry and shim coils would simply involve adding a background contribution to the field, which can be handled by all background field removal techniques. In the process of extracting tissue susceptibility values, only the local fields are of interest. The background fields are mainly caused by air-tissue interfaces which generate strong fields due to the large susceptibility difference between air and tissue. These background fields penetrate deeply into the tissue and are significantly stronger than the local tissue fields by a factor of 1 to 2 orders of magnitude. Consequently, the background field must be removed to obtain the local susceptibility maps. Most methods perform the background field removal as an independent step [42, 44, 79–83]. These methods rely on the ability to uniquely separate background and local field contributions [41].

Background field removal techniques can be loosely categorized by their inherent assumption including i) no harmonic internal and background fields in the boundary region [42, 83], ii) no sources close to the boundary [79, 81] and iii) minimization of an objective function [44, 82]. However, all of them show more or less strong artifacts leading to an improper removal of the background fields. For example, the assumption that only background fields are present in the boundary region is unjustified and is equivalent to the assumption that local susceptibility is zero in the boundary. While this assumption is better justified in the brain, this can lead to severe artifacts in body regions where the air tissue interface boundary can contain subcutaneous fat (∼0.6ppm, [43]) or in the case of arbitrary ROIs other strong sources such as cortical bone (∼2ppm). Although the background field removal step can introduce artifacts, these are generally confined to regions close to the defined boundary. When the tissue of interest is situated at a distance from the boundary, its susceptibility can often be estimated reliably. However, this approach may not be suitable for tissues located near the boundary, such as the cerebral cortex, liver, or heart.

Another class of background field removal techniques try to simultaneously remove background fields and estimate local susceptibility values [48, 84–86], so-called single

step methods. However, single step methods that use a Laplacian operation to remove the background field [84, 85] are known to significantly underestimate local susceptibility. Recently, the so-called total field inversion method was proposed that is particularly successful in the joint susceptibility estimation and background field removal. TFI generally uses the same problem formulation as a traditional QSM inversion algorithms such as MEDI [46], however, not only the local susceptibility is estimated but simultaneously the susceptibility in the entire image volume. Similarily to projection onto dipole fields, in the background region TFI algorithms estimate a heuristic susceptibility distribution that model the harmonic background fields. TFI algorithms have the advantage that they do not violate the orthogonality assumption in the boundary regions [48, 50, 69] and thus yield accurate background field removal in the internal boundary region.

4.1.4 Field-to-susceptibility Inversion

The main premise of QSM is to overcome the limitations of Susceptibility-Weighted Imaging (SWI, [87]) and R2*-mapping, where differentiating between sources of opposing susceptibility is difficult (R2*-mapping) or only limited differentiation is possible (SWI). For example, in both SWI and R2*-mapping, intracranial calcifications and hemorrhages appear similar; however, in QSM images, these two conditions can be clearly distinguished due to the differing signs of their susceptibility [88].

A plethora of field-to-susceptibility inversion algorithms have been developed to solve the ill-posed and ill-conditioned inverse problem. Most of the developed methods use regularization to stabilize and improve the conditioning of the inverse problem [89]. In the Bayesian interpretation of regularization, the regularization term is viewed as a prior probability distribution over the solution space that acts as a way to encode prior knowledge or assumptions about the problem into the solution process. A large variety of regularization terms and optimization algorithms have been applied in the literature. The most common optimization algorithms are alternating direction method of multipliers (ADMM) [68, 84, 90–92] and quasi-Newton fixed-point solver where at each step a linearized problem is solved using conjugate gradient [46–48, 50, 69, 93]. Furthermore, so-called direct methods with a closed-form solution exist [67, 94]. A big advantage of the direct methods is their incredibly speed in the order of seconds compared to minutes for the above iterative methods. However, the direct methods perform considerably worse when compared to iterative methods [95]. Despite its limitations, total-variation regularization [96] with sparsity emphasis using ℓ_1 norm and morphological edge weightings has been widely used [46]. While total

variation regularization promotes piece-wise constant distributions that do not reflect the underlying physiology, a more anatomically correct approach has been proposed and explored using Total Generalized Variation (TGV), which promotes piece-wise smooth distributions [97]. However, the fact that a new set of dipole inversion algorithms is proposed each year for different anatomies and pathologies indicates that a more generalizable method has yet to be found [14, 95, 98].

QSM has been mainly performed in the brain to study the presence of iron [99–104], myelin [105–107], and calcifications [88, 108] but has become increasingly being used outside the body to characterize lesions and calcifications in breast disease [13, 109], to measure bone density [23–25, 110], prostatic calcifications [111, 112] liver iron overload [20, 113, 114], cardiac oxygenation [115], placental oxygenation [116, 117], knee cartilage degeneration [118] and to quantify calcium changes in the fetal spine [119]. Many of the studies mentioned above utilize methods designed for brain imaging without incorporating additional information that might be available from, for example, the water-fat separation. Only for liver applications there have been efforts to incorporate additional information for improved accuracy [20–22]

With the recent proliferation of deep-learning techniques across a wide range of applications, there has been a growing interest in developing and employing these methods in the field of QSM [120]. As a result, significant efforts have been dedicated to exploring the potential of deep-learning-based QSM methods, with the aim of improving the accuracy and robustness of QSM [121–124]. Deep-learning methods offer several advantages over traditional iterative or direct inversion methods. Firstly, they are computationally efficient and can process high-resolution 3D scans within seconds. Secondly, while deep-learning methods may not achieve the same level of accuracy as iterative methods, they can still produce results that are very close [95]. This makes them a promising tool for applications where speed is a critical factor and/or qualitative values are sufficient. Additionally, the visual quality of QSM maps generated by deep-learning methods is often superior to that of maps generated by traditional methods. This improvement is due to higher apparent SNR and a reduction in well-known artifacts such as streaking and shadowing.

4.2 Present Work

This work represents a significant advancement in the field of quantitative susceptibility mapping by developing new techniques specifically tailored for application in the body. This contribution is particularly important given the unique challenges of body QSM

and the need for robust and accurate methods to obtain high-quality QSM maps. By addressing these challenges, this work not only improves our understanding of the underlying physical principles of QSM, but also expands the potential clinical applications of this imaging modality. Overall, this work has important implications for the field of medical imaging and demonstrates the potential of QSM as a powerful diagnostic tool.

4.2.1 Novelty and Impact

The field-mapping algorithm presented in Section 3.2, is the first method specifically designed for body QSM applications, with a primary focus on accurate field map estimation. This proposed algorithm builds on previous work, which aimed to improve water-fat separation [40]. The novelty of this approach lies in its graph construction technique [125], which theoretically ensures the global optimal solution of whole 3D data sets in a single graph cut, while yielding non-smoothed, high-resolution field maps. However, the implementation in [40] did not account for the possibility of varying local minima per period and voxel. This can lead to the accidental dismissal of correct voxel solutions or unbearable computation times, or both (see Figure 4 in 3.2). To address this issue, a new variable-layer graph construction was developed that accounts for the underlying properties of the voxel-wise problem formulation while simultaneously ensuring the estimation of the global optimal solution in the defined field map interval. The proposed graph-cut approach also enables the direct estimation of a non-wrapped field map, making the additional unwrapping step unnecessary. Joint problem formulation can prevent errors from propagating from one step to the next by reducing the risk of artifacts or errors being amplified due to the recognition of an earlier error as true and reliable.

The QSM algorithm developed in 3.3 is specifically designed to correct MR thermometry by removing susceptibility-induced background fields caused by motion between shots. These background fields can introduce phase changes that are much larger than temperature-induced phase changes (10^3), rendering the obtained temperature maps useless. Although the Laplacian boundary value method and the Projection onto dipole fields background field removal techniques have previously been successful in correcting temperature maps [126], they suffer from problems such as overfitting (PDF) and pixel-layer erosion and strong dependence on the chosen ROI (LBV). In contrast, the proposed TFI method provides a robust and automatic removal of susceptibility-induced phase changes, making it unnecessary to manually draw and test ROIs. By

demonstrating the effectiveness of the TFI method in MR thermometry correction, the work presented in 3.3 emphasizes the robustness of TFI algorithms even when used solely for background field removal.

The wfTFI dipole inversion algorithm presented in 3.4 is a significant contribution to the field of quantitative susceptibility mapping as it is the first general-purpose algorithm specifically tailored for body applications, or more specifically, for regions where water and fat are present. The proposed method belongs to the subclass of total field inversion algorithms [48, 50, 69] that jointly estimate the local susceptibility distribution and remove the background field without the use of the implicit assumptions usually employed in background field removal methods. Unlike most previous methods that relied on estimating susceptibility based on the field map, the proposed approach directly estimates the susceptibility from the complex multi-echo data. This approach shows promising improvements in accuracy and precision of susceptibility values in body regions. Furthermore, the problem formulation of the proposed method enhances noise modeling, as the implicit assumption shared by all dipole inversion algorithms—that noise follows a Gaussian distribution—is well-justified for complex multi-echo data. The results demonstrate the reduction of streaking artifacts and an increase in apparent SNR. Moreover, as the proposed method is an TFI algorithm, it enables the free selection of the ROI in the body without introducing artifacts. This feature offers the flexibility to choose the ROI freely.

The developed acquisition method in 3.5 shows three main improvements over previously proposed techniques. Firstly, it allows for susceptibility mapping in the body without the need for water-fat separation, which is a computationally intensive step that requires optimized processing and acquisition methods [27, 31, 127]. This makes the method faster and more efficient. Secondly, it does not rely on more prior knowledge assumptions than most water-fat separation methods, which assume a prior known and cross-subject similar fat model. This reduces the potential for errors due to inaccurate assumptions. Thirdly, it allows for the reduction of necessary echo times below three, which is typically required for water-fat separation methods. This enables the acquisition of high-resolution susceptibility maps in the body much faster, or with greater spatial detail [128].

The dipole inversion algorithm presented in 3.6 improves accuracy of susceptibility mapping for breast applications when chemical shift encoding field-mapping is employed. Specifically, the work proposes a specific QSM methodology for breast applications in the presence of silicone breast implants. The approach involves using a graph-cut algorithm to obtain water-, fat-, and silicone-separated images from multi-echo gradient-

echo images and introducing an additional term in the dipole inversion to enforce homogeneous susceptibility within regions of silicone and the incorporation of silicone in the preconditioner. The proposed method is able to reduce the normalized root mean squared error and shows reduced artifacts in residual breast tissue next to silicone implants in vivo. Compared to previously proposed QSM methods, this methodology accounts for the strong susceptibility and chemical shift of silicone and allows for the visualization of local susceptibility values in proximity to silicone breast implants. Most importantly, it does not yield single voxels of strong negative susceptibility close to the silicone implant resembling calcifications. For the first time, this method enables robust MR-based screening for calcifications in the presence of silicone.

4.2.2 Limitations

While the present work represents a significant advancement in the technical development of QSM methods for body applications, and demonstrates improved accuracy and precision, limitations still persist for the adoption for some applications.

As the name indicates, *quantitative* susceptibility mapping aims to estimate a quantitative parameter. However, QSM does not yet provide meaningful results for individual patients in body applications, as the accuracy is insufficient to derive staging of pathologies in a single subject. Especially accuracy across subjects remains challenging [23, 24, 129] and only correlation in cohorts have been obtained. The ill-posedness of the dipole inversion problem necessitates the use of regularization, which largely determines the resulting susceptibility maps by balancing data fidelity and regularization term. Typically, the regularization parameter is determined by either visually comparing different parameters or by using L-curves heuristic. Subsequently, the same regularization parameter is applied to all subjects in conjunction with a standardized imaging protocol. However, this approach can be affected by the ratio of the size of the imaging object to the field of view, and the imaged anatomy can differ substantially between individuals, leading to significant variations in regularization strength. This variation might be difficult to detect by visual inspection, but it can have a negative impact on the accuracy of quantitative values.

Furthermore, an additional fundamental challenge is posed for QSM in measuring the bone mineral density (BMD) by measuring the trabecular bone density and ultimately allow to estimate bone strength, fracture risk and associated diseases such as osteoporosis. This is mainly caused by the cortical bone shell that surrounds the inner trabecular bone. The cortical bone shell is invisible to conventional echo times later than 1 ms due

to its high relaxtion rate of over 2600 Hz [130]. The so-called hollow cylinder problem introduces an additional systematic error in the measurement of the trabecular bone that is correlated to the ratio of cortical bone volume to total bone volume [131]. The hollow cylinder problem can be overcome by means of ultra-short echo time imaging (UTE) [110, 132, 133]. However, UTE imaging poses a challenge to field-mapping algorithms. Different solutions have been presented by for example ignoring the R_2^*-decay of fat and only modeling the transverse relaxation rate of water [110, 132] or more physiologically accurate, different models for different regions, assuming a single component and single R_2^* in the cortical bone and a multipeak single-R_2^* for the rest of the tissue [133]. However, the latter approach suffers from the difficult segmentation of cortical bone. Furthermore, cortical bone shows significant different field map values than the bone marrow and tissue outside of the bone posing additional challenges on the smoothness assumption of many field-mapping methods (see section 4.1.1)

A common constraint of the computational techniques presented in Sections 3.2 - 3.3 and 3.6 is their considerable computational expense and the consequent lengthy processing durations. Dipole inversion approaches can only be executed within a clinically acceptable timeframe, under 2 minutes, when employing a GPU. For the graph cut-based field-mapping method in 3.2, processing times of under 5 minutes are achievable exclusively in scans with a relatively small matrix size, such as the lumbar spine scan featuring $122 \times 122 \times 44$ voxels. Consequently, large matrix sizes and high-resolution scans present significant challenges, particularly in light of the growing accessibility of advanced acceleration techniques like compressed sensing [134–136] and high-resolution deep-learning reconstruction methods [137–139].

Although the method proposed in Section 3.3 effectively removes susceptibility-induced phase changes, the MR-based temperature maps still exhibit variability that precludes their use in guiding clinical decisions such as adjusting heating during RF-HT treatments. This variability is evident in the correlation between the temperature maps and measurements obtained by temperature sensors placed inside the tissue of interest. Consequently, the use of temperature sensors remains a necessary component of clinical routine. However, improving further on the accuracy of temperature maps lies beyond the realm of susceptibility-induced phase removal.

4.3 Perspectives

As discussed in the limitations section, the quantitative nature of QSM is not yet firmly established. Nevertheless, QSM may still prove valuable for enhancing the contrast

of calcified structures, with potential applications in the body targeting bones and calcifications, such as those in the breast, blood vessels, or prostate. In the context of calcifications, achieving robust visualization alone could be highly beneficial in clinical practice.

For example, the acquisition methodology introduced in Section 3.5 holds promise for high-resolution QSM applications, enabling the assessment of previously inaccessible structures, such as microcalcifications, which are responsible for detecting up to 50% of non-palpable breast tumors [140]. Currently, clinical routine relies on X-ray mammography. However, for young patients, particularly women with a genetic predisposition to breast cancer requiring screening as early as 25-30 years old [141–143], X-ray mammography is not ideal due to increased radiation sensitivity [144]. As an alternative, a radiation-free MR-based technique using the proposed acquisition methodology could be more desirable. Initial work has demonstrated the feasibility of high-resolution QSM maps for visualizing microcalcifications [128], but validation in larger patient cohorts is needed to promote clinical adoption.

The proposed acquisition method offers two distinct advantages: first, it enables high-resolution QSM, making it suitable for applications that necessitate detailed structural information; second, it facilitates faster acquisitions, making QSM appealing for dynamic scans, including those with contrast agent-enhanced scans. Given that contrast agents exhibit a substantially stronger susceptibility compared to tissue, this approach could potentially serve as an alternative means of measuring perfusion.

Moreover, field-mapping method presented here, when combined with the general-purpose dipole inversion method for body regions discussed in Sections 3.2 and 3.4, offers a robust approach for estimating susceptibility maps across various body regions. Nevertheless, these methods have only been tested in a small sample size and with a single pathology. Future studies should aim to extend the evaluation to a broader range of anatomies, larger sample sizes, and multiple pathologies.

Regarding silicone implants, the performance of the effective in-phase echoes from Section 3.5 remains to be investigated. Women with silicone implants also require regular checkups for non-palpable tumors. Silicone implants can obscure large portions of breast tissue due to the limited two-dimensional nature of mammography, potentially hiding masses or calcifications. Consequently, MRI or ultrasound imaging proves more effective for visualizing implants in the breast, as supported by literature [145, 146]. However, the effective in-phase echoes used for high-resolution QSM only remove the phase contributions from fat from the phasor, while the phase of silicone remains. The question arises whether silicone should be masked and labeled as a background region,

requiring a segmentation method, or if the acquisition of chemical shift encoded echo times is the better option. An additional advantage of chemical shift encoded imaging and subsequent parameter separation is the wealth of information available, such as water-, fat-, and silicone-separated images and the derived proton density fat fraction and proton density silicone fraction (PDSF). The PDSF itself might hold significant clinical relevance for monitoring implant integrity or quantifying silicone accumulation in lymph nodes following implant ruptures [147].

In general, the methods presented in this work could be useful for re-evaluating anatomies that have previously been assessed using brain mapping techniques, as they might lead to improved accuracy and precision in various imaging situations.

List of Abbreviations

Abbreviations

ADMM	Alternating Direction Method of Multipliers
BFR	Background Field Removal
BMD	Bone Mineral Density
CEST	Chemical Exchange Saturation Transfer
CSF	Cerebrospinal Fluid
CT	Computed Tomography
CUDA	Compute Unified Device Architecture
DEGRE	Double Echo Gradient Echo
DOI	Digital Object Identifier
DWI	Diffusion-Weighted Imaging
fMRI	functional Magnetic Resonance Imaging
FOV	Field-Of-View
HIFU	High Intensity Focused Ultrasound
IDEAL	Iterative Decomposition of water and fat with Echo Asymmetry and Least squares estimation
ISMRM	The International Society for Magnetic Resonance in Medicine
ISSN	International Standard Serial Number
LBV	Laplacian Boundary Value method

MC	Microcalcifications
mcTFI	Multi-Echo Complex Total Field Inversion
MEDI	Morphology Enabled Dipole Inversion
MERIT	Model Error Reduction through Iterative Tuning
mGRE	Multi-Echo Gradient Echo
MR	Magnetic Resonance
MRE	Magnetic Resonance Elastography
MRI	Magnetic Resonance Imaging
MRS	Magnetic Resonance Spectroscopy
MT	Magnetization Transfer Imaging
PDF	Projection Onto Dipole Fields
PDFF	Proton Density Fat Fraction
PDSF	Proton Density Silicone Fraction
PRFS	Proton Resonance Frequency Shift
PWI	Perfusion-Weighted Imaging
qMRI	Quantitative Magnetic Resonance Imaging
QSM	Quantitative Susceptibility Mapping
R-GOOSE	Rapid GlObally Optimal Surface Estimation
RF-HT	Radiofrequency Hyperthermia
SWI	Susceptibility-Weighted Imaging
TFI	Total Field Inversion
TGV	Total Generalized Variation
TV	Total Variation

UTE   Ultra Short Echo time

VARPRO   Variable Projection

wfTFI   water–fat Total Field Inversion

List of Figures

Bibliography

[1] V. Baliyan, C. J. Das, R. Sharma, and A. K. Gupta, "Diffusion weighted imaging: Technique and applications," *World Journal of Radiology*, vol. 8, no. 9, p. 785, 2016.

[2] W. Xu, Q. Wang, A. Shao, B. Xu, and J. Zhang, "The performance of MR perfusion-weighted imaging for the differentiation of high-grade glioma from primary central nervous system lymphoma: a systematic review and meta-analysis," *PLOS ONE*, vol. 12, no. 3, p. e0173430, 2017.

[3] T. Martín-Noguerol, P. Montesinos, O. L. Casado-Verdugo, L. S. Beltrán, and A. Luna, "Susceptibility weighted imaging for evaluation of musculoskeletal lesions," *European Journal of Radiology*, vol. 138, no. 138, p. 109611, 2021.

[4] A. Rubin, Łukasz Waszczuk, G. Trybek, S. Kapetanakis, and J. Bladowska, "Application of susceptibility weighted imaging (SWI) in diagnostic imaging of brain pathologies - a practical approach," *Clinical Neurology and Neurosurgery*, vol. 221, p. 107368, 2022.

[5] S. Sharma, J. Neelavalli, T. Shah, and R. K. Gupta, "Susceptibility-weighted imaging: an emerging technique for evaluation of the spine and spinal cord," *The British Journal of Radiology*, vol. 95, no. 1138, p. 20211294, 2022.

[6] P. Jezzard and A. W. Song, "Technical foundations and pitfalls of clinical fMRI," *NeuroImage*, vol. 4, no. 3, pp. S63–S75, 1996.

[7] M. H. Buonocore and R. J. Maddock, "Magnetic resonance spectroscopy of the brain: a review of physical principles and technical methods," *Reviews in the Neurosciences*, vol. 26, no. 6, pp. 609–632, 2015.

[8] J. Li, S. K. Venkatesh, and M. Yin, "Advances in magnetic resonance elastography of liver," *Magnetic Resonance Imaging Clinics of North America*, vol. 28, no. 3, pp. 331–340, 2020.

[9] L. V. Hiscox, H. Schwarb, M. D. McGarry, and C. L. Johnson, "Aging brain mechanics: Progress and promise of magnetic resonance elastography," *NeuroImage*, vol. 232, p. 117889, 2021.

[10] M. Zaiss, T. Jin, S.-G. Kim, and D. F. Gochberg, "Theory of chemical exchange saturation transfer MRI in the context of different magnetic fields," *NMR in Biomedicine*, vol. 35, no. 11, p. e4789, 2022.

[11] S. Jiang, Z. Wen, S. S. Ahn, K. Cai, D. Paech, C. G. Eberhart, and J. Zhou, "Applications of chemical exchange saturation transfer magnetic resonance imaging in identifying genetic markers in gliomas," *NMR in Biomedicine*, p. e4731, 2022.

[12] S. D. Wolff and R. S. Balaban, "Magnetization transfer contrast (MTC) and tissue water proton relaxationin vivo," *Magnetic Resonance in Medicine*, vol. 10, no. 1, pp. 135–144, 1989.

[13] Y. Wang and T. Liu, "Quantitative susceptibility mapping (QSM): Decoding MRI data for a tissue magnetic biomarker," *Magnetic Resonance in Medicine*, vol. 73, no. 1, pp. 82–101, 2014.

[14] A. V. Dimov, J. Li, T. D. Nguyen, A. G. Roberts, P. Spincemaille, S. Straub, Z. Zun, M. R. Prince, and Y. Wang, "QSM throughout the body," *Journal of Magnetic Resonance Imaging*, 2023.

[15] F. Schweser, A. Deistung, B. W. Lehr, K. Sommer, , and J. R. Reichenbach, " SEMI-TWINS: Simultaneous Extraction of Myelin Iron using a T2*-Weighted Imaging Sequence," in *Proceedings 19. Annual Meeting International Society for Magnetic Resonance in Medicine*, vol. 19, (Montreal, Canada), p. 0120, `http://archive.ismrm.org/2011/0120.html`, 2011.

[16] J. Lee, Y. Nam, J. Y. Choi, H. Shin, T. Hwang, and J. Lee, "Separating positive and negative susceptibility sources in QSM ," in *Proceedings 25. Annual Meeting International Society for Magnetic Resonance in Medicine*, vol. 25, (Honolulu, Hawaii), p. 0751, `http://archive.ismrm.org/2017/0751.html`, 2017.

[17] S. Nielles-Vallespin, P. F. Ferreira, A. D. Scott, D. J. Pennell, D. N. Firmin, A. E. Arai, and R. de Silva and, "Diffusion Tensor CMR a potential early marker of remodelling after myocardial infarction," in *Proceedings 27. Annual Meeting International Society for Magnetic Resonance in Medicine*, vol. 27, (Montreal, Canada), p. 0790, `http://archive.ismrm.org/2019/0790.html`, 2019.

[18] J. Emmerich, F. L. Sandig, and S. Straub, "Separation of positive and negative susceptibility contrast at 7 Tesla allows for a more detailed characterization of multiple sclerosis lesions," in *Proceedings 29. Annual Meeting International Society for Magnetic Resonance in Medicine*, vol. 29, (online), p. 3989, `http://archive.ismrm.org/2021/3989.html`, 2021.

[19] J. Dong, T. Liu, F. Chen, D. Zhou, A. Dimov, A. Raj, Q. Cheng, P. Spincemaille, and Y. Wang, "Simultaneous phase unwrapping and removal of chemical shift (SPURS) using graph cuts: Application in quantitative susceptibility mapping," *IEEE Transactions on Medical Imaging*, vol. 34, no. 2, pp. 531–540, 2015.

[20] S. D. Sharma, D. Hernando, D. E. Horng, and S. B. Reeder, "Quantitative susceptibility mapping in the abdomen as an imaging biomarker of hepatic iron overload," *Magnetic Resonance in Medicine*, vol. 74, no. 3, pp. 673–683, 2014.

[21] J. V. Velikina, R. Zhao, C. Buelo, A. A. Samsonov, S. Reeder, and D. Hernando, "Improved Regularization for Quantitative Susceptibility Mapping of Liver Iron Overload," in *Proceedings 29. Annual Meeting International Society for Magnetic Resonance in Medicine*, vol. 29, (online), p. 3995, `http://archive.ismrm.org/2021/3995.html`, 2021.

[22] J. Velikina, R. Zhao, C. J. Buelo, A. A. Samsonov, S. B. Reeder, , , and D. H. and, "Accuracy, Repeatability, and Reproducibility of Regularized Inversions for Abdominal Quantitative Susceptibility Mapping," in *Proceedings 30. Annual Meeting International Society for Magnetic Resonance in Medicine*, vol. 30, (London, England), p. 0109, `http://archive.ismrm.org/2022/0109.html`, 2022.

[23] M. N. Diefenbach, J. Meineke, S. Ruschke, T. Baum, A. Gersing, and D. C. Karampinos, "On the sensitivity of quantitative susceptibility mapping for measuring trabecular bone density," *Magnetic Resonance in Medicine*, 2018.

[24] Y. Guo, Y. Chen, X. Zhang, Y. Mei, P. Yi, Y. Wang, Q. Feng, L. L. Tegola, G. Guglielmi, X. Zhang, and Y. Feng, "Magnetic susceptibility and fat content in the lumbar spine of postmenopausal women with varying bone mineral density," *Journal of Magnetic Resonance Imaging*, vol. 49, no. 4, pp. 1020–1028, 2018.

[25] Y. Chen, Y. Guo, X. Zhang, Y. Mei, Y. Feng, and X. Zhang, "Bone susceptibility mapping with MRI is an alternative and reliable biomarker of osteoporosis in

postmenopausal women," *European Radiology*, vol. 28, no. 12, pp. 5027–5034, 2018.

[26] C. Caussy, S. B. Reeder, C. B. Sirlin, and R. Loomba, "Noninvasive, quantitative assessment of liver fat by MRI-PDFF as an endpoint in nash trials," *Hepatology*, vol. 68, no. 2, pp. 763–772, 2018.

[27] J. K. Stelter, C. Boehm, S. Ruschke, K. Weiss, M. N. Diefenbach, M. Wu, T. Borde, G. P. Schmidt, M. R. Makowski, E. M. Fallenberg, and D. C. Karampinos, "Hierarchical multi-resolution graph-cuts for water-fat-silicone separation in breast mri," *IEEE Transactions on Medical Imaging*, vol. 41, no. 11, pp. 3253–3265, 2022.

[28] E. Alonso-Ortiz, I. R. Levesque, and G. B. Pike, "MRI-based myelin water imaging: a technical review," *Magnetic Resonance in Medicine*, vol. 73, no. 1, pp. 70–81, 2014.

[29] F. Wiesinger, E. Weidl, M. I. Menzel, M. A. Janich, O. Khegai, S. J. Glaser, A. Haase, M. Schwaiger, and R. F. Schulte, "IDEAL spiral CSI for dynamic metabolic MR imaging of hyperpolarized [1-13c]pyruvate," *Magnetic Resonance in Medicine*, vol. 68, no. 1, pp. 8–16, 2011.

[30] J. Berglund, H. Ahlström, and J. Kullberg, "Model-based mapping of fat unsaturation and chain length by chemical shift imaging-phantom validation and in vivo feasibility," *Magnetic Resonance in Medicine*, vol. 68, no. 6, pp. 1815–1827, 2012.

[31] M. N. Diefenbach, C. Liu, and D. C. Karampinos, "Generalized parameter estimation in multi-echo gradient-echo-based chemical species separation," *Quantitative Imaging in Medicine and Surgery*, vol. 10, no. 3, pp. 554–567, 2020.

[32] J. Ren, I. Dimitrov, A. D. Sherry, and C. R. Malloy, "Composition of adipose tissue and marrow fat in humans by1h nmr at 7 tesla," *Journal of Lipid Research*, vol. 49, no. 9, pp. 2055–2062, 2008.

[33] G. Hamilton, T. Yokoo, M. Bydder, I. Cruite, M. E. Schroeder, C. B. Sirlin, and M. S. Middleton, "In vivo characterization of the liver fat 1H MR spectrum," *NMR in Biomedicine*, vol. 24, no. 7, pp. 784–790, 2010.

[34] G. Hamilton, A. N. Schlein, M. S. Middleton, C. A. Hooker, T. Wolfson, A. C. Gamst, R. Loomba, and C. B. Sirlin, "In vivo triglyceride composition of abdomi-

nal adipose tissue measured by 1H MRS at 3T," *Journal of Magnetic Resonance Imaging*, vol. 45, no. 5, pp. 1455–1463, 2016.

[35] H. Yu, A. Shimakawa, C. A. McKenzie, E. Brodsky, J. H. Brittain, and S. B. Reeder, "Multiecho water–fat separation and simultaneous R2* estimation with multifrequency fat spectrum modeling," *Magnetic Resonance in Medicine*, vol. 60, no. 5, pp. 1122–1134, 2008.

[36] S. B. Reeder, A. R. Pineda, Z. Wen, A. Shimakawa, H. Yu, J. H. Brittain, G. E. Gold, C. H. Beaulieu, and N. J. Pelc, "Iterative decomposition of water and fat with echo asymmetry and least-squares estimation (IDEAL): Application with fast spin-echo imaging," *Magnetic Resonance in Medicine*, vol. 54, no. 3, pp. 636–644, 2005.

[37] D. Hernando, J. P. Haldar, B. P. Sutton, J. Ma, P. Kellman, and Z.-P. Liang, "Joint estimation of water/fat images and field inhomogeneity map," *Magnetic Resonance in Medicine*, vol. 59, no. 3, pp. 571–580, 2008.

[38] J. Berglund and M. Skorpil, "Multi-scale graph-cut algorithm for efficient water–fat separation," *Magnetic Resonance in Medicine*, vol. 78, no. 3, pp. 941–949, 2016.

[39] D. Hernando, P. Kellman, J. P. Haldar, and Z.-P. Liang, "Robust water/fat separation in the presence of large field inhomogeneities using a graph cut algorithm," *Magnetic Resonance in Medicine*, vol. 63, no. 1, pp. 79-90, 2009.

[40] C. Cui, A. Shah, X. Wu, and M. Jacob, "A rapid 3D fat-water decomposition method using globally optimal surface estimation (R-GOOSE)," *Magnetic Resonance in Medicine*, vol. 79, no. 4, pp. 2401–2407, 2017.

[41] F. Schweser, S. D. Robinson, L. de Rochefort, W. Li, and K. Bredies, "An illustrated comparison of processing methods for phase MRI and QSM: Removal of background field contributions from sources outside the region of interest," *NMR in Biomedicine*, vol. 30, no. 4, p. e3604, 2016.

[42] D. Zhou, T. Liu, P. Spincemaille, and Y. Wang, "Background field removal by solving the laplacian boundary value problem," *NMR in Biomedicine*, vol. 27, no. 3, pp. 312–319, 2014.

[43] A. T. Van, M. N. Diefenbach, J. Meineke, H. Kooijman, A. Haase, and D. C. Karampinos, "Background field removal in the presence of subcutaneous fat in body QSM," in *International Workshop on MRI Phase Contrast & Quantitative Susceptibility Mapping*, vol. 4, (Vienna, Austria), p. 11, `http://www.neuroimaging.at/qsm2016/`, 2016. Poster presentation.

[44] T. Liu, I. Khalidov, L. de Rochefort, P. Spincemaille, J. Liu, A. J. Tsiouris, and Y. Wang, "A novel background field removal method for MRI using projection onto dipole fields (PDF)," *NMR in Biomedicine*, vol. 24, no. 9, pp. 1129–1136, 2011.

[45] R. A. Kennedy and P. Sadeghi, *Hilbert Space Methods in Signal Processing*. Cambridge University Press, 2013.

[46] J. Liu, T. Liu, L. de Rochefort, J. Ledoux, I. Khalidov, W. Chen, A. J. Tsiouris, C. Wisnieff, P. Spincemaille, M. R. Prince, and Y. Wang, "Morphology enabled dipole inversion for quantitative susceptibility mapping using structural consistency between the magnitude image and the susceptibility map," *NeuroImage*, vol. 59, no. 3, pp. 2560–2568, 2012.

[47] T. Liu, C. Wisnieff, M. Lou, W. Chen, P. Spincemaille, and Y. Wang, "Nonlinear formulation of the magnetic field to source relationship for robust quantitative susceptibility mapping," *Magnetic Resonance in Medicine*, vol. 69, no. 2, pp. 467–476, 2012.

[48] Z. Liu, Y. Kee, D. Zhou, Y. Wang, and P. Spincemaille, "Preconditioned total field inversion (TFI) method for quantitative susceptibility mapping," *Magnetic Resonance in Medicine*, vol. 78, pp. 303–315, Jul 2016.

[49] Z. Liu, Y. Wen, P. Spincemaille, S. Zhang, Y. Yao, T. D. Nguyen, and Y. Wang, "Automated adaptive preconditioner for quantitative susceptibility mapping," *Magnetic Resonance in Medicine*, vol. 83, no. 1, pp. 271–285, 2019.

[50] Y. Wen, P. Spincemaille, T. Nguyen, J. Cho, I. Kovanlikaya, J. Anderson, G. Wu, B. Yang, M. Fung, K. Li, D. Kelley, N. Benhamo, and Y. Wang, "Multiecho complex total field inversion method (mcTFI) for improved signal modeling in quantitative susceptibility mapping," *Magnetic Resonance in Medicine*, vol. 86, no. 4, pp. 2165–2178, 2021.

[51] NVIDIA, "Cuda, release: 12.1," 2023.

[52] M. Bydder, T. Yokoo, G. Hamilton, M. S. Middleton, A. D. Chavez, J. B. Schwimmer, J. E. Lavine, and C. B. Sirlin, "Relaxation effects in the quantification of fat using gradient echo imaging," *Magnetic Resonance Imaging*, vol. 26, no. 3, pp. 347–359, 2008.

[53] H. Yu, S. B. Reeder, A. Shimakawa, J. H. Brittain, and N. J. Pelc, "Field map estimation with a region growing scheme for iterative 3-point water–fat decomposition," *Magnetic Resonance in Medicine*, vol. 54, no. 4, pp. 1032–1039, 2005.

[54] D. Hernando, P. Kellman, J. Haldar, and Z.-P. Liang, "Estimation of water/fat images, B0 field map and T2* map using VARPRO," in *ISMRM 16th Scientific Meeting & Exhibition*, vol. 16, (Toronto, Canada), p. 1517, `https://cds.ismrm.org/ismrm-2008/files/01517.pdf`, 2008.

[55] S. Ruschke, C. Zoellner, C. Boehm, M. N. Diefenbach, and D. C. Karampinos, *Chapter 14 - Chemical Shift Encoding-Based Water-Fat Separation*, vol. 7 of *Advances in Magnetic Resonance Technology and Applications*. Academic Press, 2022.

[56] J. Berglund, L. Johansson, H. Ahlström, and J. Kullberg, "Three-point dixon method enables whole-body water and fat imaging of obese subjects," *Magnetic Resonance in Medicine*, vol. 63, no. 6, pp. 1659–1668, 2010.

[57] Q.-S. Xiang, "Two-point water–fat imaging with partially-opposed-phase (POP) acquisition: An asymmetric dixon method," *Magnetic Resonance in Medicine*, vol. 56, no. 3, pp. 572–584, 2006.

[58] Q.-S. Xiang and L. An, "Water–fat imaging with direct phase encoding," *Journal of Magnetic Resonance Imaging*, vol. 7, no. 6, pp. 1002–1015, 1997.

[59] W. Lu and B. A. Hargreaves, "Multiresolution field map estimation using golden section search for water–fat separation," *Magnetic Resonance in Medicine*, vol. 60, no. 1, pp. 236–244, 2008.

[60] J. Berglund, H. Ahlström, L. Johansson, and J. Kullberg, "Two-point dixon method with flexible echo times," *Magnetic Resonance in Medicine*, vol. 65, no. 4, pp. 994–1004, 2010.

[61] H. Eggers, B. Brendel, A. Duijndam, and G. Herigault, "Dual-echo dixon imaging with flexible choice of echo times," *Magnetic Resonance in Medicine*, vol. 65, no. 1, pp. 96–107, 2010.

[62] J. Tsao and Y. Jiang, "Hierarchical IDEAL: Fast, robust, and multiresolution separation of multiple chemical species from multiple echo times," *Magnetic Resonance in Medicine*, vol. 70, no. 1, pp. 155–159, 2012.

[63] C. Cui, X. Wu, J. D. Newell, and M. Jacob, "Fat water decomposition using globally optimal surface estimation (GOOSE) algorithm," *Magnetic Resonance in Medicine*, vol. 73, no. 3, pp. 1289–1299, 2014.

[64] D. Zhou, J. Cho, J. Zhang, P. Spincemaille, and Y. Wang, "Susceptibility underestimation in a high-susceptibility phantom: Dependence on imaging resolution, magnitude contrast, and other parameters," *Magnetic Resonance in Medicine*, vol. 78, no. 3, pp. 1080–1086, 2016.

[65] S. D. Sharma, N. S. Artz, D. Hernando, D. E. Horng, and S. B. Reeder, "Improving chemical shift encoded water–fat separation using object-based information of the magnetic field inhomogeneity," *Magnetic Resonance in Medicine*, vol. 73, pp. 597–604, feb 2014.

[66] M. N. Diefenbach, S. Ruschke, H. Eggers, J. Meineke, E. J. Rummeny, and D. C. Karampinos, "Improving chemical shift encoding-based water–fat separation based on a detailed consideration of magnetic field contributions," *Magnetic Resonance in Medicine*, vol. 80, no. 3, pp. 990–1004, 2018.

[67] K. Shmueli, J. A. de Zwart, P. van Gelderen, T.-Q. Li, S. J. Dodd, and J. H. Duyn, "Magnetic susceptibility mapping of brain tissue in vivo using MRI phase data," *Magnetic Resonance in Medicine*, vol. 62, no. 6, pp. 1510–1522, 2009.

[68] C. Milovic, B. Bilgic, B. Zhao, J. Acosta-Cabronero, and C. Tejos, "Fast nonlinear susceptibility inversion with variational regularization," *Magnetic Resonance in Medicine*, vol. 80, no. 2, pp. 814–821, 2018.

[69] T. D. Nguyen, Y. Wen, J. Du, Z. Liu, K. Gillen, P. Spincemaille, A. Gupta, Q. Yang, and Y. Wang, "Quantitative susceptibility mapping of carotid plaques using nonlinear total field inversion: Initial experience in patients with significant carotid stenosis," *Magnetic Resonance in Medicine*, vol. 84, no. 3, pp. 1501–1509, 2020.

[70] W. Li, A. V. Avram, B. Wu, X. Xiao, and C. Liu, "Integrated laplacian-based phase unwrapping and background phase removal for quantitative susceptibility mapping," *NMR in Biomedicine*, vol. 27, no. 2, pp. 219–227, 2013.

[71] S. D. Robinson, K. Bredies, D. Khabipova, B. Dymerska, J. P. Marques, and F. Schweser, "An illustrated comparison of processing methods for MR phase imaging and QSM: Combining array coil signals and phase unwrapping," *NMR in Biomedicine*, vol. 30, no. 4, p. e3601, 2016.

[72] S. Witoszynskyj, A. Rauscher, J. R. Reichenbach, and M. Barth, "Phase unwrapping of MR images using Phi UN - a fast and robust region growing algorithm," *Medical Image Analysis*, vol. 13, no. 2, pp. 257–268, 2009.

[73] V. Fortier and I. R. Levesque, "Phase processing for quantitative susceptibility mapping of regions with large susceptibility and lack of signal," *Magnetic Resonance in Medicine*, 2017.

[74] X. Wang, "Phase unwrapping based on branch cut placing and reliability ordering," *Optical Engineering*, vol. 44, no. 5, p. 055601, 2005.

[75] M. Jenkinson, "Fast, automated,n-dimensional phase-unwrapping algorithm," *Magnetic Resonance in Medicine*, vol. 49, no. 1, pp. 193–197, 2002.

[76] H. S. Abdul-Rahman, M. A. Gdeisat, D. R. Burton, M. J. Lalor, F. Lilley, and C. J. Moore, "Fast and robust three-dimensional best path phase unwrapping algorithm," *Applied Optics*, vol. 46, no. 26, p. 6623, 2007.

[77] A. Karsa and K. Shmueli, "SEGUE: a speedy region-growing algorithm for unwrapping estimated phase," *IEEE Transactions on Medical Imaging*, vol. 38, no. 6, pp. 1347–1357, 2019.

[78] B. Dymerska, K. Eckstein, B. Bachrata, B. Siow, S. Trattnig, K. Shmueli, and S. D. Robinson, "Phase unwrapping with a rapid opensource minimum spanning tree algorithm (ROMEO)," *Magnetic Resonance in Medicine*, vol. 85, no. 4, pp. 2294–2308, 2020.

[79] F. Schweser, A. Deistung, B. W. Lehr, and J. R. Reichenbach, "Quantitative imaging of intrinsic magnetic tissue properties using MRI signal phase: An approach to in vivo brain iron metabolism?," *NeuroImage*, vol. 54, no. 4, pp. 2789–2807, 2011.

[80] R. Topfer, F. Schweser, A. Deistung, J. R. Reichenbach, and A. H. Wilman, "Sharp edges: Recovering cortical phase contrast through harmonic extension," *Magnetic Resonance in Medicine*, vol. 73, no. 2, pp. 851–856, 2014.

[81] B. Wu, W. Li, A. Guidon, and C. Liu, "Whole brain susceptibility mapping using compressed sensing," *Magnetic Resonance in Medicine*, vol. 67, no. 1, pp. 137–147, 2011.

[82] H. Sun and A. H. Wilman, "Background field removal using spherical mean value filtering and tikhonov regularization," *Magnetic Resonance in Medicine*, vol. 71, no. 3, pp. 1151–1157, 2013.

[83] Y. Wen, D. Zhou, T. Liu, P. Spincemaille, and Y. Wang, "An iterative spherical mean value method for background field removal in MRI," *Magnetic Resonance in Medicine*, vol. 72, no. 4, pp. 1065–1071, 2013.

[84] I. Chatnuntawech, P. McDaniel, S. F. Cauley, B. A. Gagoski, C. Langkammer, A. Martin, P. E. Grant, L. L. Wald, K. Setsompop, E. Adalsteinsson, and B. Bilgic, "Single-step quantitative susceptibility mapping with variational penalties," *NMR in Biomedicine*, vol. 30, no. 4, p. e3570, 2016.

[85] M. N. Diefenbach, A. Van, J. Meineke, A. Scharr, J. S. Kirschke, A. Gersing, T. Baum, B. Schwaiger, and D. C. Karampinos, "Vertebral Column Quantitative Susceptibility Mapping using Joint Background Field Removal and Dipole Inversion," in *Proceedings 26. Annual Meeting International Society for Magnetic Resonance in Medicine*, vol. 26, (Paris, France), p. 0191, `http://archive.ismrm.org/2018/0191.html`, 2018. Oral presentation, Magna cum laude merit award.

[86] T. Liu, D. Zhou, P. Spincemaille, and Y. Wang, "Differential approach to quantitative susceptibility mapping without background field removal," in *Proceedings 22. Annual Meeting International Society for Magnetic Resonance in Medicine*, vol. 22, (Milan, Italy), p. 0597, `http://archive.ismrm.org/2014/0597.html`, 2014.

[87] S. Ciraci, K. Gumus, S. Doganay, M. Dundar, G. K. Ozcora, S. Gorkem, H. Per, and A. Coskun, "Diagnosis of intracranial calcification and hemorrhage in pediatric patients: Comparison of quantitative susceptibility mapping and phase images of susceptibility-weighted imaging," *Diagnostic and Interventional Imaging*, vol. 98, no. 10, pp. 707–714, 2017.

[88] W. Chen, W. Zhu, I. Kovanlikaya, A. Kovanlikaya, T. Liu, S. Wang, C. Salustri, and Y. Wang, "Intracranial calcifications and hemorrhages: Characterization with quantitative susceptibility mapping," *Radiology*, vol. 270, no. 2, pp. 496–505, 2014.

[89] L. de Rochefort, T. Liu, B. Kressler, J. Liu, P. Spincemaille, V. Lebon, J. Wu, and Y. Wang, "Quantitative susceptibility map reconstruction from MR phase data using bayesian regularization: Validation and application to brain imaging," *Magnetic Resonance in Medicine*, vol. 63, no. 1, pp. 194–206, 2009.

[90] C. Milovic, B. Bilgic, B. Zhao, C. Langkammer, C. Tejos, and J. Acosta-Cabronero, "Weak-harmonic regularization for quantitative susceptibility mapping," *Magnetic Resonance in Medicine*, 2018.

[91] M. Lambert, C. Tejos, C. Langkammer, and C. Milovic, "Hybrid data fidelity term approach for quantitative susceptibility mapping," *Magnetic Resonance in Medicine*, vol. 88, no. 2, pp. 962–972, 2022.

[92] S. K. Iyer, B. F. Moon, N. Josselyn, R. M. Kurtz, J. W. Song, J. B. Ware, S. A. Nabavizadeh, and W. R. Witschey, "Quantitative susceptibility mapping using plug-and-play alternating direction method of multipliers," *Scientific Reports*, vol. 12, no. 1, p. 21679, 2022.

[93] Z. Liu, P. Spincemaille, Y. Yao, Y. Zhang, and Y. Wang, "MEDI+0: Morphology enabled dipole inversion with automatic uniform cerebrospinal fluid zero reference for quantitative susceptibility mapping," *Magnetic Resonance in Medicine*, vol. 79, no. 5, pp. 2795–2803, 2017.

[94] B. Bilgic, I. Chatnuntawech, A. P. Fan, K. Setsompop, S. F. Cauley, L. L. Wald, and E. Adalsteinsson, "Fast image reconstruction with l2-regularization," *Journal of Magnetic Resonance Imaging*, vol. 40, no. 1, pp. 181–191, 2013.

[95] Q. C. . O. Committee, B. Bilgic, C. Langkammer, J. P. Marques, J. Meineke, C. Milovic, and F. Schweser, "QSM reconstruction challenge 2.0: Design and report of results," *Magnetic Resonance in Medicine*, vol. 86, no. 3, pp. 1241–1255, 2021.

[96] B. Kressler, L. de Rochefort, T. Liu, P. Spincemaille, Q. Jiang, and Y. Wang, "Nonlinear regularization for per voxel estimation of magnetic susceptibility distri-

butions from MRI field maps," *IEEE Transactions on Medical Imaging*, vol. 29, no. 2, pp. 273–281, 2010.

[97] C. Langkammer, K. Bredies, B. A. Poser, M. Barth, G. Reishofer, A. P. Fan, B. Bilgic, F. Fazekas, C. Mainero, and S. Ropele, "Fast quantitative susceptibility mapping using 3D EPI and total generalized variation," *NeuroImage*, vol. 111, pp. 622–630, 2015.

[98] C. Langkammer, F. Schweser, K. Shmueli, C. Kames, X. Li, L. Guo, C. Milovic, J. Kim, H. Wei, K. Bredies, S. Buch, Y. Guo, Z. Liu, J. Meineke, A. Rauscher, J. P. Marques, and B. Bilgic, "Quantitative susceptibility mapping: Report from the 2016 reconstruction challenge," *Magnetic Resonance in Medicine*, vol. 79, no. 3, pp. 1661–1673, 2017.

[99] C. Langkammer, F. Schweser, N. Krebs, A. Deistung, W. Goessler, E. Scheurer, K. Sommer, G. Reishofer, K. Yen, F. Fazekas, S. Ropele, and J. R. Reichenbach, "Quantitative susceptibility mapping (QSM) as a means to measure brain iron? a post mortem validation study," *NeuroImage*, vol. 62, no. 3, pp. 1593–1599, 2012.

[100] G. de Hollander, M. C. Keuken, P.-L. Bazin, M. Weiss, J. Neumann, K. Reimann, M. Wähnert, R. Turner, B. U. Forstmann, and A. Schäfer, "A gradual increase of iron toward the medial-inferior tip of the subthalamic nucleus," *Human Brain Mapping*, vol. 35, no. 9, pp. 4440–4449, 2014.

[101] J. H. O. Barbosa, A. C. Santos, V. Tumas, M. Liu, W. Zheng, E. M. Haacke, and C. E. G. Salmon, "Quantifying brain iron deposition in patients with parkinson's disease using quantitative susceptibility mapping, R2 and R2*," *Magnetic Resonance Imaging*, vol. 33, no. 5, pp. 559–565, 2015.

[102] C. Wisnieff, S. Ramanan, J. Olesik, S. Gauthier, Y. Wang, and D. Pitt, "Quantitative susceptibility mapping (QSM) of white matter multiple sclerosis lesions: Interpreting positive susceptibility and the presence of iron," *Magnetic Resonance in Medicine*, vol. 74, no. 2, pp. 564–570, 2014.

[103] L. Chen, A. Soldan, K. Oishi, A. Faria, Y. Zhu, M. Albert, P. C. M. van Zijl, and X. Li, "Quantitative susceptibility mapping of brain iron and β-amyloid in MRI and PET relating to cognitive performance in cognitively normal older adults," *Radiology*, vol. 298, no. 2, pp. 353–362, 2021.

[104] K. R. Li, J. Avecillas-Chasin, T. D. Nguyen, K. M. Gillen, A. Dimov, E. Chang, C. Skudin, B. H. Kopell, Y. Wang, and A. Shtilbans, "Quantitative evaluation of brain iron accumulation in different stages of parkinson's disease," *Journal of Neuroimaging*, vol. 32, no. 2, pp. 363–371, 2021.

[105] W. Chen, S. A. Gauthier, A. Gupta, J. Comunale, T. Liu, S. Wang, M. Pei, D. Pitt, and Y. Wang, "Quantitative susceptibility mapping of multiple sclerosis lesions at various ages," *Radiology*, vol. 271, no. 1, pp. 183–192, 2014.

[106] X. Li, D. M. Harrison, H. Liu, C. K. Jones, J. Oh, P. A. Calabresi, and P. C. van Zijl, "Magnetic susceptibility contrast variations in multiple sclerosis lesions," *Journal of Magnetic Resonance Imaging*, vol. 43, no. 2, pp. 463–473, 2015.

[107] V. Lambrecht, J. Hanspach, A. Hoffmann, L. Seyler, A. Mennecke, S. Straub, F. Marxreiter, T. Bäuerle, F. B. Laun, and J. Winkler, "Quantitative susceptibility mapping depicts severe myelin deficit and iron deposition in a transgenic model of multiple system atrophy," *Experimental Neurology*, vol. 329, p. 113314, 2020.

[108] A. Deistung, F. Schweser, B. Wiestler, M. Abello, M. Roethke, F. Sahm, W. Wick, A. M. Nagel, S. Heiland, H.-P. Schlemmer, M. Bendszus, J. R. Reichenbach, and A. Radbruch, "Quantitative susceptibility mapping differentiates between blood depositions and calcifications in patients with glioblastoma," *PLoS ONE*, vol. 8, no. 3, p. e57924, 2013.

[109] F. Schweser, K.-H. Hermann, A. Deistung, M. Atterbury, P. A. Baltzer, H. P. Burmeister, W. A. Kaiser, and J. R. Reichenbach, "Quantitative Magnetic Susceptibility Mapping (QSM) in Breast Disease Reveals Additional Information for MR-Based Characterization of Carcinoma Calcification," in *Proceedings 19. Annual Meeting International Society for Magnetic Resonance in Medicine*, vol. 19, (Montreal), p. 1014, `http://archive.ismrm.org/2011/1014.html`, 2011.

[110] A. V. Dimov, Z. Liu, P. Spincemaille, M. R. Prince, J. Du, and Y. Wang, "Bone quantitative susceptibility mapping using a chemical species-specific R2* signal model with ultrashort and conventional echo data," *Magnetic Resonance in Medicine*, vol. 79, no. 1, pp. 121–128, 2017.

[111] S. Straub, F. B. Laun, J. Emmerich, B. Jobke, H. Hauswald, S. Katayama, K. Herfarth, H.-P. Schlemmer, M. E. Ladd, C. H. Ziener, D. Bonekamp, and M. C. Röthke, "Potential of quantitative susceptibility mapping for detection of

prostatic calcifications," *Journal of Magnetic Resonance Imaging*, vol. 45, no. 3, pp. 889–898, 2016.

[112] H. Kan, T. Tsuchiya, M. Yamada, H. Kunitomo, H. Kasai, and Y. Shibamoto, "Delineation of prostatic calcification using quantitative susceptibility mapping: Spatial accuracy for magnetic resonance-only radiotherapy planning," *Journal of Applied Clinical Medical Physics*, vol. 23, no. 2, p. e13469, 2021.

[113] H. Lin, H. Wei, N. He, C. Fu, S. Cheng, J. Shen, B. Wang, X. Yan, C. Liu, and F. Yan, "Quantitative susceptibility mapping in combination with water–fat separation for simultaneous liver iron and fat fraction quantification," *European Radiology*, vol. 28, no. 8, pp. 3494–3504, 2018.

[114] R. Jafari, S. Sheth, P. Spincemaille, T. D. Nguyen, M. R. Prince, Y. Wen, Y. Guo, K. Deh, Z. Liu, D. Margolis, G. M. Brittenham, A. S. Kierans, and Y. Wang, "Rapid automated liver quantitative susceptibility mapping," *Journal of Magnetic Resonance Imaging*, vol. 50, no. 3, pp. 725–732, 2019.

[115] Y. Wen, T. D. Nguyen, Z. Liu, P. Spincemaille, D. Zhou, A. Dimov, Y. Kee, K. Deh, J. Kim, J. W. Weinsaft, and Y. Wang, "Cardiac quantitative susceptibility mapping (QSM) for heart chamber oxygenation," *Magnetic Resonance in Medicine*, 2017.

[116] N. S. Dellschaft, G. Hutchinson, S. Shah, N. W. Jones, C. Bradley, L. Leach, C. Platt, R. Bowtell, and P. A. Gowland, "The haemodynamics of the human placenta in utero," *PLOS Biology*, vol. 18, no. 5, p. e3000676, 2020.

[117] Z. Zun, K. Kapse, J. Quistorff, N. Andescavage, A. C. Gimovsky, H. Ahmadzia, and C. Limperopoulos, "Feasibility of QSM in the human placenta," *Magnetic Resonance in Medicine*, vol. 85, no. 3, pp. 1272–1281, 2020.

[118] B. Dymerska, K. Bohndorf, P. Schennach, A. Rauscher, S. Trattnig, and S. D. Robinson, "In vivo phase imaging of human epiphyseal cartilage at 7 T," *Magnetic Resonance in Medicine*, vol. 79, no. 4, pp. 2149–2155, 2017.

[119] C. Sun, K. Ghassaban, J. Song, Y. Chen, C. Zhang, F. Qu, J. Zhu, G. Wang, and E. M. Haacke, "Quantifying calcium changes in the fetal spine using quantitative susceptibility mapping as extracted from stage imaging," *European Radiology*, vol. 33, no. 1, pp. 606–614, 2022.

[120] J. Yoon, E. Gong, I. Chatnuntawech, B. Bilgic, J. Lee, W. Jung, J. Ko, H. Jung, K. Setsompop, G. Zaharchuk, E. Y. Kim, J. Pauly, and J. Lee, "Quantitative susceptibility mapping using deep neural network: QSMnet," *CoRR*, 2018.

[121] W. Jung, S. Bollmann, and J. Lee, "Overview of quantitative susceptibility mapping using deep learning – current status, challenges and opportunities," *arXiv*, p. 1912.05410, 2019.

[122] S. Bollmann, K. G. B. Rasmussen, M. Kristensen, R. G. Blendal, L. R. Østergaard, M. Plocharski, K. O'Brien, C. Langkammer, A. Janke, and M. Barth, "DeepQSM - using deep learning to solve the dipole inversion for quantitative susceptibility mapping," *NeuroImage*, vol. 195, pp. 373–383, 2019.

[123] Y. Gao, X. Zhu, B. A. Moffat, R. Glarin, A. H. Wilman, G. B. Pike, S. Crozier, F. Liu, and H. Sun, "xQSM: Quantitative susceptibility mapping with octave convolutional and noise-regularized neural networks," *NMR in Biomedicine*, vol. 34, no. 3, 2020.

[124] W. Jung, J. Yoon, S. Ji, J. Y. Choi, J. M. Kim, Y. Nam, E. Y. Kim, and J. Lee, "Exploring linearity of deep neural network trained QSM: QSMnet+," *NeuroImage*, vol. 211, p. 116619, 2020.

[125] A. Shah, J. Bai, M. D. Abramoff, and X. Wu, "Optimal multiple surface segmentation with convex priors in irregularly sampled space," *CoRR*, 2016.

[126] M. Wu, H. T. Mulder, P. Baron, E. Coello, M. I. Menzel, G. C. Rhoon, and A. Haase, "Correction of motion-induced susceptibility artifacts and B_0 drift during proton resonance frequency shift-based MR thermometry in the pelvis with background field removal methods," *Magnetic Resonance in Medicine*, vol. 84, no. 5, pp. 2495–2511, 2020.

[127] S. Ruschke, H. Eggers, H. Kooijman, M. N. Diefenbach, T. Baum, A. Haase, E. J. Rummeny, H. H. Hu, and D. C. Karampinos, "Correction of phase errors in quantitative water–fat imaging using a monopolar time-interleaved multi-echo gradient echo sequence," *Magnetic Resonance in Medicine*, vol. 78, no. 3, pp. 984–996, 2016.

[128] C. Boehm, A. Komenda, K. Weiss, J. K. Stelter, T. Borde, J. Meineke, M. R. Makowski, E. M. Fallenberg, and D. C. Karampinos, "High spatial resolution

quantitative susceptibility mapping using in-phase echoes enables the depiction of breast microcalcifications," in *Proceedings 31. Annual Meeting International Society for Magnetic Resonance in Medicine*, vol. 31, (Toronto, Canada), 2023. <u>Summa cum laude merit award</u>.

[129] Z. Qu, S. Yang, F. Xing, R. Tong, C. Yang, R. Guo, J. Huang, F. Lu, C. Fu, X. Yan, S. Hectors, K. Gillen, Y. Wang, C. Liu, S. Zhan, and J. Li, "Magnetic resonance quantitative susceptibility mapping in the evaluation of hepatic fibrosis in chronic liver disease: a feasibility study," *Quantitative Imaging in Medicine and Surgery*, vol. 11, no. 4, pp. 1170–1183, 2021.

[130] J. Du, J. C. Hermida, E. Diaz, J. Corbeil, R. Znamirowski, D. D. D'Lima, and G. M. Bydder, "Assessment of cortical bone with clinical and ultrashort echo time sequences," *Magnetic Resonance in Medicine*, vol. 70, no. 3, pp. 697–704, 2012.

[131] C. Böhm, M. N. Diefenbach, J. Meineke, and D. C. Karampinos, "Estimating Magnetic Susceptibility Within a Hollow Cylinder and its Implications in Body QSM," in *5th International Workshop on MRI Phase Contrast & QSM*, vol. 5, (Seoul, Korea), p. 26, 2019.

[132] S. Jerban, X. Lu, H. Jang, Y. Ma, B. Namiranian, N. Le, Y. Li, E. Y. Chang, and J. Du, "Significant correlations between human cortical bone mineral density and quantitative susceptibility mapping (QSM) obtained with 3D cones ultrashort echo time magnetic resonance imaging (ute-mri)," *Magnetic Resonance Imaging*, vol. 62, pp. 104–110, 2019.

[133] C. Böhm, S. Kronthaler, M. N. Diefenbach, J. Meineke, and D. C. Karampinos, "Sampling and Modeling UTE Signals is Important to Estimate Bone Marrow Susceptibility," in *Proceedings 28. Annual Meeting International Society for Magnetic Resonance in Medicine*, vol. 28, (online), p. 3212, `http://archive.ismrm.org/2020/3212.html`, 2020.

[134] M. Lustig, D. Donoho, and J. M. Pauly, "Sparse MRI: The application of compressed sensing for rapid MR imaging," *Magnetic Resonance in Medicine*, vol. 58, no. 6, pp. 1182–1195, 2007.

[135] M. Doneva, P. Börnert, H. Eggers, C. Stehning, J. Sénégas, and A. Mertins, "Compressed sensing reconstruction for magnetic resonance parameter mapping," *Magnetic Resonance in Medicine*, vol. 64, no. 4, pp. 1114–1120, 2010.

[136] M. Doneva, P. Börnert, H. Eggers, A. Mertins, J. Pauly, and M. Lustig, "Compressed sensing for chemical shift-based water–fat separation," *Magnetic Resonance in Medicine*, vol. 64, no. 6, pp. 1749–1759, 2010.

[137] Z. Zhou, A. Ma, Q. Feng, R. Wang, L. Cheng, X. Chen, X. Yang, K. Liao, Y. Miao, and Y. Qiu, "Super-resolution of brain tumor MRI images based on deep learning," *Journal of Applied Clinical Medical Physics*, vol. 23, no. 11, p. e13758, 2022.

[138] M. Chaika, S. Afat, D. Wessling, C. Afat, D. Nickel, S. Kannengiesser, J. Herrmann, H. Almansour, S. Männlin, A. E. Othman, and S. Gassenmaier, "Deep learning-based super-resolution gradient echo imaging of the pancreas: Improvement of image quality and reduction of acquisition time," *Diagnostic and Interventional Imaging*, vol. 104, no. 2, pp. 53–59, 2023.

[139] S. Maennlin, D. Wessling, J. Herrmann, H. Almansour, D. Nickel, S. Kannengiesser, S. Afat, and S. Gassenmaier, "Application of deep learning-based super-resolution to T1-weighted postcontrast gradient echo imaging of the chest," *La radiologia medica*, vol. 128, no. 2, pp. 184–190, 2023.

[140] A. F. Logullo, K. C. K. Prigenzi, C. C. B. A. Nimir, A. F. V. Franco, and M. S. D. A. Campos, "Breast microcalcifications: Past, present and future (review)," *Mol Clin Oncol*, vol. 16, p. 81, Feb. 2022.

[141] J. O. P. Wanders, K. Holland, N. Karssemeijer, P. H. M. Peeters, W. B. Veldhuis, R. M. Mann, and C. H. van Gils, "The effect of volumetric breast density on the risk of screen-detected and interval breast cancers: a cohort study," *Breast Cancer Research*, vol. 19, no. 1, p. 67, 2017.

[142] S. Saadatmand, I.-M. Obdeijn, E. J. Rutgers, J. C. Oosterwijk, R. A. Tollenaar, G. H. Woldringh, E. Bergers, C. Verhoef, E. A. Heijnsdijk, M. J. Hooning, H. J. de Koning, and M. M. Tilanus-Linthorst, "Survival benefit in women with *BRCA1* mutation or familial risk in the MRI screening study (MRISC)," *International Journal of Cancer*, vol. 137, no. 7, pp. 1729–1738, 2015.

[143] R. S. C. Guindalini, Y. Zheng, H. Abe, K. Whitaker, T. F. Yoshimatsu, T. Walsh, D. Schacht, K. Kulkarni, D. Sheth, M. S. Verp, A. R. Bradbury, J. Churpek, E. Obeid, J. Mueller, G. Khramtsova, F. Liu, A. Raoul, H. Cao, I. L. Romero, S. Hong, R. Livingston, N. Jaskowiak, X. Wang, M. Debiasi, C. C. Pritchard, M.-C. King, G. Karczmar, G. M. Newstead, D. Huo, and O. I. Olopade, "Intensive

surveillance with biannual dynamic contrast-enhanced magnetic resonance imaging downstages breast cancer in *BRCA1* mutation carriers," *Clinical Cancer Research*, vol. 25, no. 6, pp. 1786–1794, 2019.

[144] C. Colin, N. Foray, G. D. Leo, and F. Sardanelli, "Radiation induced breast cancer risk in BRCA mutation carriers from low-dose radiological exposures: a systematic review," *Radioprotection*, vol. 52, no. 4, pp. 231–240, 2017.

[145] S. Juanpere, E. Perez, O. Huc, N. Motos, J. Pont, and S. Pedraza, "Imaging of breast implants-a pictorial review," *Insights into Imaging*, vol. 2, no. 6, pp. 653–670, 2011.

[146] A. Stivala, K. Rem, S. Leuzzi, V. Moris, C. François, M. Revol, and S. Cristofari, "Efficacy of ultrasound, mammography and magnetic resonance imaging in detecting breast implant rupture: a retrospective study of 175 reconstructive and aesthetic sub-pectoral breast augmentation cases," *Journal of Plastic, Reconstructive amp; Aesthetic Surgery*, vol. 70, no. 11, pp. 1520–1526, 2017.

[147] L. Elahi, M.-G. Meuwly, J.-Y. Meuwly, W. Raffoul, and N. Koch, "Management of contralateral breast and axillary nodes silicone migration after implant rupture," *Plastic and Reconstructive Surgery - Global Open*, vol. 10, no. 5, p. e4290, 2022.

Acknowledgments

"There has not been a single bad day"

After the last meeting with my supervisors and mentor where we agreed that I can submit my doctoral thesis, I uttered the above quote, and I sincerely meant it. These past few years have been an incredible journey, fueled primarily by the exceptional guidance of the best doctoral supervisor one could ask for, Prof. Dr. Dimitrios Karampinos. He is not only a dedicated educator and a caring mentor but also a true friend. I will be forever grateful for my time in the Body Magnetic Resonance Research Group (BMRR) and the support during the challenging times when my family faced adversity.

I would like to express my appreciation to all the members of the BMRR family for the great times we shared in the office, during lunch, and at conferences. It truly is a remarkable research group build by Dimitris. Throughout my years as a PhD student in the group, I've had the pleasure of mentoring, guiding, and befriending brilliant master's students such as Julio Oscanoa, who went on to pursue a PhD at Stanford, and Jonathan Stelter, who joined our group and became a valued collaborator.

I would also like to thank my mentor Dr. Jakob Meineke, with whom I had the pleasure of working in the Philips Research Lab, welcoming him to our lab, and enjoying memorable times at conferences, particularly the QSM conferences in Seoul and Lucca. He ignited my passion for inverse problem-solving early in my PhD, a skill that carried me throughout my entire journey. I am immensely proud of our sustainability project, which I hope will significantly influence future ISMRM conference site selections.

I firmly believe that much of my creativity and the ideas necessary for conducting research stem not from my time at the desk, but from the leisure activities I cherish—hiking, skiing, and climbing, to name just a few. I am grateful to everyone who has accompanied me on these adventures and shared their valuable time away from work with me.

Lastly, I want to express my deepest gratitude to my family. To my parents, who have always supported me and my young family; to my partner Anne, who is now my wife, and has been my pillar of strength throughout this journey; and to my son Mattis,

who was born a few months ago and accompanied me during the entire thesis-writing process. I dedicate this work to all of you.